

UNIVERSITÉ PARIS DIDEROT (PARIS 7)
ÉCOLE DOCTORALE 127 : ASTRONOMIE & ASTROPHYSIQUE

THÈSE DE DOCTORAT
ANITA ZANELLA
SERVICE D'ASTROPHYSIQUE – CEA SACLAY

STRUCTURAL PROPERTIES
OF CLUMPY GALAXIES AND SPHEROIDS
AT HIGH REDSHIFT

THÈSE DIRIGÉE PAR EMERIC LE FLOC'H

SOUTENUE LE 21 SEPTEMBRE 2016

JURY

Simona Mei	Présidente
Mauro Giavalisco	Rapporteur
Stijn Wuyts	Rapporteur
Françoise Combes	Examinatrice
Olivier Le Fèvre	Examineur
Claudia Scarlata	Examinatrice
Emeric Le Floc'h	Directeur de thèse

Abstract

This thesis explores with a two-fold approach the still unanswered question of how distant galaxies evolve through cosmic time: on one side it focusses on star-forming clumpy galaxies, on the other it investigates the size evolution of passive compact ones.

The irregular morphology of a large fraction of star-forming galaxies at cosmic noon (redshift $1 \lesssim z \lesssim 3$) was firstly pointed out thanks to the high spatial resolution and sensitivity of the *Hubble Space Telescope (HST)*. Bright patches of star formation (clumps) have been identified in ultraviolet and optical rest-frame images: they appear to have blue colors and to form new stars at a high rate. Clumps can contribute up to $\sim 40\%$ of the total star formation rate of the host galaxy, but they contain only $\sim 10\%$ of the total mass. Despite they have been observed in high-redshift galaxies since a while, clumps nature and fate are still highly debated, and numerical simulations present very different predictions. Violent gravitational disk instability in gas-rich, turbulent, high-redshift galaxies has been proposed as the main cause for in-situ clumps formation, although a fraction of them might have an ex-situ origin (e.g. small companions that merged with the host galaxy, or clumps of gas that have been accreted). Furthermore, clumps contribution to galaxy evolution is highly debated: it is not clear yet if they are long-lived and can migrate inward being responsible for bulge growth, or if stellar feedback rapidly disrupts them. In this thesis I analyze a sample of ~ 50 clumpy galaxies at redshift $1 \lesssim z \lesssim 3$ observed with *HST*/Wide Field Camera 3 (WFC3) providing both broad-band images and slitless spectroscopic data. This allowed me to select and study clumps with young and intermediate ages that show very bright emission lines, sensitive to the gas ionized by O and B stars. It enabled the investigation of a portion of the parameter space that was not explored by previous studies based on broad-band imaging only, since the latter only probes longer timescales (ages $\gtrsim 100$ Myr) than the emission lines. From both the in-depth study of an extremely young clump (age $\lesssim 10$ Myr) that we discovered in the disk of a galaxy at redshift $z \sim 2$, and the analysis of the full statistical sample of clumps that we assembled, I concluded that at least some clumps

form in-situ due to violent disk instability, and at young ages they show an enhanced, starburst-like star formation efficiency. Finally, I computed the clump formation rate and lifetime, concluding that clumps likely have typical lifetimes of ~ 500 Myr, supporting numerical simulations indicating that clumps are long-lived and could migrate inward playing an important role in bulge growth.

Cosmological and hydrodynamical simulations show that clumps migration can bring inward large amounts of gas due to gravitational torques, leading to disk contraction and stabilization due to the growth of the central bulge. This might be linked with the formation of compact, passive galaxies that are commonly observed at high redshift. Thanks to *HST* observations in fact, it has been discovered a population of passive galaxies at redshift ~ 2 with significant smaller sizes, at fixed stellar mass, than local counterparts. This discovery has ignited an important debate concerning the possible mechanisms that could inflate the galaxy sizes without altering much their mass. Two main scenarios are generally counterposed. On one side, it is possible to assume that galaxies individually change their size as time passes: minor mergers could be the underlying cause. On the other side, it is possible that on average the population of passive galaxies changes with time with larger quenched sources appearing later: this could be linked to the evolution of the average density of the Universe due to Hubble expansion, with lower density halos collapsing later in time than denser ones. The relative importance of the two mechanisms is still controversial. In this thesis I analyze a sample of 32 passive galaxies at redshift $z \sim 1.5$ observed with *HST*/WFC3 as part of the WFC3 Infrared Spectroscopic Parallel survey. No clear trends have been found between the size and age (or formation redshift) of our sample galaxies, at fixed stellar mass. It indicates that if a relation exists between the galaxy age and its distance from the mass – size relation, it is rather shallow. At face value, this result suggests that multiple minor mergers could be the main drivers of the observed time evolution of the mass – size relation of passive galaxies.

The work started during this thesis will be further developed thanks to new observations taken as part of accepted proposals that I led as PI or I participated to as co-I. In particular the extremely young clump that was discovered in a disk galaxy at redshift $z \sim 2$ will be soon followed-up with VLT/SINFONI and ALMA, and recently it has been observed with VLT/MUSE and VLT/KMOS. These new data will allow me to conduct an in-depth study of the nature and physics of this star-forming region that can be considered as a representative case of high-redshift young clumps. Furthermore, this pilot study will provide the needed information to propose for future multi-wavelength follow-ups of statistical samples of high-redshift clumps.

Résumé

Cette thèse explore avec une double approche la question ouverte des mécanismes selon lesquels les galaxies lointaines évoluent au cours du temps. D'un côté elle se concentre sur l'étude des galaxies irrégulières qui forment leurs étoiles activement, de l'autre côté elle cherche la cause de l'évolution en taille des galaxies passives et compactes.

La morphologie irrégulière d'une grande fraction de galaxies qui produisent activement des étoiles au pic de l'histoire de la formation stellaire de l'Univers (redshift $1 \lesssim z \lesssim 3$) a été révélée pour la première fois grâce à l'excellente résolution et la sensibilité du *Télescope Spatial Hubble (HST)*. Des régions de formation stellaire très lumineuses (clumps) ont été identifiées dans des images aux longueurs d'onde ultraviolettes et optiques au repos. Elles ont généralement une couleur bleue et forment beaucoup de nouvelles étoiles. Jusqu'à $\sim 40\%$ des étoiles produites chaque année par ces galaxies peuvent naître dans des clumps, même s'ils contiennent seulement $\sim 10\%$ de la masse totale de la source. Bien qu'ils soient observés dans des galaxies à haut redshift depuis longtemps, la nature des clumps et leur évolution sont encore très débattues et les simulations numériques présentent des prédictions très différentes. Les violentes instabilités gravitationnelles des disques de galaxies riches en gaz turbulent, à haut redshift, ont été proposées comme la cause principale pour la formation in-situ des clumps, même si une fraction d'entre eux pourrait avoir une origine ex-situ (par exemple ils pourraient être des compagnons qui ont fusionné avec la galaxie hôte, ou des clumps de gaz qui ont été accrétés). De plus, le rôle des clumps dans l'évolution des galaxies est très débattu : il n'est pas encore clair s'ils peuvent vivre longtemps, migrer vers l'intérieur et contribuer à la croissance du noyau de la galaxie, ou si les vents stellaires les détruisent rapidement. Dans cette thèse j'analyse un échantillon de ~ 50 galaxies irrégulières à redshift $1 \lesssim z \lesssim 3$. Elles ont été observées avec *HST/Wide Field Camera 3 (WFC3)* qui nous a fourni des images photométriques et des données spectrales sans fente. Cela m'a permis de sélectionner et d'étudier des clumps jeunes qui montrent des raies d'émission très brillantes, puisque elles sont sensibles au gaz ionisé par les étoiles O et B. J'ai donc exploré une portion de

l'espace des paramètres qui n'a pas été analysée par les études précédentes basées seulement sur des images photométriques : en fait ces dernières, contrairement aux raies d'émission, sont sensibles à l'émission des étoiles plus âgées (âge $\gtrsim 100$ Myr). À partir de l'étude détaillée d'un clump très jeune (âge $\lesssim 10$ Myr) que nous avons découvert dans le disque d'une galaxie à redshift $z \sim 2$ et de l'analyse d'un échantillon statistique de régions de formation stellaire que nous avons assemblé, j'ai conclu que les clumps peuvent se former in-situ à cause de l'instabilité gravitationnelle du disque. J'ai aussi trouvé que les plus jeunes d'entre eux forment leurs étoiles très efficacement, avec un comportement similaire à celui des starbursts. Finalement, j'ai calculé le taux de formation des clumps et leur durée de vie : j'ai conclu qu'ils vivent typiquement ~ 500 Myr. Ce résultat conforte donc les simulations numériques qui indiquent que les clumps peuvent migrer vers le coeur de leur galaxie et ont un rôle important pour la croissance de leur noyau.

Les simulations cosmologiques et hydrodynamiques montrent que la migration des clumps peut amener vers l'intérieur une grande quantité de gaz en raison des couples gravitationnels présents dans la galaxie. Cela provoque la contraction du disque et sa stabilisation à cause de la croissance du noyau de la galaxie. Il pourrait donc y avoir également un lien avec la formation des galaxies compactes et passives qui sont communément observées à haut redshift. Les observations du *HST* ont permis de découvrir une population de galaxies passives à redshift ~ 2 avec des tailles significativement plus petites, à masse égale, que celles de leur homologues locales. Cette découverte a déclenché un débat important concernant les possibles mécanismes qui peuvent augmenter la taille des galaxies sans altérer leur masse. Deux scénarios principaux sont généralement opposés. D'un côté, on peut supposer que les sources changent individuellement leur taille au cours du temps : des interactions entre galaxies (minor mergers) en pourraient être la cause. De l'autre côté, il est possible qu'en moyenne la population des galaxies passives change et que les sources de plus grande taille apparaissent plus tard : cela pourrait être relié avec l'évolution de la densité moyenne de l'Univers en raison de l'expansion de Hubble, les halos moins denses s'effondrant plus tardivement que les plus denses. L'importance relative des deux mécanismes est encore controversée. Dans cette thèse j'analyse un échantillon de 32 galaxies passives à redshift $z \sim 1.5$ observées avec *HST*/WFC3 dans le cadre du relevé cosmologique WISP. Nous n'avons pas trouvé de relation claire entre la taille et l'âge (ou le redshift de formation), à masse égale, pour les galaxies de notre échantillon. Cela indique que, si une relation existe entre l'âge d'une galaxie et sa distance à la relation "masse - taille", elle est plutôt faible. Ce résultat suggère que des multiples fusions mineures de galaxies pourraient être les responsables principaux de l'évolution temporelle observée dans la relation "masse - taille" pour les galaxies passives.

Le travail commencé pendant cette thèse sera développé encore plus profon-

dément grâce à des nouvelles observations qui ont été obtenues dans le cadre de propositions de temps d'observation que j'ai menées comme PI, ou auxquelles j'ai participé comme co-I. En particulier le très jeune clump qui a été découvert dans le disque d'une galaxie à redshift $z \sim 2$ sera bientôt observé avec VLT/SINFONI et ALMA, et il a récemment été observé avec VLT/MUSE et VLT/KMOS. Ces nouvelles données nous permettront de conduire une étude détaillée de la nature et la physique de cette région de formation stellaire qui peut être considérée comme un cas représentatif des jeunes clumps à haut redshift. De plus, cette étude pilote nous fournira les informations nécessaires pour proposer dans le futur des observations complémentaires multi-longueurs d'onde d'un échantillon statistique de clumps à haut redshift.

Contents

1	Introduction	8
1.1	What do galaxies look like at cosmic noon?	8
1.1.1	Star-forming clumpy galaxies	12
1.1.2	Passive compact galaxies	17
1.2	<i>HST</i> : a key telescope for high-redshift research	20
1.3	Aim and summary of this thesis	21
2	Star-forming clumpy galaxies	23
2.1	Introduction	23
2.2	Data	24
2.3	Creating spatially resolved emission line maps	25
2.4	In depth study of an extremely young clump	28
2.4.1	Analysis	29
2.4.2	Results and discussion	46
2.4.3	Conclusions	50
2.5	Study of a statistical sample of clumps	51
2.5.1	Analysis	52
2.5.2	Results and discussion	59
2.5.3	Conclusions	64
3	Passive compact galaxies	66
3.1	Introduction	66
3.2	Data	68
3.3	Analysis	68
3.4	Results and discussion	73
3.5	Conclusions	77
4	Conclusions and perspectives	79
	Appendix A Contribution to other papers as co-author	86

Appendix B Our sample of clumpy galaxies	88
Appendix C First author papers	127
List of Abbreviations	149
Bibliography	150

Chapter 1

Introduction

This thesis has been developed in the frame of the largely unanswered question of galaxy formation and evolution. How distant galaxies formed in the early Universe and how their properties evolved until the present day? It is a wide and long-lasting issue that astronomers are trying to tackle from many different points of view. During my thesis I mainly focussed on the morphological analysis of both star-forming and passive galaxies in the distant Universe, to understand their physical properties and infer their possible structural evolution with cosmic time. In particular, my work deals with two distinct and specific populations of sources that have been discovered thanks to the *Hubble Space Telescope (HST)*: clumpy star-forming galaxies and compact passive ones. In this Chapter I will describe the properties of galaxies observed in the distant Universe, mainly focussing on the two classes that I looked at in detail (Section 1.1), and I will report on the great importance that *HST* had, in general for the study of galaxy formation and evolution, and in particular for this thesis work (Section 1.2). Finally, I will present the aim and an overview of this thesis in Section 1.3.

1.1 What do galaxies look like at cosmic noon?

Galaxies are usually considered to be the fundamental building blocks of the Universe. Part of the reason why they hold this special role is probably due to the fact that when astronomers observed the night sky with the first telescopes, galaxies stood out due to the contrast between their brightness and the darkness of their surroundings. This is likely a human bias: if our eyes were able to see the X-ray part of the spectrum rather than the optical light, then galaxy clusters would be noticed as the dominant and most impressive individual structures. But there might be also a second, and perhaps better, explanation to the enduring

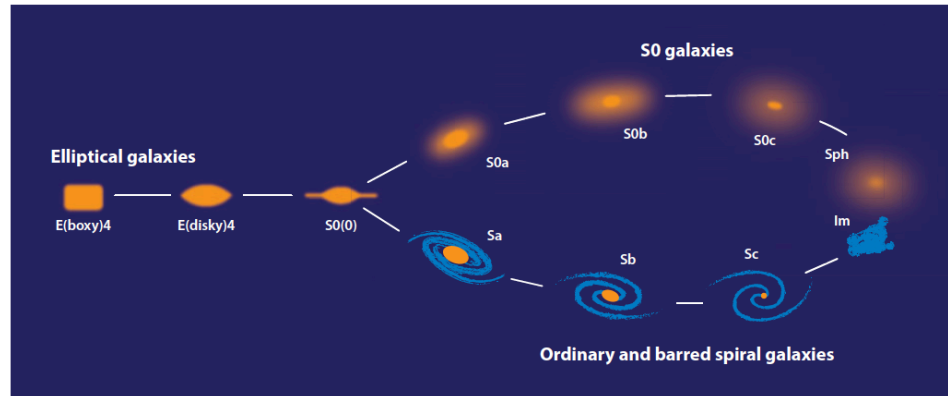


Figure 1.1 – A modern representation of the Hubble “tuning fork”, showing the sequence of ellipticals, SO, and spirals. The spirals are divided into different types (a – c), depending on the smoothness of the spiral arms, their pitch angle, and the dimensions of the bulge. At the end of this sequence dwarf spheroidal galaxies and irregular galaxies are shown (Kormendy & Bender 2012).

appeal of galaxies to astronomers: with their huge variety of shapes, incredibly different colors, and intricate spiral patterns, they provide the most visually impressive phenomena in the sky. Galaxy morphology has always been intriguing for astronomers who tried to describe and later classify galaxies based on their shape even before photography revolutionized our way to study the sky. Some examples are Charles Messier, William and John Herschel, and William Parsons who observed the sky trying to catalogue galaxies: they noted that some of them had a spiral appearance and first used this term to describe these “nebulae”. However, it has been the advent of photography that completely transformed our way to study the morphology, allowing astronomers to create schemes to classify galaxies based on their shapes. Probably the most famous and used one is the so called “Hubble tuning fork” or “Hubble sequence” established by Hubble (1936) and Sandage (1961). It mainly divides galaxies into two classes (Figure 1.1): ellipticals and spheroids (also dubbed “early-type” galaxies), and spirals (or “late type” galaxies), with the latter further distinguished into those with a bar and those without. Elliptical galaxies and spheroids have roundish and smooth morphologies, red colors typically due to their old stellar population content, and are often passive (namely, their star formation rate is very low). Spirals instead show a central bulge (that can be more or less prominent) surrounded by a star-forming disk and spiral arms that typically show blue colors and host relatively young stellar populations. The Hubble classification has been progressively refined, including new criteria to better group galaxies based on their appearance, using both visual

and automatic classification methods (Conselice 2014). The main reason why galaxy morphology has been studied so deeply and still has a crucial importance nowadays, is mainly because it is possible to link galaxy structures with their internal physical characteristics (e.g. stellar populations, dust and gas properties, dynamics). However, in spite of the large amount of work done in the local Universe to study galaxy structure, it is still difficult to investigate more than the basics of morphology when observing distant sources. This is mainly due to the fact that current technology does not allow us to resolve distant galaxies in the same detail as closer systems when using ground-based facilities. Nevertheless, the advent of *HST* made it possible to considerably progress in this field, opening the doors to many surprises and great discoveries (Section 1.2). One of the main achievements has been the finding that galaxy morphology significantly evolves over time and the structure of distant sources often appears to be significantly different with respect to local ones (Conselice 2014). Studying how morphology changes over time helps to understand how galaxies formed and evolved. According to the current, standard cosmological scenario known as “ Λ CDM”, structures in the Universe formed as a consequence of the growth of primordial tiny fluctuations due to gravitational instability driven by cold, collisionless dark matter (Peebles 1982). The formation and evolution of the dark matter content of galaxies has been explored in great detail and can be accurately modelled by N -body numerical simulations (e.g. Stadel et al. 2009; Klypin et al. 2011), but the same does not hold for baryons. Many complex processes are still poorly understood as the transformation of cold gas into stars, the formation of disks and spheroids, the role played by stellar winds. Studying galaxy morphology is a possible way to solve some of the questions that are still unsolved (e.g. do galaxies form “inside-out” or “outside-in”? How long do they retain their morphology and which are the phenomena that can alter it? Which is the relative role of star formation and mergers in shaping galaxies?). *HST* observations suggested that there is a progression from the high-redshift galaxies – that are mainly small, peculiar, and highly star-forming – to the relatively quiescent ones that we find in the nearby Universe. In particular, it appears crucial to study galaxies in the redshift range $1 \lesssim z \lesssim 3$, what is generally called the “cosmic noon”. In fact, a consistent picture is emerging, indicating that the Universe was much more active in the past, where stars formed at a rate almost ten times higher than today (Madau & Dickinson 2014). It seems that almost 50% of the present-day stellar mass density formed at redshift $1 \lesssim z \lesssim 3$. The star formation rate density appears in fact to peak approximately 3.5 Gyr after the Big Bang, at $z \sim 2$, dropping exponentially at $z < 1$ (Figure 1.2, Madau & Dickinson 2014). Thus, it is crucial to directly study this redshift range to understand what were the driving forces creating galaxies, and to comprehend which are the physical processes that brought to the buildup

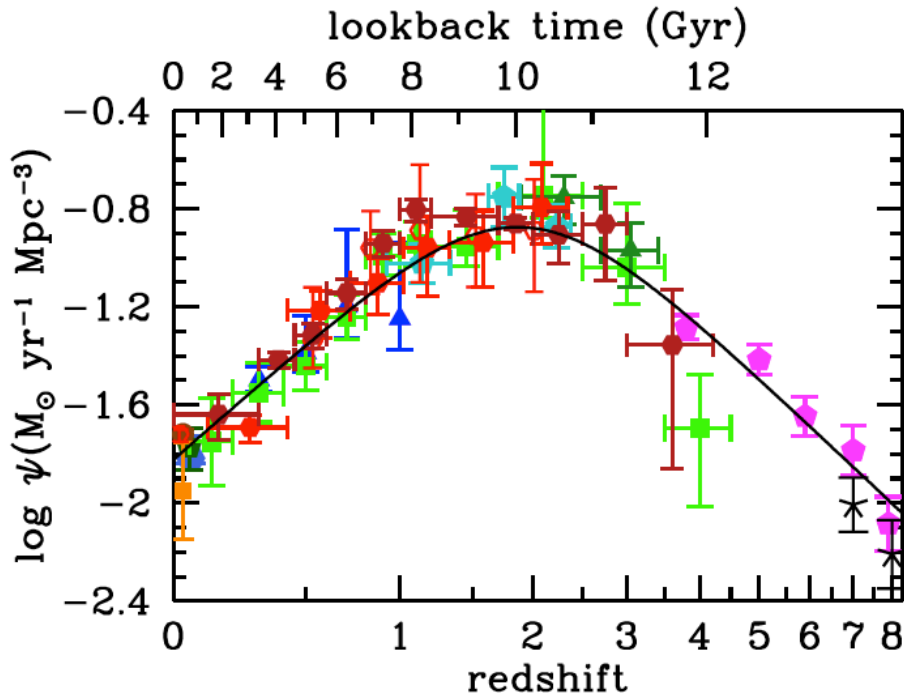


Figure 1.2 – The history of cosmic star formation from far-ultraviolet and infrared measurements (Madau & Dickinson 2014).

of their mass.

Since the pioneering observations of van den Bergh et al. (1996) it appeared that the Hubble sequence was not in place at $z \gtrsim 1$. This result has been later confirmed and expanded by many other works showing that this morphological sequence was completely absent at $z \gtrsim 2$, and only at $z \sim 1.5$ spirals and ellipticals started to become as common as peculiar galaxies (e.g. Ravindranath et al. 2004; Conselice et al. 2005, Buitrago et al. 2013). This is shown in Figure 1.3 that reports the fraction of spheroids, disks, and peculiar galaxies with stellar masses $M_* > 10^{10} M_\odot$, as a function of redshift (Mortlock et al. 2013). At $z \gtrsim 2$ the dominant morphological type is peculiar, whereas disks start to be more common only at lower redshift. Spiral arms appear very rare at high redshift, and likely only a small number of galaxies form them before $z \sim 1$. Many sources instead show clumpy features that are potentially spiral arms and disks in formation (e.g. Elmegreen et al. 2007; Conselice 2014). From Figure 1.3 it is also evident that a substantial population of spheroids is already in place at $z \sim 2$. In particular, it has been recently pointed out that distant passive spheroids are on

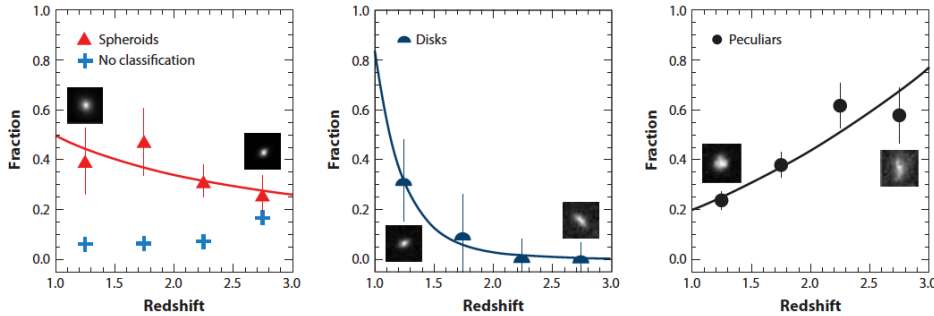


Figure 1.3 – Evolution of the Hubble sequence with redshift for galaxies with $M_* > 10^{10} M_\odot$. Image degradation is taken into account when classifying galaxies, such that misclassifications due to distance are accounted for. The insets show examples of rest-frame optical images of galaxies in each bin (Mortlock et al. 2013).

average more compact than systems of the same stellar mass in the local Universe (e.g. Daddi et al. 2005; Williams et al. 2014). These results show that both galaxy morphology and structure evolve over time. However, the question of what are the mechanisms driving this evolution and which are the reasons why local and high-redshift galaxies are intrinsically different, still remains largely unanswered.

My thesis work fits in the high-redshift ($1 \lesssim z \lesssim 2$) scenario described above and investigates the structural and physical properties of galaxies in an attempt of understanding their evolution with time. In particular I focussed on the two main classes of galaxies observed at high redshift: star-forming, clumpy galaxies and passive compact spheroids. I will describe the first in Section 1.1.1 and the latter in Section 1.1.2.

1.1.1 Star-forming clumpy galaxies

The highly irregular structure of high-redshift star-forming galaxies was first observed in the Hubble Deep Field (Abraham et al. 1996; van den Bergh et al. 1996; Cowie et al. 1996): they are dominated by bright patches on top of a diffuse emission. The most striking examples are the so-called “chain galaxies”, sources where the patches are almost linearly aligned. Before *HST* observations, these kind of irregular morphologies were usually observed in nearby dwarf galaxies. However, the clumpy sources observed at high redshift are 10 – 100 times more massive, a mass regime where local galaxies are mostly regular disks or spheroid-dominated early type galaxies. The first deep near-infrared (IR) surveys at high redshift confirmed that the patchy morphology was intrinsic and it was not the result of band-shifting effects, namely the fact that optical observations at $z > 1$

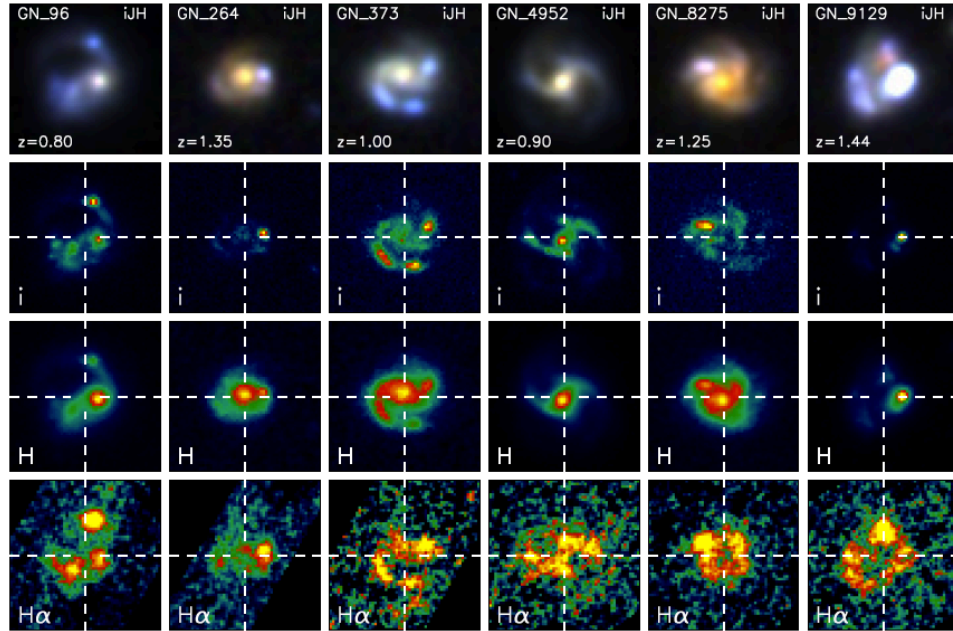


Figure 1.4 – Examples of massive $z \sim 1$ star-forming clumpy galaxies. First row: PSF-matched three-color images, sized $3'' \times 3''$. Second row: surface brightness distributions in I band. Third row: surface brightness distributions in H band. Fourth row: surface brightness distributions in $H\alpha$ (Wuyts et al. 2013).

probe the ultraviolet (UV) emission, strongly dominated by star-forming regions, rather than the underlying mass distribution dominated by older stars (Figure 1.4). Thanks to spatially-resolved stellar population studies it has been found that the bright patches clearly visible in optical observations were not just transient associations of bright stars, but they were massive clumps with sizes of approximately 100 – 1000 pc, stellar masses of $10^7 - 10^9 M_{\odot}$, and stellar ages typically younger than the host galaxy (Elmegreen & Elmegreen 2005). From the first observations and computations it seemed that these structures could live at least 10 – 20 Myr, thus longer than random associations of stars that generally would be disrupted in shorter timescales. It suggested that these bright regions were gravitationally bound (Elmegreen & Elmegreen 2005; Elmegreen et al. 2007). These structures are generally dubbed “giant clumps”, and their host galaxies “clumpy galaxies”. They are likely the majority of the intermediate- and high-mass galaxies at redshift $1 \lesssim z \lesssim 3$, although their fraction is still quite debated and ranges between 50% and 75% (Elmegreen et al. 2007; Guo et al. 2012; Wuyts et al. 2012).

Giant clumps are mostly identified in deep and high-resolution rest-frame

UV images (e.g. Elmegreen & Elmegreen 2005; Elmegreen et al. 2007; Guo et al. 2012), and rest-frame optical images (e.g. Elmegreen et al. 2009; Förster Schreiber et al. 2011), but they are also observed in rest-frame optical line emission from spatially-resolved near-IR spectroscopy (e.g. Genzel et al. 2008; Genzel et al. 2011), or CO line emission of lensed galaxies (e.g. Jones et al. 2010; Swinbank et al. 2010). They appear with blue colors and are shown to be regions with enhanced specific star formation rate, typically higher than their surroundings by a factor of several (e.g. Guo et al. 2012; Wuyts et al. 2012; Wuyts et al. 2013).

Studies of the kinematics of clumpy galaxies enabled by spatially-resolved spectroscopy of the ionized gas (Genzel et al. 2006; Förster Schreiber et al. 2009; Epinat et al. 2012; Newman et al. 2012a) probed their disk-like nature. In fact, these galaxies have in great majority disk-like velocity fields, showing the typical signature of rotation, and no signs of on-going or recent mergers, despite their clumpy morphology. Although on a single-case basis a merger might mimic the regular velocity field of a disk, depending on the interaction orbit and on the observer's line-of-sight, large surveys assembled statistical samples of clumpy galaxies, confirming that only a minority of them display potential signatures of mergers (Genzel et al. 2006; Förster Schreiber et al. 2009).

Despite the presence of giant clumps in high-redshift galaxies is known since a while, their real nature and formation process remain still uncertain and quite debated: do these clumps form in-situ or do they have an external origin (e.g. are they small companion galaxies that merged with the host, or clumps of primordial gas that have been accreted before starting to form stars)? Some works suggest that the hypothesis that clumps are star-free accreted gas clouds might be ruled out, since the average gas density in the clumps is high (hundreds of atoms or molecules per cm^3), thus making star formation very efficient (e.g. Elmegreen & Elmegreen 2005). Another possibility is that clumps are accreted companion galaxies instead. At redshift $1 \lesssim z \lesssim 2$ about one third of galaxies with stellar masses $\sim 10^{10} M_{\odot}$ are surrounded by a small companion with a stellar mass $\sim 10^9 M_{\odot}$, within a projected distance of 10 kpc (Bournaud 2016). If these satellites are not fully disrupted by galactic tides during the merger event, their nuclei should look like giant clumps. These ex-situ clumps are indeed sometimes observed: they show an underlying relatively old stellar population, typically red colors, and often a large deviation from the host disk velocity field (e.g. Bournaud et al. 2008; Förster Schreiber et al. 2011; Wuyts et al. 2012). However, these ex-situ clumps cannot fully explain the average young ages (~ 100 Myr) of the clumps population, significantly younger than small galaxies at the same redshift, suggesting that the majority of the clumps are formed in-situ (Bournaud 2016). Cosmological simulations estimated that only $\sim 20\%$ of the clumps formed ex-situ, whereas the remaining 80% were born in the galaxy disk due to violent disk

instability (Mandelker et al. 2014). However, observational constraints are still missing. If clumps (or part of them) really formed in-situ in their host galaxy, some newly formed ones (age $\lesssim 20$ Myr) should be observed: capturing the early formation of clumps is one of the main drivers of this thesis (Chapter 2).

In parallel to observations, high-resolution and cosmological simulations are investigating clump properties from a theoretical point of view, with the aim of clarifying how they form, which is their fate, and how they impact the evolution of their host galaxy. Cosmological simulations show that high-redshift galaxies are continuously fed by inflows of cold gas that flows in narrow streams along the filaments of the cosmic web (e.g. Birnboim & Dekel 2003; Dekel et al. 2009). It maintains galaxies gas fraction high, replenishing losses due to star formation and outflows (e.g. Bournaud et al. 2011; Tacchella et al. 2015). These high gas fractions ($\sim 50\%$ of the baryonic mass) have been indeed measured in star-forming galaxies at $z > 1$ thanks to CO line observations (Daddi et al. 2010; Tacconi et al. 2010), CO spectral line energy distribution (Daddi et al. 2015), and dust properties (Sargent et al. 2014; Magnelli et al. 2014; Genzel et al. 2014). The high gas fraction and density of galaxies in the early Universe lead to a violent gravitational instability (Toomre 1964). It is named “violent” in opposition to slow “secular” instabilities in today’s disks (Mandelker et al. 2014). During this unstable phase, the high surface density of gas and young stars, Σ , drives the Toomre parameter Q below unity, $Q \sim \sigma\Omega/(\pi G\Sigma) \lesssim 1$, where σ is the one-dimensional velocity dispersion and Ω is the angular frequency, a proxy for the epicyclic frequency which is related to the potential well (Toomre 1964). Under such conditions the galaxy disk fragments, producing large star-forming clumps, as shown in both isolated galaxies (e.g. Noguchi 1999; Bournaud et al. 2009; Hopkins et al. 2012) and cosmological (e.g. Agertz et al. 2009; Genel et al. 2012; Mandelker et al. 2014) simulations. These perturbed, turbulent disks seem to self-regulate, in a marginally stable state that can last for more than a Gyr, if the external gas accretion is not interrupted (e.g. Ceverino et al. 2010; Forbes et al. 2014).

Although the majority of simulations seem to agree on the scenario for clumps formation presented above, a hot debate is going on concerning their fate. The open question is whether giant clumps are long-lived phenomena and eventually migrate toward the center of the galaxy, where they might coalesce forming the bulge (e.g. Bournaud et al. 2014; Mandelker et al. 2015). If this scenario is confirmed, clumps inward migration could potentially be an efficient mechanism to form bulges, alternative to galaxy mergers. However, other simulations suggest a conflicting scenario where clumps are disrupted by stellar feedback in short timescales (e.g. Genel et al. 2012; Oklopčic et al. 2016). A first attempt to address this issue was done by Elmegreen et al. (2008): they concluded that if feedback was strong enough to disrupt the clumps within their migration timescale, it

would also severely thicken the gas disk and heat the stellar disk well above the observed levels, almost disrupting the rotation-dominated stellar disk. However, these results are based on supernovae (SNe) feedback only, while other stellar feedback mechanisms (e.g. radiation pressure from young massive stars on the surrounding gas and dust) may be more likely to disrupt clumps in a realistic way, without disrupting the whole host galaxies (Bournaud 2016). The main difficulty of addressing this issue with numerical simulations arises from the fact that stellar feedback can only be modelled through highly uncertain sub-grid models. Supernovae feedback is not well understood yet and models including other kind of feedback processes such as stellar winds, photo-ionization, and radiation pressure have been developed only recently (Hopkins et al. 2013; Renaud et al. 2013) and include free parameters that are still not well constrained from observations. This partially explains the contradictions that numerical simulations are facing. In particular, some models of gas-rich galaxies with intense feedback have found that the giant clumps could be short-lived, even the most massive ones (total mass $\sim 10^9 M_{\odot}$). This is the case of the cosmological simulations from Genel et al. (2012) and Oklopčić et al. (2016), or the idealized models of Hopkins et al. (2012). In these models, giant clumps have typical lifetimes shorter than ~ 50 Myr and they are disrupted before they can migrate inward: thus they do not have a major impact on the host galaxy morphological and structural evolution. Only in some cases, a diffuse inflow of inter-clump gas driven by the instability can reach the center of the potential well (Hopkins et al. 2012), contributing to grow a low-concentration pseudo-bulge if other relaxation processes do not affect the central region of the galaxy. In some simulations (e.g. Tamburello et al. 2015) the strong stellar feedback is also coupled with an initial low surface gas density of the disks, this latter hypothesis being mainly inspired from cosmological simulations, rather than high-redshift observations. In these cases not only the clumps are short-lived, but their formation is also highly suppressed: only low mass ($\sim 10^7 - 10^8 M_{\odot}$) clumps are formed and they are transient features that have basically no effect on galaxy evolution. On the contrary, some other models (e.g. Perret et al. 2014; Bournaud et al. 2014; Ceverino et al. 2014) including non-thermal and radiative feedback schemes predict the existence of long-lived clumps with lifetimes of $\sim 300 - 500$ Myr. These models show that clumps are not closed-box entities, but they steadily exchange mass with the surrounding medium in the host galaxy, through outflows and inflows of both gas and stars. They are expected to migrate inward, due to dynamical friction and gravitational torques, producing, as observational signature, an age gradient with older clumps found at smaller radii (Mandelker et al. 2014; Mandelker et al. 2015). Furthermore, gravitational torques generated by clump migration could funnel gas from the galaxy disk toward the center, contributing to the formation of a classical

bulge and to the feeding of the central supermassive black hole (Gabor & Bournaud 2013). Although the mass reaching the bulge might seem very high, these simulations also predict that it does not necessarily fuel a too massive bulge: in fact, a large fraction of the mass is gaseous and it can therefore be expelled outward and/or form a central rotating disk instead of a bulge (Bournaud 2016). As it appears clear from the above description, a consensus on clumps fate is far from being reached from a theoretical point of view and observations are still partially inconclusive, mainly due to the difficulty to obtain statistical samples of resolved clumps and to estimate their ages (e.g. Förster Schreiber et al. 2011; Wuyts et al. 2012; Guo et al. 2015). Therefore, part of my thesis has been employed to observationally constrain clumps lifetimes and look for potential signatures of clumps migration (Chapter 2).

Finally, clumps migration and the subsequent bulge growth might have implications in galaxies quenching (namely, the sudden stop of star formation) and in the formation of massive, compact, passive early-type galaxies. Theoretically, the strong gas inflows predicted by cosmological simulations (e.g. Dekel et al. 2009) can lead to disk contraction in a timescale of about 1 Gyr, and the instability-driven bulge growth rate could lead to a bulge-dominated system, through which the disk is stabilized and the star formation is quenched (Martig et al. 2009; Dekel & Burkert 2014). Recent cosmological simulations have probed that compact, passive, early-type galaxies (ETGs) commonly observed at high redshift (see also Section 1.1.2) could form through this mechanism where strong gas inflows first form wet compact star-forming systems, which are subsequently quenched and turned into red compact ETGs (Ceverino et al. 2014; Zolotov et al. 2015). Observations of giant clumps or clump remnants in the innermost regions of young ETGs in the Hubble Ultra Deep Field (Elmegreen & Elmegreen 2005) seem to support this scenario, but more observations are still needed to confirm it.

1.1.2 Passive compact galaxies

In recent years many efforts have been devoted to observe ETGs at high redshift to understand how these objects assembled and evolved, and how they became quenched. The discovery of a widespread population of passively evolving ETGs at redshift $z > 1.5$ showed that the star formation quenching in massive galaxies was already under way by $z \sim 2$ (e.g., Mancini et al. 2010). A large fraction of these high-redshift passive galaxies show effective radii between a factor 2 to 5 smaller than local counterparts of comparable stellar masses (Figure 1.5, Daddi et al. 2005). This result has been confirmed by several studies (e.g., Trujillo et al. 2007, Cimatti et al. 2008, Cassata et al. 2010, Carollo et al. 2013, van der Wel et al. 2014), and found to be robust with respect to bias against low

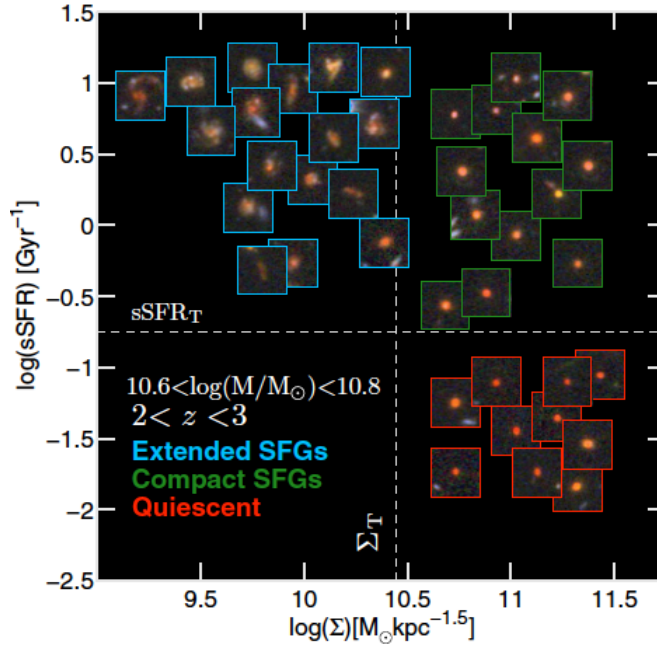


Figure 1.5 – Specific star formation rate vs stellar surface density diagram showing massive galaxies at redshift $2 < z < 3$. Three color z/H stamps with size $5'' \times 5''$ illustrate the different kind of galaxies that populate this diagram. Compact passive spheroids are located in the bottom right quadrant since they present high surface densities and their star formation rate has been shut down (Barro et al. 2014).

surface brightness at high redshifts (e.g., Valentinuzzi et al. 2010a). In the local Universe, ETGs with similar stellar densities appear to be quite rare (Trujillo et al. 2009, Poggianti et al. 2013a), although it has been suggested that they could have survived as the cores of present-day massive spheroids (Hopkins et al. 2009, van Dokkum et al. 2014).

This discovery has ignited an important debate. The problem is not mainly the existence of these very compact ETGs. In fact, $z \sim 3$ submillimeter galaxies have comparable masses and stellar sizes to these compact $z \sim 1.5$ objects, and have been identified as their possible precursors (e.g., Cimatti et al. 2008; Bedregal et al. 2013). Lyman-break galaxies at $z \sim 3$ (Williams et al. 2014) and compact star-forming galaxies at redshift $2 \lesssim z \lesssim 3$ (Barro et al. 2014) have been suggested as possible progenitors as well. The open issue is how these high-redshift compact galaxies can evolve to their present form, inflating their sizes up to a factor of 4, while at the same time following the tight correlations observed in the local universe (e.g., the relation between galaxies size, luminosity and velocity dispersion

dubbed as “fundamental plane”, Dressler et al. 1987).

Various mechanisms have been suggested to explain the growth of ETGs with time, although observations are still inconclusive as to which of them may be favorable. One of the most popular mechanisms invokes the accretion of multiple small satellites (e.g., Naab et al. 2009). These minor mergers leave the mass of the main galaxy relatively unchanged, while completely disrupting the satellites through strong tidal interactions. The accretion of stripped infalling stellar material is expected to increase the size of the merger remnant, without igniting intense star formation, particularly if the satellites do not contain large amounts of gas (e.g., Hopkins et al. 2009, Oser et al. 2012). Some observational studies suggest that this mechanism may account for $\sim 50\%$ of the apparent size evolution, at least at redshift $0 < z < 1$ (López-Sanjuan et al. 2012, Newman et al. 2012a). Despite the implications of these observational results, there is a problem explaining the size evolution with multiple minor mergers. Nipoti et al. (2012) found that multiple minor mergers would introduce more scatter than observed in the low-redshift scaling relations that link the galaxy stellar mass, effective radius and velocity dispersion, unless the progenitors were already finely tuned to occupy a very tight region in the mass-radius plane. Such fine tuning is difficult to explain, and leaves open the question of *when* and *how* the mass – size relation was first created. Moreover, Hopkins et al. (2009) highlighted that in the merging scenario a non-negligible fraction of compact galaxies ($\lesssim 10\%$) should survive to $z \sim 0$, while observations by Trujillo et al. (2009) show that only 0.03% of local galaxies have stellar densities comparable to those of high-redshift ETGs.

Adiabatic expansion through significant mass loss can also lead to size growth (Fan et al. 2010). A galaxy that loses mass as a result of supernova/active galactic nuclei (AGN) driven winds will adjust its size in response to the shallower central potential (Newman et al. 2012a). This mechanism would induce a sort of “puffing-up” of the galaxy arising from the loss of baryonic mass, with an effective size increase. However, the puffing-up only occurs when the system is highly active and young (in terms of its stellar population, Ragone-Figueroa & Granato 2011), and produces a fast expansion (a few dynamical times, $\sim 10^8$ yr). Thus one would expect only a minority of objects to be passive and compact, and it is difficult to reconcile with the observations that most compact sources are quiescent (Mancini et al. 2010).

The problem has also been explored from a different perspective (the so called “progenitor bias” scenario): instead of explaining the evolution of the mass-size relation with the growth of *individual* galaxies with time, it has been suggested that it is the *population* of ETGs that changes with time, with larger quenched galaxies appearing later (Saracco et al. 2011, Valentinuzzi et al. 2010b, Cassata et al. 2013). This may be linked to the evolution of the average density in the Uni-

verse due to Hubble expansion, with lower density haloes collapsing later in time than denser ones (e.g. Saracco et al. 2011, Carollo et al. 2013). However, the relative importance of the two mechanisms (individual versus population growth) is still highly controversial (van der Wel et al. 2014, Bernardi et al. 2010, Cassata et al. 2011, Poggianti et al. 2013b, Belli et al. 2015, Keating et al. 2015). If the redshift evolution of the mass–size relation is due to the appearance of newly quenched large galaxies, then one would expect that, at any given mass and time, the larger galaxies should on average be younger than the smaller ones. During my thesis I have tested this prediction using a sample of $z \sim 1.5$ passive ETGs observed as part of the Wide Field Camera 3 (WFC3) Infrared Spectroscopic Parallel (WISP) survey (Atek et al. 2010, Chapter 3).

1.2 *HST*: a key telescope for high-redshift research

HST and its various Hubble Deep Field campaigns starting in the mid-1990s have found thousands of galaxies at redshift $z > 1$, enabling astronomers to study their structure with unprecedented detail. The great number of *HST* surveys that have been carried out in the last fifteen years, such as the Hubble Deep Field South (Williams et al. 2000), the Great Observatories Origins Deep Survey (Gialalisco et al. 2004), the Hubble Ultra Deep Field (Beckwith et al. 2006), the Cosmological Evolution Survey field (Scoville et al. 2007), the Extended Growth Strip survey (Davis et al. 2007), and most recently the Cosmic Assembly Near-Infrared Deep Extragalactic Legacy Survey (Grogin et al. 2011; Koekemoer et al. 2011), have really revolutionized the field of galaxy formation and in particular the morphological studies. In fact, thanks to the high sensitivity and resolution of *HST* instruments such as the Advanced Camera for Surveys, the Near-Infrared Camera and Multi-Object Spectrometer, and WFC3, it is possible to resolve galaxies down to kpc scale to study the properties of galactic sub-structures and to analyze very compact galaxies at high redshift, opening a full new chapter in the story of astronomical observations. In particular *HST* can provide imaging from near-UV to near-IR, and both multi-object and slitless spectroscopy, allowing astronomers to obtain both photometric and spectroscopic information about their targets with the same telescope. This possibility, together with *HST* high sensitivity and resolution, has been crucial for the morphological and structural analysis that I carried on during my thesis. I mainly used WFC3 near-IR and UV imaging, together with WFC3 slitless G141 and G102 grism spectroscopy. This unique dataset allowed me on one side to analyze a sample of clumpy galaxies at redshift $1 \lesssim z \lesssim 2$, spatially resolving them to constrain the physical properties of giant clumps and investigate their evolution and impact on the host galaxy

(Chapter 2); on the other side I investigated the size evolution of compact passive galaxies at redshift $z \sim 1.5$, a task that would have been impossible without the excellent resolution of *HST* (Chapter 3).

1.3 Aim and summary of this thesis

The main aim of this thesis is to study the morphological and physical properties of star-forming and passive galaxies at the peak of cosmic star formation history ($1 \lesssim z \lesssim 3$). During my PhD I mainly focussed on clumpy galaxies, targeting preferentially young and intermediate age clumps to catch them at birth, understand how they form, which is their fate and their lifetime. In parallel I also developed and concluded a study that I started during my Master thesis, aimed at understanding which are the physical mechanisms driving the observed evolution of the mass – size relation of passive galaxies with cosmic time. These are not just two disconnected subjects, they can be considered instead two sides of the same coin: they both try to answer to the more general question of how star formation is triggered and stopped in the distant Universe. To answer this question mainly two different mechanisms have always been counterposed: on one side internal mechanisms, on the other side galaxies interaction. Only recently it has been shown that clumpy galaxies are in great majority rotation-supported disks and not mergers, but it is still debated whether clumps form in-situ due to violent disk instability in gas rich, turbulent disks, or if they are instead the result of galaxy mergers. Also bulge formation is highly debated: it is not clear yet if it grows thanks to internal processes (e.g. clumps inward migration and coalescence) or to major mergers that drive the gas toward the center of the potential well. A related issue is the possibility that once the bulge is grown the galaxy disk is stabilized and therefore it stops to form stars: it quenches. Afterwards the galaxy just evolves passively. So the observations that the mass – size relation of passive galaxies changes with cosmic time are puzzling and need to be explained. Again two main mechanisms are counterposed: galaxy minor mergers and internal, intrinsic characteristics (e.g. galaxies were born more compact in the past than in the present-day Universe). My thesis therefore addresses some of these open questions, with the aim to constrain the relative importance of the internal versus external mechanisms in shaping the different galaxy populations and determining their evolution.

This thesis is organized as follows. In Chapter 1 I introduce the properties of galaxies at cosmic noon in the context of galaxy formation and evolution, particularly focussing on clumpy star-forming sources and compact, massive, passive ones. I present the results of current researches in these fields and the main de-

bated issues. In Chapter 2 I describe the work I have done in collaboration with the research group at Commissariat à l'Énergie Atomique et aux Énergies Alternatives (CEA) in Saclay to study massive clumps particularly focussing on the young and intermediate age ones that have been rarely targeted by previous studies. In Chapter 3 I present the analysis of a sample of compact, massive, and passive galaxies that I led in collaboration with the WISP survey team and researchers at the Padova University, with the aim to understand the mechanisms producing their observed size evolution with cosmic time. Finally, in Chapter 4 I will present the future perspectives of this thesis, reporting the goals of the accepted proposals that I led as Principal Investigator (PI) or I participated to as co-Investigator (co-I).

Chapter 2

Star-forming clumpy galaxies

In this Chapter I will discuss the main subject of my thesis: the study of clumpy galaxies at high redshift ($1 \lesssim z \lesssim 2$). The works I present here have been carried on mainly in collaboration with the group of extragalactic astrophysics based at CEA in Saclay. Part of our results have been presented in a published Letter (Zanella et al. 2015, appended in Appendix C), while I am currently working at the draft of an additional paper that will be submitted to the *Astrophysical Journal*. In Section 2.1 I will introduce the main open questions that motivated our work. In Section 2.2 I will present our data and I describe in Section 2.3 the technique we developed to create spatially resolved emission line maps for our sample galaxies. I will then present in Section 2.4 the in depth study of a peculiar galaxy likely hosting an extremely young clump, whereas in Section 2.5 I will report the analysis of our full statistical sample of clumpy galaxies.

2.1 Introduction

The high spatial resolution and sensitivity of *HST* imaging and spectroscopy routinely allow us to resolve giant star-forming regions (clumps) inside galaxies at $z \sim 2$. Rest-frame UV and optical observations have probed that kpc-size, star-forming regions (clumps) are an ubiquitous feature of galaxies at this redshift (Guo et al. 2015). On the theoretical side many efforts have been done to understand clumps formation and evolution in the context of fragmentation of turbulent gas-rich disks at high redshift (Bournaud 2016), a scenario for which there is a growing observational support, although the debate is still open (see also Section 1.1.1). If this scenario for clumps formation is correct, some young clumps recently formed by gravitational instability should be observed in high-redshift galaxies. So far, most of the studies have selected clumpy galaxies in observed op-

tical and/or IR broad-band imaging and stellar population modelling has revealed a wide range of ages for those clumps (Elmegreen et al. 2009; Wuyts et al. 2012; Guo et al. 2012; Elmegreen et al. 2013), with average age ~ 100 Myr. However, the continuum alone cannot robustly pinpoint young ages ($\lesssim 30$ Myr Wuyts et al. 2012) and therefore spectroscopy, sensitive to gas ionized by very young stars, is needed. With the aim of looking for a population of young clumps, we analyzed a sample of galaxies observed with both rest-frame optical and UV imaging, together with slitless spectroscopy from WFC3. This data set allowed us to search for clumps with high equivalent width (EW) emission lines, a signature for young ages (see Section 2.4).

Understanding how giant clumps form and evolve is essential to clarify the mechanisms that drive high-redshift star formation and to shed light on key aspects of the morphological transformation of galaxies with cosmic time, such as bulge growth. To this aim, it is crucial to estimate the clumps formation rate (CFR) and lifetime, two quantities that are still poorly constrained, although their assessment is important to clarify whether clumps migration can be an efficient channel to build bulges, alternative or complementary to galaxy mergers. Simulations suggest that dynamical friction and gravitational torques would lead massive clumps to migrate inward where they might coalesce to form a bulge (Dekel et al. 2009; Ceverino et al. 2012), powering bright AGN episodes (Gabor & Bournaud 2013). Whether such a scenario can occur depends on the longevity of the clumps, which may be severely limited by stellar feedback processes (Tamburello et al. 2015; Oklopčić et al. 2016). With our observations, we thus attempted an estimate of the CFR and lifetime, and through the analysis of a statistical sample of clumps we looked for possible signatures of clumps migration toward the center of galaxies (Section 2.5).

2.2 Data

Our data have been taken as part of a project aimed at observing the distant galaxy cluster Cl J1449+0856 (Gobat et al. 2013) obtained in Cycle 18 (PI: E. Daddi). Spectroscopic and photometric observations performed with the *HST*/WFC3 using the G141 grism and F140W filter respectively have been completed between June and July 2010. The imaging was mainly taken to provide information on source positions and morphologies, to correctly model the spectra and facilitate the extraction. The grism observations were executed along three position angles ($\sim 0, -30, +15$ degrees) due to the high density of sources in the field: this allows to correct each spectrum for contamination of nearby sources. Thus we obtained 16 G141 orbits that cover a total area of 6.4 arcmin^2 , with $\sim 3 \text{ arcmin}^2$ uniformly

covered by three orientations. Additional *HST*/WFC3 observations were taken with the F105W and F606W filters in May 2013 (Table 2.1) during Cycle 21 (PI: V. Strazzullo).

The spectroscopic data were reduced using the aXe pipeline (Kümmel et al. 2009) which creates spectral cutouts calibrated in wavelength and models of the continuum emission, based on input multi-wavelength spectral energy distributions (SEDs), for all objects of the field, independently for each position angle. Residual defective pixels not identified by the pipeline (e.g. bad pixels, cosmic ray hits) were identified and removed with the L.A.Cosmic algorithm (van Dokkum 2001).

A *Subaru*/MOIRCS near-IR spectroscopic follow-up of 76 sources in the cluster Cl J1449+0856 field has been performed in April 2013 (Valentino et al. 2015). The data have been reduced with the MCSMDP pipeline (Yoshikawa et al. 2010) combined with custom IDL scripts (Valentino et al. 2015).

The cluster field has been also followed-up with a great number of multi-wavelength observations, including data taken with Spitzer (IRAC and MIPS), Herschel (PACS and SPIRE), JVLA, LABOCA, IRAM, ALMA, Keck-LRIS, Chandra, and XMM.

2.3 Creating spatially resolved emission line maps

Due to the slitless nature of our WFC3 spectroscopic survey, the shape of the emission lines is determined by the morphology of the galaxy. Thanks to the high *HST* resolution we can therefore spatially resolve the emission line images and perform a kpc-scale morphological study. In particular, we aim at identifying giant star-forming clumps in both spectroscopic and broad-band data to compare their emission line and continuum properties. To this purpose, we created spatially resolved emission line maps, processing each two-dimensional (2D) spectrum cutout as follows. First, the overall sky background level was estimated with SExtractor (Bertin & Arnouts 1996) and subtracted. Second, we removed the stellar continuum emission of the central object in the cutout (the main target) as well as the contamination introduced by the spectral traces of all potentially surrounding sources, including also higher and lower order dispersion spectra, that due to the slitless nature of the survey can overlap with one another. This step was carried out using the continuum emission models provided by aXe and normalizing these models independently for each object in the field. It finally led to spectral images where only emission lines were left.

In slitless spectroscopic data, emission lines with full width at half maximum (FWHM) narrower than the spectral resolution (2000 km s^{-1} in our case, thus

basically all narrow lines) result in a nearly-monochromatic emission line image of the observed target obtained at the *HST* spatial resolution (0.2"). For a given galaxy, the detailed morphological structure observed in the imaging (probing the stellar continuum) is not necessarily identical to that visible in spatially resolved emission line maps. Therefore, it is not possible to construct astrometrically calibrated emission line images directly cross-correlating the spectra and the continuum. For each detected line, spatially-resolved emission line maps properly calibrated in astrometry were instead obtained by maximizing the cross-correlation between the spectral images with the three different position angles and the continuum probed by the F606W filter. For each orientation, in fact, the 2D spectral images of each emission line are identical, the astrometrically aligned spectra differing only for the relative direction of the dispersed continuum. We also considered the F606W imaging in the cross-correlation since at the redshift of our sources ($1 \lesssim z \lesssim 2$) it probes the rest-frame UV continuum, expected to have a morphology qualitatively similar to the one of the emission line maps as it traces the star formation distribution. We iteratively shifted the 2D spectral maps along the dispersion direction, computing the cross-correlation between them and the F606W image at each step. Finally we fitted the curve obtained considering the cross-correlation as a function of the shift of each image: the maximum of the curve indicates the relative position of the images that gives the correct astrometric calibration. The uncertainty associated to our best solution has been computed by propagating the errors of the parameters of the fit. Once the relative position of the images that maximizes the cross-correlation has been found, the spectral maps were combined with the IRAF task WDRIZZLE (Fruchter & Hook 2002), weighting each single orientation by its corresponding exposure time. The absolute astrometric calibration along the dispersion direction of the grism was determined from the cross-correlation of the [OIII] or H α spectral images (depending on the redshift of the source), as these are the lines detected with the highest signal-to-noise ratio (S/N). The astrometry of the H β and [OII] emission maps was afterwards tied to that of the [OIII] or H α maps. Knowing the wavelength solution of each spectrum and the shift applied to obtain the correct astrometric calibration, we could associate a redshift to each emission line map ($z_{\text{map},i,j}$, for the map of the i -th galaxy with the j -th position angle). Propagating the uncertainties on the cross correlation, we determined the error on the redshift of each emission line map. We note that, for the same galaxy, maps with different position angles could have a different associated redshift due to astrometric and spectral distortions. Furthermore, during the cross-correlation we only allowed the maps to shift along the dispersion direction, assuming that the spectra were perfectly aligned with the broad-band imaging along the cross-

dispersion direction (e.g. the spectral trace of the continuum is aligned with the barycenter of the galaxy in the imaging). This was in general correct, although distortions might introduce some scatter. Due to the different position angles of each map, misalignments along one spatial direction would also partially affect the other. To quantify the effect of the distortions, we proceeded as follows. We computed a weighted mean redshift for each galaxy ($z_{\text{aver},i}$, for the i -th galaxy), averaging the $z_{\text{map},i,j}$ over the different position angles. To estimate the distortions, for each position angle, we forced the reduced Chi square to be equal to 1:

$$\chi_{\text{red}}^2 = \frac{1}{N} \sum_{i=0}^N \frac{(D_i - D_{\text{aver}})^2}{\epsilon_{z,i}^2 + \epsilon_{z,\text{aver}}^2 + \sigma_D^2} \quad (2.1)$$

where N are the degrees of freedom (e.g. the number of our sample galaxies), D_i is the difference $z_{\text{map},i,j} - z_{\text{aver},i}$, and D_{aver} is the average of these differences over the whole sample of galaxies for the j -th orientation. We notice that D_{aver} is null only if the orientation is not affected by distortions ($z_{\text{map},i,j} - z_{\text{aver},i} = 0$). Moreover, D_{aver} can be different for different position angles. Besides, $\epsilon_{z,i}$ and $\epsilon_{z,\text{aver}}$ are the uncertainties associated to D_i and D_{aver} respectively. Finally, σ_D is an additional term needed to obtain $\chi_{\text{red}}^2 = 1$: it accounts for the average distortion affecting the maps with the considered position angle. We concluded that the distortions are smaller than 0.06", for all position angles, and repeating the analysis separately on the [OIII], H α and [OII] emission line maps, we checked that they do not depend on the wavelength. We also tried to divide the galaxies based on their location in the field of view, to check if the distortions could depend on it. We concluded that there is no trend with the right ascension and declination of the galaxy and therefore we can consider that the distortions in the dispersion and cross-dispersion directions of the spectral images are comparable.

A possibility to correct for these distortions is to run iteratively our cross-correlation procedure allowing the spectra to shift along the dispersion direction first, then to fix the solution that has been found, and to repeat the cross-correlation allowing offsets along the cross-dispersion direction instead. This procedure would need to be repeated until convergence is reached. However, this method is extremely time consuming, therefore we decided to apply the cross-correlation procedure shifting the spectra along the dispersion direction only, and to refine *a posteriori* potential misalignments affecting some galaxies. To this aim we used two methods, as I will more diffusely detail later: first, when in a galaxy multiple clumps were detected, we used them to compute the additional offset needed to better overlap imaging and spectral maps; second when fitting each galaxy light profile to estimate the clumps flux, we allowed the best fit model

to rigidly shift to correct for possible residual misalignments of the continuum and emission line maps (Section 2.5).

A subsample of our galaxies was followed-up with longslit MOIRCS spectroscopy: we verified that the average redshift z_{aver} that we computed for each galaxy with the cross-correlation technique was in agreement with the one derived from higher resolution MOIRCS spectra (Valentino et al. 2015).

Finally, we note that the [OIII] doublet is resolved at the spectral resolution of our data for relatively compact galaxies, but given the fairly small separation in wavelength the [OIII] $\lambda 4959\text{\AA}$ component results in an independent image that is blurred with that of the stronger [OIII] $\lambda 5007\text{\AA}$ emission. It produces ghosts with one-third of the [OIII] $\lambda 5007\text{\AA}$ flux that are spatially offset in the 2D spectral datasets along directions that are different for each grism orientation. We decided to remove the contribution of [OIII] $\lambda 4959\text{\AA}$ in the combined spectral map obtained after the cross-correlation of the three grism orientations, in order to work with higher S/N. We created an effective point-spread function (PSF) of the [OIII] doublet for the combination of our three orientations, which consists of a main lobe corresponding to the 5007\AA line and three fainter ones with a flux of $\sim 1/9^{\text{th}}$ of the [OIII] $\lambda 5007\text{\AA}$ peak each. With GALFIT (Peng et al. 2010) we modelled our combined emission line images using this PSF and finally subtracted the contribution due to the 4959\AA lines using the best fitted model, to obtain cleaned [OIII] $\lambda 5007\text{\AA}$ emission line maps. We verified that a similar approach applied instead at each single spectrum orientation would provide entirely consistent results.

2.4 In depth study of an extremely young clump

When comparing the astrometrically calibrated emission line images of our galaxies with their continuum, one source stood out of the sample: in the broadband imaging it appeared as a smooth disk, whereas the emission line maps were showing, on top of a faint diffuse emission, a remarkably bright, off-nuclear clump visible in the [OIII], $H\beta$, and [OII] images, but lacking any obvious counterpart in the continuum. Triggered by this discovery, we deeply analyzed this galaxy (labelled ID568 as in Gobat et al. 2013 and Valentino et al. 2015), to assess the nature of the bright emission lines of its clump (dubbed “Vyc1”). We note that ID568 has a redshift $z = 1.987$ as determined from MOIRCS slitless spectroscopy, and therefore the F140W and F105W filters probe the rest-frame optical wavelengths, tracing the stellar mass distribution of the galaxy, whereas the F606W imaging traces the UV-rest frame regime, probing the star formation distribution.

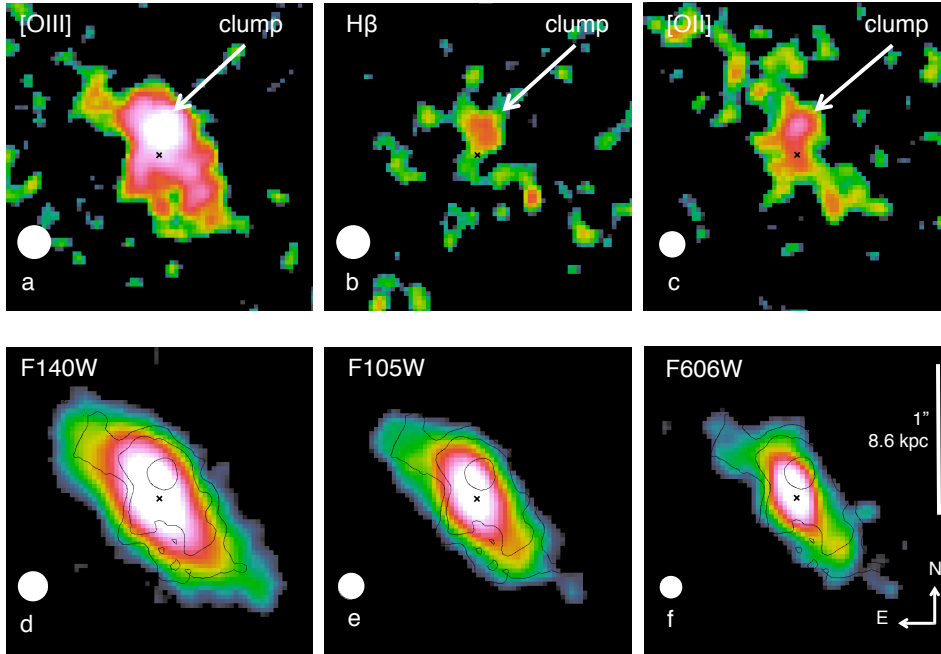


Figure 2.1 – A massive, very young clump in a disk galaxy at $z = 1.987$. The emission line maps show off-nuclear, unresolved, bright [OIII] together with $H\beta$ and [OII] emissions (a - c), respectively 18σ , 3σ and 3.5σ significant. No counterpart in the direct images is detected (d - f). The flux contours of the [OIII] map have been overplotted on the direct images. The color scales logarithmically with flux from the minimum (black) to maximum (white) level displayed (different for a - c, d - f). The black cross in each panel indicates the barycenter of the stellar optical rest-frame continuum and the white circle the PSF FWHM.

2.4.1 Analysis

I will report in the following our analysis of Vyc1, specifying in particular how we estimated the flux of the clump's emission lines and continuum, together with its dust extinction. I will also detail how we measured its offset from the galaxy barycenter, a crucial quantity to probe that the observed emission is coming from the galaxy disk and it is not related with the nucleus. I will discuss as well why we concluded that the emission is coming from an extremely young clump, discarding alternative hypothesis (e.g. an AGN, shocks, an extremely low-metallicity region, a transient). Finally, I will report how we constrained the clump physical properties like age, SFR, stellar mass, gas mass, and its dynamical

time.

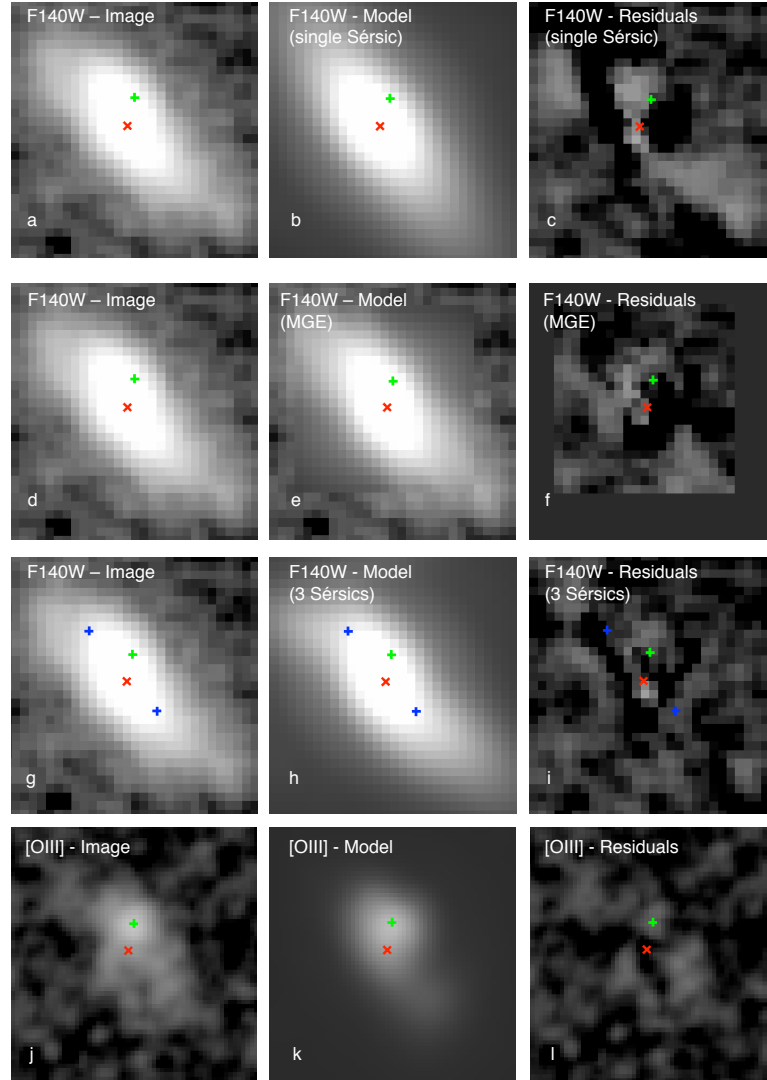


Figure 2.2 – Modelling of the galaxy light profile. The F140W direct image and [OIII] emission line map (a, d, g and j), the GALFIT models (b, e, h, k) and the residuals (c, f, i, l) are shown. The first row shows the single Sérsic profile solution, the MGE model is in the second row, and our baseline model (the sum of three Sérsic profiles; blue crosses mark the additional components) in the third row. The red cross indicates the barycenter of the stellar light and the green one marks the center of the [OIII] off-nuclear component.

Clump flux estimate Although the clump is very bright in the [OIII], $H\beta$, and [OII] emission line maps, visual inspection of the multi-band *HST* images did not reveal any evidence of the off-nuclear emission, and the evaluation of their isophotal contours did not show disturbances at its location (Figure 2.1). Thus we searched for its presence modelling the imaging with GALFIT (Figure 2.2). A single Sérsic (Sérsic 1968) profile provided a simplified fit, leaving strong positive and negative residuals near the expected position of the clump. Such a pattern is a systematic effect due to the presence of clumps at the outskirts of the galaxy major axis, as they are not symmetrically located with respect to the nucleus, resulting in an effective bending of the galaxy isophotes. The single Sérsic fit is attempting an intermediate solution that produces strong systematic residuals. Masking the external regions and fitting the central part of the galaxy with a single Sérsic profile left negligible residuals ($\lesssim 5\%$). As a further check, we fitted the direct images with the Multi-Gaussian Expansion parametrization (MGE) algorithm (Cappellari 2002), fitting average azimuthal light profiles with ellipsoidal isophotes to the central part of the galaxy. We restricted the area of the fit to the central part of the galaxy avoiding again the top left and bottom right wings: the residuals are negligible ($\lesssim 5\%$). Analogous residuals resulted using three spatially offset Sérsic profiles: one centered at the barycenter of the stellar light (as determined by SExtractor from the F140W image) and other two, an order of magnitude fainter, to the top left and bottom right. This is our best fit (baseline) model for the galaxy continuum.

This three-component fit is a technical solution adopted due to the irregular morphology of our target, typical of clumpy high-redshift disks, and should not mislead to conclude that the galaxy is an ongoing merger. In this regard, we classified the galaxy as a disk based on the Asymmetry and M_{20} parameters measured on stellar mass maps derived from pixel-to-pixel SED fitting (Figure 2.3, Conselice 2003; Lotz et al. 2004; Cibinel et al. 2015), which allow us to reliably distinguish between disks and mergers. Comparing the location of our galaxy in this plane with disks and mergers from MIRAGE numerical simulations (Perret et al. 2014), we see that the host galaxy is fully consistent with being a disk. Finally, the F105W/F140W ratio (Figure 2.4) provides no evidence for a bulge.

A PSF profile, added to the GALFIT best fit model and fixed at the position of the off-nuclear [OIII] emission, is not detected in the F140W and F105W direct images and is tentatively recovered at only 1.5σ significance in the F606W image. Upper limits on the stellar light continuum emission of the off-nuclear unresolved component were thus obtained with dedicated simulations, for each of the three broad-band images obtained with the WFC3 camera. We artificially injected a PSF (in the $\sim 25 - 27$ magnitude range) on top of the galaxy continuum emission, one at a time, for many different positions at approximately the same

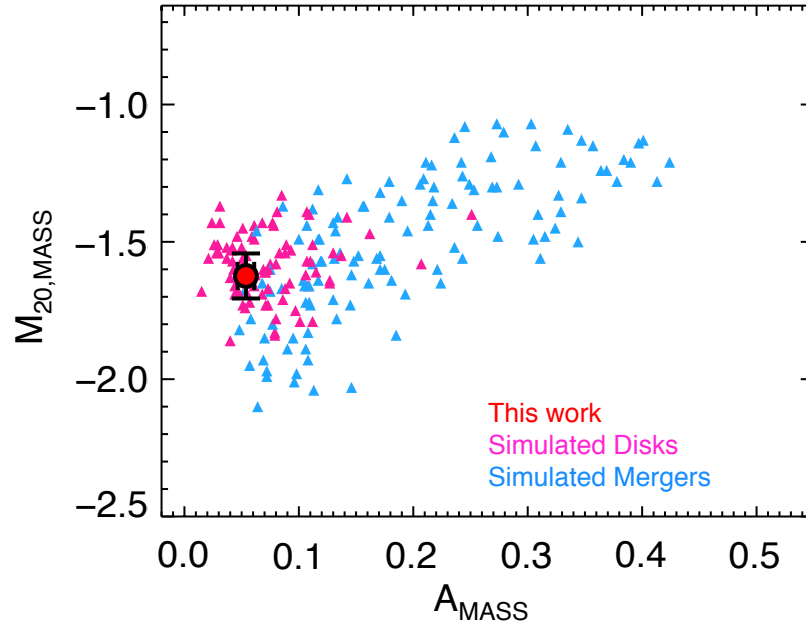


Figure 2.3 – The Asymmetry and M_{20} morphological parameters as determined from the spatial distribution of the galaxy stellar mass. Pink and light blue triangles represent disks and mergers from MIRAGE numerical simulations (Perret et al. 2014), respectively. The galaxy presented in this work (red filled circle with s. d. error bars) is located in the typical region occupied by disk galaxies (Cibinel et al. 2015) while the vast majority of mergers have higher Asymmetry and/or M_{20} parameters. We note that the figure shows the same number of mergers and disks even if in optical samples mergers are expected to be a minority.

isophotal level of the expected clump position. For each simulated image, the model was analyzed with GALFIT assuming our baseline global fit plus an additional point-source component. The 3σ dispersion of the differences between the input PSF fluxes and those recovered by GALFIT was then taken as the estimate of the flux upper limit contributed by the clump in the broad-band imaging. We finally subtracted from these estimates the known contribution of emission lines ([OIII] and $H\beta$ for F140W, [OII] for F105W) to obtain cleaned constraints on the stellar continuum flux, resulting in a factor of 2 (1.3) deeper flux upper limit for F140W (F105W). Figure 2.5 shows the derived upper limits compared to a series of Starburst99 stellar population synthesis models (Leitherer et al. 1999) with

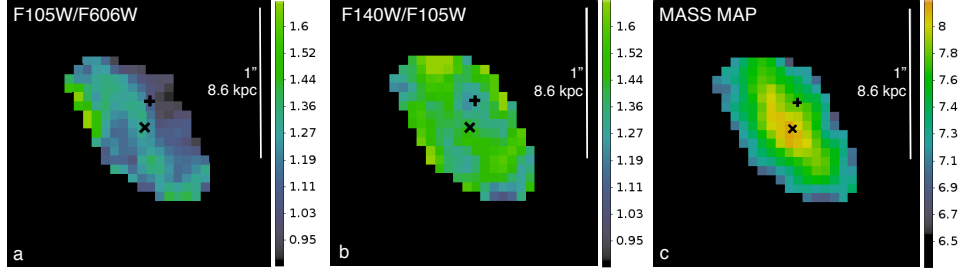


Figure 2.4 – Images ratios and mass map. The ratio of F105W/F606W imaging in F_y scale (a), a proxy for the dust reddening of the stellar continuum, and F140W/F105W imaging, sensitive to the M/L ratio (b), are shown. The position of the nucleus and the clump are shown as crosses. The maps show only small variations: the observed F_y ratios for the nucleus (clump) positions are 1.34 (1.16) for F105W/F606W and 1.39 (1.25) for F140W/F105W. Galaxy-wide ratios are 1.27 and 1.37 for F105W/F606W and F140W/F105W, respectively. The mass map (c) is shown in units of $\log_{10}(M_{\odot}/\text{pixel})$.

different stellar ages, normalized to the most constraining upper limit which is the one obtained for the F105W filter. This process allowed us to derive more stringent upper limits on the continuum underlying the [OIII] and $H\beta$ emission lines, which we determined from the flux density of the synthetic spectra at the corresponding line wavelength (Figure 2.5). We only considered synthetic spectra with ages ≤ 20 Myr since, given the upper limits directly measured from the data, we constrained the age of the clump $\lesssim 15$ Myr (as detailed below). We found that up to ~ 20 Myr, the stellar age of the model had a negligible impact on the more stringent upper limits we determined. This allowed us to refine the F140W limit, which is relevant for calculating the [OIII] and $H\beta$ emission line EW (see below).

The [OIII], $H\beta$, and [OII] fluxes of the clump have been determined by fitting with GALFIT the emission line maps using our baseline model plus an off-nuclear PSF. All the structural parameters of the baseline model have been forced to be the same as for the broad-band imaging, allowing only for a renormalization of its magnitude. The off-nuclear emission is well fitted by a PSF, being spatially unresolved (radius < 500 pc): subtracting a point-like emission in fact leaves no significant residuals in the maps (Figure 2.6).

We report the flux of the [OIII], $H\beta$, and [OII] emission lines of Vyc1, together with the upper limits on its F140W, F105W, and F606W continuum in Table 2.2.

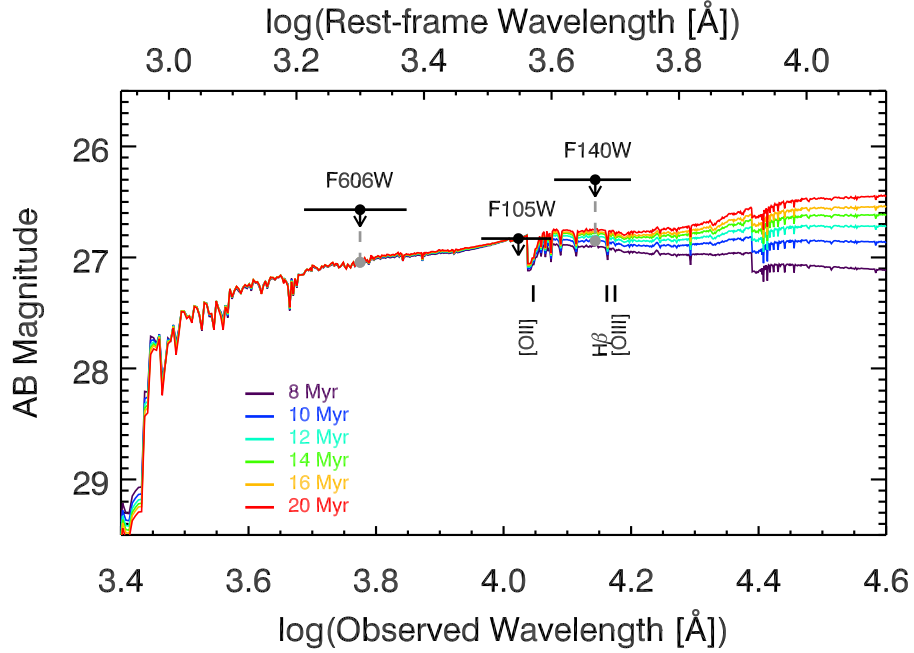


Figure 2.5 – Clump continuum flux upper limits. The observed flux upper limits estimated from simulations and GALFIT modelling in the three bands are shown as black filled circles. The black horizontal lines indicate the bandpass width of each filter. Colored curves represent reddened Starburst99 stellar population synthesis models (Leitherer et al. 1999; $E(B-V) = 0.3$ as estimated in Section 2.4.1) with different ages (from 8 to 20 Myr), normalized to the most stringent upper limit (F105W band). The corresponding upper limits in F140W and F606W obtained considering a spectrum with an age ~ 10 Myr are shown as grey filled circles.

Dust reddening To obtain the intrinsic emission line luminosities and the star formation rate of a stellar population it is crucial to estimate a proper dust extinction correction (this is less relevant, though, for estimating emission line EWs as they are affected only by the differential reddening between lines and continuum). We obtained estimates of the dust reddening affecting the galaxy as a whole and the clump individually.

For the whole galaxy (hence including the clump), several estimates are available. We used stellar population modelling of the UV-to-NIR galaxy SED (Strazzullo et al. 2013) assuming the Calzetti et al. (2000) reddening law and constant star formation rate to measure the stellar continuum reddening. We converted this measure into nebular reddening using the correlation observed in

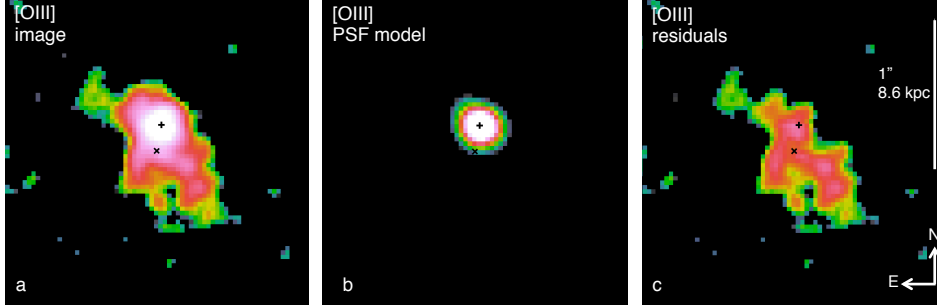


Figure 2.6 – GALFIT decomposition of the clump. The [OIII] map (a) and the model of the point source component for the clump (b) are shown. No strong residuals or artifacts are left after removal of the point source component (c). The position of the nucleus and of the clump are shown as crosses.

star-forming galaxies at high redshifts between the emission line and stellar light continuum attenuations ($E(B - V)_{\text{nebular}} = E(B - V)_{\text{continuum}}/0.83$, Kashino et al. 2013), obtaining a line reddening $E(B - V)_{\text{nebular}} = 0.30^{+0.09}_{-0.07}$. Independent estimates of the nebular reddening were also obtained on the basis of the following emission line ratios: (i) $H\alpha/H\beta$, assuming an extinction-free ratio of 2.86 (Osterbrock 1989) appropriate for an electron density of 100 cm^{-3} and a temperature of 10^4 K (case B recombination conditions); (ii) $[OII]/H\alpha$, assuming an intrinsic ratio of 1 (Kewley et al. 2004), and (iii) $[OII]/H\beta$, assuming an intrinsic ratio of 2.86 derived from the two previous hypothesis. For these estimates we used $H\alpha$ fluxes from Subaru/MOIRCS ancillary data, $[OII]$ from WFC3 and $H\beta$ from the weighted average of MOIRCS and WFC3 measurements, following also the analysis of Valentino et al. (2015). Using the Calzetti et al. (2000) reddening law we obtained reddening estimates of: $E(B - V)_{H\alpha/H\beta} = 0.24 \pm 0.12$; $E(B - V)_{[OII]/H\alpha} = 0.32 \pm 0.11$; $E(B - V)_{[OII]/H\beta} = 0.40 \pm 0.25$. The average of these estimates is nearly identical to the nebular reddening inferred correcting the stellar continuum one. We use therefore a value of $E(B - V)_{\text{nebular}} = 0.30$ in our study.

For the clump taken individually, only a single estimate of the reddening can be obtained using the WFC3 grism data alone, from the ratio of the $[OII]$ and $H\beta$ line fluxes. We derived a fairly noisy measurement that is nevertheless consistent with that obtained for the whole galaxy ($E(B - V)_{[OII]/H\beta, \text{off-nuclear}} = 0.24 \pm 0.37$). While formally this is also consistent with zero attenuation towards the clump, we emphasise how this is unlikely to be the case, as the galaxy is seen nearly edge-

on, and the clump light is thus necessarily reaching us after passing through much of the galaxy’s disk. To improve this estimate, we attempted a derivation of the $H\alpha$ flux of the clump in the MOIRCS spectroscopic data, decomposing the 2D spectrum with a PSF-like component for the clump and a single Sérsic profile accounting for the host galaxy. The estimate of $H\alpha = 7 \pm 2 \times 10^{-17} \text{ erg s}^{-1} \text{ cm}^{-2}$ for the clump is $\sim 50\%$ of the total $H\alpha$ emission of the galaxy obtained from the MOIRCS spectrum (Valentino et al. 2015). Comparing the reddening affecting the clump with the $H\alpha/H\beta$ and $H\alpha/[\text{OII}]$ ratios and averaging these estimates with that from $[\text{OII}]/H\beta$, we obtained $E(B - V)_{\text{nebular}} = 0.55 \pm 0.20$, consistent with the reddening of the host galaxy. We thus assumed that the clump nebular reddening is identical to that of the parent galaxy. Notice that approximately half of the galaxy emission line fluxes originate from the clump, hence the nebular reddening estimates for the whole galaxy are already strongly driven by the clump properties. Also, literature works show that there are no systematic differences in the reddening between clumps and their parent galaxies (Elmegreen et al. 2007, Wuyts et al. 2013). Figure 2.4 shows the observed F606W/F105W ratio, probing the stellar continuum reddening, which is homogeneous over the galaxy. The optical attenuation (A_V) at the clump position is similar to that at the galaxy nucleus within 0.1 – 0.2 mag, and close to the galaxy average. The position of the galaxy nucleus (measured as the light barycenter, light peak, or with GALFIT) is stable and not changing with the wavelength from F606W to F105W and F140W. $[\text{OIII}]$ and F105W continuum should be affected by a similar attenuation and much less than the F606W continuum. Together with the flatness of the reddening map, this demonstrates that the clump emission lines are not an artifact due to reddening modifying the galaxy nucleus position, as an even stronger effect would be seen in F606W. Reddening correcting the emission line maps and the imaging does not significantly alter the nucleus-clump distance. Adopting the Cardelli et al. (1989) extinction law (see, e.g., Steidel et al. 2014) would produce reddening values $\lesssim 15\%$ higher, consistent within the uncertainties. We report the flux of the clump’s emission lines and continuum in Table 2.2.

Clump offset from the galaxy nucleus The comparison of our broad-band imaging and the emission line imaging (Figure 2.1) clearly shows that the clump is offset from the center of the galaxy. This is an important finding, as it implies that the phenomenon we are observing is not related to the galaxy nucleus but it is instead happening in the outer disk. We discuss here the evaluation of the distance of the clump from the nucleus, and its significance.

The observed distance between the point-like $[\text{OIII}]$ emission and the barycenter of the galaxy is 1.6 kpc, with formally negligible measurement error. How-

ever, systematic uncertainties exist, related to the astrometric calibration of the direct imaging and slitless data, and to the stability of the wavelength solution.

We proceeded empirically to estimate the uncertainties considering the full survey data as follows: for each position angle of the grism, the total uncertainties along the dispersion and cross-dispersion directions of the spectra were estimated, respectively, using bright emission lines (H α and [OIII]) and the stellar light continuum. For the emission lines we compared the distribution of the differences between the measured and expected wavelengths in the three independent orientations, yielding information on the systematic uncertainties along the dispersion direction. Comparing the position of galaxies in the direct imaging with the position of the continuum emission in the grism data we evaluated the systematics in the cross-dispersion direction. Should the formal measurement errors on the emission lines and continuum positions (σ_p) represent a reliable determination of the total uncertainties, the reduced Chi square would be:

$$\chi_{\text{red}}^2 = \frac{1}{N_{\text{dof}}} \sum_{i=1}^N \left(\frac{s_{\text{meas},i} - s_{\text{exp}}}{\sigma_{p,i}} \right)^2 \approx 1 \quad (2.2)$$

where N_{dof} refers to the degrees of freedom of the system, and where $s_{\text{meas},i}$ and s_{exp} are respectively the measured and expected positions of the emission lines (or the continuum) of each galaxy. However, we found that the χ_{red}^2 measured above are well above unity, pointing to an additional uncertainty (σ_A) related to the absolute calibration of the image astrometry. Thus, σ_A was estimated for each orientation of the grism (assuming it is constant across the whole field of view for a given position angle) and independently for the dispersion and cross-dispersion directions, so as to obtain

$$\chi_{\text{red}}^2 = \frac{1}{N_{\text{dof}}} \sum_{i=1}^N \left(\frac{s_{\text{meas},i} - s_{\text{exp}}}{\sqrt{\sigma_{p,i}^2 + \sigma_A^2}} \right)^2 = 1. \quad (2.3)$$

The procedure has been repeated separately for the three orientations of the spectra. On average, we find that the systematic uncertainties are $\sigma_A = 0.067''$ ($\sigma_A = 0.035''$) along the dispersion (cross-dispersion) direction. For each cutout, we combined the uncertainties that we estimated along the dispersion and the cross-dispersion direction considering the orientation of the grism. Finally, since the emission line maps are the result of the weighted average of spectra with three different orientations (with the exposure time used as a weight), we estimated the resulting uncertainties affecting the combination, assuming that the errors (ϵ_i) in

each orientation are independent, as

$$\epsilon = \frac{\sqrt{\sum_{i=1}^3 (t_i \epsilon_i)^2}}{\sum_{i=1}^3 t_i} \quad (2.4)$$

where t_i is the exposure time of the i -th orientation. The uncertainties estimated by GALFIT on the coordinates of the center of the PSF-like, off-nuclear component have been finally added in quadrature.

The clump offset is detected at 7.6σ and its projected distance from the galaxy nucleus (defined as the barycenter of the stellar light) is 1.6 ± 0.3 kpc. If we had chosen the light peak of the direct images as the nucleus, the offset would be comparable in magnitude and significance. We prefer the light barycenter definition as it coincides with the peak of the mass map (Figure 2.4).

To determine the deprojected distance, the axial ratio of the galaxy and the angle θ between the galaxy major axis and the clump-nucleus direction are needed. We estimated them from the range of solutions obtained modelling the direct images and the mass map with GALFIT and considering the outer isophotes of the PSF-deconvolved galaxy. To further account for systematic effects we also considered plausible uncertainties in the PSF derivation, and further estimates based on the MGE software as an alternative to GALFIT. Given an axial ratio $0.21 \leq q \leq 0.35$ (inclination $i \sim 70 - 78^\circ$) and $48 \leq \theta \leq 52^\circ$, we computed a “maximum plausible range” for the deprojected distance of the clump from the nucleus of $3.6 \leq d \leq 6.2$ kpc, beyond the galaxy effective radius $R_e = 2.8 \pm 0.4$ kpc (Table 2.2). We did not account for the disk thickness: this uncertain correction could imply a larger deprojected distance by 10 – 15% (for a typical thickness of a few hundreds of pc).

Discarding the AGN, shock, transient, and low-metallicity region hypotheses The galaxy has three Chandra photons (1 soft and 2 hard; $\sim 2\sigma$ detection) in 146 ks data giving $L_{2-10\text{keV}} \sim 2.9 \times 10^{42}$ erg s $^{-1}$ (photon index $\Gamma = 1.8$). This is 10 times higher than expected from the galaxy star formation (Persic et al. 2004). If an AGN were present, it would produce (Panessa et al. 2006) an [OIII] luminosity ~ 20 times fainter than that of the clump. Furthermore, the MOIRCS longslit spectroscopy allowed us to measure the integrated H α line luminosity and place an upper limit on the [NII] emission over the whole galaxy. Considering the case B recombination conditions ($H\alpha = 2.86 \cdot H\beta$, Osterbrock 1989), a reddening $E(B - V)_{\text{nebular}} = 0.3$ and the H β line luminosity of the clump as derived from our spatially-resolved emission line maps, we obtained a “synthetic” H α estimate for the clump (which is consistent with the MOIRCS measurements within the uncertainties) and an upper limit on its [NII]/H α ratio, us-

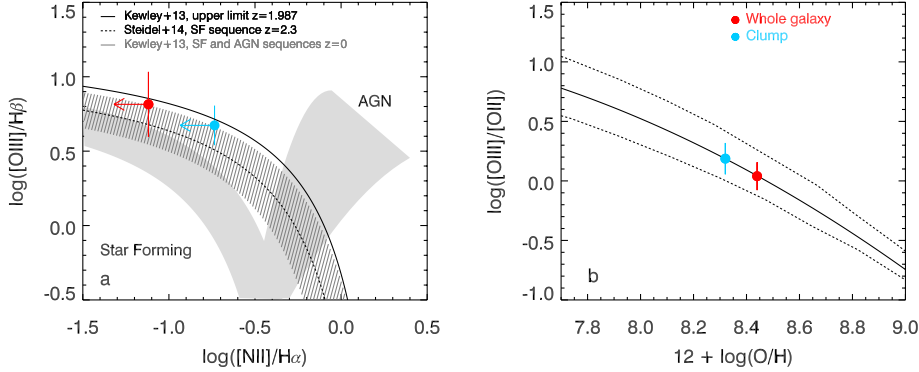


Figure 2.7 – Emission line diagnostics. The BPT diagram (a) shows that the emission line ratios of the whole galaxy and of the clump (red and light blue points with s. d. error bars) are consistent with being powered by star formation. The $[\text{NII}]$ upper limit and $\text{H}\alpha$ emission of the whole galaxy are measured from the Subaru/MOIRCS longslit spectroscopy follow-up and the $[\text{NII}]/\text{H}\alpha$ upper limit for the clump is computed assuming the $[\text{NII}]$ of the whole galaxy. The metallicities of the whole galaxy and that of the clump have been determined from the $[\text{OIII}]/[\text{OII}]$ ratio (b).

ing the conservative relation $[\text{NII}]_{\text{clump}} \lesssim [\text{NII}]_{\text{galaxy}}$. Using the BPT (Baldwin et al. 1981) emission line diagnostic diagram to distinguish between star formation and AGN, we found that the constraints on the emission line ratios obtained for both the clump and the entire galaxy are fully consistent with those characterizing star-forming galaxies at $z \sim 2$ (Steidel et al. 2014), thus pointing to a gas ionization state mostly powered by star formation (Figure 2.7). The constraint on the $[\text{OIII}]/[\text{NII}]$ luminosity ratio obtained in a similar way for the clump is also much lower than the ratio typically observed in Type 1 AGNs (Stern & Laor 2013), suggesting again that star formation is the dominant source of ionization in this compact region. The extremely high EW observed in the clump also disfavors the hypothesis of an off-nuclear AGN, since typically AGNs have $\text{EW}_{[\text{OIII}]} < 500 \text{ \AA}$ (Caccianiga et al. 2001). Besides, no AGN signature was found from the SED fitting of the galaxy, and no excess possibly arising from nuclear accretion is detected in our $24\mu\text{m}$ –Spitzer, Herschel and deep JVLA ancillary data.

The clump emission line luminosity is comparable with that of the whole galaxy, hence it cannot be due to shock from external outflows impacting the gas. The host SFR would generate ~ 30 times weaker galaxy-integrated, shock-excited line luminosities (Hong et al. 2013). The brightest shock powered off-nuclear

clouds in local IR luminous galaxies are > 50 times weaker (Soto & Martin 2012). Explicit calculations (Binette et al. 1985) for $z = 2$ galaxies using appropriate wind mass loads (Genzel et al. 2014; Renaud et al. 2013) and velocities (Förster Schreiber et al. 2014) lead to analogous conclusions. The kinetic energy available in winds cannot account for the clump line luminosities.

There is not evidence for substantial line luminosities variability over a ~ 3 yr timescale. The field around the cluster Cl J1449+0856 was observed with *HST*/WFC3 G141 spectroscopy in June and July 2010, and MOIRCS spectroscopy was obtained in April 2013 (Table 2.1). Although at a lower resolution than the *HST* data (seeing of $0.6''$) the MOIRCS spectra show the bright, unresolved emission line component of our clump, for both [OIII] and $H\alpha$ with a flux consistent with expectations.

Low-mass ($< 10^9 M_{\odot}$), very metal poor galaxies ($Z \sim 0.1 Z_{\odot}$) can display extremely high EW emission lines (Amorín et al. 2014). Our target is substantially more massive than such extreme emitters. Also, given the [OIII]/[OII] ratio and the calibration by Maiolino et al. (2008), we estimated for both the clump and the whole galaxy a higher gas phase metallicity of $Z \sim 0.4 \pm 0.1 Z_{\odot}$ and $Z \sim 0.6 \pm 0.2 Z_{\odot}$, respectively (Figure 2.7). The latter estimate is 0.25 dex lower than the typical metallicity of galaxies with comparable stellar masses at redshift $z \sim 2$ ($M_{*} \sim 2 \cdot 10^{10} M_{\odot}$, determined with SED fitting, Table 2.2).

Therefore, we concluded that a young star-forming clump formed *in situ* is the most plausible interpretation of our observations. Due to its young age in fact, it is expected to show extremely bright emission lines, powered by O- and B-type stars, together with very faint continuum. Our discovery confirms that to pinpoint newly formed clumps it is essential to have broad-band data together with spectroscopic observations, and it likely explains why previous surveys based on continuum observations only did not find any clump in this early phase. Furthermore, the metal deficiency observed in ID568 is shared by the full population of star-forming galaxies belonging to the same cluster CL J1449+0856, suggesting that the $z = 2$ cluster environment has likely been enriched with pristine gas (Valentino et al. 2015). This extra gas-feeding could have enhanced the clump formation rate (CFR) of the cluster galaxies, increasing our chance for observing this phase.

Constraining the age of the clump Emission line EWs of star-forming regions are tightly correlated to the age of their underlying stellar population. To constrain the age of the clump, we computed the evolution of the $H\beta$ EW as a func-

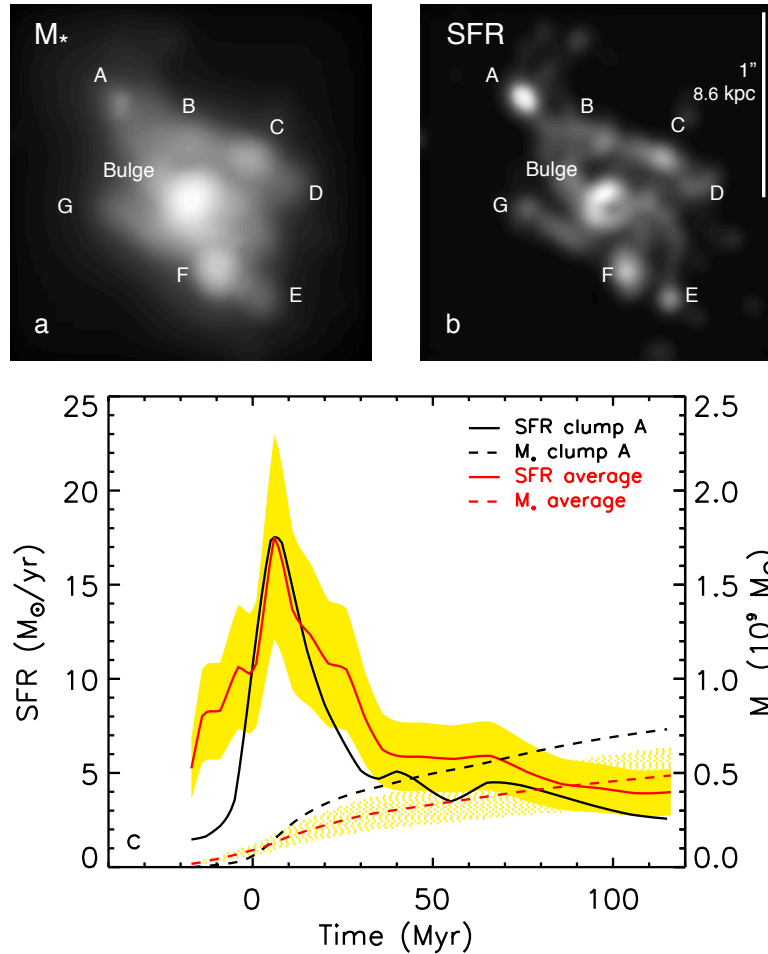


Figure 2.8 – Numerical simulations of a high-redshift clumpy galaxy seen face-on. Maps of stellar mass and SFR are shown at *HST*-like resolution (a, b). All clumps have elevated SFR compared with M_* , but this property is extreme for clump A, observed 12 Myr after its formation. Panel c shows the time evolution of the SFR and M_* for clump A and for all the clumps (each star formation history is arbitrarily shifted in time to align the SFR peaks). All clumps experience an internal burst of star formation before evolving into a long-lasting regulated regime within 20 Myr. Yellow shaded regions indicate s.d. uncertainties.

tion of time, using stellar population synthesis models (Leitherer et al. 1999). We adopted a metallicity $Z = 0.4 Z_\odot$, a Salpeter (1955) initial mass function (IMF) and three different star formation histories (SFHs): an instantaneous burst, a constant star formation law and a SFH characterized by an initial burst of star formation

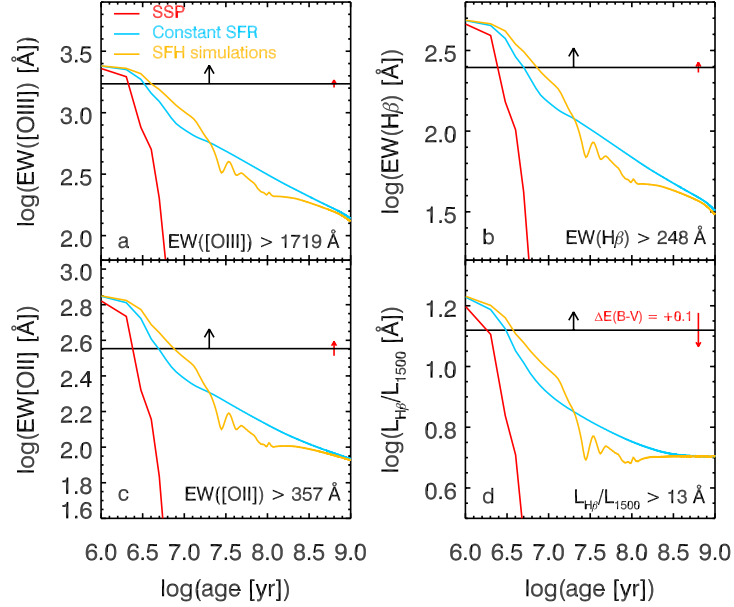


Figure 2.9 – Constraints on the clump’s age from reddening corrected, rest-frame, emission line EWs. Lower limits on the clump EW (black solid line) of [OIII], $H\beta$, [OII] (a - c) and the ratio between the $H\beta$ luminosity and the continuum at 1500 \AA (d) are compared with theoretical tracks. A Salpeter initial mass function is assumed and different star formation histories are compared (single burst, constant star formation rate, and a star formation history predicted by the simulations shown in Figure 2.8). The effect of reddening ($\Delta E(B-V) = +0.1$) is indicated in each panel (red arrow). The age of the clump is constrained to be $< 10 \text{ Myr}$.

followed by a rapid decline, as obtained from our high-resolution hydrodynamical simulations (Figure 2.8 bottom panel). The three models show a very high $H\beta$ EW at young ages ($\log(\text{EW}) \gtrsim 2$, independent on the SFH). It then drops quickly in the case of the instantaneous burst, whereas it declines in a smoother way in the two other cases. Similarly, we computed the expected [OIII] and [OII] EWs (Figure 2.9), assuming the [OIII]/ $H\beta$ ratio typically observed in star-forming galaxies at $z = 2$ (Steidel et al. 2014) as well as the case B recombination conditions ($H\alpha/H\beta = 2.86$ Osterbrock (1989)) and an $H\alpha/[OII]$ luminosity ratio of 1 (Kewley et al. 2004). Comparing these model predictions with the EW lower limits, we inferred an age $< 10 \text{ Myr}$ for the clump (Figure 2.9). Assuming the continuum upper limits directly measured from the data rather than the

more stringent limits imposed from the synthetic spectra (Figure 2.5), the age constraint is $\lesssim 15$ Myr.

This upper limit on the age of the clump weakly depends on the metallicity and the IMF assumed in the synthetic stellar spectra. For instance, a metallicity variation of 1.6 dex produces a 0.2 dex age difference only. Similarly, the derived age constraint remains unchanged if we adopt e.g., a Kroupa (2001) or a Scalo & Struck-Marcell (1986) IMF, and a top-heavy one results in line EWs 0.2 dex higher only (which would relax the age upper limit to ~ 15 Myr only).

On the basis of stellar population synthesis modelling for galaxies with active star formation, the observed EWs require very young ages for the star formation event, with a firm upper limit of 10 Myr (Figure 2.9). Thus, while the ubiquity of clumps in high-redshift galaxies has been known for a decade, we are witnessing here for the first time the formation of a star-forming clump in the early stage of its gravitational collapse.

SFR estimate Star formation rates are commonly derived from the luminosity of the Hydrogen lines using the relation proposed by Kennicutt (1998). However, this relation was calibrated for ~ 100 Myr stellar populations and an appropriate conversion coefficient needs to be estimated for younger star-forming region as studied in this work.

To derive the proper conversion between the SFR and the line luminosities of the clump, we considered the average SFH of 7 clumps extracted from our numerical simulations, and computed their $H\beta$ luminosity ($L_{H\beta}$) as a function of stellar age using Starburst99 models (Figure 2.10, yellow curve). At $t = 10$ Myr it leads to the relation $\text{SFR} = 3.04 \cdot 10^{-41} \cdot L_{H\beta}$, which translates to a SFR estimate of $27 \pm 9 M_{\odot} \text{ yr}^{-1}$ for the clump (here and in the following we are using $E(B - V)_{\text{nebular}} = 0.3 \pm 0.1$). Following the same procedure we also estimated the SFR using the [OII] luminosity and the $L_{[\text{OII}]} \sim L_{H\alpha}$ (Kewley et al. 2004) approximation, which yielded $\text{SFR} = 30 \pm 10 M_{\odot} \text{ yr}^{-1}$. From the $H\alpha$ flux derived in the MOIRCS ancillary data we estimated a higher (but noisier) $\text{SFR} = 57 \pm 17 M_{\odot} \text{ yr}^{-1}$. Averaging the three estimates, we thus obtained a combined $\text{SFR} = 32 \pm 6 M_{\odot} \text{ yr}^{-1}$ for the clump, where the error is computed considering the uncertainty associated with the emission line luminosities and the reddening.

The SFR of the whole galaxy was determined from the total $H\alpha$ luminosity measured from the MOIRCS slitless spectroscopy, assuming the standard Kennicutt law. This led to a SFR estimate of $77 \pm 4 M_{\odot} \text{ yr}^{-1}$, in agreement with the SFR obtained through the SED fitting ($\sim 100 M_{\odot} \text{ yr}^{-1}$, Table 12.2).

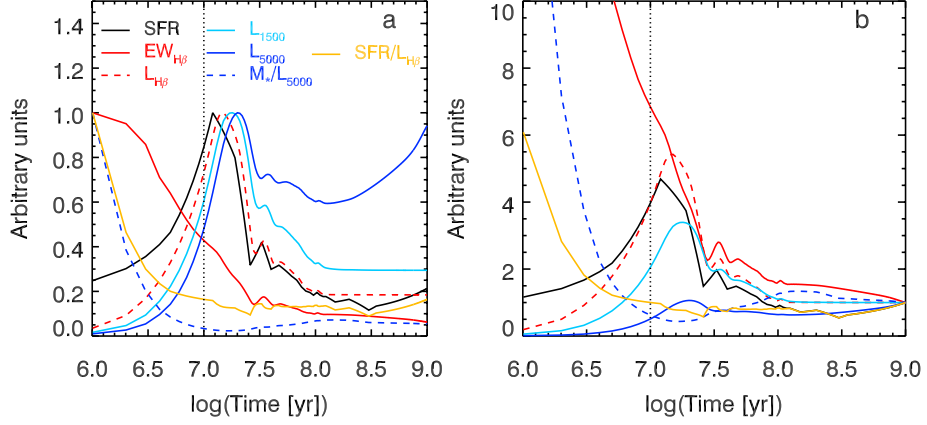


Figure 2.10 – Time evolution of physical quantities based on the clump $SFR(t)$ from our simulations. In panel **a** the peak of all the curves is normalized to 1 to highlight the time delay occurring between the peak of the SFR and of the luminosities $L_{H\beta}$, $L_{1500\text{\AA}}$, $L_{5000\text{\AA}}$, whereas in panel **b** they are normalized to 1 at $t = 1 \text{ Gyr}$ to stress the relative intensity of the observables at the peak and later phases. The vertical black dotted line indicates the upper limit on the age of the clump ($t = 10 \text{ Myr}$). The units of the plotted quantities are: SFR ($M_{\odot} \text{ yr}^{-1}$), $EW_{H\beta}$ (\AA), $L_{H\beta}$, $L_{1500\text{\AA}}$, $L_{5000\text{\AA}}$ (erg s^{-1}), $M_*/L_{5000\text{\AA}}$ ($M_{\odot} \text{ erg}^{-1} \text{ s}$), $SFR/L_{H\beta}$ ($M_{\odot} \text{ yr}^{-1} \text{ erg}^{-1} \text{ s}$).

Stellar mass estimate Assuming the mass-to-light ratio (M/L) of the galaxy, the flux upper limit on the continuum emission of the clump can be translated into a stellar mass upper limit $M_* \lesssim 3 \cdot 10^8 M_{\odot}$. This estimate is fully consistent with that independently obtained from the simulated SFH of the clump at $t = 10 \text{ Myr}$ (Figure 2.8), after normalizing the 5000 \AA continuum emission of the synthetic spectrum derived with Starburst99 to our observed upper limit at the same wavelength ($M_* = (M/L_{5000})_{\text{simul}} \cdot L_{5000, \text{obs}} \lesssim 2.1 \cdot 10^8 M_{\odot}$). Normalizing this simulated spectrum to the $H\beta$ line luminosity of the clump (corrected for extinction) finally yields a stellar mass $M_* \sim 3.9 \cdot 10^8 M_{\odot}$, still consistent with the two previous estimates given the uncertainties on the measured fluxes and the simulations (a factor ~ 2 , mainly related to the gas fraction of the modelled galaxies and the details of feedback and stellar mass loss modelling at small scales).

Gas mass estimate We inferred an upper limit to the gas mass in the clump from the Jeans mass (M_J) of the galaxy, which is close to the maximum gas mass that can collapse in a rotation disk (Dekel et al. 2009; Bournaud et al. 2014; Bournaud et al. 2009; Elmegreen & Burkert 2010). In fact, in a rotating disk, the

maximum mass that can collapse is the Toomre mass $M_T = Q_T M_J$, where Q_T is the Toomre parameter. From both, observations and theory, it seems that in unstable, clumpy disks $Q_T \lesssim 1$ (Genzel et al. 2011; Dekel et al. 2009; Bournaud et al. 2014). Therefore, the Jeans mass can be considered as the maximum mass that can collapse, given the properties of the disk. Assuming a reasonable upper limit for the typical gas velocity dispersion in high-redshift disk galaxies ($\sigma_V \lesssim 80 \text{ km s}^{-1}$ Mandelker et al. 2014; Förster Schreiber et al. 2009), we obtained $M_{\text{gas}} \lesssim M_J = 2.5 \cdot 10^9 M_\odot$. Using the $M_{\text{gas}}/H\beta$ ratio from simulations leads to a gas mass of $M_{\text{gas}} \sim 2.7 \cdot 10^9 M_\odot$. Comparing with older clumps from the literature (Förster Schreiber et al. 2011), using our numerical simulations to relate the physical properties at the “peak” and later phases, yields:

$$M_{\text{gas,clump}} = \frac{\text{SFR}_{\text{clump}}}{\text{SFR}_{\text{lit}}} \cdot M_{*,\text{lit}} \cdot \left(\frac{M_{\text{gas,young}}}{M_{*,\text{old}}} \right)_{\text{sim}} \cdot \left(\frac{\text{SFR}_{\text{old}}}{\text{SFR}_{\text{young}}} \right)_{\text{sim}} \quad (2.5)$$

where SFR_{lit} and $M_{*,\text{lit}}$ refer to older clumps reported in the literature. $M_{*,\text{old,sim}}$ and $\text{SFR}_{\text{old,sim}}$ are for old clumps in the simulations, while $M_{\text{gas,young,sim}}$ and $\text{SFR}_{\text{young,sim}}$ are computed at $t = 10 \text{ Myr}$, as our young clump. This approach leads to $M_{\text{gas}} = 3 \cdot 10^9 M_\odot \pm 0.2 \text{ dex}$, consistent with the independent estimates discussed above. We note that this agreement suggests that the SFH obtained from our simulations (with an initial burst where the SFR is highly enhanced with respect to later times) is representative of the typical way in which clumps form and evolve.

It is interesting to formally compare these estimates to what would be obtained, given the SFR of the clump, assuming the Schmidt-Kennicutt relation, for the limiting cases of main-sequence (MS) or starburst galaxy behaviours. Assuming the relation for MS galaxies would suggest that about half of the total gas mass of the whole galaxy is collapsing in an ultra-compact region, which appears hardly believable, confirming that this young clump has a star formation efficiency (SFE) more closely similar to starburst galaxies. Assuming the starburst relation instead, we obtained $M_{\text{gas}} = 2 \cdot 10^{9+0.36\text{dex}-0.23\text{dex}} M_\odot$, thus consistent with the previous estimates.

We note that all these estimates assume an age of the clump equal to the upper limit $t = 10 \text{ Myr}$ determined with the emission lines EW. Considering an even younger age would not affect our conclusion on the starburst nature of the clump, as shown by our simulations (Figure 2.8). In fact, should the clump be younger, the SFR estimate would be higher (see yellow curve in Figure 2.10) as well as its stellar mass upper limit (see blue, dashed line in Figure 2.10). Since the SFR increases faster than the stellar mass, the specific star formation rate (sSFR)

Table 2.1 – *HST*/WFC3 and Subaru/MOIRCS observations.

Instrument	Date	Time (direct imaging) (hr)	Time (spectroscopy) (hr)
<i>HST</i> /WFC3	2010, 6 th June	0.3 (F140W)	2.7
<i>HST</i> /WFC3	2010, 25 th June, 1 st July	0.6 (F140W)	7
<i>HST</i> /WFC3	2010, 9 th July	0.3 (F140W)	2.7
<i>HST</i> /WFC3	2013, 20 th May	3.3 (F105W)	-
<i>HST</i> /WFC3	2013, 20 th May	0.3 (F606W)	-
Subaru/MOIRCS	2013, 7 th - 9 th April	-	7.3

at younger ages would be even more extreme, confirming the starburst behaviour of the clump during the formation phase.

Dynamical time estimate Measuring the FWHM of the H α line detected in the MOIRCS longslit spectroscopic data, we determined a first upper limit on the gas velocity of the clump $v_{\text{FWHM}} \lesssim 450 \text{ km s}^{-1}$ (equal to the MOIRCS instrumental resolution). Given the upper limits on the radius of the clump ($R < 500 \text{ pc}$) and on its dynamical mass ($M_{\text{dyn}} = M_{\text{gas}} + M_{\star} \lesssim 2.8 \cdot 10^9 M_{\odot}$), we then refined our estimate to $v_{\text{FWHM}} < \sqrt{M_{\text{dyn}} G/R} \sim 200 \text{ km s}^{-1}$ (G is the gravitational constant), consistent with clump velocities typically observed in high-redshift galaxies (Genzel et al. 2011). This leads to a dynamical timescale $t_{\text{dyn}} = 2\pi R/(v_{\text{FWHM}}/2) \sim 29 \text{ Myr}$, reasonably in agreement with the free-fall time of the clump $t_{\text{ff}} \sim \sqrt{R^3/M_{\text{dyn}}} \sim 17 \text{ Myr}$. Based on these estimates we find that the clump properties are also consistent with the universal relation observed between Σ_{SFR} and $\Sigma_{\text{gas}}/t_{\text{dyn}}$ (Daddi et al. 2010; Genzel et al. 2010; Krumholz et al. 2012).

2.4.2 Results and discussion

Our finding of an extremely young, massive, star-forming clump in a $z \sim 2$ galaxy offers new insights into the physics of *clump formation* in gas-rich turbulent media at high redshift. Using the estimate of its underlying gas mass, stellar mass and SFR we can constrain the nature of its star formation mode. Its specific star formation rate ($\text{sSFR} = \text{SFR}/M_{\star}$) is > 30 times higher than that of its host galaxy, a typical MS galaxy at $z \sim 2$. Similarly, the lower limit on the clump star formation efficiency ($\text{SFE} = \text{SFR}/M_{\text{gas}}$) is > 10 times higher than that of “nor-

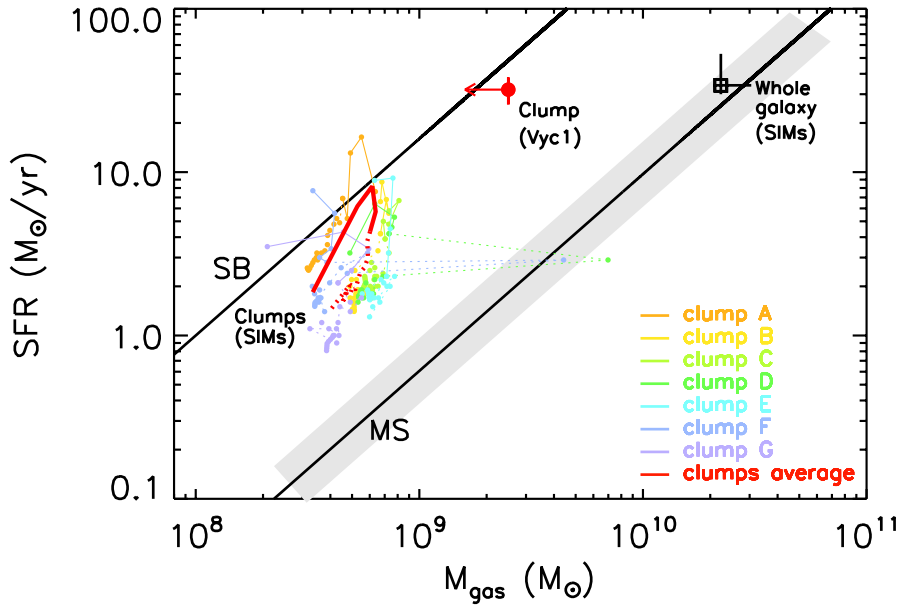


Figure 2.11 – Schmidt-Kennicutt plane. We compare the trends for starbursts and MS galaxies (black solid lines and shaded region indicating the 0.2 dex dispersion of the MS, Sargent et al. 2014) with the location of observed (red filled circle with s. d. error bars) and simulated clumps (colored dots connected with lines; solid and dashed lines for ages ≤ 30 Myr and > 30 Myr, respectively). The average location of simulated clumps (red, thick line) and host simulated galaxy (square with s. d. error bars) are shown. Sudden variations in clumps’ M_{gas} are likely due to the accretion of gas-rich clouds or small clumps.

mal”, MS galaxies (Figure 2.11), a behaviour that at galaxy-wide scales is only observed for extreme starbursts (Rodighiero et al. 2011). At sub-galactic scales such a high SFE is observed for nearby molecular clouds (Lada et al. 2010), which are small and transient features a thousand times less massive than the present clump. Possibly at odds with what has been assumed so far (Förster Schreiber et al. 2011; Genzel et al. 2011; Newman et al. 2012b), this provides observational evidence that giant clumps do not follow the Schmidt-Kennicutt law of normal star-forming galaxies, at least in the early stages of collapse. Instead, this luminous sub-galactic structure appears to follow the universal star formation law normalized by the dynamical time (Daddi et al. 2010; Genzel et al. 2010; Krumholz et al. 2012). Comparing with the SFRs reported for older clumps with similar masses

(Förster Schreiber et al. 2011), we estimated a SFR enhancement of $\sim 3 - 5$ at “peak formation” with respect to later phases.

Prompted by our observations, we investigated the properties of clumps in their formation phase using high-resolution simulations (Bournaud et al. 2014). We solved the dark matter, stellar and gas gravity and hydrodynamics at a resolution of 3.5 pc, gas cooling down to 100 K, and we modelled the feedback processes from young stars onto the gas: photo-ionization, radiation pressure and supernovae explosions. Figure 2.8 shows a typical, $M_* \sim 3 \times 10^{10} M_\odot$, $z = 2$ galaxy model with giant clumps formed through violent disk instability. Their formation sites are located at 2.1 – 7.0 kpc from the nucleus of the galaxy that has an half-mass radius of 4.5 kpc, consistent with many other simulations (Genel et al. 2012; Mandelker et al. 2014; Hopkins et al. 2012) and our observations. All clumps, and especially the youngest ones, are brighter in the SFR map than in the continuum: they undergo a burst of star formation during their initial collapse, with peak SFRs about $10 - 20 M_\odot \text{ yr}^{-1}$ consistent with our observations, then evolve to a lower sSFR regime within 20 Myr, once feedback regulates star formation and their stellar mass has grown. Our simulations further corroborate the idea that all clumps behave like galactic miniatures of starbursts in the Schmidt-Kennicutt diagram during their first 20 Myr (Figure 2.11). The SFE of simulated clumps decreases at later times, although it remains $\gtrsim 0.5$ dex higher than MS galaxies, consistent with their shorter dynamical times. The presence of massive clumps is probably an effective reason for the observed rise of the SFE in normal MS galaxies from $z = 0$ to $z = 2$ (Daddi et al. 2010; Tacconi et al. 2010; Sargent et al. 2014), given the increasing prevalence of clumps at high redshift. Furthermore, the violent burst-like behaviour that young clumps show at formation is consistent with simulations predicting that, thanks to their rapid collapse, giant clumps could form globular clusters by converting gas into stars faster than stars expel the gas (Shapiro et al. 2010).

We also attempted a first estimate of the clump formation rate (meaning the number of clumps formed per galaxy and per Gyr) and lifetime, two quantities that are essential to understand if clumps can potentially migrate inward and contribute to the growth of the galaxy bulge. The visibility window of a young clump with bright emission lines and no continuum counterpart as reported in this work can be defined by evaluating the time during which the EW is higher than the lower limit derived from our data, as predicted by stellar population synthesis models. Depending on the assumed SFH, this ranges between ~ 5 Myr (case of an instantaneous burst) and ~ 10 Myr in the case of the SFH predicted by our simulations. We use an average visibility window of 7 Myr.

Knowing the visibility window of the “formation event” and the number of formation events observed per galaxy, we can estimate the clump formation rate

per galaxy. Comparing the CFR to the average number of descendants observable per galaxy (virtually all at older ages) it is possible to estimate the average lifetime of the clumps.

We considered all galaxies from our survey with detectable [OIII] emission and with stellar mass high enough to host a giant clump such as the one studied here. We thus imposed: (i) $M_{\star} > 8.5 \cdot 10^9 M_{\odot}$, which represents the mass completeness limit of our survey. It also coincides with the minimum mass that a galaxy should have to host such a massive clump: we assumed that the host gas mass should be $2 - 3 \times$ higher than the one of the clump, and that the gas fraction at this redshift is $\sim 50\%$; (ii) $M_{\star} < 2 \cdot 10^{12} M_{\odot}$, since more massive galaxies would have an [OIII] emission too faint to be detected (Zahid et al. 2014); and (iii) a spectro-photometric redshift $1.2 < z < 2.4$ so that the [OIII] emission lies in the wavelength range of the G141 grism. In this estimate, we neglected the case where the [OIII] emission is missing from one of the three orientations of the grism due to contamination or detector artifacts, because of a low associated probability ($\lesssim 5\%$). Thus, in our source catalog, we thus obtained 57 galaxies with suitable properties to host a clump with the characteristics presented in this work. With one “forming clump” detected, this corresponds to a clump formation rate of 2.5 Gyr^{-1} per galaxy.

We further considered that in our survey we would have detected all formation events of clumps with $M_{\text{gas}} \gtrsim 2.5 \cdot 10^9 M_{\odot}$. Considering that almost all the initial gas mass of a given clump is consumed at initial stages to form stars, the clump stellar mass at late stages can be approximated to the gas mass at initial collapse, independently of the age of the clump, as supported by our numerical simulations. The typical number of giant clumps per galaxy above such mass threshold was estimated from the literature (Förster Schreiber et al. 2011; Genzel et al. 2011; Newman et al. 2012b) to be of the order of 1–2 per galaxy. This corresponds to an average lifetime of 500 Myr.

To compute the associated uncertainty, we considered (i) the Poisson error associated to our discovery of a single giant and young clump, (ii) the Poisson error associated to the number of clumps per galaxy taken from the literature; and (iii) the uncertainty associated to the clump visibility window. The asymmetric 1σ uncertainties that we inferred are $+0.74$ dex and -0.55 dex. Therefore, the lower-envelope of the 1σ range of the lifetime estimate is not far from the upper range of lifetimes suggested by models in which clumps suffer from strong feedback (50–100 Myr). However, we emphasize that it is unlikely that massive clumps lifetime is as short as indicated by the 1σ range lower-envelope that we estimated. We notice in fact that there could be a “discovery bias”, since other (spatially resolved) spectroscopic surveys of high-redshift galaxies like SINS or

Table 2.2 – Properties of the galaxy and the clump.

Notes: ^a The effective radius of the galaxy is the average of the R_e obtained from a single Sérsic profile fit in the F140W, F105W and F606W imaging. ^b The gas mass of the galaxy has been determined, given its SFR, as: $M_{\text{gas}} = 9.18 + 0.83 \log(\text{SFR})$ (Sargent et al. 2014). ^c The observed flux of the F140W, F105W and F606W direct images has been determined with GALFIT. We associated a standard uncertainty of 5%.

	Galaxy (ID568)	Clump (Vyc1)
Right ascension [h m s]	14:49:12.578	14:49:12.575
Declination [° ' "]	+8:56:19.42	+8:56:19.62
R_e [kpc]	2.8 ± 0.4^a	< 0.5
SFR [M_\odot/yr]	77 ± 9	32 ± 6
$\log(M_*/M_\odot)$	$10.3^{+0.2}_{-0.3}$	$\lesssim 8.5$
$\log(M_{\text{gas}}/M_\odot)$	10.7 ± 0.2^b	$\lesssim 9.4$
Z [Z_\odot]	0.6 ± 0.2	0.4 ± 0.2
$F_{\text{[OIII]}}^{\text{obs}}$ [$10^{-17} \text{ergs}^{-1} \text{cm}^{-2}$]	10.4 ± 0.7	4.3 ± 0.2
$F_{\text{H}\beta}^{\text{obs}}$ [$10^{-17} \text{ergs}^{-1} \text{cm}^{-2}$]	1.5 ± 0.8	0.9 ± 0.3
$F_{\text{[OII]}}^{\text{obs}}$ [$10^{-17} \text{ergs}^{-1} \text{cm}^{-2}$]	6.5 ± 1.7	1.9 ± 0.6
$F_{\text{F140W}}^{\text{obs}}$ [$10^{-20} \text{ergs}^{-1} \text{cm}^{-2} \text{\AA}^{-1}$]	67.5 ± 3.4^c	< 1.1
$F_{\text{F105W}}^{\text{obs}}$ [$10^{-20} \text{ergs}^{-1} \text{cm}^{-2} \text{\AA}^{-1}$]	89.2 ± 4.6^c	< 1.8
$F_{\text{F606W}}^{\text{obs}}$ [$10^{-20} \text{ergs}^{-1} \text{cm}^{-2} \text{\AA}^{-1}$]	212.3 ± 10.6^c	< 4.5

3D-HST have not reported yet the observation of a similar giant newly formed clump. Furthermore, some indications suggest that our target galaxy is living in a gas-enriched environment which could also have anomalously increased the SFR and thus the clump formation rate. This suggests that the observation of a newly formed, giant clump could be a quite rare event, and that the true average clump lifetime could likely be more compatible with the upper envelope of the range that we quoted above rather than with the lower limit. The clumps lifetime that we estimated is longer than expected in models of clump destruction by stellar feedback (Genel et al. 2012; Hopkins et al. 2012). Instead, it is representative of the timescale needed for giant clumps formed in galactic disks to migrate inward through dynamical friction and gravity torques and coalesce to grow the central galactic bulges (Bournaud et al. 2009; Dekel et al. 2009).

2.4.3 Conclusions

When the cosmic star formation history peaks ($z \sim 2$), galaxies vigorously fed by cosmic reservoirs (Kereš et al. 2005; Dekel et al. 2009) are gas dominated (Daddi et al. 2010; Tacconi et al. 2010) and contain massive star-forming clumps

(Genzel et al. 2006; Elmegreen et al. 2009), thought to form by violent gravitational instabilities in highly turbulent gas-rich disks (Elmegreen et al. 2004; Bournaud et al. 2007). However, a clump formation event has not been witnessed yet, and it is debated whether clumps survive energetic feedback from young stars, thus migrating inwards to form galaxy bulges (Bournaud et al. 2009; Genel et al. 2012; Wuyts et al. 2013; Dekel et al. 2009). Here we report spatially resolved spectroscopy of a bright off-nuclear emission line region in a galaxy at $z = 1.987$. Although this region dominates the star formation in the galaxy disk, its stellar continuum remains undetected in deep imaging, revealing an extremely young (age < 10 Myr) massive clump, forming through the gravitational collapse of $> 10^9 M_{\odot}$ of gas. Gas consumption in this young clump is $> 10\times$ faster than in the host galaxy, displaying high SFE during this phase, in agreement with our hydrodynamic simulations. The frequency of older clumps with similar masses (Förster Schreiber et al. 2011) coupled with our initial estimate of their formation rate ($\sim 2.5 \text{ Gyr}^{-1}$) supports long lifetimes (~ 500 Myr), favouring scenarios where clumps survive feedback and grow the bulges of present-day galaxies.

Our study demonstrates the detectability of ultra-young clumps in deep surveys, indicating low formation rates and long lifetimes. This is crucial to understand key issues of galaxy formation and evolution such as clumps migration, bulge formation and the role of feedback. However, future observations of larger samples of forming clumps with direct measurements of clumps' sizes, gas masses and velocity widths (and hence dynamical masses) are required for a definitive understanding. This should be within the capabilities of the complete Atacama Large Millimeter Array and James Webb Space Telescope. We note that spectroscopic surveys targeting high-redshift galaxies (e.g. SINS, 3D-HST) have not yet reported the identification of giant clumps at formation. This might suggest that they are rarer events than what appears from our survey, which finally allowed us to identify a direct signature of massive clump formation via gravitational collapse.

2.5 Study of a statistical sample of clumps

Our in-depth study of Vyc1 showed us the possibility to discover and select very young clumps with our data set. To strengthen the results that we obtained from this single-object study and further develop our analysis, we assembled a sample of ~ 50 galaxies. We astrometrically calibrated their emission line and continuum maps as detailed in Section 2.3, so that their morphology in the spectroscopic and broad-band images can be directly compared. This data set allowed us to study the physical properties of a statistical sample of clumps, particularly

focussing on massive, star-forming regions with young and intermediate ages that show bright emission lines.

2.5.1 Analysis

I will report in the following the details about the analysis we carried on of our statistical sample of clumpy galaxies at $1 \lesssim z \lesssim 3$, particularly focusing on the method we used to estimate the clumps emission line and continuum fluxes, deblending them from the underlying diffuse emission of the galaxy disk. I will also detail our estimate of the extinction affecting the clumps, together with our measurement of their ages and stellar masses.

Estimate of the clump fluxes To evaluate the clump fluxes and disentangle their emission from the contribution of the underlying, diffuse disk, we modelled the galaxy light profile adopting the following automatic procedure. First, we used GALFIT to model the light profile of the broad-band images and emission line maps using a single Sérsic profile and subtracting it. In this way, we verified whether the galaxy could be considered as a smooth disk, or if point-sources (namely unresolved clumps) were showing up in the residuals, after the disk subtraction. To identify possible clump candidates, we ran SExtractor separately on the broad-band and emission line residuals, after having masked all the pixels with a S/N lower than 3, to limit the number of spurious detections. We matched the coordinates of the blobs that have been found in the continuum and emission line maps. We considered that two detections were matched if their offset in the direct images with respect to the emission line maps was less than $\sim 0.22''$ (the FWHM of the PSF). In fact, small misalignments between the broad-band images and the spectral maps might still be present even after the cross-correlation procedure that we applied to calibrate the astrometry (Section 2.3). In case multiple clumps in a single galaxy were found, we used them to refine the alignment between maps and imaging, computing the average shift that was needed to better overlap the detected star-forming regions. We visually inspected all the shifted maps to check the reliability of the alignment.

We find that the average shift of these maps is smaller than $0.03''$, consistent with the distortions we estimated with the cross-correlation procedure. We note that these additional shifts were estimated using the [OIII] or H α emission line maps and then applied to the spectral images with lower S/N (H β and [OII]).

We created a catalogue with the coordinates of all the clump candidates that have been identified by SExtractor: we considered also blobs that were detected in the continuum (emission line maps) but not in the emission line maps (continuum) not to prevent us to study potential very young (old) clumps. Finally,

we fitted again the light profiles of our sample galaxies, this time considering a Sérsic profile to model the diffuse disk component plus PSFs at the location of the clumps. To this aim we used the fitting algorithm GALFITM (Vika et al. 2013), considering as initial guesses for the location of the model PSFs the coordinates of the clump candidates detected by SExtractor. We decided to use PSF profiles to model the clumps since they are expected to be unresolved at the *HST* resolution. GALFITM is an algorithm that allows the user to simultaneously fit multiple images of the same galaxy taken at different wavelengths. We used it to model simultaneously the F140W, F105W, and F606W direct images, together with the available emission line maps of each galaxy. The main advantage of this algorithm with respect to GALFIT is the fact that it is possible to force all the components of the model to keep the same relative distances, while the whole model can rigidly shift from one band to another to correctly fit the observations even if residual minor misalignments between imaging and maps were present. We visually inspected the residuals of every galaxy, after the subtraction of the best fit model, to check for the reliability of the fits. In some cases the procedure did not succeed, so we changed the initial guesses of the model and fitted these galaxies again, until smooth, non-structured residuals were obtained. For a fraction of galaxies ($\sim 15\%$) we had to include an off-nuclear Sérsic profile instead of a PSF at the location suggested by SExtractor. We excluded these “clumps” from our sample, as discussed below. We further checked our results in two ways: first we verified that the location of the center of the galaxy disks as determined by GALFITM in the F140W images was in agreement with the position of the barycenter estimated with SExtractor on the same images; second we checked how much GALFITM best fit models were offset in the emission line maps with respect to the continuum. We found that the shifts are smaller than $0.03''$, without any systematic trend, thus completely consistent with the effects expected due to distortions (estimated to be at maximum $0.06''$). Finally, we verified the reliability of the disks R_e determined by GALFITM by looking at the mass – size relation for our sample galaxies. We estimated the stellar masses with SED fitting (Strazzullo et al. 2013), as detailed below. Our measurements seem to be consistent with the mass – size relation for star-forming galaxies at $z \sim 2$ determined by van der Wel et al. (2014), therefore confirming the reliability of the galaxies R_e that we measured. The images showing the results of the fits of our sample galaxies light profile carried on with the procedure described above are reported in Appendix B.

To estimate the uncertainties associated to our flux measurements we used 1000 Monte Carlo simulations. We injected one fake PSF at the time, with varying magnitude in the range 24 – 31 mag, on top of our observed galaxies. The PSF location was randomly determined, but it was selected to be always inside

3 galaxy effective radii. We took care not to inject fake PSFs on top of already existing clumps, imposing a minimum distance from any detected star-forming region of about $0.22''$ (equal to the FWHM of the PSF). We treated these simulated images with the same procedure explained above, running GALFITM simultaneously on different bands. The model we used to fit the observations was created as follows: we considered the best fit GALFITM model obtained for each galaxy before the PSF injection, and we kept its structural parameters fixed, allowing only the magnitude of each component to change. This was needed not to introduce too many degrees of freedom and degeneracies in the modelling, since the issue we want to understand here is how well GALFITM retrieves PSFs on top of a disk. Then we added to this baseline model a PSF profile. The initial guesses for the magnitude and the coordinates of the PSF center were estimated by randomly perturbing the known, input values of the simulation. We did not visually inspect all the residuals after the subtraction of the best fit model, but we defined the following automatic criteria, calibrated with the real data, to decide when a fit failed. With SExtractor we created a segmentation map for each galaxy and we looked, only inside this region, at the variations of the residuals normalized by the input image. This was needed not to consider noisy pixels that were outside the galaxy and were not fitted. We computed the mean (M) and standard deviation (S) of the distribution of the normalized residuals after 3σ clipping and considered a fit as reliable if the following conditions were simultaneously satisfied: $S_{\text{imaging}} \leq 0.3$, $S_{\text{maps}} \leq 0.4$, $|M_{\text{imaging}}| \leq 3S_{\text{imaging}}$, and $|M_{\text{maps}}| \leq 3S_{\text{maps}}$. Visual inspection of the residuals of random simulated galaxies confirmed that our automatic criteria were properly selecting the good fits (e.g. the ones with small and smooth residuals), allowing us to exclude the non reliable ones in order not to pollute our uncertainties estimate.

To determine the uncertainties associated to the flux of the clumps, we divided the simulated PSFs in bins based on their distance from the galaxy barycenter and the magnitude of the underlying disk as measured by GALFITM on the real data. For each bin, we computed the difference between the know input flux of the fake injected PSF and the one retrieved by GALFITM. The standard deviation of the sigma clipped distribution of these differences gave us, in each magnitude and distance bin, the flux uncertainty. It was important to divide clumps in bins of galaxy magnitude and distance from the nucleus, since the ability of GALFITM to correctly retrieve the flux is highly dependent on the contrast of the PSF with respect to the underlying diffuse disk. If the disk is bright (faint) the contrast is low (high) and therefore the uncertainties are larger (smaller). Furthermore, if the clump is close to the nucleus of the galaxy the contrast is low due to the rise of the Sérsic profile of the disk and the uncertainties are large. On the

contrary, if the clump is located in the outskirts of the galaxy the contrast is high and the uncertainties are quite small. This is indeed the trend that we find with our simulations. We finally interpolated all the bins to get the uncertainties as a function of the galaxy magnitude and the clump distance from the center. We imposed that at large distances from the nucleus, where the contrast is very high and the uncertainty derived with our simulations is negligible, the flux error was set by the background limiting magnitude, estimated with aperture photometry on empty regions of the sky. In the emission line maps the underlying galaxy disk was usually very faint, thus the uncertainties associated to the emission line flux of the clumps are simply set by the background limiting magnitude, without any dependence on their distance from the galaxy barycenter or disk brightness.

For each observed clump, given the flux estimated with GALFITM and its associated uncertainty, we computed the S/N. We considered as true detections only the clumps with $S/N \geq 3$. If in a given band the S/N was < 3 , the flux of the clump in that band was set to 3 times the estimated uncertainty, and it was considered as an upper limit. Only the clumps that were detected (with $S/N \geq 3$) in both continuum and emission lines or at least one of the two were retained. We note that it was important to keep in our catalogue also the clumps that had detected emission lines, but not continuum, in order to study very young star-forming regions (e.g. our analysis of Vyc1 in Section 2.4). We also retained in our sample clumps that were detected in the continuum, but only had an upper limit for the emission lines, since they could be very old star-forming regions that were still interesting to analyze (see Figure B.1 for examples).

In our sample of clumps we also included Vyc1 (Section 2.4, Zanella et al. 2015) and we analyzed it with the automatic procedure that I presented above. To additionally check the correctness of our method in retrieving clump fluxes automatically, we compared the emission lines and continuum flux of Vyc1 with the values that we obtained with the careful and *ad hoc* analysis presented in Section 2.4. We found completely consistent results.

Finally, we used our Monte Carlo simulations also to estimate the uncertainties associated to the coordinates of the clumps, using an analogous method to the one presented for the flux uncertainties.

Sample completeness To estimate down to which magnitude our clumps sample is complete, we used the Monte Carlo simulations described above. We divided the sample of fake clumps that we injected on top of real galaxies in bins based on their intrinsic flux (F_{input}). For each bin we estimated the fraction of clumps whose flux was retrieved by GALFITM (F_{output}) with a relative uncertainty smaller than 50%: $(F_{\text{input}} - F_{\text{output}})/F_{\text{input}} \leq 0.5$. As expected, the fraction

of clumps that satisfy this condition decreases as their magnitude increases. We concluded that our sample is 50% complete down to 28 mag in F140W, 28.3 mag in F105W, 28.1 mag in F606W imaging, and 28.8 mag in emission line maps.

Dust reddening To estimate the EW and physical properties of the clumps (e.g. stellar mass), it was necessary to determine their intrinsic luminosity, correcting their observed flux for the effect of dust extinction. A subsample of galaxies were observed with longslit MOIRCS spectroscopy (Valentino et al. 2015) and therefore it was possible to estimate their average nebular extinction from the Balmer decrement (assuming that $H\alpha/H\beta = 2.86$ intrinsically, Osterbrock 1989). For the rest of the sample we determined the dust extinction through SED fitting, using the FAST code (Kriek et al. 2009) on the UV to IR photometry. Bruzual & Charlot (2003) stellar population models with delayed exponential SFHs, Salpeter (1955) IMF, and Calzetti et al. (2000) extinction law were used. The metallicity was a free parameter of the fit. We compared results obtained considering different photometric catalogs: one created with SExtractor based on aperture photometry, and the other one based on GALFIT photometric decomposition of galaxies. When the IRAC photometry suffered from heavy neighbours contamination we excluded the $3.6 \mu\text{m} - 4.5 \mu\text{m}$ bands from the fitting procedure (Strazzullo et al. 2013). The SED fitting results obtained with the two photometric catalogs were typically consistent. We computed the mean extinction (A_V) affecting each galaxy averaging the values obtained using different photometric catalogs, weighted for the associated uncertainties. We checked that estimating the A_V with SED fitting, fixing the metallicity to the solar value, our results would not change substantially. We therefore decided to let the metallicity as a free parameter of the fit, since in principle at redshift $z \sim 2$ galaxies could have subsolar metallicity. We finally compared, for a subsample of galaxies, the extinction derived from SED fitting with the one estimated with MOIRCS spectroscopy. The dust attenuation affecting the stellar light ($E(B - V)_{\text{cont}}$) is typically lower than the one impacting the emission lines ($E(B - V)_{\text{neb}}$). We therefore used the conversion factor estimated by Kashino et al. (2013) to link the two ($E(B - V)_{\text{neb}} = 0.83 E(B - V)_{\text{cont}}$), and to compare the estimate obtained with SED fitting with the one determined from the Balmer decrement. We find that the measurements obtained with the two different methods are consistent within the uncertainties. For the rest of our analysis we will consider that the reddening affecting the clumps is the same as the average one measured for the whole galaxy. The correctness of this assumption is supported by literature works showing that clumps and their parent galaxies typically are affected by comparable extinction (Elmegreen et al. 2007; Wuyts et al. 2013), and by our previous results obtained

for Vyc1 (Section 2.4).

Stellar masses of our sample galaxies were estimated with SED fitting, using the same setting detailed above.

Constraining the age of the clumps To constrain the age of the clumps we used the tight correlation between their EW and the evolution of their stellar population, as we did for the single case of Vyc1 (Section 2.4). We considered Starburst99 stellar population synthesis models to compute the evolution of the H α and H β EW as a function of the age of the stellar population. We considered a Salpeter (1955) IMF and two different SFHs: a constant star formation law and a SFH obtained from our hydrodynamical simulations (Section 2.4, Figure 2.8), characterized by a burst of star formation lasting for almost 20 Myr, followed by a rapid decline. To estimate the evolution of the [OIII] and [OII] emission lines that are not directly modelled by Starburst99, we rescaled respectively the H β models considering the typical [OIII]/H β line ratio for star-forming galaxies at $z \sim 2$ (Steidel et al. 2014), and the H α models assuming an intrinsic ratio H α /[OII] = 1 (Kewley et al. 2004). Comparing these model predictions with the measured EW, we estimated the age of our sample clumps. We compared the ages determined assuming the two SFHs mentioned above and we checked that our conclusions did not change substantially choosing one or the other. In the following analysis we will consider the age estimates obtained assuming a SFH with constant SFR.

Distance of the clumps from the galaxy nucleus We estimated the observed distance of the clumps from the nucleus of the host galaxy as the difference between the clump coordinates and the center of the diffuse component determined by GALFITM. We checked that the center of the disks as determined decomposing the galaxies light profiles were in agreement with the barycenters determined by SExtractor. Considering the axial ratio and position angle of the disks measured by GALFITM, we finally computed the deprojected distance of the clumps from the nucleus.

Estimate of the clumps stellar masses We estimated the clumps stellar mass multiplying the M/L of the host galaxy by the luminosity of the continuum emission of the clumps (as measured in the F140W images). This scaling crudely assumes that the M/L ratio remains constant across the galaxy disk and it does not take into account the fact that the clumps could have different colors with respect to the host galaxy, mainly due to their younger age. However, it seems that generally the M/L ratio has a fairly small scatter across the disk: Förster

Schreiber et al. (2011) report a scatter of ~ 0.2 dex in the observed $\log(M/L)$ across the galaxy, and we obtained similar results for our analysis of Vyc1 (Section 2.4, Figure 2.4). Therefore we conclude that the assumption of a constant M/L ratio is on average valid within a factor of ~ 2 . In the following we will consider a typical uncertainty on the stellar mass of our sample clumps of ~ 0.2 dex.

Sample selection We estimated the physical properties (e.g. age, stellar mass) of a sample of 83 clumps that we afterwards selected according to the following criteria. We excluded all the clumps (i) hosted in galaxies in which an AGN has been detected, (ii) with a deprojected distance from the galaxy nucleus smaller than $0.5 R_e$, and (iii) with a Sérsic light profile instead of PSF-like. I will detail these choices below. After this selection, our final sample is made of 49 clumps.

We excluded from our sample all the galaxies hosting an AGN since it might pollute the clumps emission lines, altering the EW that we measured. Therefore, it could drive us to a wrong age estimate, since the stellar population models we used assume that the emission lines are only powered by star formation. We have XMM (80 ks, Gobat et al. 2011; Brusa et al. 2005) and Chandra (94 ks, Campisi et al. 2009; Valentino et al. 2016) data centered on the cluster Cl J1449+0856, covering a total field of view of ~ 500 arcmin². None of the galaxies hosting the clumps that we included in our sample were X-ray detected. Besides, none of them were showing any AGN signature in our 24 μ m-Spitzer, Herschel, and JVLA data. For the subsample of galaxies that were followed-up with longslit MOIRCS spectroscopy we computed the galaxy-integrated $[\text{OIII}]/\text{H}\beta$ and $[\text{NII}]/\text{H}\alpha$ ratios to use the BPT diagnostic diagram to distinguish sources with emission lines powered by star formation from those excited by an AGN. We found that one galaxy (hosting only one clump) was laying in the locus statistically occupied by the AGNs and therefore we excluded it from our sample. Finally, for the same subsample of galaxies, we checked for the presence of AGNs using the $\text{H}\alpha$ EW – $[\text{NII}]/\text{H}\alpha$ diagnostics (Cid Fernandes & González Delgado 2010; Cid Fernandes et al. 2011). None of our sample galaxies were selected as AGNs according to this diagram (Valentino et al. 2015).

We decided to exclude from the sample the clumps located within $0.5 R_e$ since their location can be considered basically coincident with the galaxy nucleus: they could simply be proto-bulges or nuclear starbursts. However, we checked that keeping them in our sample would not affect our final conclusions.

Finally, we did not consider in our final sample “clumps” whose light profile had to be fitted with a Sérsic profile instead of a PSF-like one. A minority of these Sérsic profiles ($\lesssim 5\%$) had Sérsic index $\gtrsim 2.5$ and $R_e \gtrsim 0.4$: since they are too large to be clumps and are more likely spiral arms or satellites, they were

considered as part of the diffuse component of the galaxy and they were not included in our clumps catalogue. We kept instead in our initial sample of 83 clumps the ones with Sérsic index < 2.5 and $R_e \lesssim 0.4$ ”, but we finally decided to exclude them from our final sample of 49 clumps. This choice was driven by the fact that in the majority of the cases these “clumps” had very old ages (age $\gtrsim 1$ Gyr) and were preferentially located at large deprojected distances from the galaxy nucleus ($d_{\text{deproj}} \gtrsim 2R_e$). It seems therefore more likely that they are satellites or just background or foreground contaminating galaxies rather than giant star-forming clumps associated with the disk of the galaxy. This conclusion is also supported by the fact that these “clumps” are not detected in the emission line maps: it could be due to their old ages, but also to their different redshift with respect to the considered galaxy. Only three “clumps” that we modelled with a Sérsic profile have young ages (25 – 30 Myr) and are located within $3 R_e$. There are numerical simulations indicating that giant clumps are conglomerates of smaller clumps, clustered in small regions, typically unresolved even with *HST* (e.g. Bournaud 2016). In some cases this might result in a disk-like profile with Sérsic index ~ 1 and slightly resolved sizes. The three clumps we identified with young ages and Sérsic light profiles might just be the manifestation of this phenomenon. We decided however to exclude them from our sample for consistency with the elimination of the older ones. If we were to keep them instead, our conclusions would not change.

2.5.2 Results and discussion

In the astrophysical community there is still a hot debate about the mechanisms that drive the galaxies morphological transformation through cosmic time, an issue that also concerns the physical phenomena that induce bulge formation. To test the possibility that clumps migrate inward and eventually grow the bulge, we looked for a possible trend between the clumps age and their distance from the galaxy nucleus (Figure 2.12). We normalized the deprojected distance with the effective radius of the disk as determined by GALFITM, to take into account the different galaxy sizes: a clump located in the outskirts of a small galaxy has a smaller observed distance from the nucleus than one located in the outer part of a large source. Taking into account the size of the galaxy (e.g. its effective radius), we could correct for this effect. Furthermore, we considered the deprojected distance of the clumps from the nucleus rather than the observed one, to account for different galaxy inclinations that could otherwise bias our final result (e.g., a clump close to the nucleus of a highly inclined disk has a larger deprojected distance than a clump located at the same observed distance, but in a face-on source). We find that young clumps (age $\sim 20 - 30$ Myr) can form at any distance from

the galaxy nucleus, whereas older clumps are preferentially located at small galactocentric distances. The lack of old clumps in the outskirts of galaxies supports the theoretical scenario in which clumps migrate inward and coalesce potentially growing the galaxy bulge. This trend between the age of the clumps and their distance from the nucleus was indeed predicted by simulations (e.g. Mandelker et al. 2014) finding that giant clumps survive stellar feedback and are long-lived. Our finding is also qualitatively in agreement with the age – distance trend measured by Förster Schreiber et al. (2011) and Guo et al. (2012), although the first one is based on measurements of 7 clumps from a single galaxy, and the second one is only considering the observed distance of the clumps from the nucleus (and not the deprojected one as we are doing here). The main novelty of our study with respect to the previous ones is the fact that we are probing a larger parameter space, in particular extending the analysis toward younger clump ages. This was possible thanks to our sample selection that allowed us to simultaneously measure the clumps properties in emission lines and continuum maps. Although with this data set we are able to detect old clumps (e.g. those visible in the continuum, but not in the emission line maps), our analysis is by construction biased toward young ages. In fact, when we created emission line maps cross-correlating the spectral images of the same galaxy observed with different position angles (Section 2.3), we excluded all the maps where the cross-correlation was not reaching a maximum. Generally the galaxy disk is quite faint in the emission line maps, so if the galaxy does not host a young clump with bright emission lines, the cross-correlation does not show any peak since it only correlates noise. In these cases, the emission line maps were discarded and the galaxy was excluded from our sample. However, there is no reason to think that the procedure we used to create the emission line maps systematically removed only the old clumps located in the outskirts of galaxies and not the ones close to the nucleus. Therefore we conclude that the technique that we used to create emission line maps is not biasing our results. Two caveats are however needed. We decided to exclude from our sample the clump candidates whose light profile had to be fitted with a Sérsic profile instead of a PSF (Section 2.5.1). If we were to include them in the analysis, the observed relation between clumps age and distance from the nucleus (with older clumps systematically closer to the galaxy barycenter) would have been shallower. We would need even deeper spatially resolved spectroscopic data to definitely assess if these clump candidates with Sérsic profiles are not detected in the emission line maps because of their old stellar populations (therefore indicating that old star forming regions can be located in the outskirts of galaxies), or due to their different redshift with respect to the main galaxy (in which case they would be external small sources rather than clumps). A second caveat concerns the fact that, even considering only PSF-like clumps, if we were to exclude

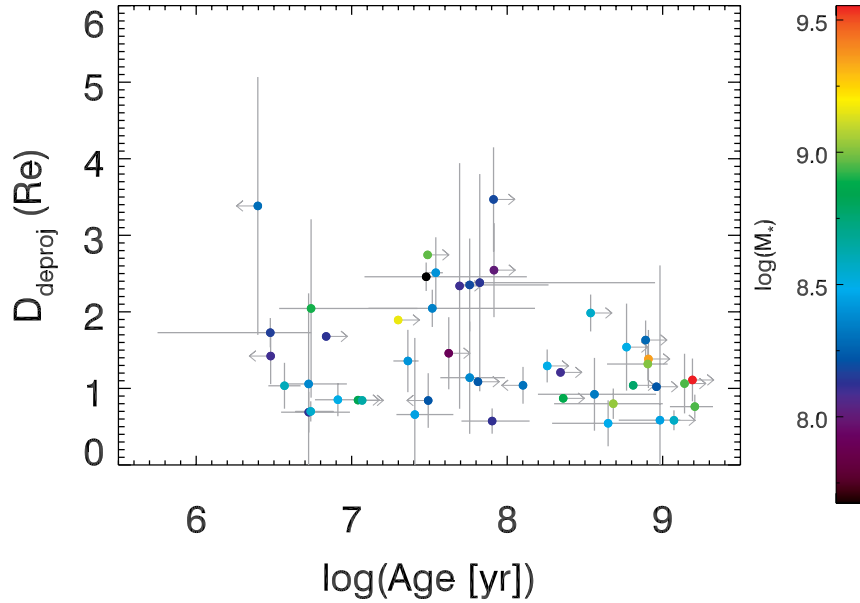


Figure 2.12 – Relation between the clumps age and their deprojected distance from the galaxy nucleus, normalized by the disk effective radius. The points are color coded by clump stellar mass.

the star forming regions with a deprojected distance $> 2R_e$ the relation between the clumps age and their distance from the nucleus would have been less evident. It could be interpreted as the evidence that some old (especially moderate-mass) star forming regions could have been scattered out to large radii due to the encounter with more massive clumps, as suggested by some numerical simulations (e.g., Bournaud 2016).

Although the scatter of the points is fairly large, we found a hint that older clumps have higher stellar masses than younger ones, as expected considering that clumps convert their gas into stars as time passes (Figure 2.13, left panel). The Spearman correlation coefficient of the clumps stellar mass and age relation is 0.27, which has a probability of 0.06 of resulting by chance. We also found a tentative trend between the mass of the clumps and their deprojected distance from the galaxy nucleus (Figure 2.13, right panel). Not to be polluted by the

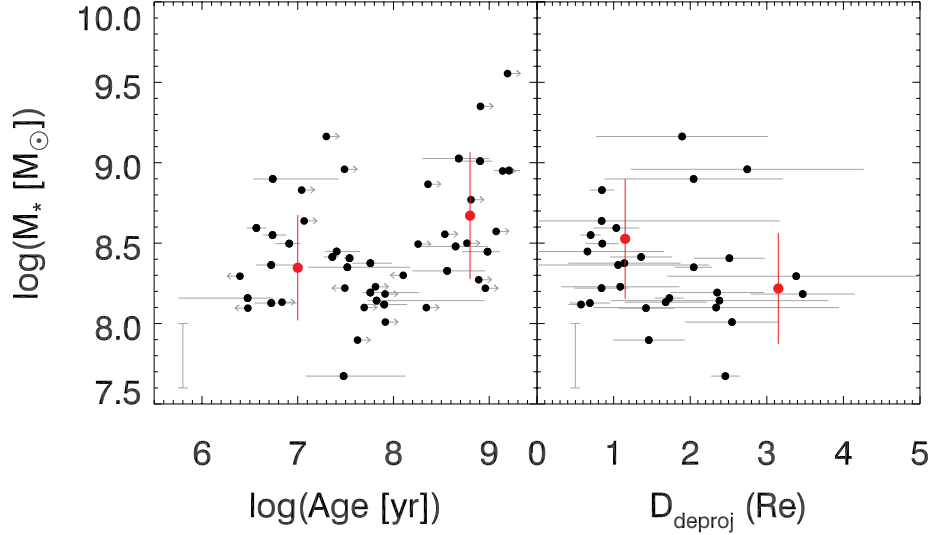


Figure 2.13 – Dependency of the clumps stellar mass on other physical quantities. Left panel: clumps stellar mass as a function of their age. Right panel: clumps stellar mass as a function of their deprojected distance from the galaxy nucleus, normalized by the disk effective radius. Only clumps with age < 100 Myr are reported in this panel. The black points indicate single clumps measurements, whereas the red filled circles with error bars indicate the mean and standard deviation of the points in two bins of age and galactocentric distance. The typical stellar mass uncertainty is reported in the bottom left corner of each panel.

stellar mass – age relation presented above, we only considered young and intermediate age clumps (age < 100 Myr). The correlation between the clumps stellar mass and distance from the galaxy barycenter has a Spearman correlation coefficient of -0.19 , that has a probability of 0.32 of resulting by chance. It seems that clumps in the outskirts typically are less massive than the ones formed in the central region of the galaxy. This might be explained with the fact that the Jeans mass, considered as the maximum mass that can collapse given the gas content of the disk, augments as the velocity dispersion increases ($M_J = \pi^3 \sigma^4 / (64 G^2 \Sigma)$, where Σ is the gas surface density of the galaxy and G is the gravitational constant). Since the velocity dispersion at the center of galaxies is typically higher than in the outskirts, we expect that a larger fraction of gas can collapse, forming on average more massive clumps.

Given our larger statistics of young clumps, we refined the computation of the clumps formation rate (CFR) and lifetime that we attempted with Vyc1 (Sec-

tion 2.4). We considered the number of observed clumps with an age ≤ 20 Myr: according to our simulations clumps younger than this age threshold should experience a burst of star formation, and therefore they should have bright emission lines. We therefore chose this age cut to be sure to have a complete sample of young clumps. We compared the number of young star-forming regions observed in our sample (N_{clumps}) with the number of galaxies in the parent sample (N_{gal}) that are massive enough to host a giant clump ($M_* > 8.5 \times 10^9 M_\odot$, coincident with the mass completeness of our galaxy sample) and have the right redshift ($0.7 < z < 3.6$) to show an emission line ([OIII], H α and/or [OII]) in the G141 grism. We added an additional constraint on the mass of the galaxies whose redshift is such that an [OIII] emission could be detected in the grism spectroscopy: we only selected those with $M_* < 2 \times 10^{11} M_\odot$, since more massive galaxies would have an [OIII] emission too faint to be detected (Zahid et al. 2014). We finally had a parent sample of 73 galaxies that have the right properties to host the giant clumps observed in our sample. We computed the clump formation rate as $\text{CFR} = N_{\text{clumps}} / (t_V N_{\text{gal}}) = 6.8^{+2.9}_{-2.1} \text{ Gyr}^{-1}$, where t_V is the visibility window during which young clumps with high EW can be detected ($t_V = 20$ Myr by construction). This estimate of the CFR is slightly higher than the one we obtained considering only Vyc1 ($\text{CFR} = 2.5^{+2.3}_{-0.8} \text{ Gyr}^{-1}$). The reason for this marginal discrepancy is likely due to the fact that we have now included in our computation all the young clumps we observed, irrespectively of their total mass. However, lower mass clumps are expected to have shorter lifetimes than high-mass ones, since they are more sensitive to stellar feedback, and to be produced at higher rates (Mandelker et al. 2015). It means that their CFR is expected to be higher. Including them in our sample we are therefore averaging the contribution of massive clumps (like Vyc1) and lower mass ones, and it results in an increase of the CFR with respect to our previous estimate.

Finally, given our new gauge of the CFR, we refined the estimate of the clumps lifetime. We determined the total clumps mass considering their stellar mass from our observations and a clumps gas fraction in a plausible range ($f_{\text{gas}} \sim 60\% - 80\%$), as estimated for young clumps from cosmological simulations (Dekel et al., in prep.). We made the assumption that all the gas content of young clumps (age $\lesssim 20$ Myr) is transformed into stars at old ages. We therefore considered the average number of old clumps per galaxy ($N_{\text{cl/gal}}$) reported in the literature (Förster Schreiber et al. 2011; Guo et al. 2012) with a stellar mass comparable or higher than the minimum gas mass of our observed young clumps. We find that $N_{\text{cl/gal}} \sim 3$, and therefore the clumps lifetime we estimated is $\text{LT} = N_{\text{cl/gal}} / \text{CFR} = 438^{+464}_{-274} \text{ Myr}$. It is consistent with our previous estimate based on the single clump Vyc1 and with the fact that in our current statistical

sample we observed a fraction of clumps with old ages ($\gtrsim 500$ Myr, Figure 2.12), indicating that clumps are long-lived. It is also in agreement with the results by Förster Schreiber et al. (2011) and Guo et al. (2012) that find clumps with ages up to $\sim 500 - 1000$ Myr. The median age of our sample is instead lower than the one obtained by Wuyts et al. (2012), likely due to our sample selection biased toward young clumps age, as detailed above. Our estimate of the clumps lifetime supports simulations predicting that massive clumps are not disrupted by stellar feedback, but on the contrary they survive, migrate inward and potentially play an important role in bulge formation and growth (e.g. Bournaud et al. 2014; Dekel et al. 2009; Mandelker et al. 2015). If we were to consider that not all the gas content of clumps is transformed into stars, but only a fraction of it (50% – 70%) is consumed, as shown by some cosmological simulations (Dekel et al., in prep.) our results would not change and, on the contrary, we would obtain even longer lifetimes.

Integrating the clumps formation rate that we measured over the typical timescale for bulge formation we attempted a first estimate of the fraction of bulge mass assembled thanks to clumps migration and coalescence. Considering that ~ 6 clumps per galaxy per Gyr are formed with total masses of $\sim 10^9 M_\odot$, integrating over ~ 2 Gyr (the timescale for bulge formation, e.g. Bournaud 2016), we obtain that $\sim 10^{10} M_\odot$ could coalesce into the bulge thanks to clumps inward migration. This is likely a lower limit, since low-mass clumps ($\sim 10^{8-8.5} M_\odot$), that are expected to be the most numerous to be formed due to disk instability, are not included in our sample since they are too faint to be detected. Furthermore, while migrating inward, clumps could funnel toward the galaxy center large amounts of gas, as shown by numerical simulations, therefore increasing the amount of mass that can contribute to bulge growth.

2.5.3 Conclusions

We presented the analysis of a statistical sample of ~ 50 clumpy galaxies observed with *HST* in and around the galaxy cluster Cl J1449+0856 (Gobat et al. 2013). We have direct images taken with WFC3 with the filters F140W, F105W, and F606W, together with slitless spectroscopic data taken with the grism G141 along three different position angles. For all the galaxies of our sample we created spatially resolved emission line maps that we calibrated astrometrically maximizing the cross-correlation between the spectral images of each galaxy taken at different position angles and the F606W continuum image. The alignment of the imaging and emission line maps allowed us to spatially compare the mass distribution (traced by the direct images, especially F140W and F105W), the past star formation distribution (with F606W), and the current star formation distribu-

tion (probed by the emission lines). We could therefore assemble a sample of ~ 50 clumps and study their physical properties comparing their continuum and emission line luminosities. This allowed us to select clumps with a wide range of ages, in particular targeting the young and intermediate age ones that show bright emission lines powered by gas ionized mainly by O and B stars. They were generally missed by surveys based on continuum selection only, due their faintness in the observed NIR and optical images. We found that old clumps (age $\gtrsim 200$ Myr) in our sample are preferentially located close to the galaxy nucleus, whereas young ones (age $\lesssim 50$ Myr) can be found both in the inner region of the galaxies and in the outskirts. It supports the scenario in which clumps can form everywhere in galaxies, but then they tend to migrate inward due to dynamical friction and gravitational torques. This is in agreement with other observational literature works (Förster Schreiber et al. 2011; Guo et al. 2012), and it extends these results to younger ages. The fact that we find clumps with ages ~ 500 Myr or slightly higher, seems to indicate that giant clumps are long-lived and they are not disrupted by stellar feedback in short timescales (~ 50 Myr). This conclusion is also supported by our computation of the clumps formation rate and lifetime. Comparing the number of youngest clumps in our sample (age < 20 Myr) with the number of galaxies of the parent sample that could host such giant clumps, we estimated that $6.8^{+2.9}_{-2.1}$ clumps per galaxy per Gyr are formed. Comparing the CFR with the average number of clumps per galaxy reported in the literature, we estimated the clumps lifetime to be $\sim 438^{+464}_{-274}$ Myr. Our results indicate that clumps are long-lived phenomena and they support simulations suggesting that clumps inward migration and coalescence might be an important mechanism to build galaxy bulges. We also find a tentative trend between the clumps stellar mass and age indicating that old clumps typically have higher stellar masses than young ones, as expected considering that the gas content of clumps is transformed into stars as time passes. Finally, there are hints that young clumps forming closer to the galaxy nucleus are typically more massive than those forming in the outskirts. This could be explained with the fact that in the central regions the Jeans mass (considered as the maximum mass that can collapse given the properties of the disk) is higher than in the outskirts, due to its dependence on the velocity dispersion of the disk.

Chapter 3

Passive compact galaxies

In this Chapter I describe the analysis of a sample of compact passive galaxies at $z \sim 1.5$ that I started during my Master thesis in the context of a studentship at the University of Minnesota, and I have then developed and completed during my PhD. This study has been done in collaboration with the WISP team and the research group of extragalactic astrophysics based at Padova University and it led to a publication (Zanella et al. 2016) that I append in Appendix C. I introduce the open questions that motivated our work in Section 3.1, while in Section 3.2 I describe our data set. Section 3.3 details our analysis, and in Section 3.4 I discuss our results. Finally I review our conclusions in Section 3.5.

3.1 Introduction

Despite the large number of studies that analysed the properties of ETGs both at low and high redshift, it is still unknown how these systems formed, if all the stars were assembled in the same object from the beginning or if they formed in lower mass galaxies that later merged. This issue is deeply rooted in the wider and longstanding debate about structures formation in the Universe. Mainly two formation models have been proposed and are usually counterposed since decades: the so-called “monolithic collapse” model (Eggen et al. 1962, Larson 1975) and the “hierarchical merging” scenario (Toomre 1977, White & Frenk 1991). In the former, ellipticals and spheroids form at very early epochs as the result of a global starburst and then they evolve passively to the present, with no or negligible new star formation episodes. If the conditions are appropriate, a spheroid can gradually grow a disk, accreting gas from the environment: in this way the monolithic-collapse model can explain the formation of disk galaxies (Renzini 2006). In the hierarchical merging scenario instead, the formation of

disks precede that of spheroids, and elliptical galaxies are the result of merging events in which the disks are mutually disrupted. The two scenarios appear to be in contradiction, but still none of the two seems to prevail over the other and there are different observational constraints that credit one or the other model. An evidence in favour of a fast and dissipative monolithic collapse is the fact that the great majority of the stars in massive, elliptical galaxies are old (Mannucci et al. 2001) and have high $[\alpha/\text{Fe}]$ ratios, implying a short star formation burst (Worthey et al. 1992). Moreover the structural and dynamical properties of ETGs are well described by cold dissipationless collapse (e.g., van Albada 1982, Trenti et al. 2005) and the high formation redshift together with the number fraction found for massive ellipticals are naturally explained by this model (e.g. McCarthy 2004). On the other hand, the hierarchical merging scenario arises directly from the cold dark matter models (e.g. White & Rees 1978). It also predicts that galaxies in high-density environments form earlier than ETGs in lower density regions (De Lucia et al. 2006), a signature that indeed has been observed (e.g. Thomas et al. 2005). Trying to understand the assembly history of massive ellipticals through the analysis of the merger rate or the number density of such systems is hard because very massive galaxies are scarce and the field-to-field variance associated with limited observed volumes strongly affects their clustering properties (e.g., Cimatti et al. 2006, Trujillo et al. 2007). A better way to investigate the assembly process of these massive galaxies is to analyze the evolution of their sizes at a given stellar mass. During the last decade an evolution of the mass–size relation of passive galaxies with cosmic time has been diffusely observed and many studies confirmed that ETGs at high redshift are more compact – namely, have smaller sizes at fixed mass – than local ones (e.g. Daddi et al. 2005; Trujillo et al. 2007; Cassata et al. 2010; Carollo et al. 2013; Belli et al. 2015). In the hierarchical merger scenario this evolution is expected: the merging events produce a continuous increase of the galaxy size. In particular if minor mergers are considered, the galaxy mass is not expected to substantially change, whereas its size augments, producing the evolutionary trend that is indeed observed. On the contrary, if the monolithic collapse scenario is correct, individual galaxies are not expected to substantially modify their dimensions, and the observed evolution has to be explained as the size increase of the average population of passive ETGs (see also Section 1.1.2). To test whether one of the two scenarios better explains the observations (or if both are needed to some extent) we have considered a sample of passive galaxies at $z \sim 1.5$ and studied how they populate the mass–size plane as a function of their stellar age. In case the average population of galaxies changes with time (e.g. larger galaxies, at fixed mass, are formed later because of the decreasing average density of the Universe with cosmic time due to Hubble expansion) galaxies with larger sizes are also expected to have younger

ages. On the contrary, if the merger scenario prevails, no trend with age is expected.

3.2 Data

Our sample includes 34 passive galaxies identified in the WISP survey, a pure-parallel *HST* program to obtain near-IR slitless spectra together with optical and IR imaging of hundreds of independent fields in the sky. The data have been presented in detail in Atek et al. (2010). Briefly, we considered for this work the first 27 fields observed with both *HST* WFC3 grisms (G102, and G141; with resolving power $R = 210$ and 130, respectively) as well as with the WFC3–UVIS camera in the optical. The IR spectra cover the wavelength range between $0.85 \leq \lambda \leq 1.6 \mu\text{m}$, with approximately $0.1 \mu\text{m}$ overlap between the two grisms that allowed us, together with the IR imaging, to check for proper photometric calibration and sky subtraction. The data were reduced and the spectra extracted with a combination of a custom pipeline described in Atek et al. (2010) and the aXe software (Kümmel et al. 2009). In addition, a new cleaning algorithm has been implemented to properly account for contamination from overlapping spectra (Bedregal et al. 2013). The imaging was obtained in the UV with the F475X and F600LP (apart from the two deepest fields that were observed with F606W and F814W instead), and in the NIR with the F110W and F160W filters.

3.3 Analysis

Bedregal et al. (2013) studied the properties of a sample of $H < 23$ mag galaxies pre-selected on the basis of their $J - H$ color ($J - H \geq 0.6$). The color cut pre-selects sources with spectral breaks broadly covered by the available spectra for which the redshifts can be measured, while the magnitude cut ensures a sufficiently high S/N in the spectra. They measured spectroscopic redshifts and stellar population properties of the galaxies by simultaneously fitting the broadband photometric points and spectra (Figure 3.1). The Bruzual & Charlot (2003) library of stellar population synthesis models have been used and 7 star formation histories have been considered (continuous, exponentially declining with e -folding times $\tau = 0.01, 0.1, 1, 5$ Gyr, and exponentially increasing with $\tau = 1, 5$ Gyr). During the fit the metallicity has been fixed to solar, in agreement with the spectroscopic results by Onodera et al. (2012) for a sample of $z \sim 1.4$ quenched galaxies. A Salpeter initial mass function (Salpeter 1955) has been used following recent results obtained for massive galaxies from stellar kinematics, stellar populations, and gravitational lensing (e.g. Cappellari et al. 2012; Conroy & van

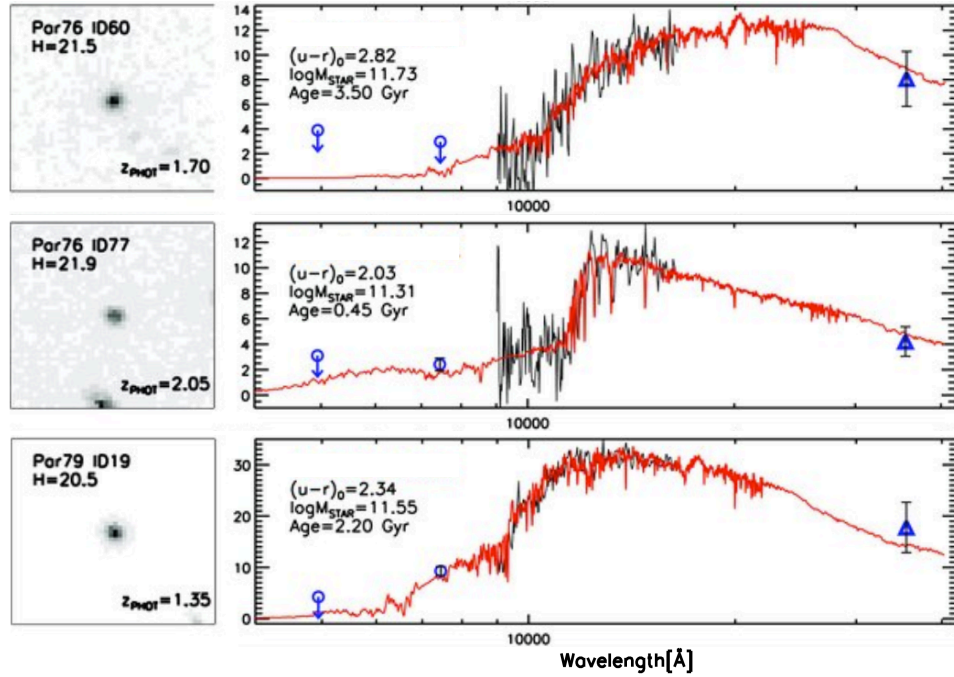


Figure 3.1 – Examples of SED fits for our sample galaxies. Left: 6'' \times 6'' image stamps in H_{F160W} band. Right: data and SED fits. G102 and G141 spectroscopic data are shown with a black curve, photometric data are indicated with blue symbols. Blue circles represent *HST*/WFC3/UVIS BF475X and RF600LP photometry (arrows correspond to 3σ upper limits). Blue triangles represent Spitzer/IRAC 3.6 μm observations (when available). The best SED model fit from the library of Bruzual & Charlot (2003) stellar population models is shown with a red curve. In the y axis, flux densities, F_{λ} , are normalized to $10^{-19} \text{ergs}^{-1} \text{cm}^{-2} \text{\AA}^{-1}$ (Bedregal et al. 2013).

Dokkum 2012; Brewer et al. 2012). However, they checked that changing the IMF (e.g. adopting a Chabrier (2003) IMF) the stellar mass and SFRs that they would retrieve from the stellar population fitting procedure would be ~ 1.7 times smaller, but they conclude that their sSFRs estimates are robust to IMF changes. Finally a range of extinction ($0 \leq A_V \leq 1$) has been considered and the Calzetti et al. (2000) extinction law has been used (Bedregal et al. 2013).

I have carried out the structural analysis of this sample of galaxies and then I complemented these results with the stellar population parameters obtained by Bedregal et al. (2013). I will describe in the following how we selected our final sample, analyzed these galaxies and interpreted the results.

From the Bedregal et al. (2013) sample we selected a subsample of passive galaxies with $\text{sSFR} \lesssim 0.01 \text{ Gyr}^{-1}$, redshift $z > 1.3$ and $M_* > 4.5 \times 10^{10} M_\odot$. This is the minimum stellar mass measurable at the depth of our data at $z \sim 1.5$ (the average redshift of the sample), for a maximally old stellar population model. These limits have been chosen to select a sample of massive and passive galaxies with robust estimates of the stellar populations. Bedregal et al. (2013) indeed, thanks to extensive simulations, showed that they were able to accurately recover only the stellar population properties of galaxies with redshift $z \gtrsim 1.3$, where the 4000 Å break was fully covered by the grism spectra. Since more degeneracies appeared when the break was only coarsely covered by the UVIS photometric data, we decided to conservatively consider in our analysis only galaxies with $z > 1.3$. If we were to consider an even more conservative sample selection based on the minimum stellar mass measurable at $z \sim 2$ (the highest redshift spanned by our sample) $M_* > 7.9 \times 10^{10} M_\odot$, our results would not change substantially (see Section 3.4). We verified that the stellar mass function of our sample of passive galaxies is consistent with the one determined by Muzzin et al. (2013), for quiescent galaxies, at the same redshift. All galaxies have accurate luminosity-weighted stellar ages derived by fitting the grism spectra with stellar population models. To quantify the uncertainties associated to the stellar population parameters that they obtained, Bedregal et al. (2013) performed a set of simulations. Briefly, they used Bruzual & Charlot (2003) models with known redshift and stellar population properties to simulate the spectroscopic and photometric data. Then these mock data were treated as the real ones, applying the same magnitude and color cuts described above, and they were fitted to recover their stellar population properties. Using the same set of simulations performed by Bedregal et al. (2013) we find that for our sample, the stellar ages are recovered with an accuracy of 35%.

For the structural analysis of the light distribution of our sample galaxies we used the J_{110} images since they were the deepest at our disposal. The sky background has been previously subtracted (Atek et al. 2010; Colbert et al. 2013). We performed the measurements with two different fitting algorithms: the widely used GALFIT code (Peng et al. 2010) and the alternative GASP2D code (Méndez-Abreu et al. 2008). To be consistent with previous works in the field, we fit the galaxy light distribution with a single Sérsic law (Sérsic 1968):

$$I(r) = I_e 10^{-b_n [(r(q,PA)/r_e)^{1/n} - 1]} \quad (3.1)$$

where I_e is the surface brightness at the effective radius (r_e), q is the axial ratio, PA is the position angle, and n is a parameter related to the curvature of the surface-brightness radial profile. The quantity b_n depends on the Sérsic index n ,

and was computed numerically to ensure that r_e includes half of the total galaxy light ($b_n = 0.868n - 0.142$, Caon et al. 1993).

Both codes require as input the instrumental PSF. Our data were taken in parallel to observations performed with the Cosmic Origin Spectrograph and Space Telescope Imaging Spectrograph, and no spatial dithering was done in between different exposures. Because of this, the final PSF is undersampled at the pixel size ($0.13'' \text{ pixel}^{-1}$) of the WFC3-IR camera. We provide both GALFIT and GASP2D with a PSF that we obtained as the median of 18 unsaturated stars across the 27 analyzed fields. We used this median PSF to fit individual stars in each field, and found residuals of at most 20%, irrespective of the field. Before fitting the galaxies, we masked any foreground and background sources, as well as detector artefacts that can contaminate the surface brightness distribution. The main differences between the two codes is in the way the initial values for the parameters are determined. GALFIT does not provide a way to estimate them, while GASP2D internally determines their values by performing a fit on the one-dimensional surface brightness profile obtained using the IRAF task `ellipse` (Méndez-Abreu et al. 2008). We visually inspected all the fits to check for their reliability and we found that, for each sample galaxy, the residuals were lower than 20%.

The galaxy effective radii (r_e) measured with the two algorithms are consistent within the uncertainties. In the following analysis we use the sizes determined by GASP2D, but our conclusions would not change if we switch to GALFIT instead. For each galaxy we compute the circularized effective radius as $r_e^{\text{circ}} = r_e \sqrt{q}$, where q is the galaxy axial ratio.

We determined the uncertainties associated to the r_e measurements through Monte Carlo simulations. We created 1000 artificial galaxies with Sérsic parameters randomly chosen in the range of values observed for real galaxies (total magnitude $19 \leq m_{\text{tot}} \leq 24$, effective radius $0.1'' \leq r_e \leq 1.5''$, Sérsic index $0.5 \leq n \leq 12$, axial ratio $0.2 \leq q \leq 1$, position angle $0^\circ \leq PA \leq 180^\circ$). All the models were convolved with the PSF image and we added Poisson noise to reproduce the observations. The best-fit Sérsic parameters were then derived using both GALFIT and GASP2D.

For each parameter, we estimated the fractional uncertainty as:

$$\epsilon = \frac{p_{\text{out}} - p_{\text{in}}}{p_{\text{out}}} \quad (3.2)$$

where p_{out} is the fitted parameter and p_{in} is the input value. We then computed the median and the 16th and 84th percentiles in bins of p_{out} , to estimate the systematics together with upper and lower uncertainties on the parameters. We

Table 3.1 – Circularized effective radius, Sérsic index, stellar mass, age, and redshift of the galaxies in the final sample.

Galaxy	r_e^{circ} (kpc)	n	$\log(M_*/M_\odot)$	Age (Gyr)	z
(1)	(2)	(3)	(4)	(5)	(6)
Par66 ID135	1.33 ± 0.35	2.24	11.24	2.00	1.80
Par67 ID108	1.05 ± 0.33	1.07	10.71	1.02	1.35
Par67 ID140	1.75 ± 0.38	0.72	11.30	2.75	2.05
Par67 ID82	1.36 ± 0.26	2.29	11.08	4.00	1.35
Par73 ID152	2.71 ± 1.19	1.23	10.74	2.75	1.50
Par73 ID47	2.74 ± 0.17	4.03	11.16	0.90	1.45
Par73 ID57	1.67 ± 0.51	1.35	11.22	0.90	1.60
Par74 ID37	2.54 ± 0.82	1.72	11.44	2.50	1.60
Par76 ID26	2.32 ± 1.02	7.38	11.77	4.25	1.40
Par76 ID41	2.29 ± 0.84	0.74	11.26	4.75	1.35
Par76 ID60	2.96 ± 1.15	3.54	11.73	3.50	1.70
Par76 ID62	1.64 ± 0.59	17.53	11.50	3.50	1.70
Par76 ID77	1.23 ± 0.37	0.69	11.31	0.45	2.05
Par79 ID19	3.06 ± 0.70	7.92	11.55	2.20	1.35
Par79 ID86	1.53 ± 0.61	8.76	11.05	1.02	1.90
Par80 ID28	5.04 ± 0.56	4.15	11.43	4.00	1.40
Par80 ID35	1.73 ± 0.54	3.33	11.14	1.61	1.55
Par80 ID50	2.19 ± 0.51	1.10	11.17	3.00	1.40
Par80 ID93	4.13 ± 0.79	2.92	11.04	3.50	1.85
Par84 ID57	1.83 ± 0.57	2.09	11.43	4.00	1.45
Par87 ID118	3.14 ± 0.40	5.14	11.38	2.20	1.70
Par87 ID125	1.34 ± 0.53	7.29	10.66	0.40	1.85
Par87 ID54	1.28 ± 0.35	1.25	11.34	3.00	1.50
Par87 ID87	1.50 ± 0.53	6.05	11.12	2.00	1.65
Par87 ID95	2.73 ± 0.35	0.83	10.71	1.02	1.60
Par96 ID62	1.28 ± 0.35	2.47	10.91	1.02	1.75
Par115 ID83	2.04 ± 0.45	2.66	11.01	1.80	1.65
Par120 ID64	1.74 ± 0.54	3.43	11.23	1.61	1.50
Par120 ID84	4.01 ± 1.60	2.21	11.28	2.20	1.65
Par136 ID55	2.79 ± 1.22	2.11	10.68	0.90	1.65
Par136 ID77	3.55 ± 0.62	0.90	10.84	1.14	1.65
Par147 ID46	2.38 ± 1.04	2.52	11.02	0.64	1.46

NOTES - Col. (1): galaxy name defined as in Bedregal et al. (2013).
Col. (2): circularized effective radius with associated relative error.
Col. (3): Sérsic index. Col. (4): logarithm of the stellar mass. Col. (5):
age. Col. (6): redshift.

excluded from the sample two galaxies with output effective radii smaller than 1

kpc since we believe that $r_e < 1$ kpc values are not reliable, and we therefore set 1 kpc as the minimum size we are able to resolve. With Monte Carlo simulations we also checked that galaxies with $r_e < 1$ kpc do not enter the sample with an overestimated size. This limit is higher than the one obtained with similar depth surveys performed with the WFC3, and results from the lack of spatial dithering between exposures. Our conclusions would not change if we were to consider also the two galaxies with $r_e < 1$ kpc. The uncertainty associated with the circularized radius is calculated as $\epsilon_{r_e}^{\text{circ}} = \epsilon_{r_e} \sqrt{q}$, because we find that the axial ratio uncertainty is negligible.

The Sérsic best-fit circularized half-light radius, Sérsic index, stellar mass, stellar age and redshift for each galaxy in the final sample are presented in Table 3.1. We notice that half of the galaxies in our sample have a Sérsic index $n < 2.5$, typically associated to disk-dominated galaxies, in agreement with, e.g., van der Wel et al. (2011) and Newman et al. (2014, N14 hereafter). The disk-like light profile of these galaxies is likely an indication that the majority of their stars formed, before the galaxy was quenched, from gas that had the time to settle into a disk, whereas the spheroids are more likely merger remnants.

3.4 Results and discussion

We compare the stellar mass and size of our galaxies with those in the literature in the top panel of Figure 3.2. Before placing the literature data on the mass-size plane, we homogenized all the masses to Salpeter IMF (Salpeter 1955)¹ and corrected them for the systematics implied by the use of different synthetic stellar population models (SPMs). We scaled all masses to the Bruzual & Charlot (2003) SPMs adopting the Salimbeni et al. (2009) relations $\log(M_{\text{M05}}) \simeq \log(M_{\text{CB07}})$ and $\log(M_{\text{M05,CB07}}) = \log(M_{\text{BC03}}) - 0.2$ where BC03, M05, and CB07 indicate Bruzual & Charlot (2003), Maraston (2005), and Bruzual (2007) SPMs, respectively.

We limit the comparison to only those works where the sample selection is based on the galaxy specific star formation rates (with a sSFR cut similar to the one we adopted) and that span a similar redshift range. These samples are therefore directly comparable to our sample. The only exception is the Mancini et al. (2010) sample, where a morphological selection criterion (based on the Sérsic index) was also applied. Figure 3.2 shows that our measurements are consistent with the results found at similar redshifts by other works in different fields, once

1. The scaling factors between the Chabrier (2003), Kroupa (2001) and Salpeter (1955) IMFs that we adopted are: $\log(M_{\text{Chabrier}}) = \log(M_{\text{Kroupa}}) - 0.04$ (Cimatti et al. 2008) and $\log(M_{\text{Chabrier}}) = \log(M_{\text{Salpeter}}) - 0.25$ (Salimbeni et al. 2009)

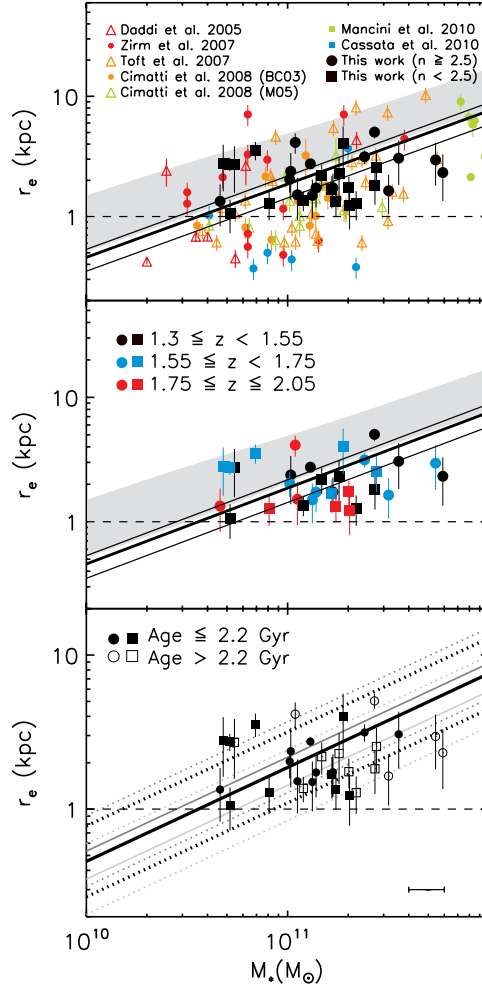


Figure 3.2 – The mass–size relation measured with the WISP data at $z \sim 1.5$. *Top*: Circularized R_c versus stellar mass for our sample (black symbols) divided into low and high Sérsic index galaxies (circles and squares). All reported literature results (colored symbols) consider circularized R_c , except for Mancini et al. (2010). The local mass–size relation and its scatter (Shen et al. 2003) are shown as a grey band. The solid thick line shows the mass–size relation from N14 at $z = 1.5$, while the thin lines were computed at the lowest (1.35) and highest (2.05) redshifts of our galaxies. *Middle*: Same as top panel, but showing our sample in three groups of redshift. *Bottom*: Same as the top panel, but showing our sample in two groups of stellar age. In the bottom corner we show the median stellar mass uncertainty. Our 1 kpc R_c measurement limit is shown (dashed line).

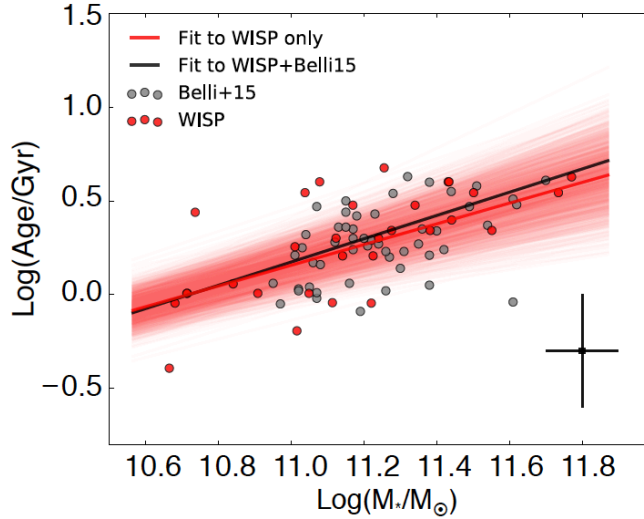


Figure 3.3 – Stellar age and mass of quenched galaxies are strongly correlated. Stellar age as a function of stellar mass for the WISP galaxies (red points) and Belli et al. (2015) sample (gray points). Belli et al. (2015) stellar masses were converted to Salpeter IMF following Salimbeni et al. (2009). The best-fit lines to the WISP sample alone and to the combined WISP and Belli et al. (2015) samples are shown with red and black lines, respectively. The red band shows the uncertainty on the fit to the WISP data alone (the uncertainty on the fit to the combined sample is similar, and not shown for clarity).

the size lower-limit (dashed horizontal line) is considered. The thick solid line shows the best-fit mass-size relation derived by N14 for field galaxies, computed at the median redshift of the sample. The thin lines were computed at the lowest and highest redshifts of our sample galaxies.

In the bottom panel of Figure 3.2 we reproduce the mass-size relation for our galaxies, dividing the sample in old (stellar age > 2.2 Gyr) and young objects (age ≤ 2.2 Gyr). The age separation was chosen to divide the galaxies in two similar size samples. Figure 3.2 shows how the most massive galaxies ($M_* > 2 \times 10^{11} M_\odot$) tend to be older than less massive ones, a trend compatible with other observational results indicating that more massive galaxies form the bulk of their stars earlier (e.g., Thomas et al. 2005; Kaviraj et al. 2013). We quantify this trend in Figure 3.3, where we show the stellar age versus the stellar mass, for the galaxies in our sample as well as for a sample of similarly selected objects identified by Belli et al. (2015). The correlation between the stellar population age and mass has a Spearman correlation coefficient of 0.66, which has a probability of 10^{-5} of resulting by chance. At any stellar mass, the stellar age (A_M) can be expressed as: $\log(A_M/\text{Gyr}) = (0.55 \pm 0.09) \log M_{10.5} - (0.12 \pm 0.07)$, where $M_{10.5}$ is the stellar

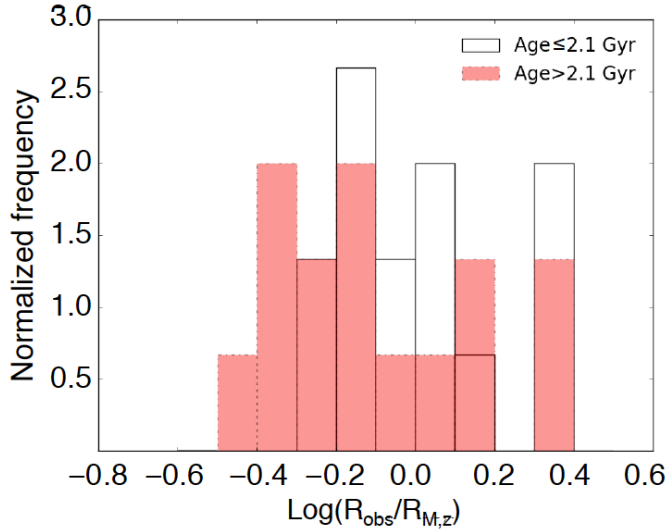


Figure 3.4 – Distribution of Δ_{lr} for the WISP passive galaxies. Although the distributions of young and old galaxies have different median values, they are not statistically different. Pink and white lines represent old and young galaxies, respectively (see text for details).

mass in units of $10^{10.5}M_{\odot}$.

To quantify whether a trend between the stellar age and the deviation from the $z \sim 1.5$ mass–size relation exists we compute for each galaxy the parameter $\Delta_{\text{lr}} = \log(R_{\text{obs}}/R_{M,z})$, i.e., the difference between the observed galaxy size (R_{obs}) and the size expected from the galaxy’s redshift and stellar mass ($R_{M,z}$), using the N14 mass–size relation. Values of $\Delta_{\text{lr}} > 0$ (< 0) indicate that galaxies are above (below) the mass–size relation at the galaxy redshift. The distributions of Δ_{lr} for the old and young galaxies with $M_* > 4.5 \times 10^{10}M_{\odot}$ are shown in Figure 3.4. The medians of the two distributions are $-0.04^{+0.15}_{-0.24}$ and $-0.14^{+0.21}_{-0.26}$, for the young and old samples, respectively (the upper and lower range show the 84th and 16th percentiles). The result of a two-sample Kolmogorov–Smirnov (KS) test ($D_{\text{KS}} = 0.4$ and $p = 0.2$), however, indicates that we cannot exclude that the two samples are drawn from the same parent distribution and thus the observed age difference is not significant. More conservatively considering only galaxies with $M_* > 7.9 \times 10^{10}M_{\odot}$ (our mass limit at $z \sim 2$, Section 3.3) we obtain consistent results (the medians of the young and old galaxy distributions of Δ_{lr} are $-0.10^{+0.09}_{-0.16}$ and $-0.18^{+0.17}_{-0.14}$, respectively).

The size measurement limit ($r_e > 1$ kpc) may introduce a bias particularly at the smallest masses, where our galaxies tend to populate the mass–size plane

above the best-fit relation derived at similar redshifts (N14): it could couple with the observed dependency between the galaxy stellar age and mass, and hide a possible dependence of galaxies size on age. To test to what extent we can detect with our data a possible trend of the distance from the best-fit mass-size relation with age, we performed a simulation that accounts for both the size selection bias and the observed mass-age trend. We generated 1000 samples of 32 galaxies with masses and half-light radii distributed according to the field mass-size relation and its scatter, determined by N14 at $z \sim 1.5$. To each galaxy we assign an age (A) that depends on its stellar mass and the distance to the mass-size relation, such that $A = A_M + \alpha \Delta_{lr}$. We randomize the simulated ages and stellar masses according to the typical uncertainties of our observations. We then apply the WISP survey limits to the simulated galaxy samples (i.e., $M_* > 4.5 \times 10^{10} M_\odot$, and $r_e \geq 1$ kpc), and recompute the distributions of Δ_{lr} for the subsamples of old and young galaxies. For each of the 1000 samples we performed the same analysis described above, and compute the KS test between the distributions of Δ_{lr} for the young and old subsamples. For $\alpha = 0$ (i.e., no correlation), we find that only 10% of the simulated samples show a detectable difference between the old and young galaxies due to our size limit and the correlation between the age and stellar mass. We consider decreasing values of α in steps of 0.1, from zero to the α that produces distinguishable distributions. Our simulations show that for any $\alpha < -0.6$ we would be able to recover the difference between old and young population at 95% confidence level in more than 85% of the simulated samples. Repeating the same simulations applying a mass limit $M_* > 7.9 \times 10^{10} M_\odot$ instead, we find $\alpha < -0.7$. Our data, therefore, suggest that the relation between the galaxy age and its distance from the mass-size relation, if it exists, must have $\alpha > -0.6$. Performing these simulations considering the galaxies formation redshift (z_f) instead of age, given the observed redshift and the current cosmology, we conclude that, if a relation $R \sim (1 + z_f)^\beta$ exists, then it must be $\beta > -0.67$, otherwise we would have detected the correlation with our current sample.

3.5 Conclusions

We studied the mass-size relation of a sample of 32 passive galaxies at $z \sim 1.5$ selected from the WISP survey to have $\text{sSFR} < 0.01 \text{ Gyr}^{-1}$ and $M_* > 4.5 \times 10^{10} M_\odot$. All galaxies have accurately determined stellar ages from fitting the galaxy rest-frame optical spectra with stellar population models (Bedregal et al. 2013). We investigate whether younger galaxies have preferentially larger sizes than older ones with the same stellar mass. Such an observation would indicate that the mass-size relation evolves due to the appearance of newly quenched large objects

in passive samples.

Dividing our sample in young and old galaxies we find no significant difference in the distributions of Δ_{lr} , suggesting that the appearance of newly quenched galaxies may not be the dominant mechanism for the evolution of the mass–size relation. Our simulations also indicate that, if a relation exists between the galaxy age and the distance to the mass–size relation, it has a slope $\alpha > -0.6$, otherwise we would have detected it. If we consider in our analysis more conservatively only galaxies with $M_* > 7.9 \times 10^{10} M_{\odot}$ we obtain consistent results.

Our results suggest that the evolution of the mass–size relation of quiescent galaxies is mainly due to the physical growth of individual sources. Recently Belli et al. (2015) have found that progenitor bias can explain half of the size growth of compact ETGs and that the remaining observed size evolution arises from a genuine growth of individual galaxies. The discrepancy is likely due to the fact that they include in the sample “green valley” sources, with $\text{sSFR} < 0.1 \text{ Gyr}^{-1}$, while we limit the analysis to those galaxies with $\text{sSFR} < 0.01 \text{ Gyr}^{-1}$. In fact, it is exactly these sources with higher sSFR that drive the correlation between the age and the size evolution (see Figure 9 in Belli et al. 2015). Our finding is in agreement with the results by Trujillo et al. (2011) and Whitaker et al. (2012) which do not see any age segregation depending on the galaxy size. Sonnenfeld et al. (2014) suggest that the observed size growth can not be explained with models invoking only dry mergers, because they would result in a strong flattening of the mass density profile with time. This flattening is not observed in the samples of strong early-type lenses for which the total mass–density profile could be constrained (Sonnenfeld et al. 2014). The size growth could instead be due to a combination of dry and wet minor mergers: the outer regions of massive ETGs could grow by accretion of stars and dark matter, while a small amount of nuclear star formation could keep the mass density profile constant with time (e.g., Rutkowski et al. 2014).

Chapter 4

Conclusions and perspectives

Most of my thesis has been devoted to the spatially resolved study of star-forming galaxies at cosmic noon ($1 \lesssim z \lesssim 3$), with the main aim to constrain the physical properties of giant star-forming regions (clumps) and their impact on the evolution of the host galaxy. The properties and fate of giant clumps has become a subject of growing interest in the last decade, when their investigation has been made possible thanks to the unprecedented *HST* resolution and sensitivity. So far most of the studies analyzed clumps first in the broad-band imaging, but this alone only allows to select relatively evolved clumps. Thanks to *HST* imaging and slitless spectroscopy I developed a technique to simultaneously study clumps in the direct images and emission line maps (Chapter 2). This allowed me to expand the age regime probed so far, identifying young and intermediate age star-forming regions. In particular I deeply studied an extremely young (age < 10 Myr), massive (total mass $> 10^9 M_{\odot}$) clump, dubbed “Vyc1”, in a disk galaxy at redshift $z \sim 2$ (Section 2.4). This discovery has important implications on the study of how clumps are born, on their mode of star formation (e.g. their star formation efficiency) at young ages, and on the estimate of their lifetime. To further develop this work I led as PI VLT/SINFONI and ALMA accepted proposals, and I contributed as co-I to VLT/MUSE and VLT/KMOS proposals that have been recently observed. I will report in the following the main goals of these proposals, highlighting which will be the natural developments of this thesis.

VLT/SINFONI proposal (PI: Zanella) We proposed deep integral field spectroscopy of $H\alpha$ to study the velocity field and definitely probe the nature of Vyc1. With these 6 hours of SINFONI observations in Seeing Enhanced mode the following scientific results will be achieved.

- Studying the H α velocity and dispersion field of the galaxy we will dynamically confirm if it is a disk or a merger.
- Examining if the off-nuclear emission's individual velocity matches that of the underlying large-scale velocity field, we will confirm that Vyc1 is an extremely young clump (belonging to the galaxy itself) and not an external satellite that has been accreted and is undergoing an intense burst due to dynamical friction.
- We will resolve the emission in the velocity space to analyze if it is consistent with the typical gas velocity in clumps. Given the upper limit radius of the clump that we measured ($R_e \sim 0.5$ kpc) and assuming a typical dynamical mass $M_{\text{dyn}} \sim 10^9 M_\odot$ we expect to measure a gas velocity $v_{\text{FWHM}} \sim \sqrt{M_{\text{dyn}}/R_e} \sim 120 \text{ km s}^{-1}$. Measuring the FWHM of the H α emission in our in-hand Subaru/MOIRCS data we could only put an upper limit $v_{\text{FWHM}} \lesssim 450 \text{ km/s}$. Hence, deep SINFONI H α observations are indispensable to firmly measure v_{FWHM} and to estimate M_{dyn} for the system.

Should the H α off-nuclear emission of Vyc1 remain unresolved in the velocity space, these observations would put the stringent constraint $v_{\text{FWHM}} \lesssim 30 - 40 \text{ km/s}$. This 3 - 5 \times lower velocity than expected would be translated into a dynamical mass 10 - 20 \times smaller than the one we assumed, meaning that the emission can not be powered by star formation in a collapsing clump. It would mean that we have found an even more extreme case of a remarkably bright PSF-like emission coming from a very compact object of unknown nature.

Some additional goals might be directly achieved with these observations of further follow-up, in case SINFONI data would confirm the clump nature of Vyc1.

- Resolving the velocity profile at the position of the off-nuclear emission we will be able to study the presence of infalls that could flatten the profile itself. It would be the first discovery of subgalactic infalls at high redshift.
- Looking for wings of the H α emission line we will probe the presence of stellar feedback processes.
- Measuring the velocity along the line of sight at the position of the off-nuclear emission we will infer the dynamical stage of the clump. Comparing the observed velocity (v) with the escape velocity (v_{esc} , that is also equal to the free-fall velocity) we will understand if the clump is collapsing ($v \sim v_{\text{esc}}$) or virialized ($v \sim v_{\text{esc}}/2$). In the former case, it would be the first observed in situ gravitational collapse. The comparison of our clump velocity with the one of older, virialized clumps from the literature will confirm our finding.

- Measuring the underlying gas mass (given the dynamical mass that could be estimated with the proposed observations and constraints on the stellar mass from the in-hand data), we will measure the star formation efficiency of the clump and confirm its starburst-like behaviour and position in the Schmidt-Kennicutt plane (Figure 2.11).

This proposal has been submitted as DDT and accepted in May 2014, but it was not observed. We resubmitted it at the regular call for proposals in October 2014: it was A-ranked, but not observed that semester. It was therefore carried-over for 6 months, during which the target was not visible, and therefore carried-over again for other 6 months (this semester). The first 1.5 hours of observations have been performed on July 4th 2016 and we are now waiting for the program to be completed.

ALMA (PI: Zanella) We asked for 7 hours on-source in Band 4 to measure the CO(4-3) line emission of Vyc1 since it can be considered as a template to study the early formation phase of giant clumps in distant galaxies. Since the SFR of the clump is $\sim 40\%$ of the total SFR of the galaxy and the latter is spread over a much more extended disk, we expect the CO line emission of the clump not to be polluted by the signal of the host at the requested resolution of $0.2''$. With these observations we expect to achieve the following goals.

- We will resolve the clump in the velocity space and derive its dynamical mass ($M_{\text{dyn}} \sim R_e \times v_{\text{FWHM}}^2$, where R_e is the effective radius of the clump determined from our *HST*/WFC3 data and v_{FWHM} is the gas velocity measured from the required observations). Given the estimate of its stellar mass from in-hand data and the fact that the expected dark matter content is negligible, we will measure the gas mass of this newly born clump. This will also allow us to securely determine its SFE and understand how it compares with “normal” main-sequence distant galaxies, possibly confirming its starburst-like behaviour.
- Complementing our H α accepted SINFONI observations with the ALMA ones, we will quantify the fraction of ionized and molecular gas in the early phase of high-redshift clumps. We will understand if the molecular gas continuously forms stars and the ionized one is only a small fraction of the total, or if the gas is fully ionized and only at later stages it cools down and forms stars.

With our current measurements of the clump SFR, the literature correlations between IR and CO(5-4) luminosity together with the spectral line energy distributions (SLEDs) used to estimate the CO(4-3) luminosity (Daddi et al. 2015), we expect to detect the CO line with a $S/N = 10$. It will allow us to reach a veloc-

ity accuracy of $\sim 10\%$ and to fit the line profile, although if we account for the uncertainty on the different correlations and SLEDs, we could reach a lower (or higher) S/N. In case we reach the expected S/N = 10 (or higher) the following additional science will be achieved.

- Resolving the velocity profile at the clump position we will study the presence of infalls that could flatten the profile itself. It would be the first discovery of subgalactic infalls at high redshift.
- Comparing the velocity dispersion of the molecular (CO) and ionized (H α) gas we could gain fundamental information about the feedback processes acting on the interstellar medium (ISM) in the early phase of clumps formation. In case the turbulence and gas accretion in the galaxy disk are induced by gravitation instability, the feedback is moderate and it only regulates the cloud collapse at the smallest scales. Thus, the H α velocity dispersion will be higher than the CO one, the ionized gas being more concentrated in the densest clumps. Instead, in case the feedback is strong, the H α width is highly increased, while the CO one remains almost unaffected. We note that the H α alone cannot distinguish the two scenarios, since absolute measurements of the velocity dispersion depend on beam smearing and galaxy inclination. The relative estimate of the H α – CO velocity dispersion is actually the only way to constrain feedback scenarios.
- We will compute an alternative estimate of the gas mass of the clump using the CO(4-3) flux and conversion factors (α_{CO}) from high-resolution hydrodynamical simulations (Bournaud et al. 2015).
- Converting the CO(4-3) into CO(5-4) luminosity using standard CO SLEDs from observations and simulations (Daddi et al. 2015; Bournaud et al. 2015), we will investigate if our young clump follows the L_{CO} - SFR relation (Daddi et al. 2015).

This proposal has been accepted in ALMA Cycle 3 and it is in queue to be observed.

VLT/MUSE proposal (PI: Valentino) We proposed to point at the field centered on the CL J1449+0856 cluster (Gobat et al. 2011; Gobat et al. 2013; Strazullo et al. 2013; Valentino et al. 2015; Valentino et al. 2016) for 1.5 hours with MUSE. Given its wide field of view, high resolution and exceptional sensitivity, it is the perfect instrument to observe at the same time both large and small scale features. Therefore we proposed to observe simultaneously an extended Ly α nebula discovered in the core of the cluster (Valentino et al. 2016), and Vyc1 whose host galaxy is located in the same field. These observations will allow us to obtain

the first UV rest-frame spectrum of a massive clump at formation. In case of normal star formation the CLOUDY photoionization modelling that I did (Ferland et al. 2013) predicts a range of observable fluxes up to 5.2×10^{-18} , 8.9×10^{-18} , and 4.3×10^{-18} erg cm⁻² s⁻¹ for, respectively, CIII] λ 1909, He II λ 1640, and Mg II λ 2798, under reasonable assumptions based on our in-hand data. This is comparable to the upper limits reached by the required observations. A detection of brighter lines would signal harder ionizing radiation, likely due to numerous O-type stars. Assuming a standard IMF, stronger fluxes would imply an unrealistic stellar mass, largely exceeding the current upper limit of $< 3 \times 10^8 M_{\odot}$. Then, a top-heavy IMF could be more suitable for the SF in the clump, even considering its starburst-like properties (Baugh et al. 2005). Should strong lines be present, a broad component in line profiles will provide a clear indication of strong stellar feedback. This will have direct implications on the current clump lifetime estimate and its role in bulge formation and on the interpretation of the nature of the clump. On the other hand, a non-detection of exceedingly bright UV lines would be an excellent starting point to prepare deeper integrations in the future, aimed at estimating temperature and density of the ionized gas due to normal star formation.

As a byproduct these observations will also provide data for all the other clumpy galaxies included in our statistical sample (Section 2.5).

This proposal was submitted as a DDT in March 2015 and observed. The data have been almost fully reduced, but their analysis has not been started yet.

VLT/KMOS proposal (PI: Gobat) We proposed to observe 9 member galaxies of the CL J1449+0856 cluster for 16 hours with KMOS in the YJ band. Among these galaxies the host of Vyc1 was also included. At redshift $z \sim 2$, [OII] is covered in the YJ band: we already had an [OII] emission line map of this galaxy thanks to *HST* slitless spectroscopy, but the spectral resolution of the G141 grism was too low to separate the [OII] doublet. KMOS spectral resolving power in this band is instead $R = 3500$, enough to separate [OII] λ 3727 from [OII] λ 3729. Thanks to these observations we will directly probe the physical conditions of the ISM in a high-redshift star-forming region, constraining for the first time the gas electron density in an extremely young clump, together with its electron temperature.

This proposal has been accepted and we recently received the data.

Thanks to the multi-wavelength data set that we are gathering, we will study in deep detail the nature and the physics of Vyc1, considering it as a representative

case of young clumps at high redshift. The pilot study of Vyc1 will provide the needed information to propose future multi-wavelength follow-ups also for the statistical sample of clumpy galaxies that we assembled and we are currently investigating (Section 2.5). Finally, the next generation of telescopes (e.g. James Webb Space Telescope, the Square Kilometer Array, the Extremely Large Telescope) and instruments (e.g. VLT/KMOS with adaptive optics) with high spectral and spatial resolution, will definitely open a new era in the field of the resolved study of high-redshift galaxies. They will allow the systematic analysis of statistical samples of high-redshift star-forming regions and to probe an even larger parameter space, searching for lower mass and lower SFR clumps than found today. This is fundamental to progress: low-mass clumps (dynamical mass $M_c \lesssim 10^8 M_\odot$) are expected to be disrupted by stellar feedback on short timescales (Mandelker et al. 2015), whereas there are observational preliminary results suggesting that massive clumps ($M_c \gtrsim 10^9 M_\odot$) are long-lived (Förster Schreiber et al. 2011; Guo et al. 2012; Zanella et al. 2015). However, observations of intermediate-mass clumps ($M_c \sim 1 - 5 \times 10^8 M_\odot$) are still lacking, although they are expected to be the most numerous and potentially most critical to bulge growth (Bournaud 2016). A natural future development of this thesis is to pinpoint young clumps (ages $\lesssim 30$ Myr) with dynamical masses down to $\sim 10^8 M_\odot$ to determine the CFR and lifetime as a function of their mass. It will permit to evaluate the total mass that can reach the galaxy center due to clumps migration in ~ 2 Gyr (the timescale for bulge formation). The fraction of bulge mass assembled in clumps can be compared with the one inferred by merger rates to understand which is the main driver of bulge growth. To this aim it will be necessary to obtain resolved spectroscopy of a sample of high-redshift clumpy galaxies with moderate mass ($10^9 - 10^{10} M_\odot$), since they are more gravitationally unstable (Bournaud et al. 2014). It will be possible to pre-select galaxies hosting potential very young clumps using deep direct imaging, to identify bright patches of star formation that are visible in the UV and are not detected in optical/NIR bands. Afterwards, a spectroscopic follow-up would be needed to confirm their young age (e.g. through the estimate of their EW and assuming some standard stellar population models). A minimum sample size of ~ 10 galaxies will be required to robustly determine clumps lifetimes and distinguish different theoretical scenarios. In fact, depending on the adopted feedback recipes, simulations either predict that clumps are short-lived (lifetime $\lesssim 50$ Myr) or they are long-lived (lifetime ~ 500 Myr). Given an average of 5 clumps per galaxy (Bournaud et al. 2014) with $10^8 \lesssim M_c/M_\odot \lesssim 10^{9.5}$ we would get a CFR $\gtrsim 0.1 \text{ Myr}^{-1}$ in the first case and $\sim 0.01 \text{ Myr}^{-1}$ in the latter. Considering that young clumps with extreme EW are visible for ~ 20 Myr, we would expect 1 – 2 young clumps per galaxy if they are short-lived and 1 – 2 every 10 galaxies if they are long-lived. A sample of $\gtrsim 10$ galaxies is therefore needed to

safely compare observational results with theory. Thanks to these deep spectroscopic observations, integrating the dynamical mass of the clumps that can reach the galaxy center in ~ 2 Gyr, we could understand if clumps migration can be an important channel for bulge growth. Additionally, determining the clumps dynamical mass function down to $\sim 3 \times 10^8 M_{\odot}$ observationally and comparing it with simulations, it would be possible to constrain the strength of the feedback acting on the ISM. I have already done a first step in this direction by submitting to VLT/KMOS a proposal that is currently being evaluated by the Telescope Allocation Committee. Further developments will be possible thanks to the new telescopes and instruments mentioned above, which will help to definitely answer whether clumps have an important role in shaping galaxies, and eventually to start looking for possible connections between clumps migration, bulge growth, disk stabilization, and galaxies quenching.

Appendix A

Contribution to other papers as co-author

During my PhD I contributed as a co-author to three published papers concerning the analysis of galaxies in clusters at high redshift. For each of them I participated to the discussion for the analysis and interpretation of the results, and I commented the manuscript. I briefly summarize below the main conclusions of each paper and I report more specific details about my contribution if needed.

Valentino et al. (2015) study the mass – metallicity relation for a sample of 6 galaxies in the cluster CL J1449+0856 (Gobat et al. 2011; Gobat et al. 2013; Strazzullo et al. 2013), and it compares it with the properties of 13 galaxies in the field. The main goal of the paper was to investigate which is the role of the environment in the metal enrichment of star-forming galaxies. Stacking the spectra of the cluster and field galaxies an enhancement of the $H\alpha$ luminosity and equivalent width has been observed in the cluster rather than in the field. This might be due to a higher specific star formation rate or lower dust attenuation in the cluster. These results might be explained assuming the presence of gas reservoirs around the cluster members and at cluster scale, likely due to external accretion of pristine gas from the cosmic web. The host galaxy of the extremely young clump I analyzed in detail was in the sample of cluster members selected in this study. I provided the SFR and metallicity estimates that have been used to compare with those obtained with the MOIRCS longslit spectroscopy presented in Valentino et al. (2015).

Valentino et al. (2016) reports the discovery of an extended $Ly\alpha$ nebula in the core of the X-ray detected cluster CL J1449+0856 thanks to Keck/LRIS narrow-band imaging. After the exclusion of other scenarios (e.g. cooling from the X-ray

phase, gas replenishment of cold gas from the cosmic web), the most plausible explanation is that the cold gas emitting the Ly α radiation is supplied by cluster galaxies through outflows generated by AGNs and SNe. The energy injected in the cluster environment through this mechanisms could furthermore explain the thermodynamical properties of local clusters, a longstanding issue still highly debated.

Wang et al. (2016) presents the discovery of an X-ray detected cluster at $z = 2.5$, the most distant cluster known so far, and analyzes the properties of its member galaxies. The core of this structure is dominated by star-forming galaxies, suggesting that we are likely probing the link between high-redshift groups (dominated by star-forming galaxies) and local clusters (always showing an important fraction of passive members). I have done the morphological analysis of the cluster members, providing estimates for the structural properties of these sources decomposing their light profiles with the fitting algorithm GALFIT.

The full list of my publications is reported in the following. It also includes papers that are in still preparation, but the draft has already been circulated among the co-authors, and will be published soon.

- **A. Zanella**, E. Daddi, E. Le Floch et al. 2015, “The gravitational collapse of a giant clump in a primordial galaxy”, *Nature*, 521, 54
- **A. Zanella**, C. Scarlata, E. Corsini et al. 2016, “The role of quenching time in the evolution of the mass-size relation of passive galaxies from the WISP survey”, *ApJ*, 824, 68
- **A. Zanella**, E. Le Floch et al. 2016, “Physical properties of an emission line-selected sample of clumps at the peak of cosmic star formation history”, in preparation
- F. Valentino, E. Daddi, V. Strazzullo, ..., **A. Zanella**, ..., et al. 2015, “Metal deficiency in cluster star-forming galaxies at $z = 2$ ”, *ApJ*, 801, 132
- F. Valentino, E. Daddi, A. Finoguenov, ..., **A. Zanella**, ..., et al. 2015, “A giant Ly α nebula revealing early energy injection in the hot intracluster medium”, *ApJ*, under revision
- T. Wang, D. Elbaz, E. Daddi, ..., **A. Zanella**, ..., et al. 2015, “The most massive dark matter halo identified 2.5 billion years after the Big Bang”, *ApJ*, accepted
- Z. Ma, E. Daddi, V. Strazzullo, **A. Zanella**, ..., et al. 2016, “The size of passive galaxies as regulated by their formation redshift”, in preparation

Appendix B

Our sample of clumpy galaxies

We report below the results that we obtained fitting the light profiles of our sample galaxies with the algorithm GALFITM, according to the procedure described in Section 2.5. We show the stamps only for the 38 galaxies hosting the final sample of 49 clumps discussed in Section 2.5.1.

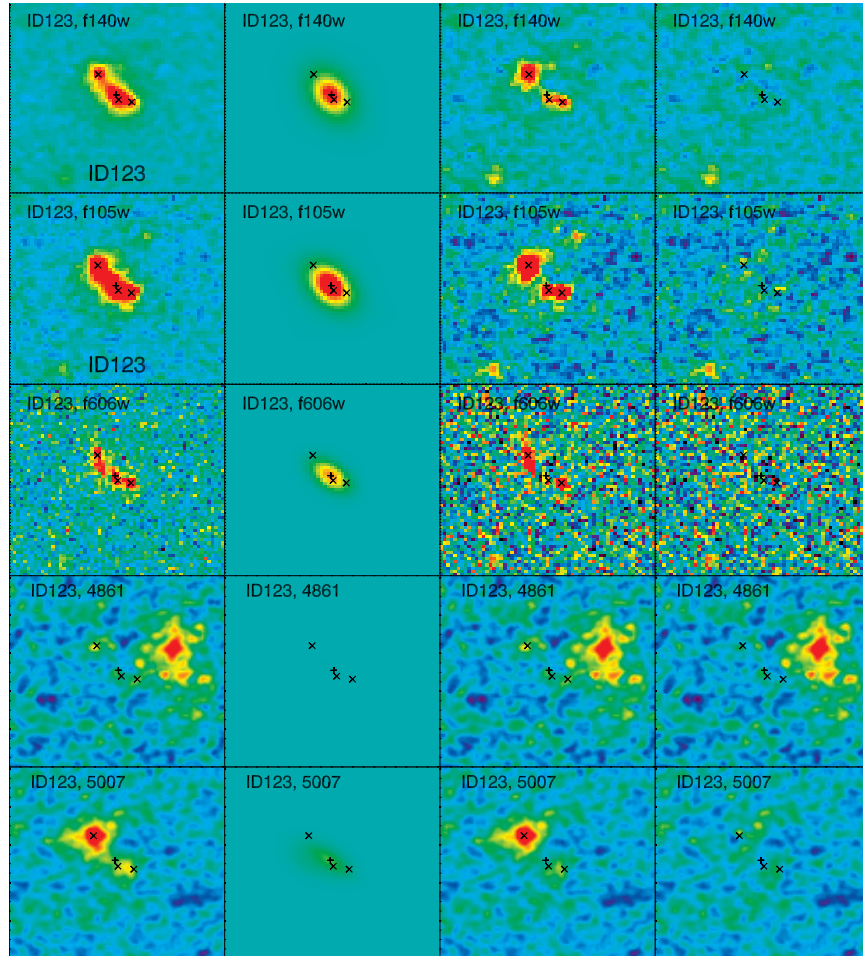


Figure B.1 – Decomposition of the sample galaxies light profile. The light profile of each galaxy has been modelled with the algorithm GALFITM, fitting a diffuse component (Sérsic profile) plus PSFs at the location of the clumps. The center of the diffuse component and the location of the PSFs are indicated with crosses. In each row, from top to bottom, we report the results of the imaging (three different bands: F140W, F105W, F606W) and the available emission line maps. In each column, from left to right, we report the initial image, GALFITM model of the diffuse component, the residuals obtained subtracting the diffuse component modelled by GALFITM from the initial image, and finally the residuals obtained subtracting the whole model (diffuse component plus PSFs) from the input image.

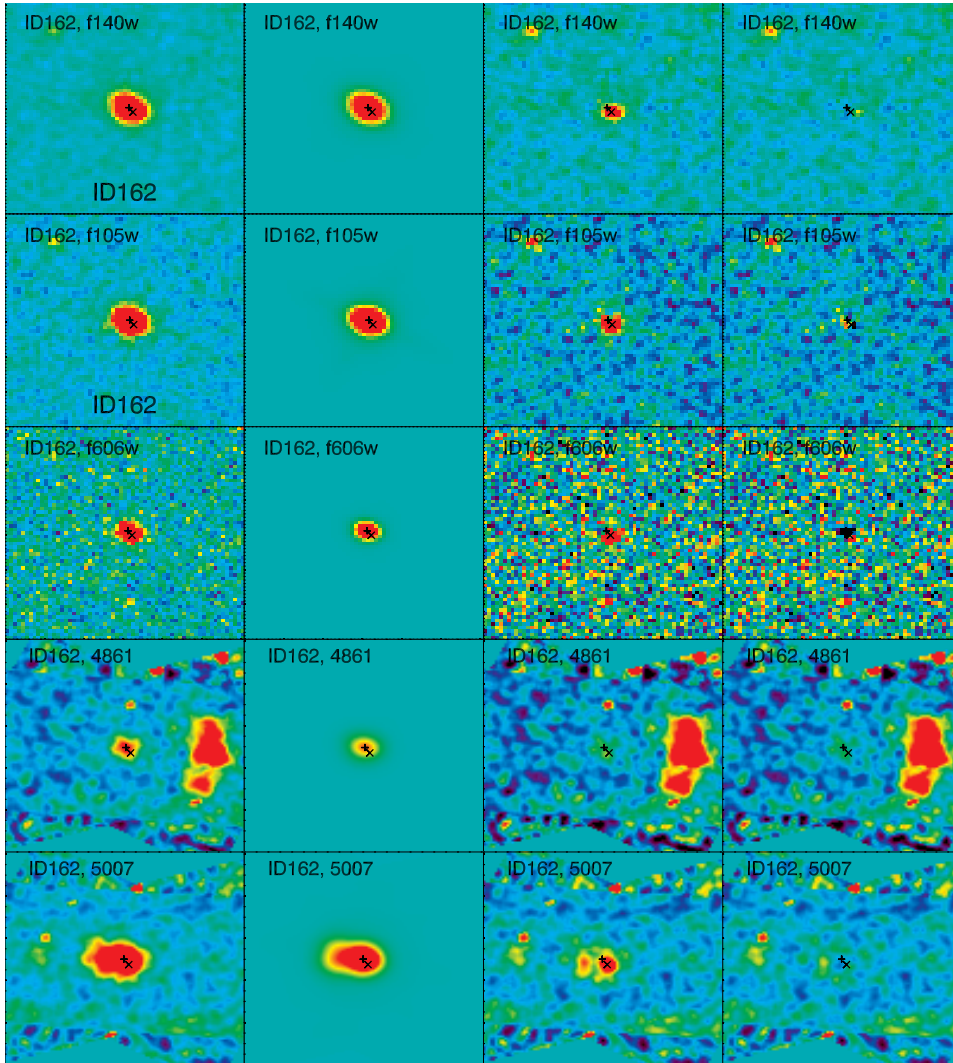


Figure B.1 - Continued.

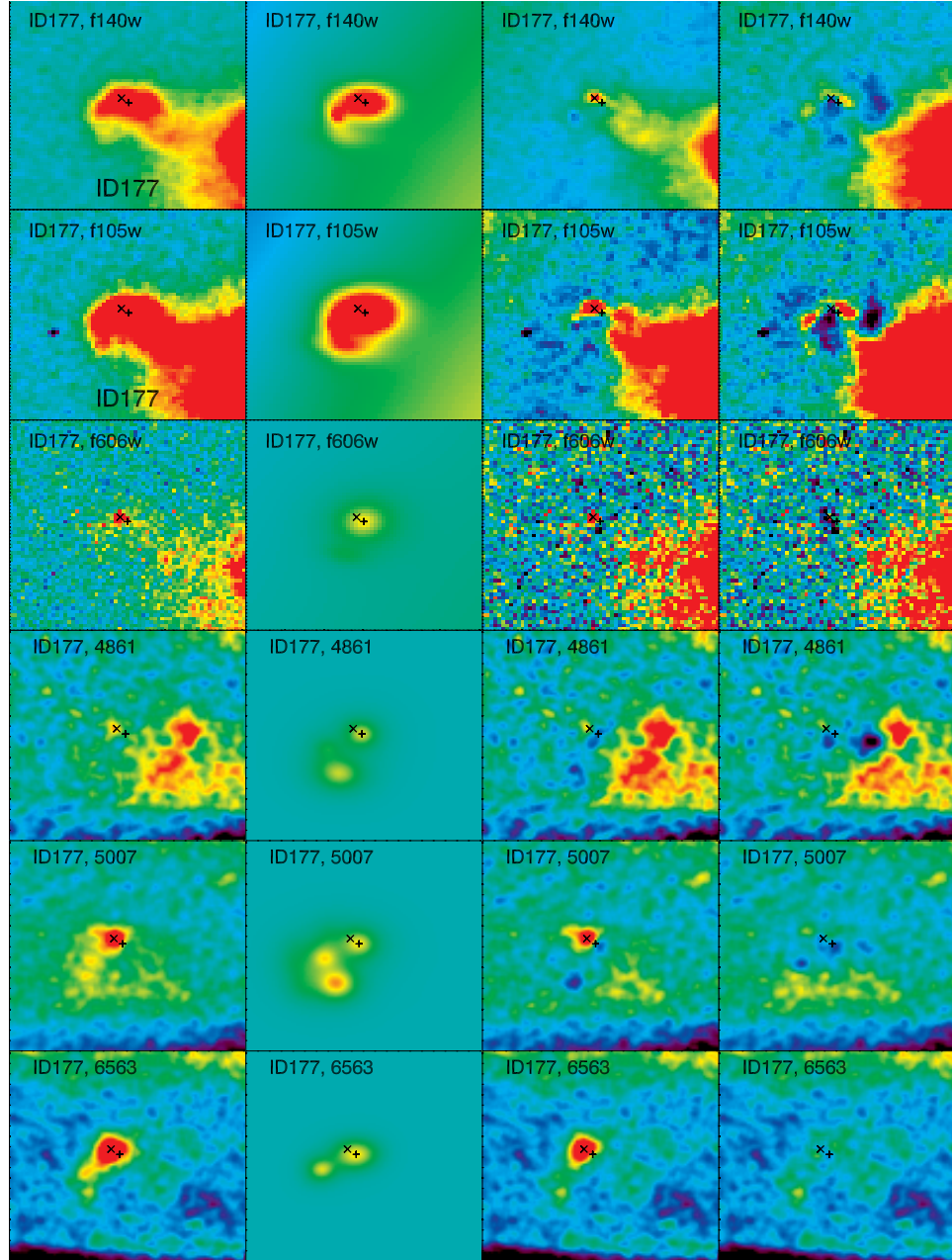


Figure B.1 – Continued.

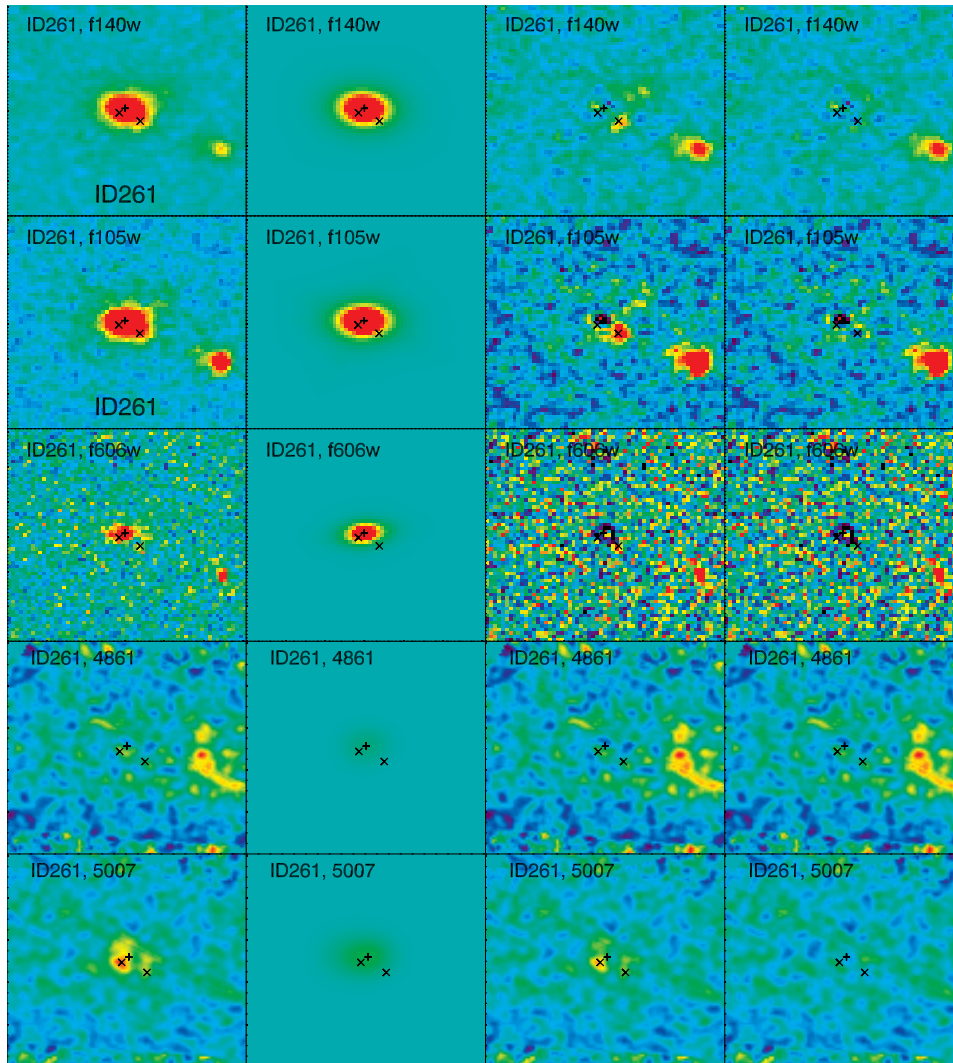


Figure B.1 - Continued.

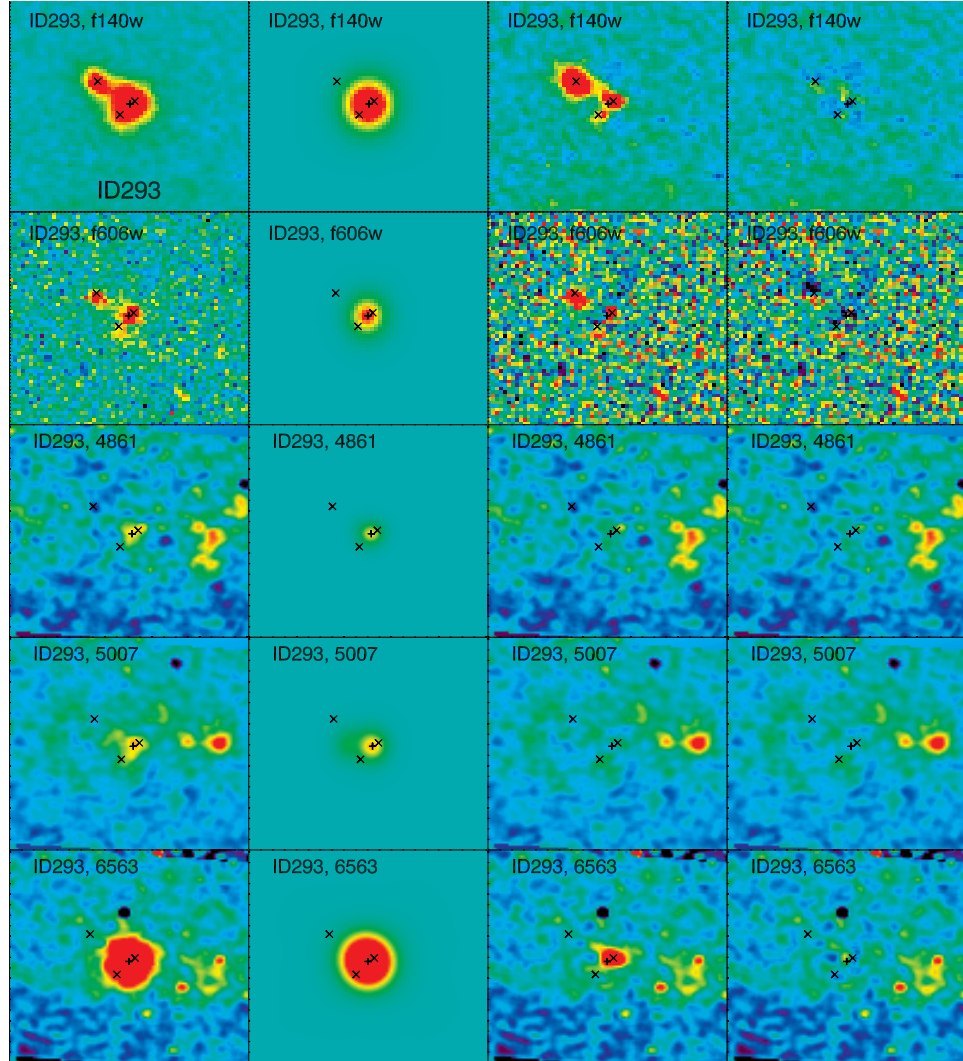


Figure B.1 – Continued.

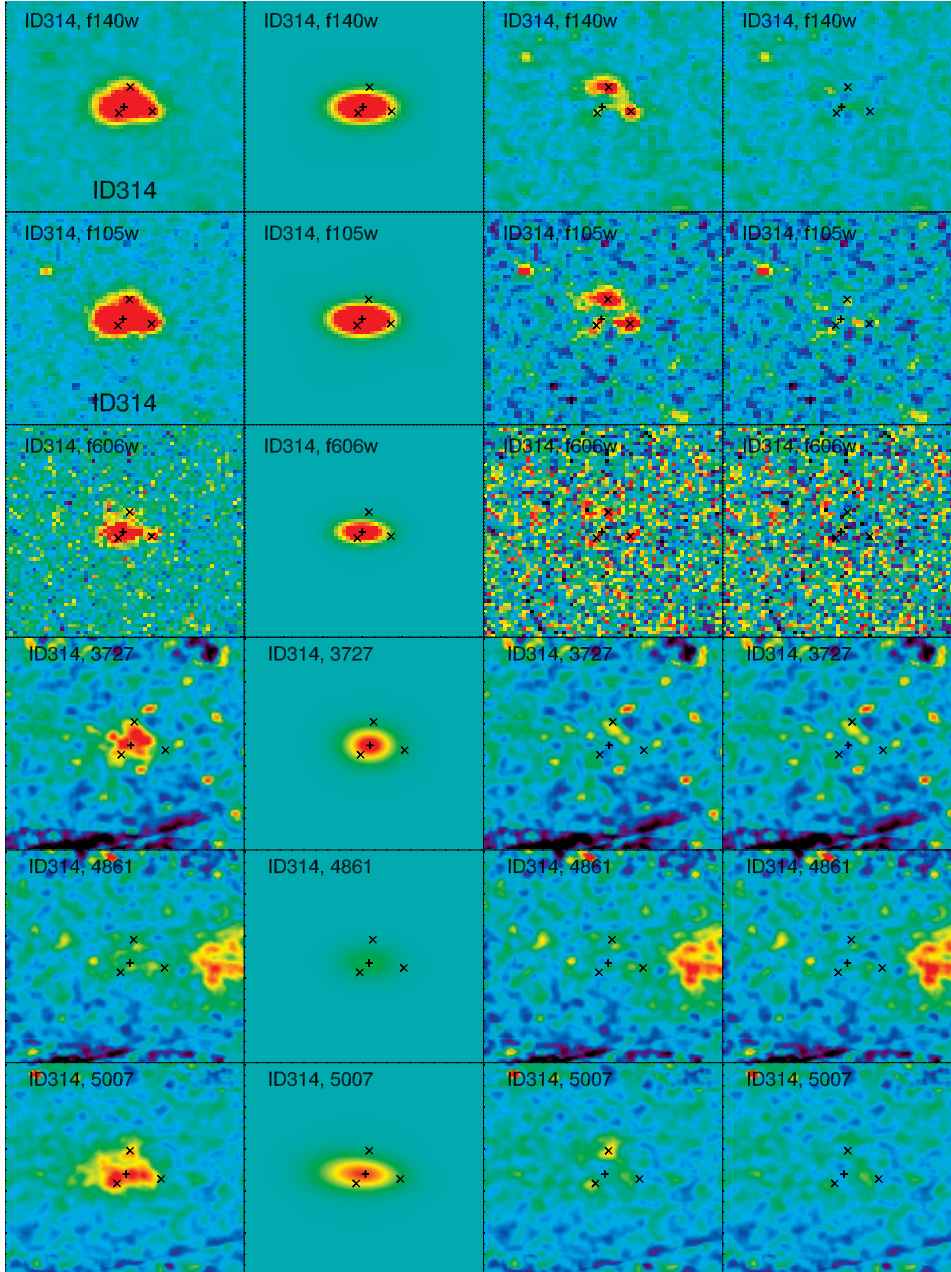


Figure B.1 - Continued.

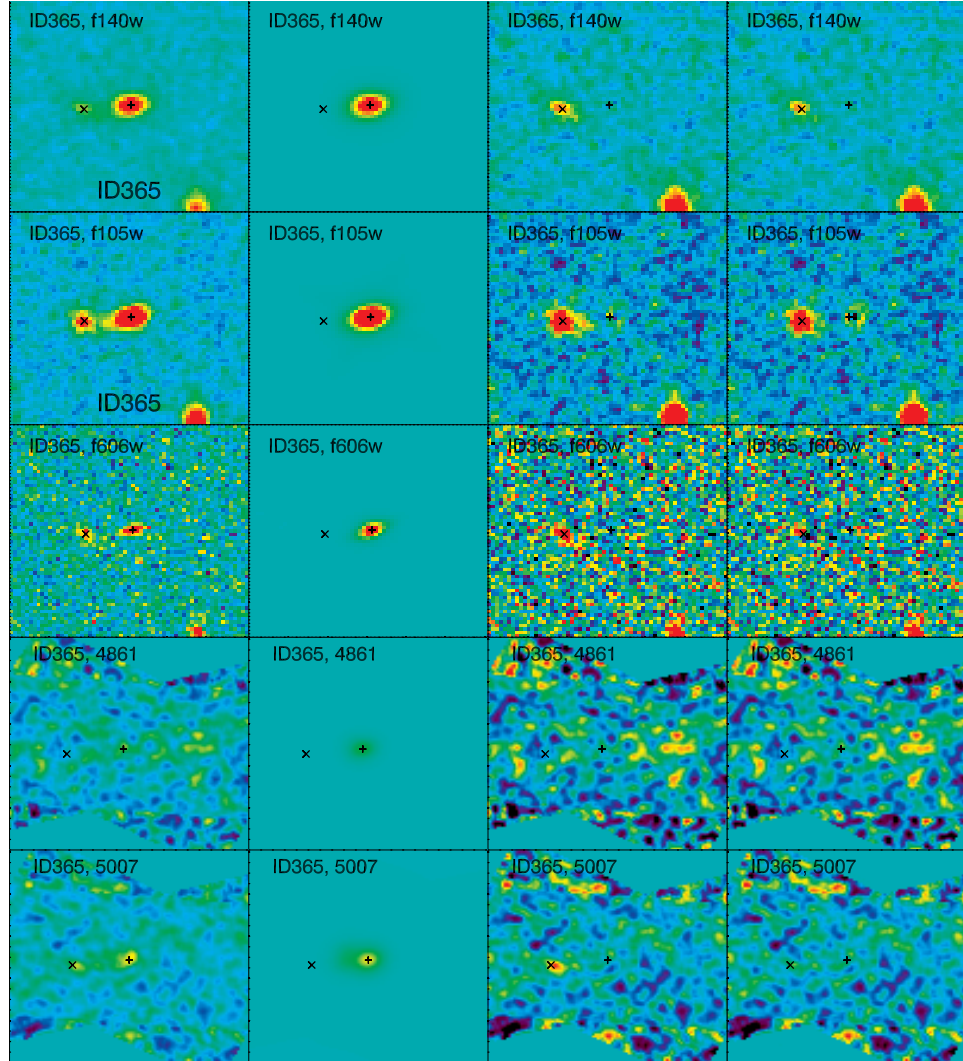


Figure B.1 – Continued.

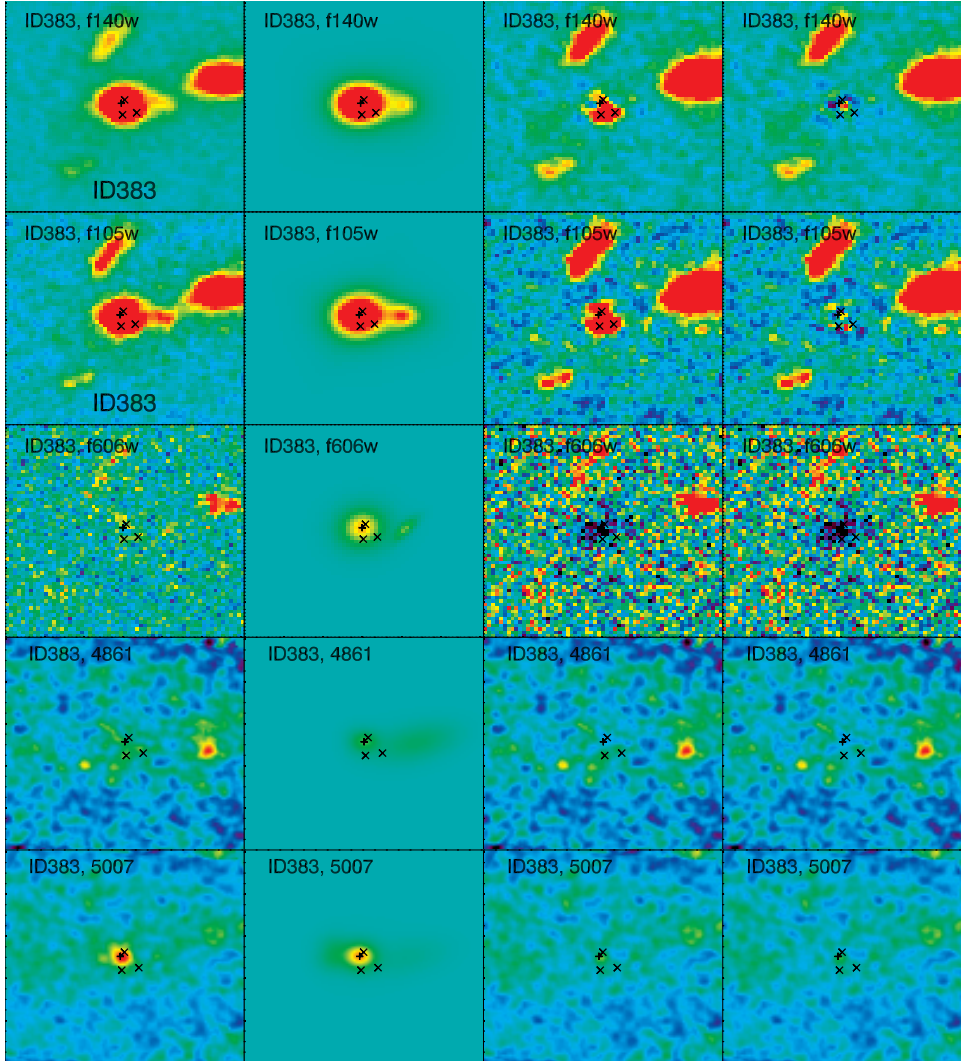


Figure B.1 - Continued.

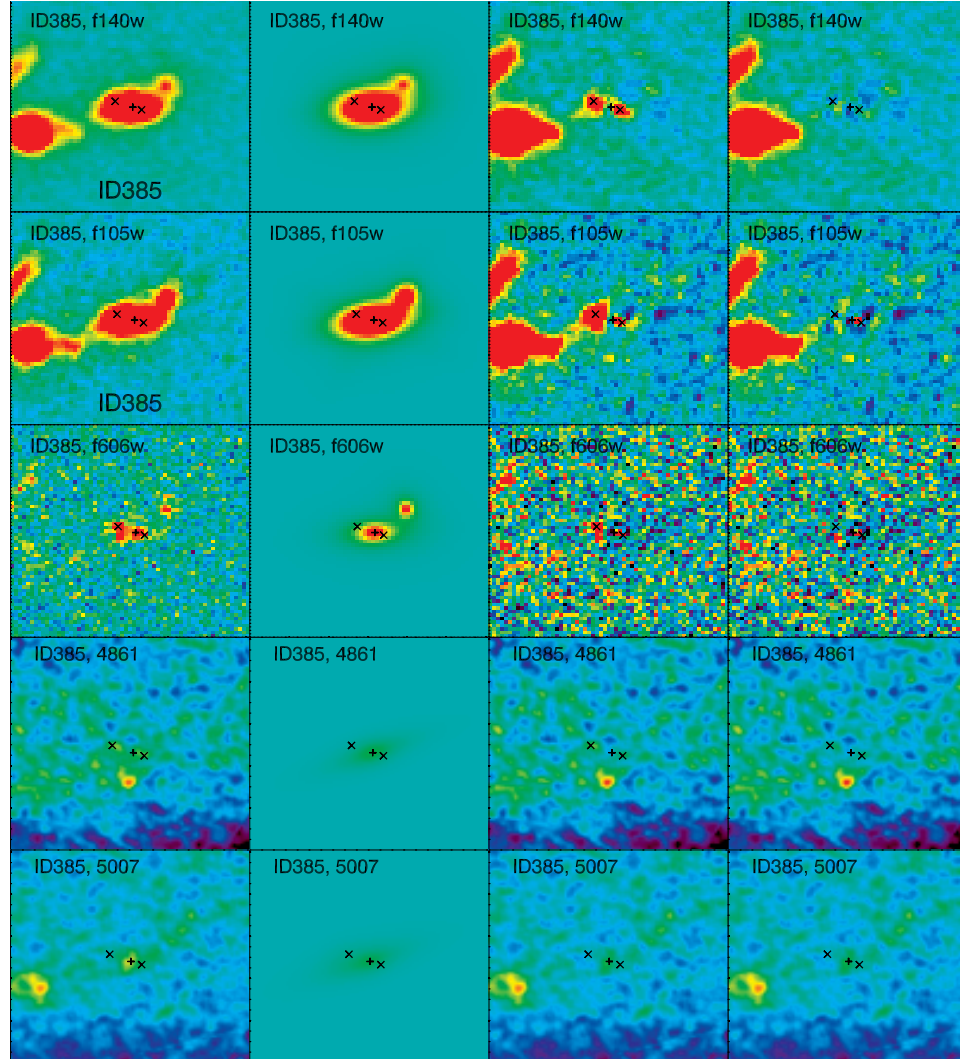


Figure B.1 – Continued.

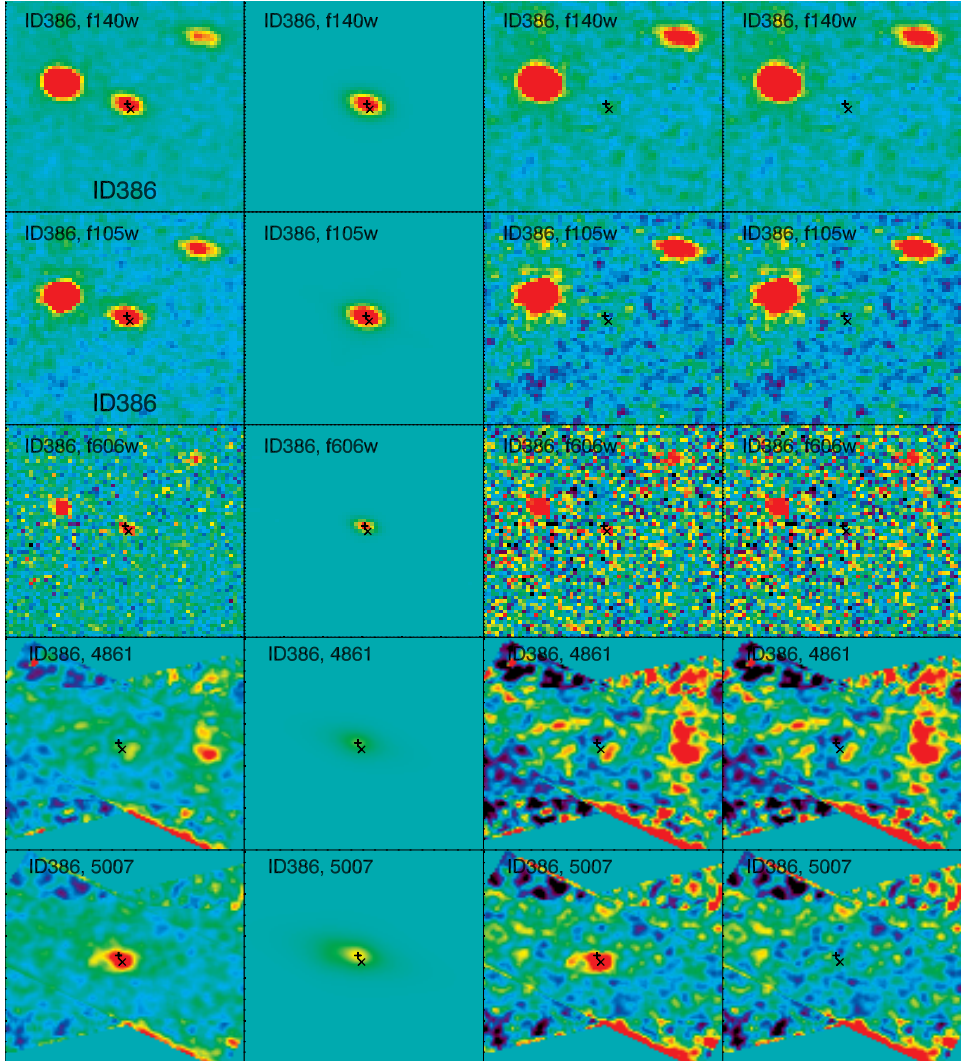


Figure B.1 - Continued.

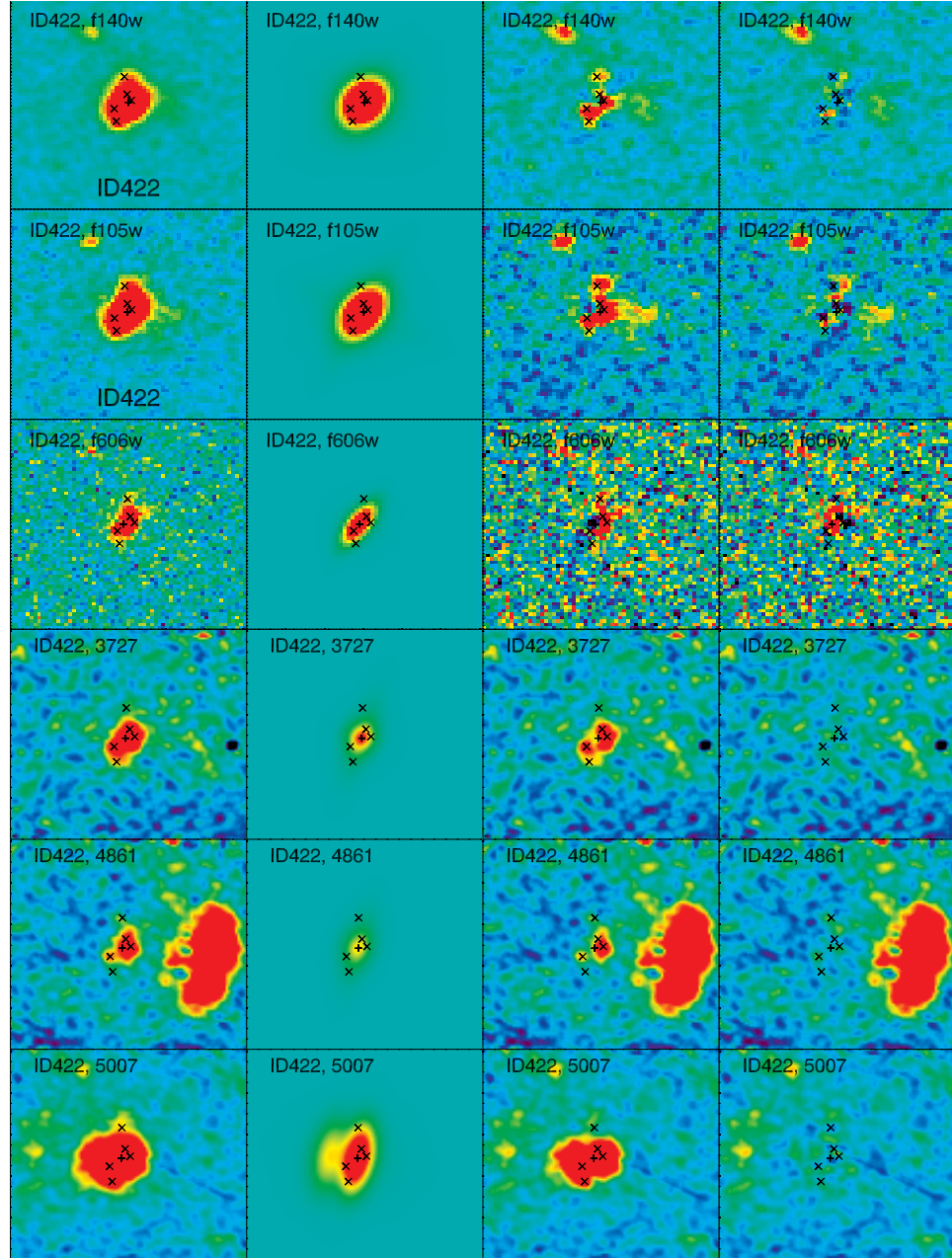


Figure B.1 – Continued.

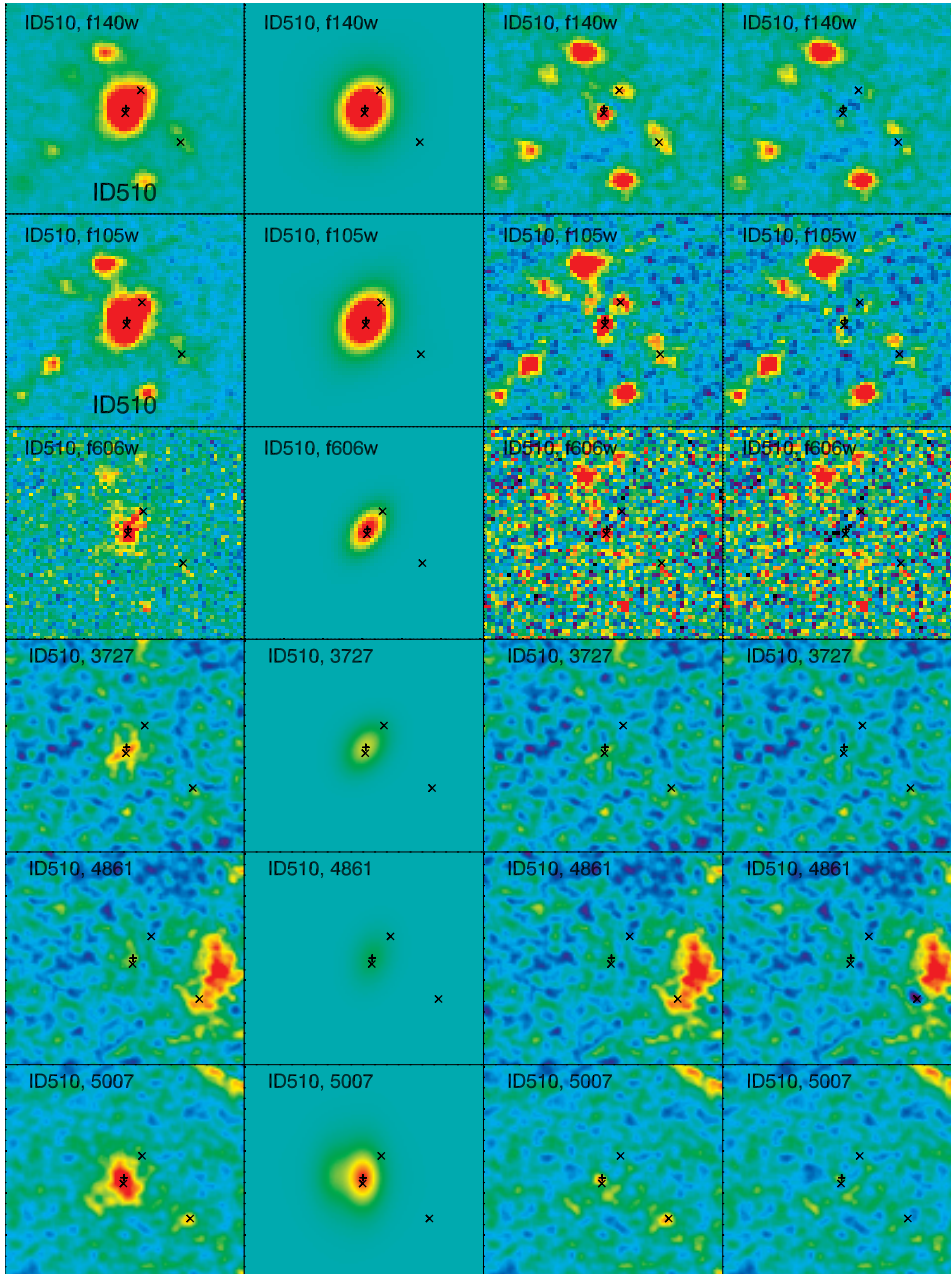


Figure B.1 – Continued.

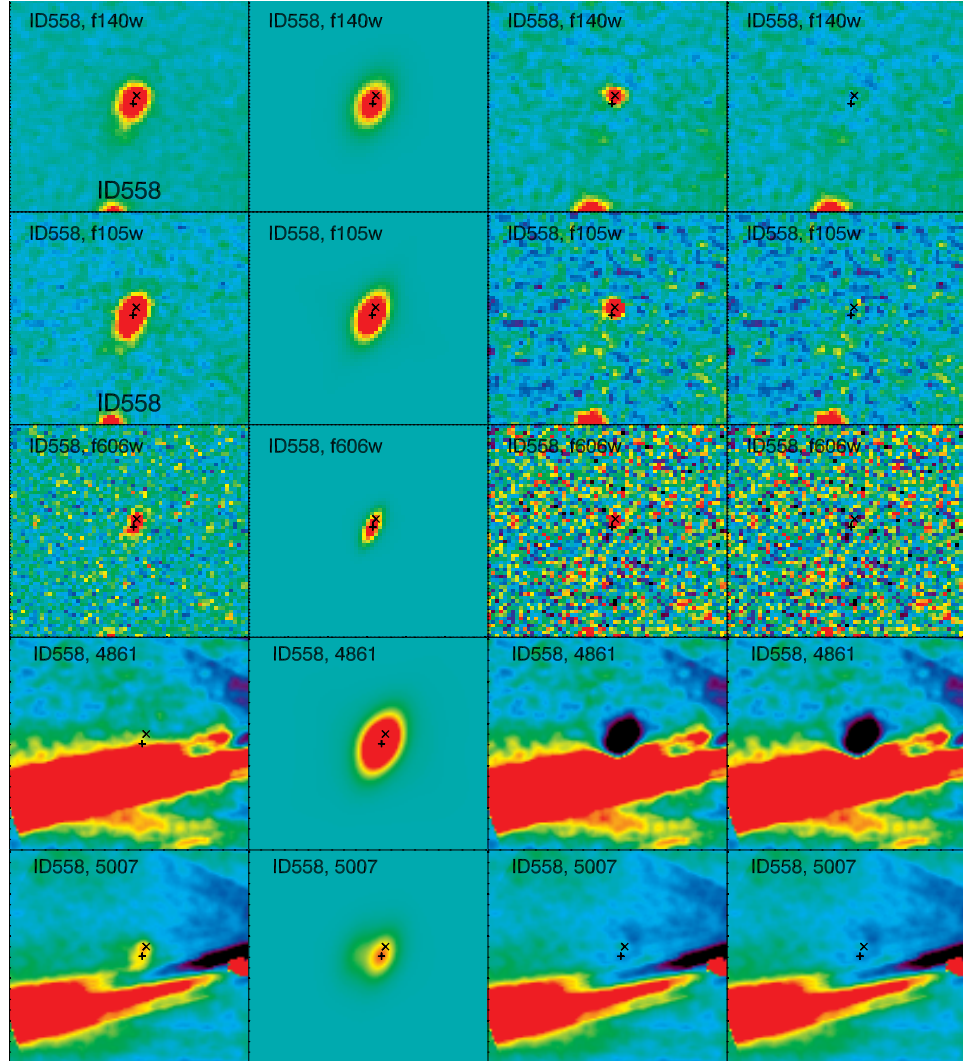


Figure B.1 – Continued.

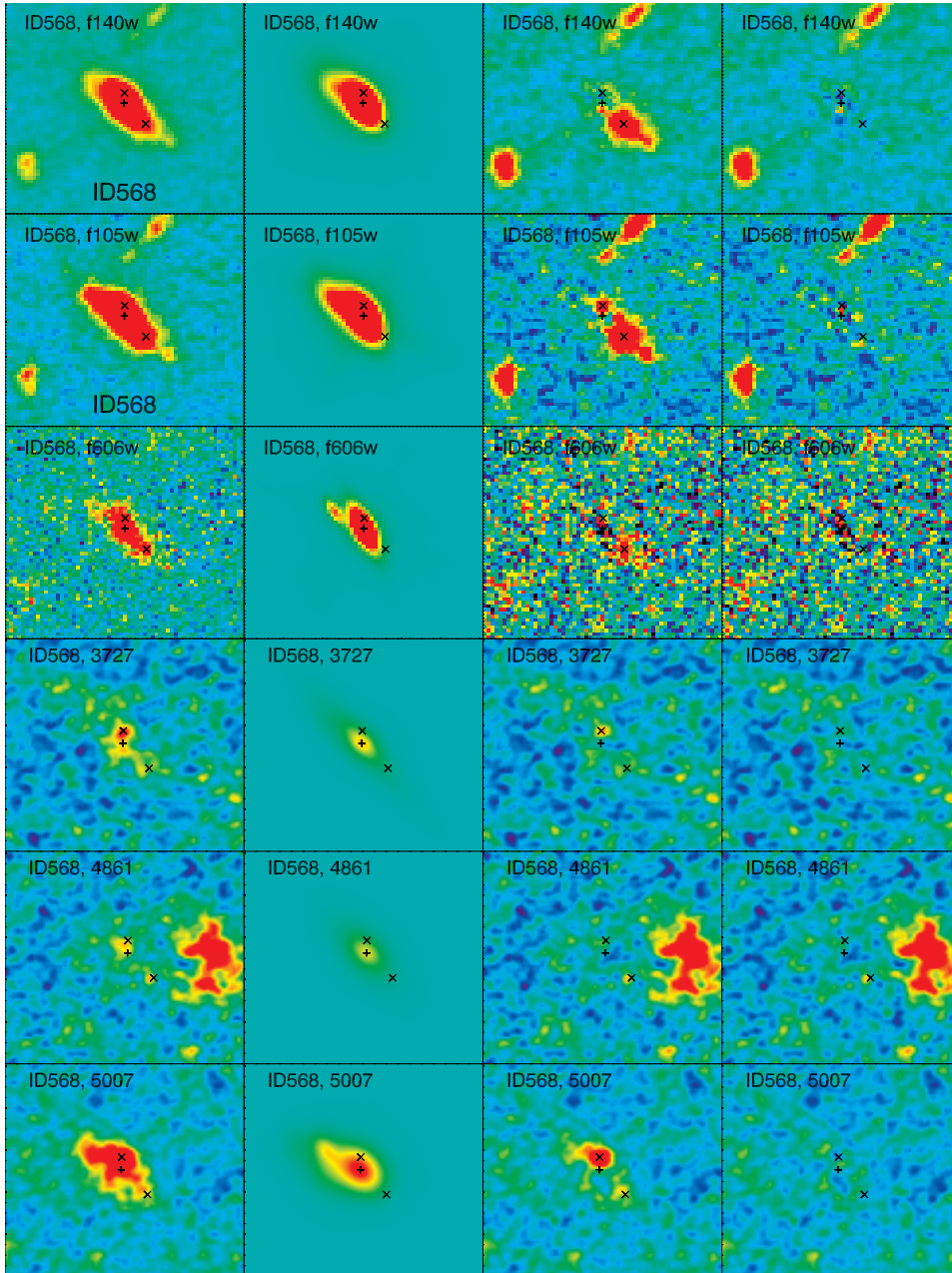


Figure B.1 - Continued.

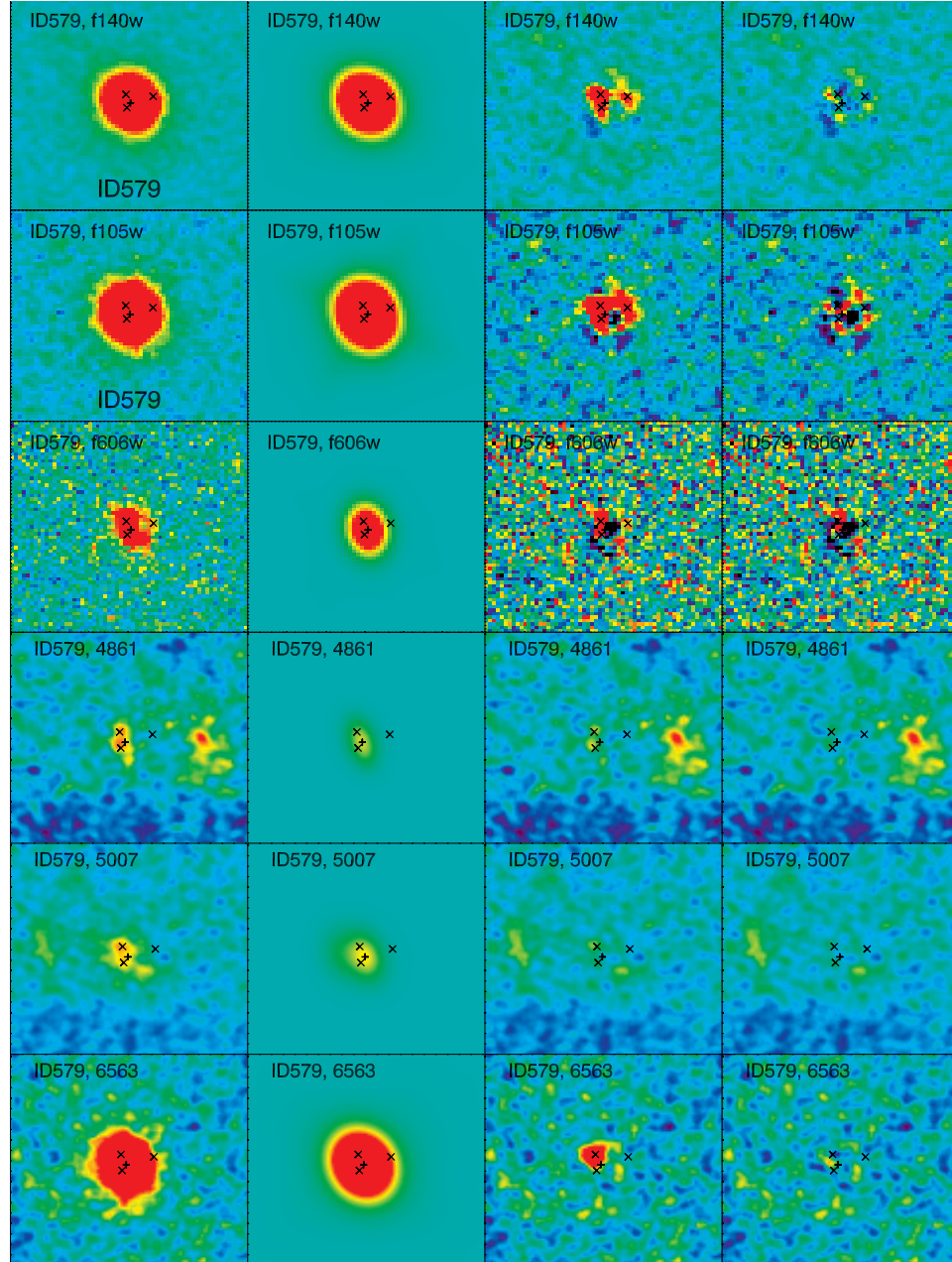


Figure B.1 – Continued.

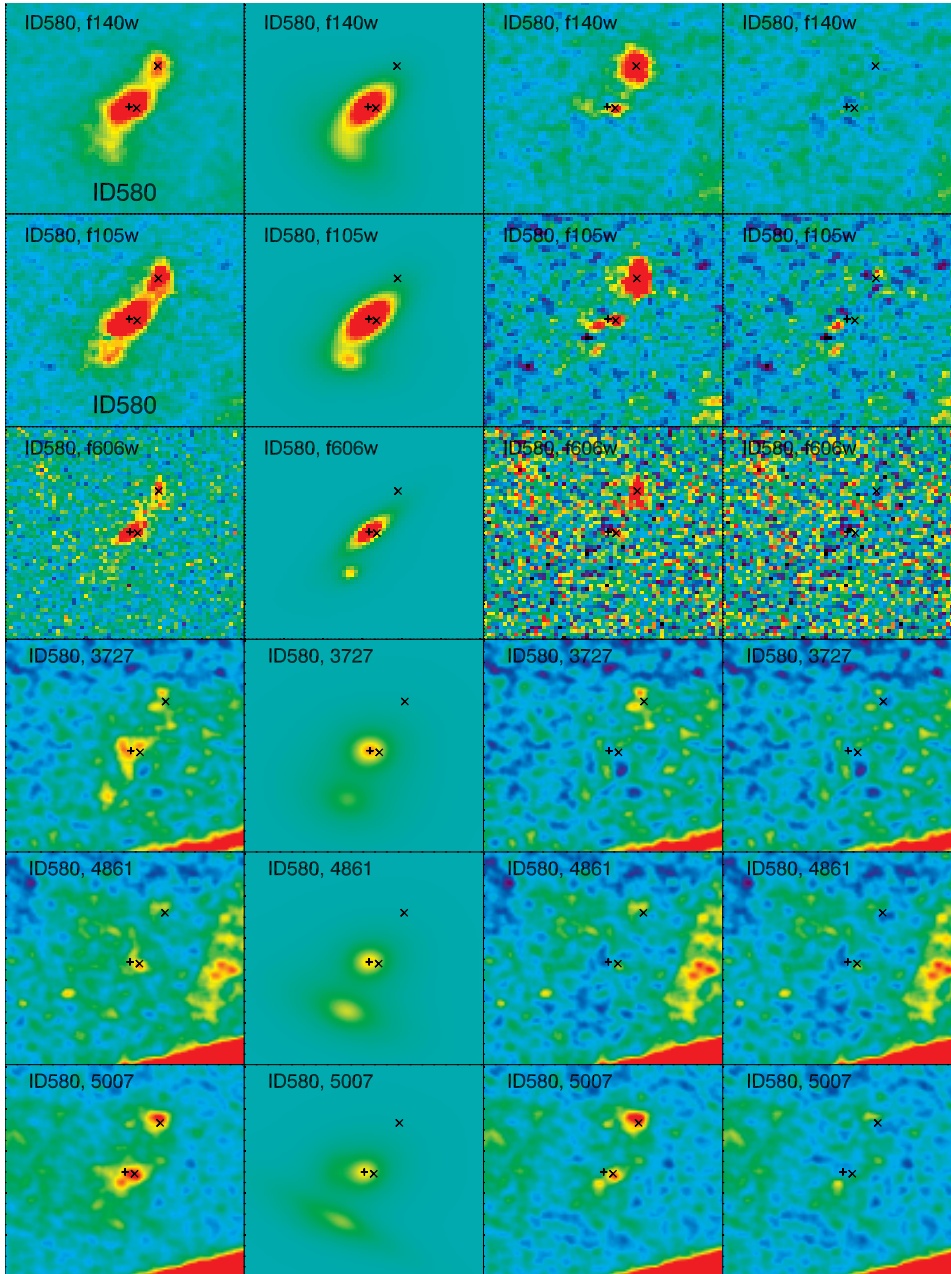


Figure B.1 - Continued.

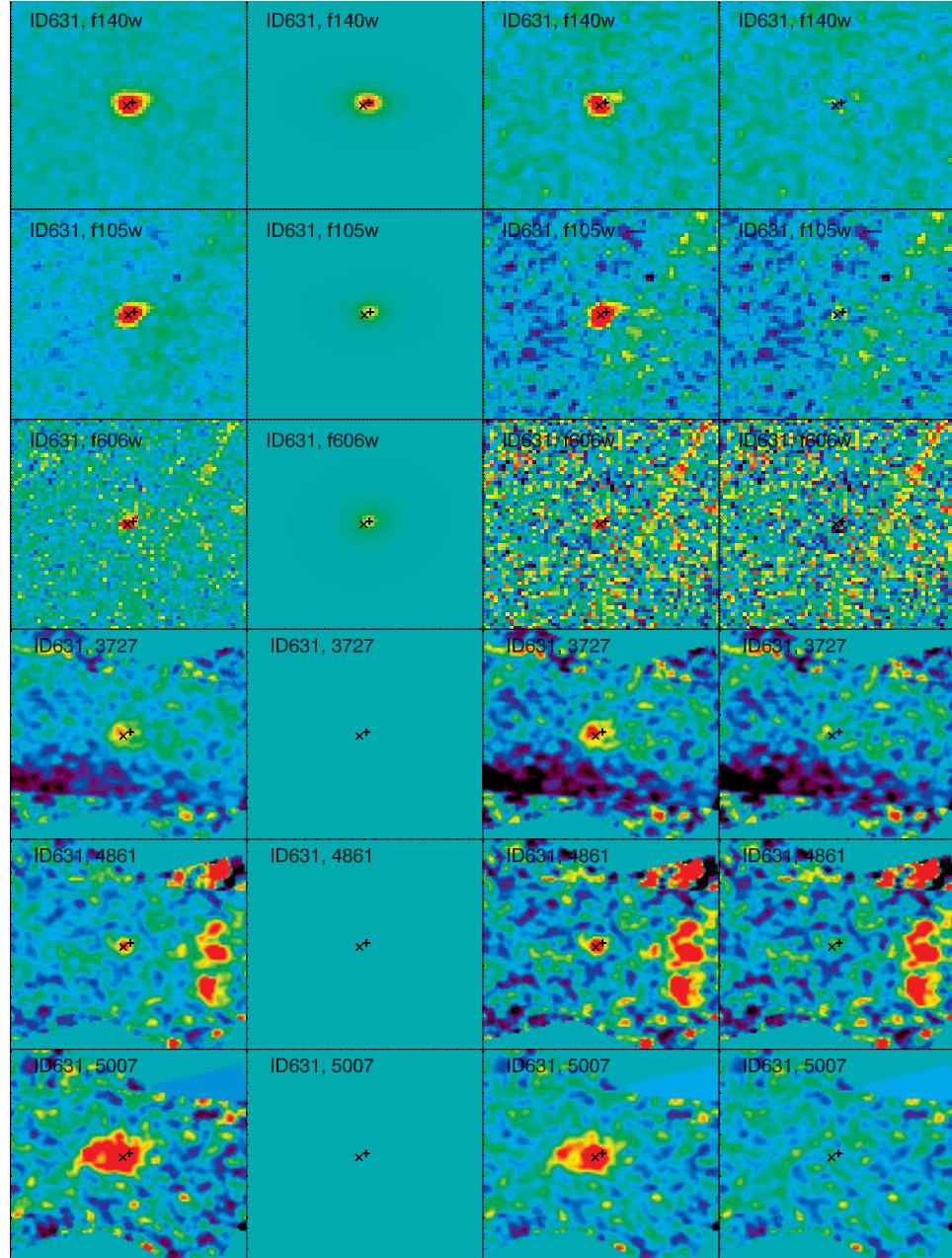


Figure B.1 – Continued.

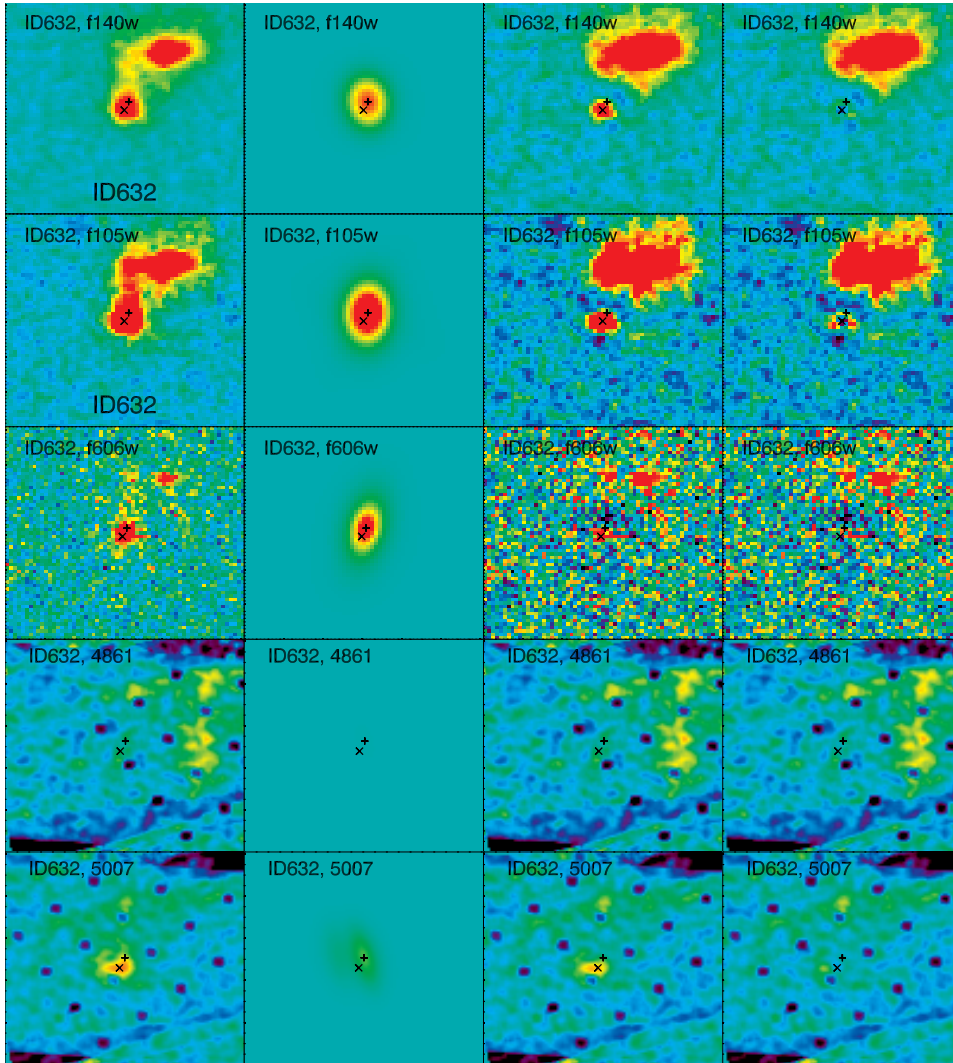


Figure B.1 - Continued.

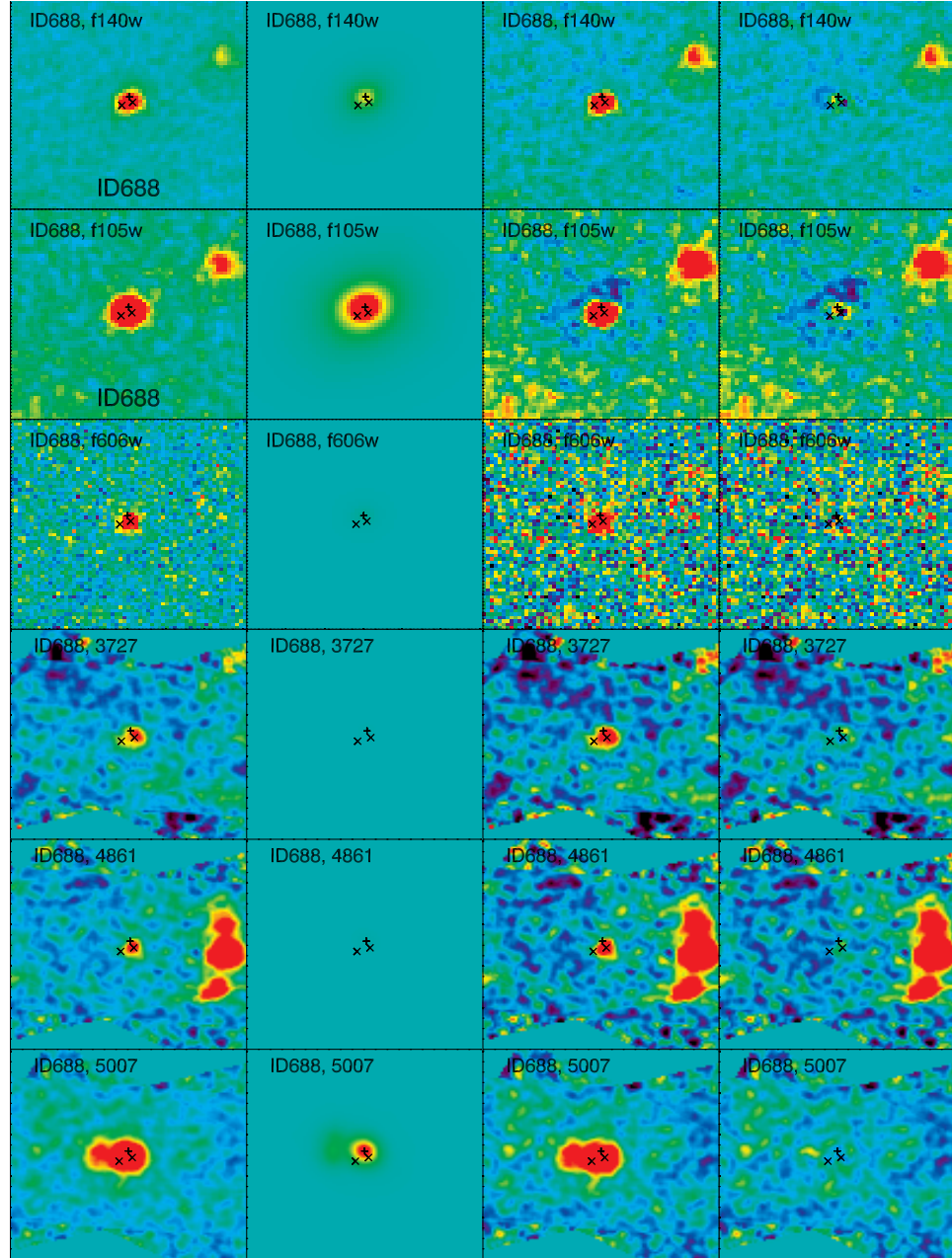


Figure B.1 – Continued.

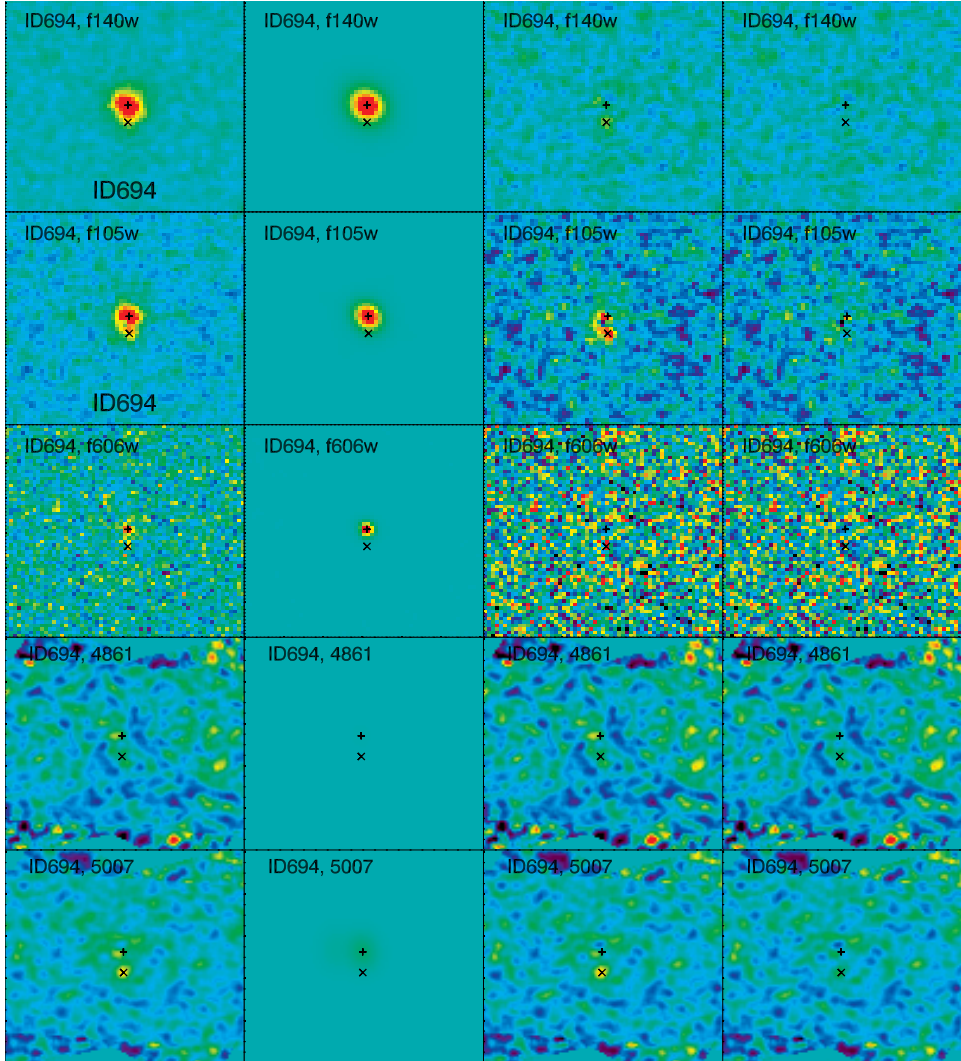


Figure B.1 - Continued.

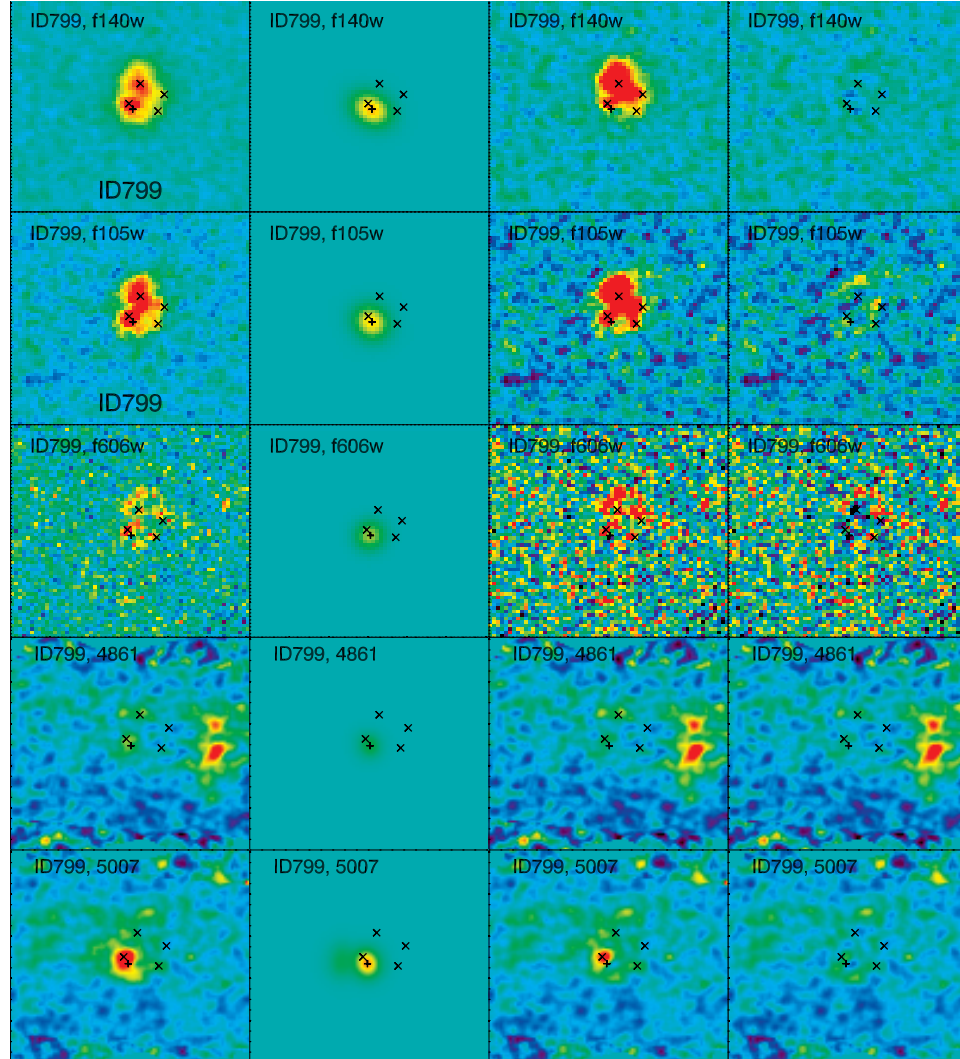


Figure B.1 – Continued.

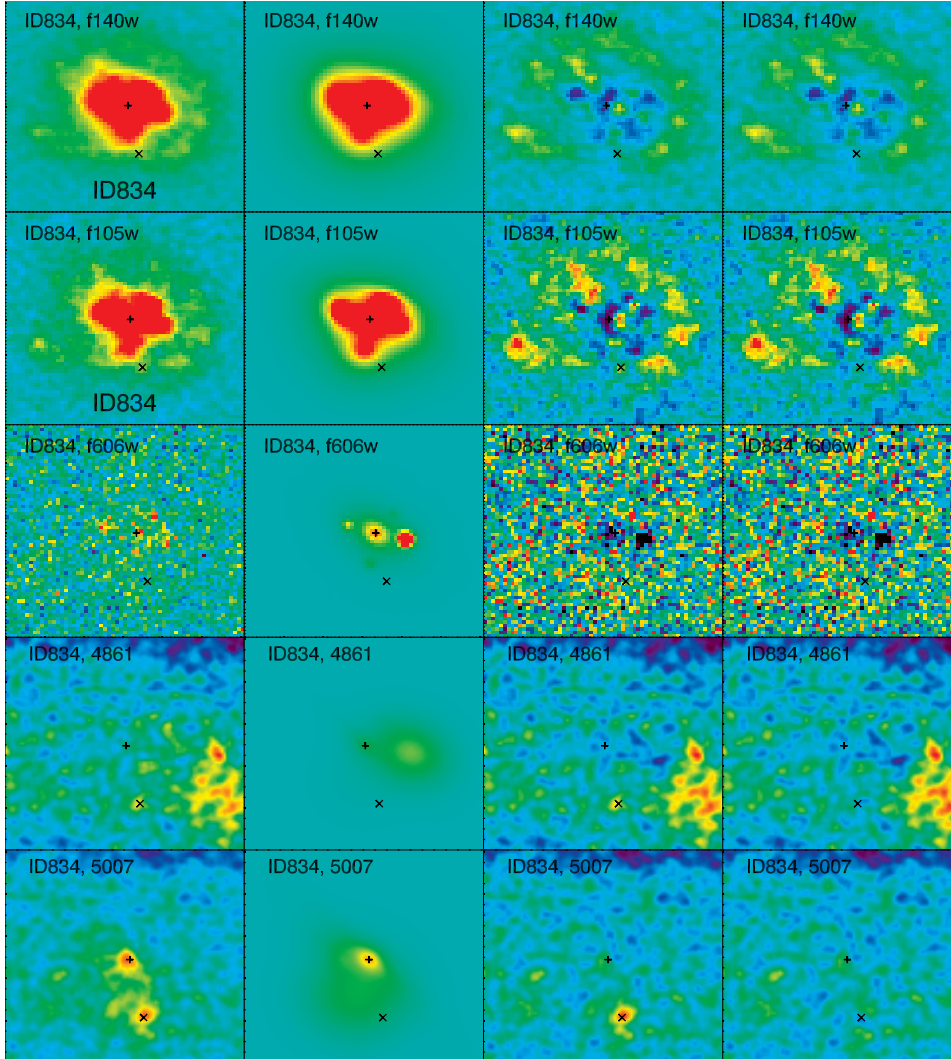


Figure B.1 - Continued.

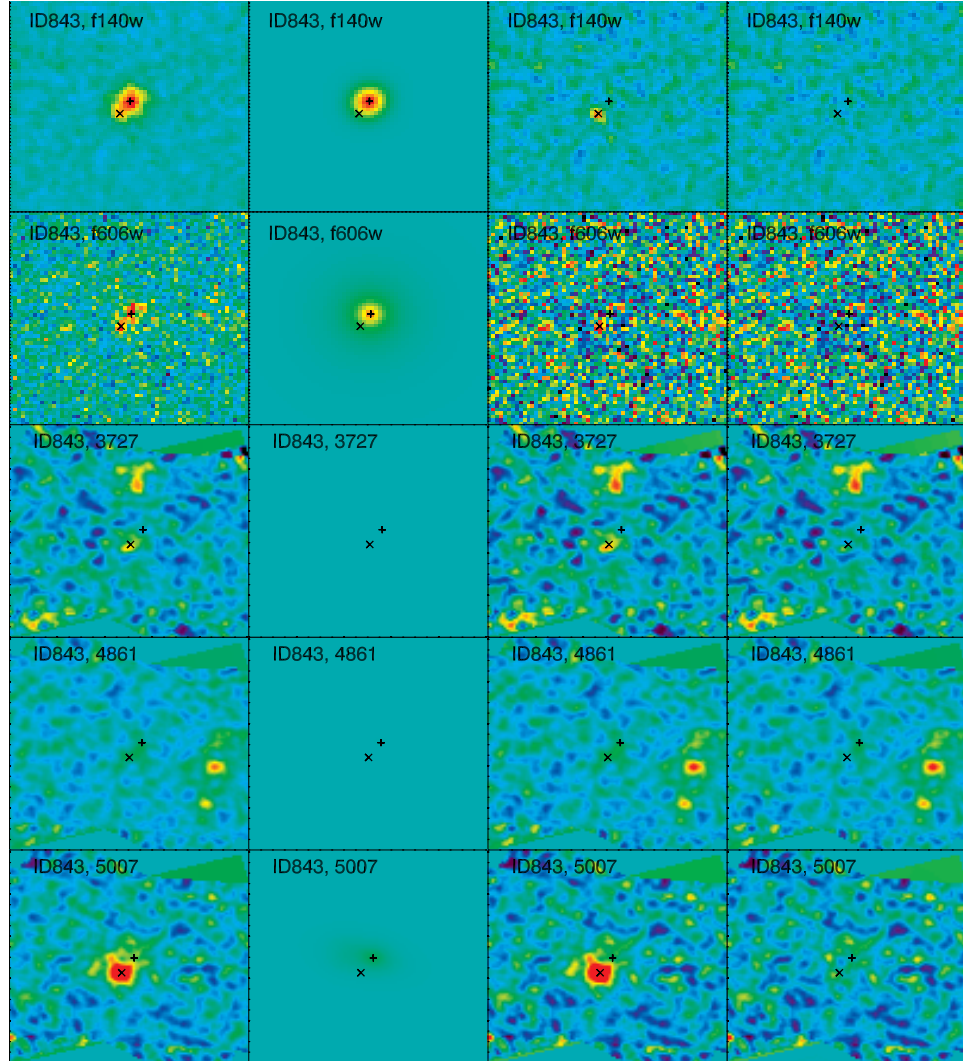


Figure B.1 – Continued.

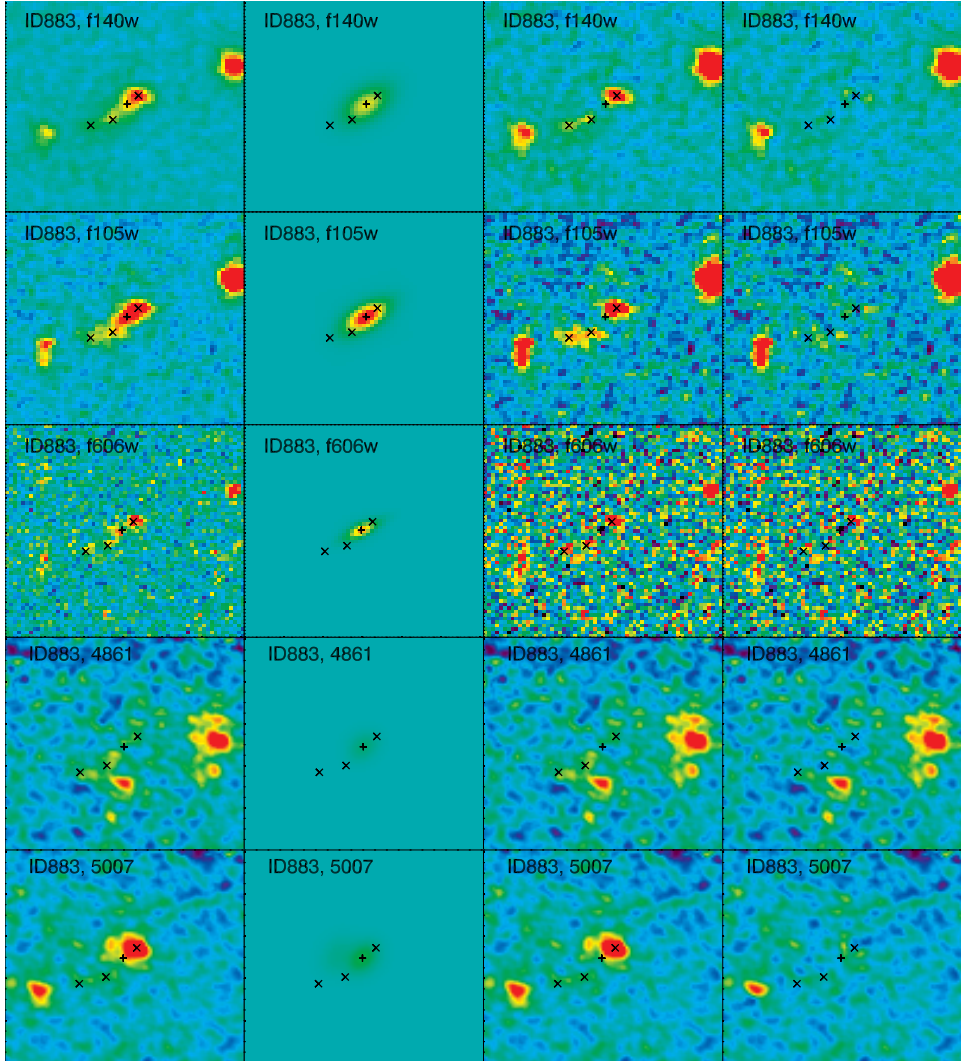


Figure B.1 - Continued.

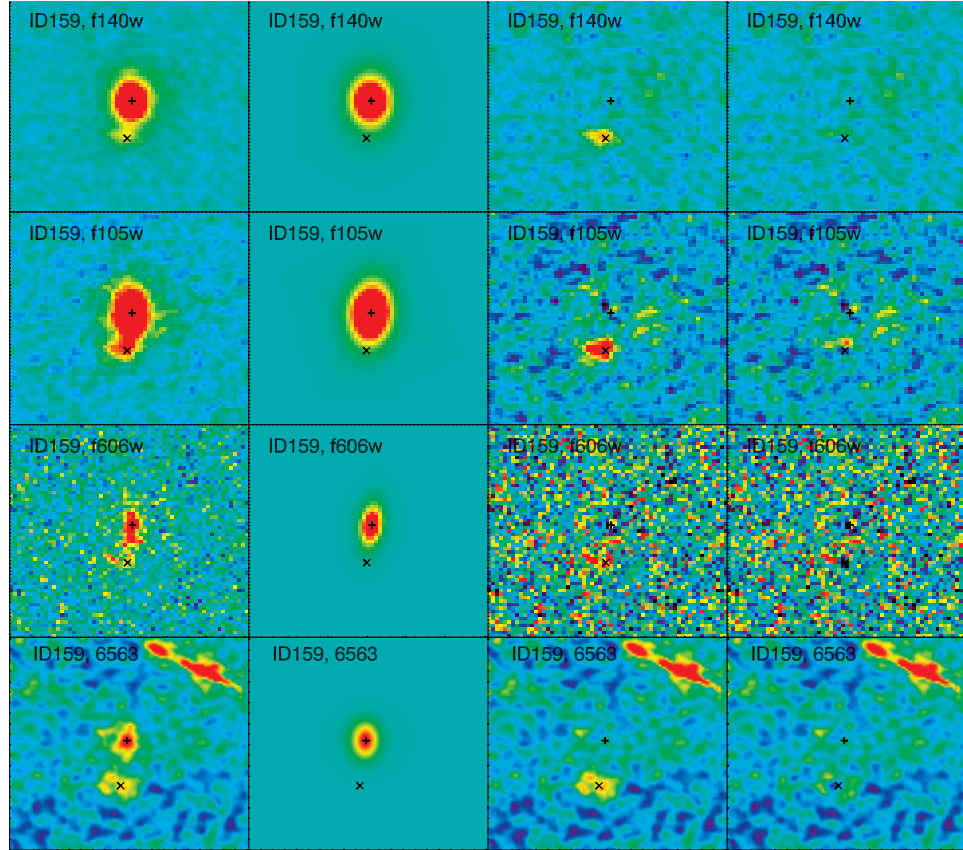


Figure B.1 – Continued.

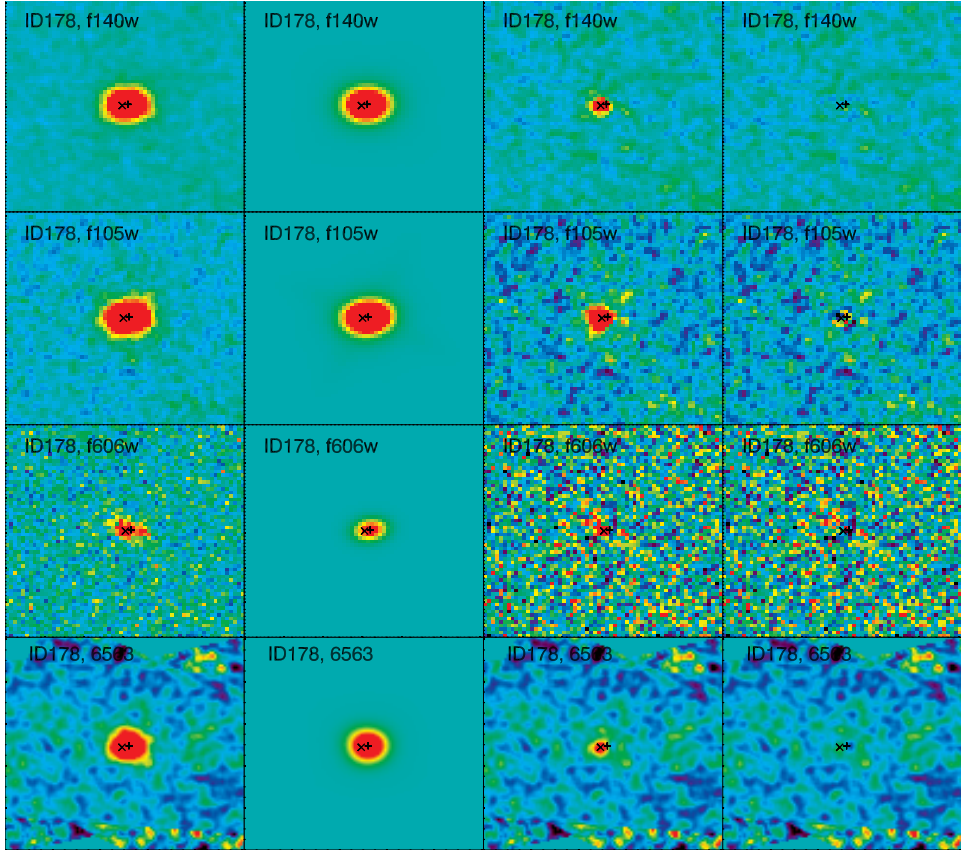


Figure B.1 - Continued.

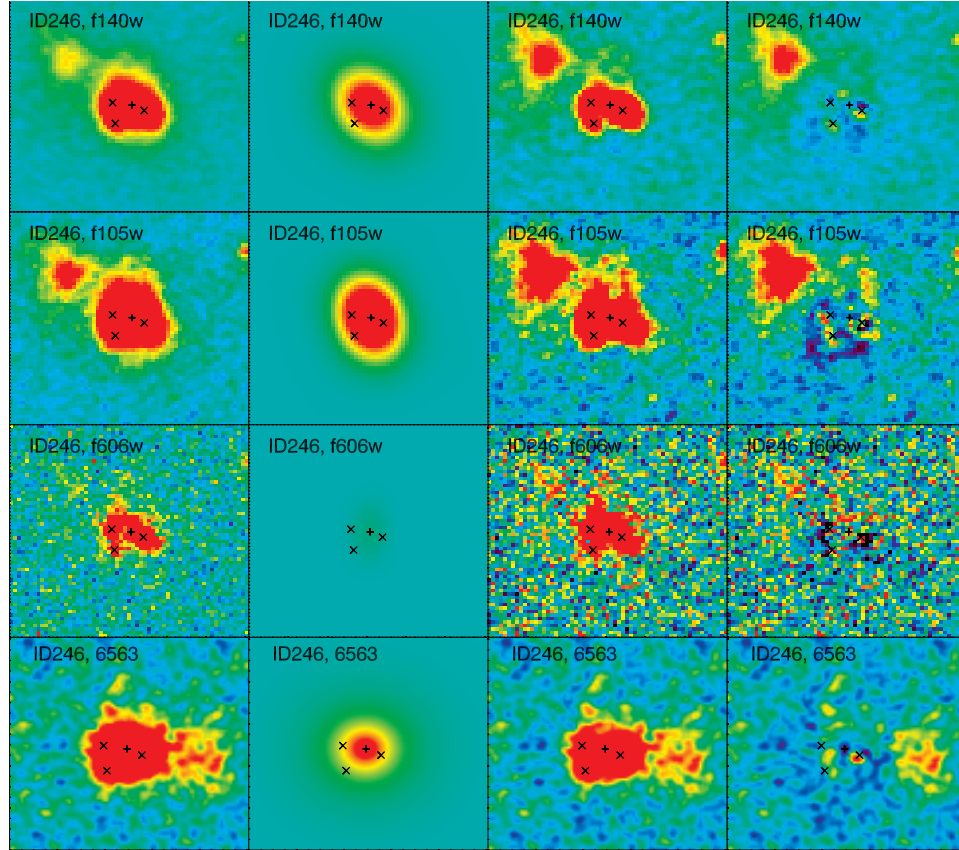


Figure B.1 – Continued.

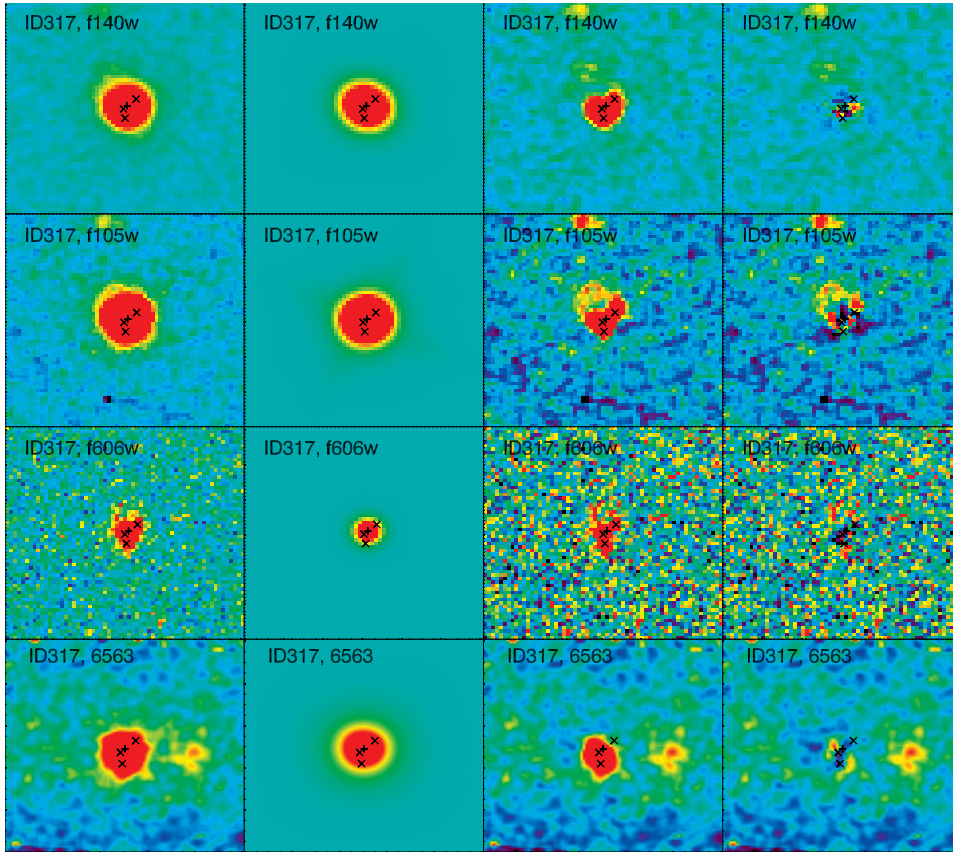


Figure B.1 - Continued.

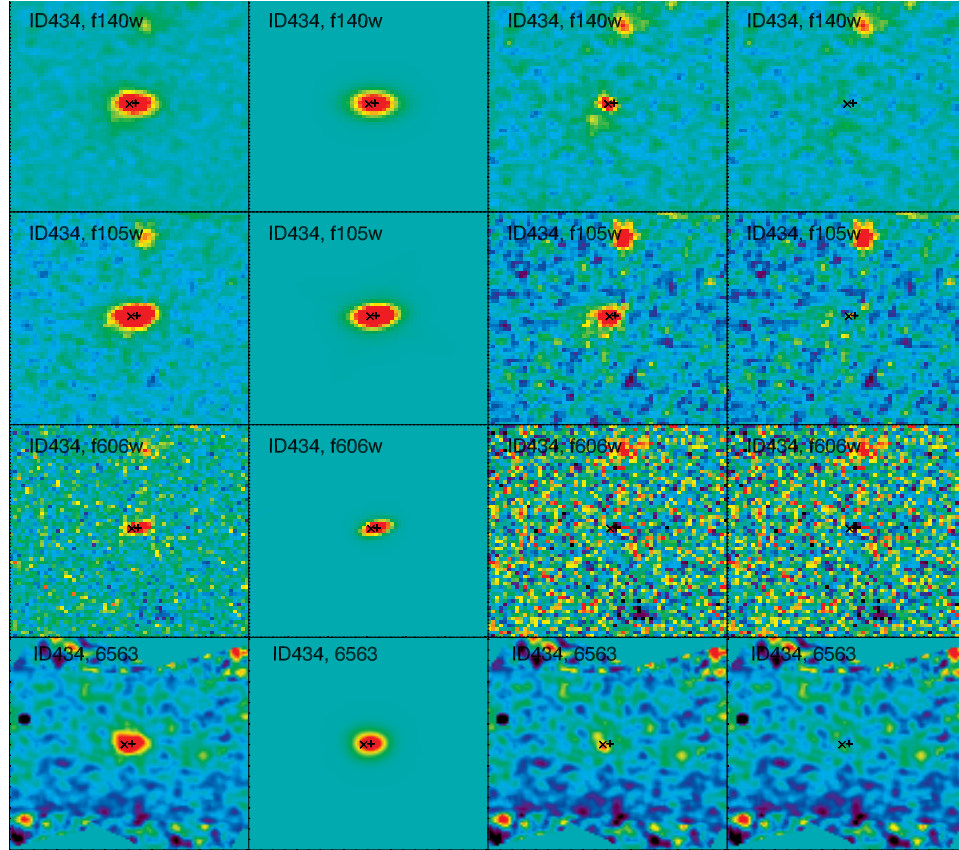


Figure B.1 – Continued.

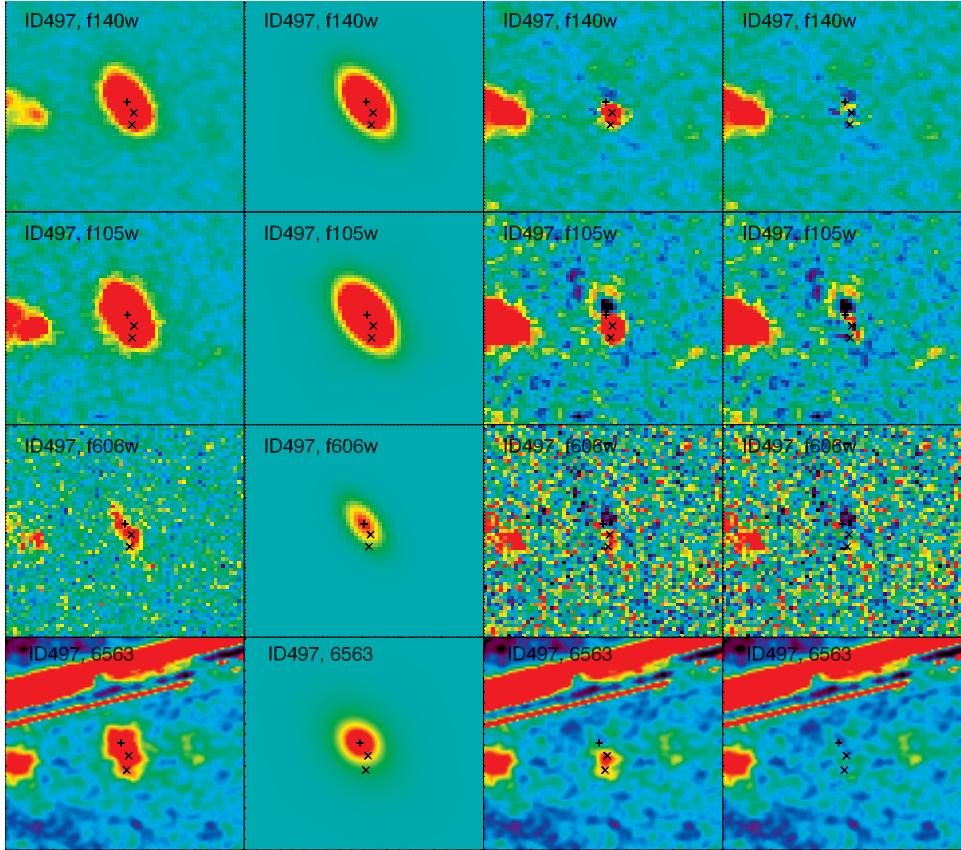


Figure B.1 - Continued.

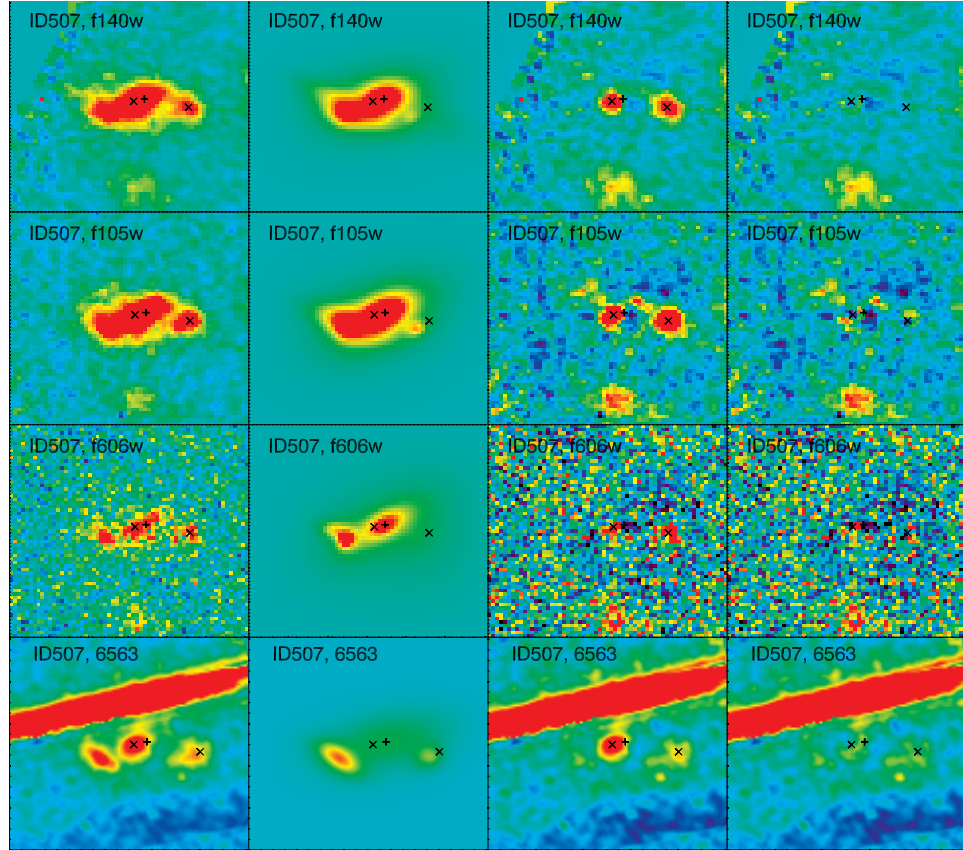


Figure B.1 – Continued.

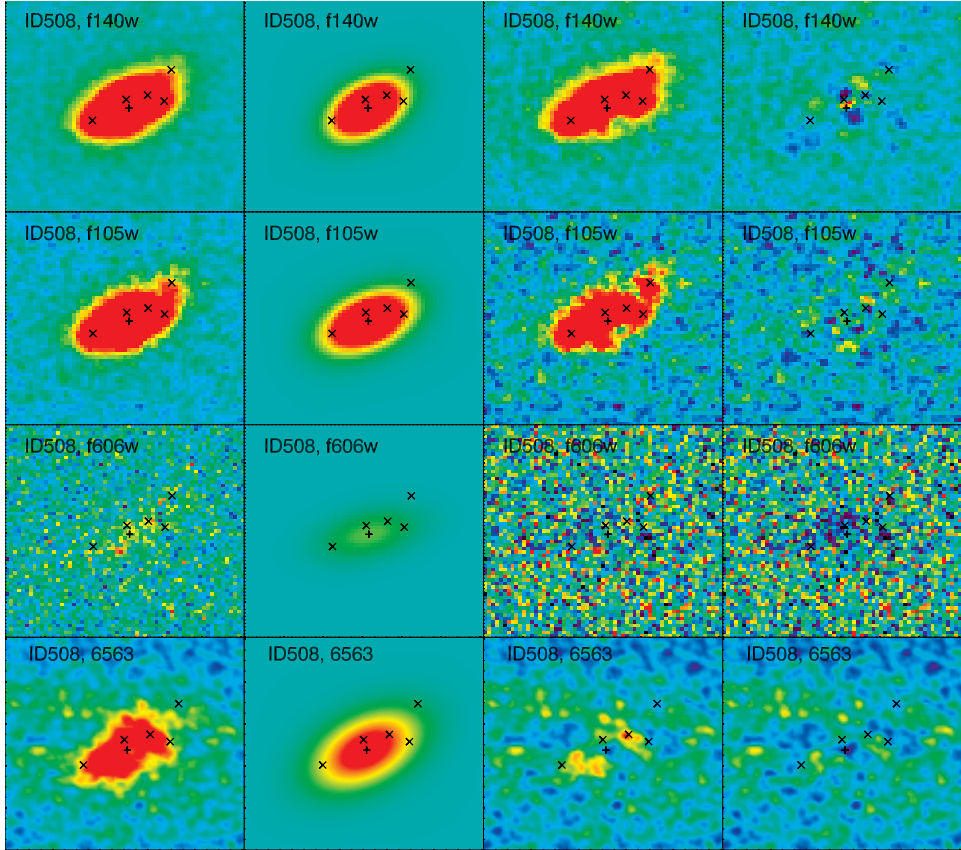


Figure B.1 - Continued.

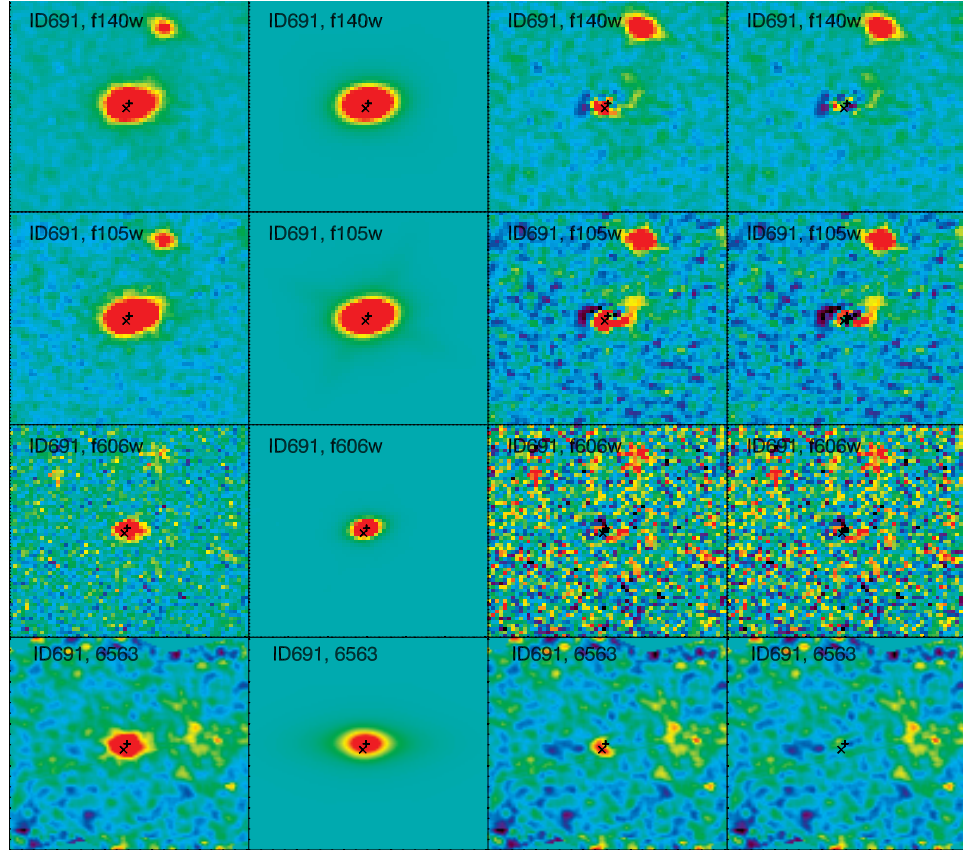


Figure B.1 – Continued.

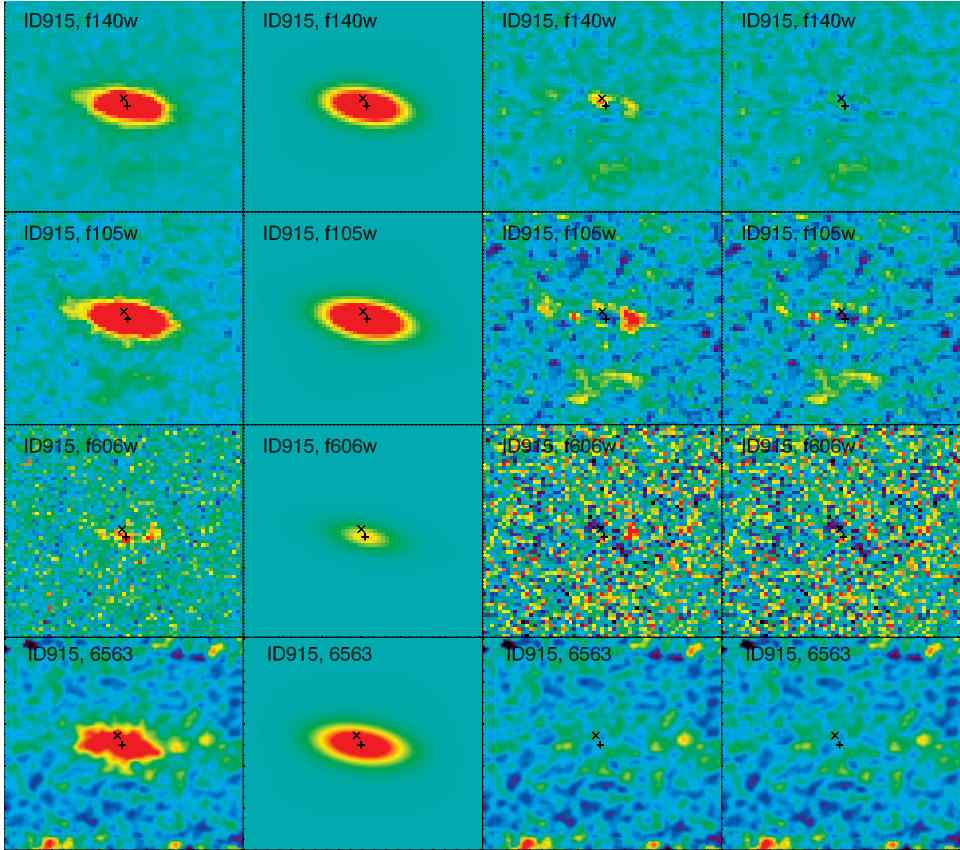


Figure B.1 - Continued.

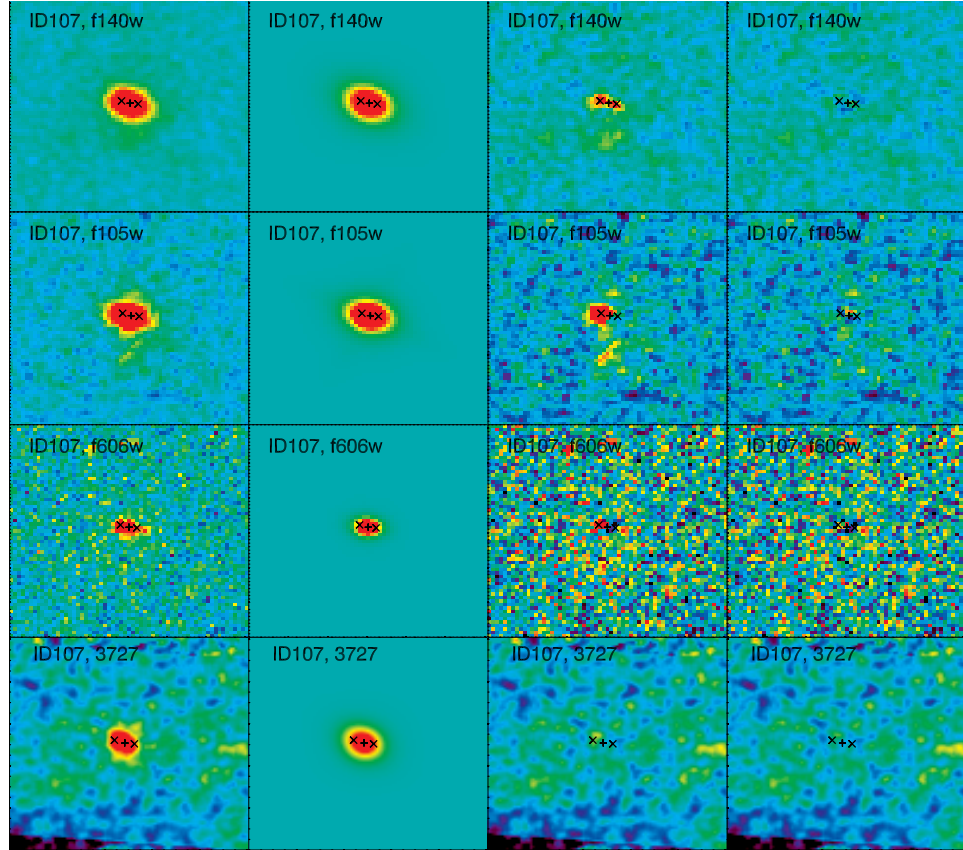


Figure B.1 - Continued.

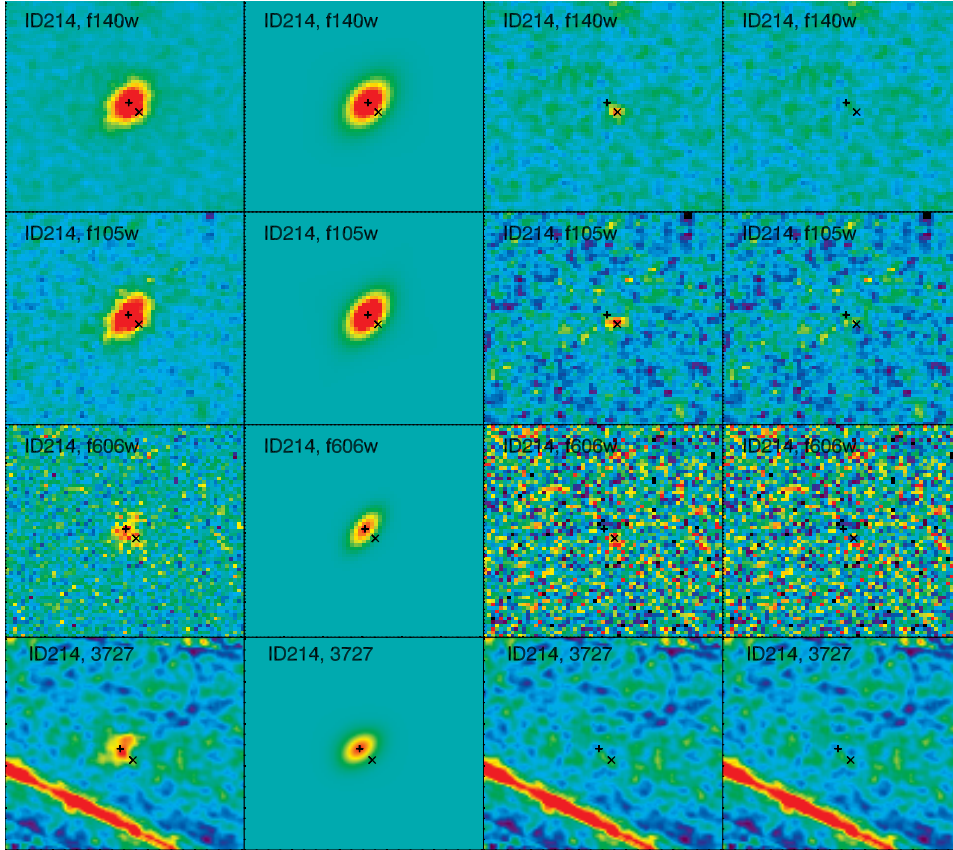


Figure B.1 - Continued.

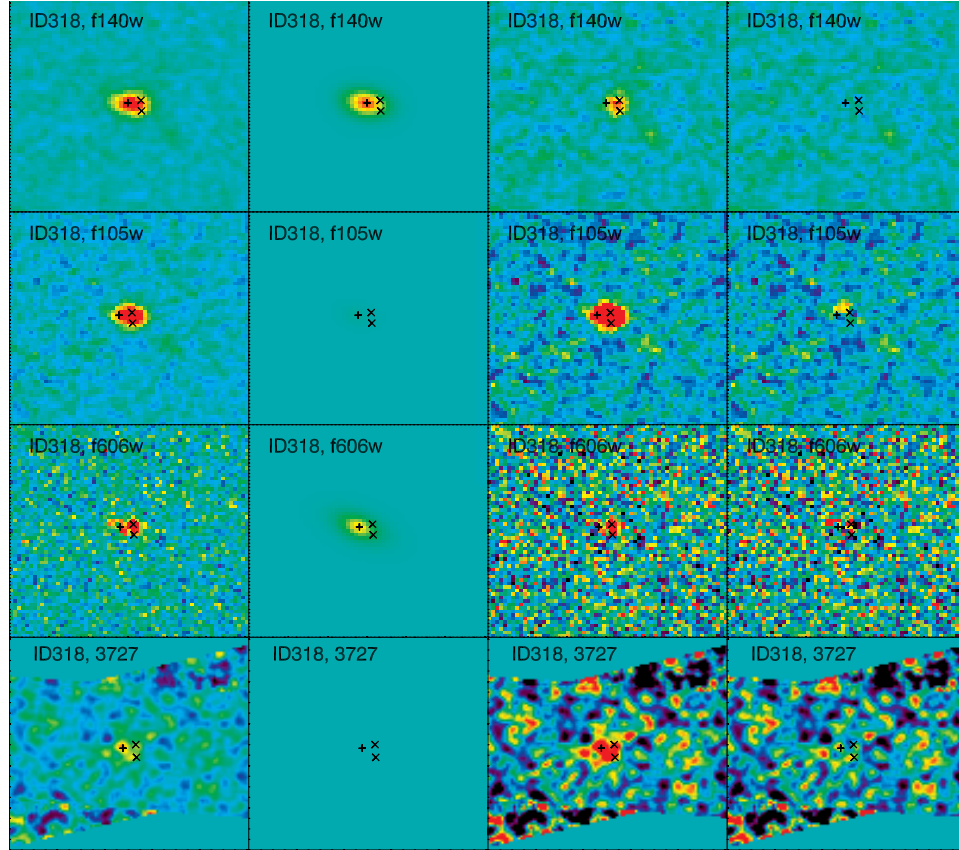


Figure B.1 – Continued.

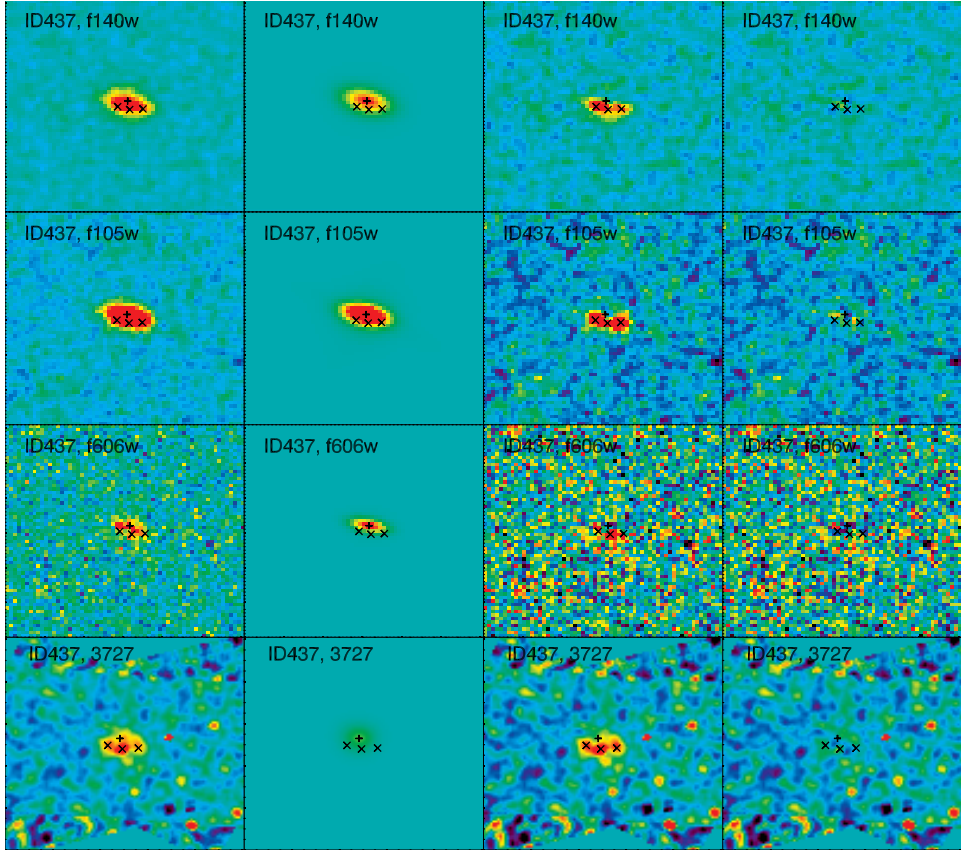


Figure B.1 - Continued.

Appendix C

First author papers

I report in the following the papers that I led as first author and that have been already published (Zanella et al. 2015; Zanella et al. 2016). A third paper is in preparation and likely the draft will be circulated among the co-authors before the date of the defense.

An extremely young massive clump forming by gravitational collapse in a primordial galaxy

A. Zanella¹, E. Daddi¹, E. Le Floch¹, F. Bournaud¹, R. Gobat^{1,2}, F. Valentino¹, V. Strazzullo^{1,3}, A. Cibinel^{1,4}, M. Onodera⁵, V. Perret⁶, F. Renaud^{1,7} & C. Vignali^{8,9}

When cosmic star formation history reaches a peak (at about redshift $z \approx 2$), galaxies vigorously fed by cosmic reservoirs^{1,2} are dominated by gas^{3,4} and contain massive star-forming clumps^{5,6}, which are thought to form by violent gravitational instabilities in highly turbulent gas-rich disks^{7,8}. However, a clump formation event has not yet been observed, and it is debated whether clumps can survive energetic feedback from young stars, and afterwards migrate inwards to form galaxy bulges^{9–12}. Here we report the spatially resolved spectroscopy of a bright off-nuclear emission line region in a galaxy at $z = 1.987$. Although this region dominates star formation in the galaxy disk, its stellar continuum remains undetected in deep imaging, revealing an extremely young (less than ten million years old) massive clump, forming through the gravitational collapse of more than one billion solar masses of gas. Gas consumption in this young clump is more than tenfold faster than in the host galaxy, displaying high star-formation efficiency during this phase, in agreement with our hydrodynamic simulations. The frequency of older clumps with similar masses¹³, coupled with our initial estimate of their formation rate (about 2.5 per billion years), supports long lifetimes (about 500 million years), favouring models in which clumps survive feedback and grow the bulges of present-day galaxies.

The high spatial resolution and sensitivity of Hubble Space Telescope (HST) imaging and spectroscopy routinely allows us to resolve giant star-forming regions (clumps) inside galaxies at $z \approx 2$, at 3 Gyr after the Big Bang. Stellar population modelling has revealed a wide range of ages for clumps observed in the continuum^{6,14–16}, with an average age of ~ 100 Myr. However, clump formation rates and lifetimes remain poorly constrained^{11,14,17,18}. Continuum-based stellar ages are probably underestimated because clumps lose stars and re-accrete gas during their evolution⁹, whereas very young ages (< 30 Myr) cannot be probed with continuum imaging alone. High equivalent width (EW) emission lines are required.

We obtained 16 orbits of HST Wide Field Camera 3 (WFC3) G141 slitless spectroscopy and imaging with the F140W, F105W and F606W filters targeting a galaxy cluster at $z = 2$ (ref. 19). The F606W band traces the star formation distribution in the ultraviolet rest frame, and the F140W probes the optical rest frame, reflecting the stellar mass distribution. Nebular [O III] $\lambda 5007$ Å emission was detected for 68 galaxies with stellar masses $9.5 < \log(M/M_{\odot}) < 11.5$ and redshifts $1.3 \leq z_{\text{spec}} \leq 2.3$, with measurements or upper limits for H β , [O II] $\lambda 3727$ Å and H α when available. From spatially resolved emission line maps we discovered a galaxy at $z = 1.987$ with a remarkably bright, off-nuclear emission line region ($F_{[\text{O III}]}$ = $(4.3 \pm 0.2) \times 10^{-17}$ erg cm⁻² s⁻¹, observed, plus H β and [O II]; Methods), lacking any obvious counterpart in broadband imaging (Fig. 1). The [O III] emission is spatially unresolved (radius < 500 pc) and located at the apparent distance of 1.6 ± 0.3 kpc (offset significance 7.6 σ ; Methods) from the nucleus (that is, the barycentre of the stellar continuum). The

deprojected distance is constrained within $3.6 \leq d \leq 6.2$ kpc, corresponding to 1.3–2.2 times the galaxy half-light radius (Methods). Subtracting a point-like emission leaves no significant residuals in the [O III] map. The continuum reddening and mass-to-light ratio (M/L) maps are flat over the galaxy, excluding the possibility that the feature is artificially induced by dust lanes or inhomogeneous attenuation (Extended Data Figs 1 and 2 and Methods).

From emission line ratios we estimated a reddening $E(B-V) \approx 0.3$ and a gas-phase metallicity $Z \approx 0.4Z_{\odot}$ for this region, consistent with the host galaxy. Robust upper limits on its stellar continuum were estimated with detailed simulations, leading to remarkably high lower limits on the emission-line EWs. Given these limits and the line luminosities, the emitting region cannot be powered by a massive black hole or by shock ionization from wind outflows. We similarly disfavour the hypothesis of a transient, because the line luminosities remain constant over time, or an *ex situ* merging system, because its older underlying stellar continuum would be detected²⁰. In addition, this galaxy is classified as a disk (not a merger) from its Asymmetry and M_{20} parameters (Methods). A young star-forming clump formed *in situ* is therefore the most plausible interpretation. On the basis of stellar

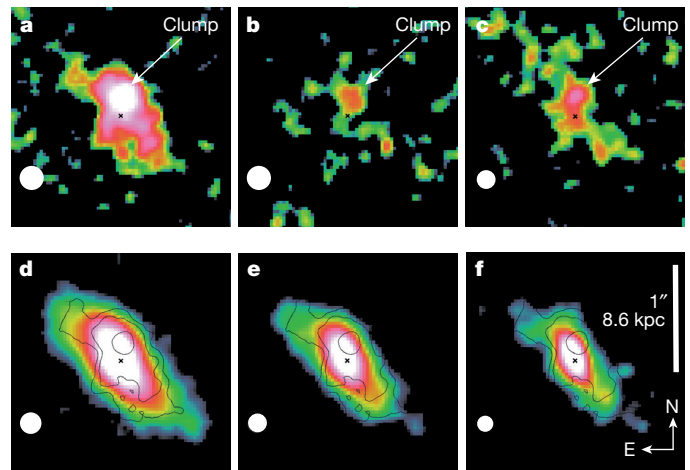


Figure 1 | A massive, very young clump in a disk galaxy at $z = 1.987$. a–c, Emission line maps showing off-nuclear, unresolved, bright [O III] (a), H β emissions (b) and [O II] emissions (c), with significances of 18 σ , 3 σ and 3.5 σ . d–f, No counterpart is detected in the F140W (d), F105W (e) and F606W (f) direct images. The flux contours of the [O III] map in a have been overplotted on the direct images. The colour scales logarithmically with flux from the minimum (black) to maximum (white) level displayed (they are different for a–c and d–f). The black cross in each panel indicates the barycentre of the stellar optical rest-frame continuum; the white circle indicates the point-spread function full-width at half-maximum.

¹Laboratoire AIM-Paris-Saclay, CEA/DSM-CNRS-Université Paris Diderot, Irfu/Service d'Astrophysique, CEA Saclay, Orme des Merisiers, F-91191 Gif sur Yvette, France. ²School of Physics, Korea Institute for Advanced Study, Heogiro 85, Seoul 130-722, Republic of Korea. ³Department of Physics, Ludwig-Maximilians-Universität, Scheinerstrasse 1, 81679 München, Germany. ⁴Astronomy Centre, Department of Physics and Astronomy, University of Sussex, Brighton BN1 9QH, UK. ⁵Institute for Astronomy, ETH Zürich, Wolfgang-Pauli-strasse 27, 8093 Zürich, Switzerland. ⁶Aix Marseille Université, CNRS, LAM (Laboratoire d'Astrophysique de Marseille), F-13388 Marseille, France. ⁷Department of Physics, University of Surrey, Guildford GU2 7XH, UK. ⁸Dipartimento di Fisica e Astronomia, Università degli Studi di Bologna, Viale Berti Pichat 6/2, 40127 Bologna, Italy. ⁹INAF Osservatorio Astronomico di Bologna, Via Ranzani 1, 40127 Bologna, Italy.

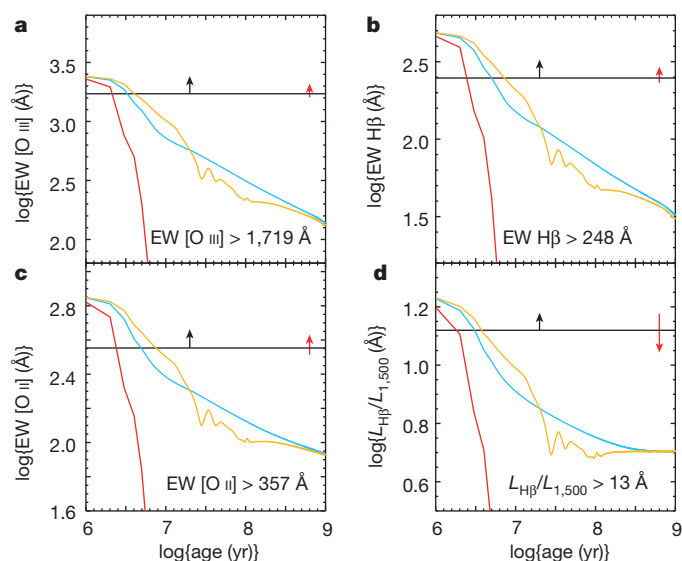


Figure 2 | Constraints on the clump's age from reddening-corrected, rest-frame, emission-line EWs. Lower limits on the clump EW (black solid line) of [O III] (a), H β (b) and [O II] (c) and the ratio between the H β luminosity and the continuum at 1,500 Å (d) compared with theoretical tracks. A Salpeter initial mass function is assumed, and different star formation histories are compared: red lines, single burst; blue lines, constant SFR; yellow lines, star formation history predicted by simulations⁹ (Fig. 4). The effect of reddening ($\Delta E(B-V) = +0.1$) is indicated in each panel (red arrow). The age of the clump is constrained to be <10 Myr.

population synthesis modelling for galaxies with active star formation, the observed EWs require very young ages for the star formation event, with a firm upper limit of 10 Myr (Fig. 2). Thus, although the ubiquity of clumps in high- z galaxies has been known for a decade, we are witnessing here the formation of a star-forming clump in the early stage of its gravitational collapse. From the reddening-corrected line luminosities we estimate a clump star formation rate (SFR) of $(32 \pm 6) M_{\odot} \text{ yr}^{-1}$, comparable to that of the rest of the host galaxy disk (Methods). The F140W continuum non-detection translates into a stellar mass limit $M_{\star} \lesssim 3 \times 10^8 M_{\odot}$. To infer the underlying gas mass of the clump we considered the Jeans mass of the galaxy as a plausible upper limit, because fragmentation at higher masses is unlikely. This constrains the clump gas mass to $M_{\text{gas}} \lesssim 2.5 \times 10^9 M_{\odot}$, assuming a maximal gas velocity dispersion $\sigma_v \approx 80 \text{ km s}^{-1}$ (refs 21, 22; Methods).

This finding offers new insights into the physics of clump formation in gas-rich turbulent media at high z . Using the estimate of its underlying gas mass, stellar mass and SFR we can constrain the nature of its star formation mode. Its specific SFR (defined as SFR/M_{\star}) is more than 30-fold that of its host galaxy, a typical Main Sequence galaxy at $z \approx 2$. Similarly, the lower limit on the clump star formation efficiency (SFE = $\text{SFR}/M_{\text{gas}}$) is more than tenfold that of normal galaxies (Fig. 3), a behaviour that at galaxy-wide scales is observed only for extreme starbursts²³. At sub-galactic scales such a high SFE is observed for nearby molecular clouds²⁴, which are small and transient features 1,000-fold less massive than the present clump. Possibly at odds with what has been assumed so far^{13,17,18}, this provides observational evidence that giant clumps do not follow the Schmidt–Kennicutt law of normal star-forming galaxies, at least in the early stages of collapse. Instead, this luminous sub-galactic structure seems to follow the universal star-formation law normalized by the dynamical time^{25–27}. Comparing with the SFRs reported for older clumps with similar masses¹³, we estimated a SFR enhancement of ~ 3 – 5 -fold at ‘peak formation’ with respect to later phases. This massive star-forming clump has a robust age estimate that is similar to or shorter than its dynamical time (Methods).

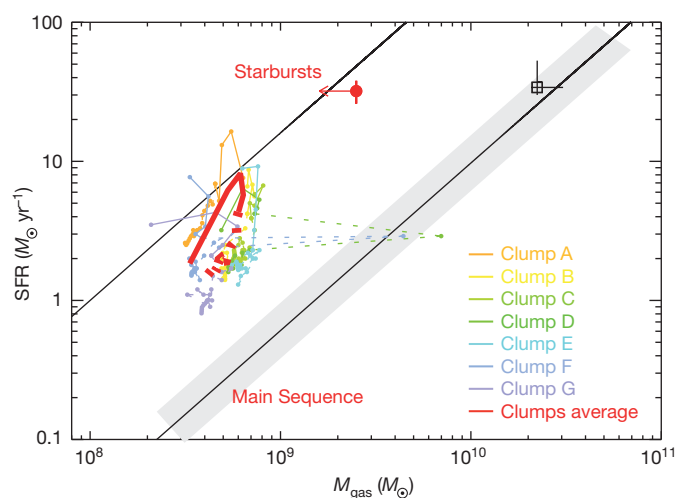


Figure 3 | The Schmidt–Kennicutt plane. Comparison of the trends for starbursts and Main Sequence galaxies²⁹ (black solid lines and shaded region indicating the 0.2 dex dispersion of the Main Sequence) with the location of observed (Vyc1, red filled circle with error bars indicating s.d.) and simulated clumps (coloured dots connected with lines; solid and dashed lines for ages ≤ 30 Myr and >30 Myr, respectively). The average locations of simulated clumps (red, thick line) and host simulated galaxy (square with error bars indicating s.d.) are shown. Sudden variations in the M_{gas} of clumps are probably due to the accretion of gas-rich clouds or small clumps.

Prompted by our observations, we investigated the properties of clumps in their formation phase by using high-resolution simulations⁹. We solved the dark matter, stellar and gas gravity and hydrodynamics at a resolution of 3.5 pc and gas cooling down to 100 K, and we modelled the feedback processes from young stars onto the gas: photo-ionization, radiation pressure and supernova explosions. Figure 4 shows a typical, $M_{\star} \approx 3 \times 10^{10} M_{\odot}$, $z = 2$ galaxy model with giant clumps formed through violent disk instability. Their formation sites are located 2.1–7.0 kpc from the nucleus of a galaxy that has an half-mass radius of 4.5 kpc, consistent with many other simulations^{10,20,28} and our observations. All clumps, and especially the youngest ones, are brighter in the SFR map than in the continuum: they undergo a burst of star formation during their initial collapse, with peak SFRs about $(10\text{--}20) M_{\odot} \text{ yr}^{-1}$, consistent with our observations, then evolve to a lower specific SFR regime within 20 Myr, once feedback has regulated star formation and their stellar mass has grown. Our simulations further corroborate the idea that all clumps behave like galactic miniatures of starbursts in the Schmidt–Kennicutt diagram during their first 20 Myr (Fig. 3). The SFE of simulated clumps decreases at later times, although it remains ≥ 0.5 dex higher than that of Main Sequence galaxies, consistent with their shorter dynamical times. The presence of massive clumps is probably an effective reason for the observed rise of the SFE in normal Main Sequence galaxies from $z = 0$ to $z = 2$ (refs 3, 4, 29), given the increasing prevalence of clumps at high z . Furthermore, the violent burst-like behaviour that young clumps show at formation is consistent with simulations predicting that, because of their rapid collapse, giant clumps could form globular clusters by converting gas into stars faster than stars expel the gas³⁰.

The short visibility window at high EWs ($\lesssim 10$ Myr, independently of the star formation history) has probably prevented the detection of the formation phase of clumps before now. From this timing constraint and the single discovery in our survey, we attempted an estimate of the clump formation rate of 2.5 Gyr^{-1} per galaxy (for $M_{\text{clump}} \gtrsim 2.5 \times 10^9 M_{\odot}$; Methods). Given the observation of one or two clumps per galaxy with similar masses^{13,17,18}, this converts into a lifetime of ~ 500 Myr (Methods). This is longer than expected in models of clump destruction by stellar feedback^{10,28}. Instead, it is representative of the timescale needed for giant clumps formed in galactic

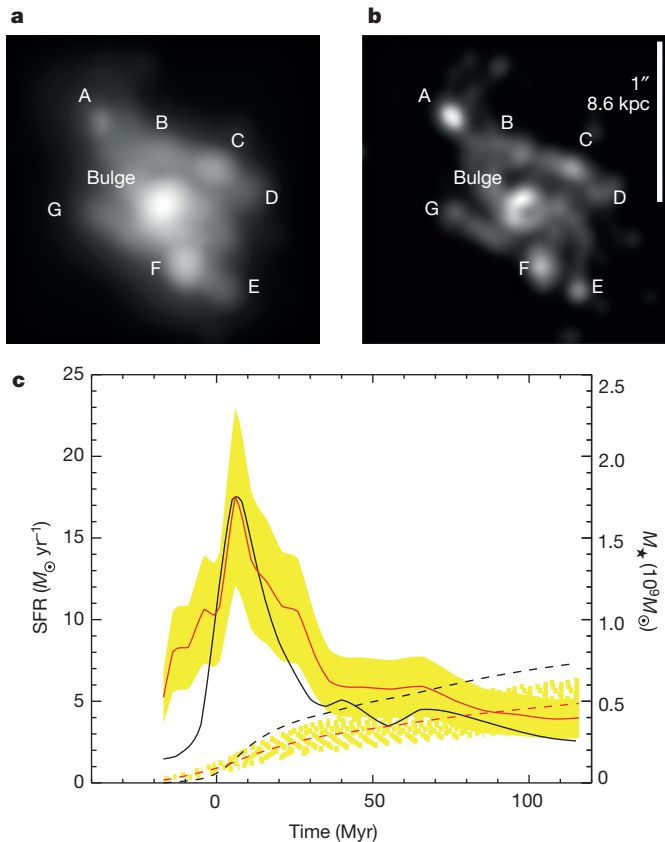


Figure 4 | Numerical simulations of a high-redshift clumpy galaxy seen face-on. **a, b**, Maps of stellar mass (**a**) and SFR (**b**) at HST-like resolution. All clumps have elevated SFR compared with M_{\star} , but this property is extreme for clump A, observed 12 Myr after its formation. **c**, Time evolution of the SFR (black solid line) and M_{\star} (black dashed line) for clump A and for all the clumps (red solid line, average SFR; red dashed line, average M_{\star}); each star formation history is arbitrarily shifted in time to align the SFR peaks. All clumps experience an internal burst of star formation before evolving into a long-lasting regulated regime within 20 Myr. Yellow shaded regions indicate s.d. uncertainties.

disks to migrate inwards through dynamical friction and gravity torques and to coalesce to grow the central galactic bulges^{9,12}.

Our study demonstrates the detectability of ultra-young clumps in deep surveys, indicating low formation rates and long lifetimes. This is crucial to an understanding of key issues of galaxy formation and evolution such as clump migration, bulge formation and the role of feedback. However, future observations of larger samples of forming clumps with direct measurements of the sizes, gas masses and velocity widths (and hence dynamical masses) of clumps are required for a complete understanding. This should be within the capabilities of the complete Atacama Large Millimeter Array and James Webb Space Telescope. We note that spectroscopic surveys targeting high- z galaxies (for example SINFONI integral field spectroscopy (SINS) and 3D-HST) have not yet reported the identification of giant clumps at formation. This might suggest that they are rarer events than suggested by our survey, which allowed us to identify a direct signature of massive clump formation by means of gravitational collapse.

Online Content Methods, along with any additional Extended Data display items and Source Data, are available in the online version of the paper; references unique to these sections appear only in the online paper.

Received 20 October 2014; accepted 26 February 2015.

1. Kereš, D. How do galaxies get their gas? *Mon. Not. R. Astron. Soc.* **363**, 2–28 (2005).
2. Dekel, A. *et al.* Cold streams in early massive hot halos as the main mode of galaxy formation. *Nature* **457**, 451–454 (2009).

3. Daddi, E. *et al.* Very high gas fractions and extended gas reservoirs in $z = 1.5$ disk galaxies. *Astrophys. J.* **713**, 686–707 (2010).
4. Tacconi, L. J. *et al.* High molecular gas fractions in normal massive star forming galaxies in the young Universe. *Nature* **463**, 781–784 (2010).
5. Genzel, R. *et al.* The rapid formation of a large rotating disk galaxy three billion years after the Big Bang. *Nature* **442**, 786–789 (2006).
6. Elmegreen, B. G. *et al.* Bulge and clump evolution in Hubble Ultra Deep Field clump clusters, chains and spiral galaxies. *Astrophys. J.* **692**, 12–31 (2009).
7. Elmegreen, D. M., Elmegreen, B. G. & Hirst, A. C. Discovery of face-on counterparts of chain galaxies in the Tadpole Advanced Camera for Surveys field. *Astrophys. J.* **604**, 21–23 (2004).
8. Bournaud, F., Elmegreen, B. G. & Elmegreen, D. M. Rapid formation of exponential disks and bulges at high redshift from the dynamical evolution of clump-cluster and chain galaxies. *Astrophys. J.* **670**, 237–248 (2007).
9. Bournaud, F. *et al.* The long lives of giant clumps and the birth of outflows in gas-rich galaxies at high-redshift. *Astrophys. J.* **780**, 57–75 (2014).
10. Genel, S. *et al.* Short-lived star-forming giant clumps in cosmological simulations of $z \sim 2$ disks. *Astrophys. J.* **745**, 11–21 (2012).
11. Wuyts, S. *et al.* A CANDELS-3D-HST synergy: resolved star formation patterns at $0.7 < z < 1.5$. *Astrophys. J.* **779**, 135–151 (2013).
12. Dekel, A. *et al.* Formation of massive galaxies at high redshift: cold streams, clumpy disks, and compact spheroids. *Astrophys. J.* **703**, 785–801 (2009).
13. Förster-Schreiber, N. *et al.* Constraints on the assembly and dynamics of galaxies. II. Properties of kiloparsec-scale clumps in rest-frame optical emission of $z \sim 2$ star-forming galaxies. *Astrophys. J.* **739**, 45–69 (2011).
14. Wuyts, S. *et al.* Smooth(er) stellar mass maps in CANDELS: constraints on the longevity of clumps in high-redshift star-forming galaxies. *Astrophys. J.* **753**, 114–139 (2012).
15. Guo, Y. *et al.* Multi-wavelength view of kiloparsec-scale clumps in star-forming galaxies at $z \sim 2$. *Astrophys. J.* **757**, 120–142 (2012).
16. Elmegreen, B. *et al.* Massive clumps in local galaxies: comparison with high-redshift clumps. *Astrophys. J.* **774**, 86–100 (2013).
17. Genzel, R. *et al.* The SINS survey of $z \sim 2$ galaxy kinematics: properties of the giant star-forming clumps. *Astrophys. J.* **733**, 101–131 (2011).
18. Newman, S. *et al.* The SINS/zC-SINF survey of $z \sim 2$ galaxy kinematics: outflow properties. *Astrophys. J.* **761**, 43–50 (2012).
19. Gobat, R. *et al.* WFC3 GRISM confirmation of the distant cluster CLJ1449 + 0856 at $z = 2.00$: quiescent and star-forming galaxy populations. *Astrophys. J.* **776**, 9–21 (2013).
20. Mandelker, N. *et al.* The population of giant clumps in simulated high- z galaxies: *in situ* and *ex situ* migration and survival. *Mon. Not. R. Astron. Soc.* **443**, 3675–3702 (2014).
21. Förster-Schreiber, N. *et al.* The SINS survey: SINFONI integral field spectroscopy of $z \sim 2$ star-forming galaxies. *Astrophys. J.* **706**, 1364–1428 (2009).
22. Contini, T. *et al.* MASSIV: Mass Assembly Survey with SINFONI in VVDS. *Astron. Astrophys.* **593**, 91–106 (2012).
23. Rodighiero, G. *et al.* The lesser role of starbursts in star formation at $z = 2$. *Astrophys. J.* **739**, 40–45 (2011).
24. Lada, C. J., Lombardi, M. & Alves, J. F. On the star formation rates in molecular clouds. *Astrophys. J.* **724**, 687–693 (2010).
25. Daddi, E. *et al.* Different star formation laws for disks versus starbursts at low and high redshifts. *Astrophys. J.* **714**, 118–122 (2010).
26. Genzel, R. *et al.* A study of the gas-star formation relation over cosmic time. *Mon. Not. R. Astron. Soc.* **407**, 2091–2108 (2010).
27. Krumholz, M. R., Dekel, A. & McKee, C. F. A. Universal, local star formation law in galactic clouds, nearby galaxies, high-redshift disks, and starbursts. *Astrophys. J.* **645**, 69–84 (2012).
28. Hopkins, P. F. *et al.* Stellar feedback and bulge formation in clumpy discs. *Mon. Not. R. Astron. Soc.* **427**, 968–978 (2012).
29. Sargent, M. T. *et al.* Regularity underlying complexity: a redshift-independent description of the continuous variation of galaxy-scale molecular gas properties in the mass-star formation rate plane. *Astrophys. J.* **793**, 19–55 (2014).
30. Shapиро, K. L., Genzel, R. & Förster-Schreiber, N. M. Star-forming galaxies at $z \sim 2$ and the formation of the metal-rich globular cluster population. *Mon. Not. R. Astron. Soc.* **403**, 36–40 (2010).

Acknowledgements We thank S. Juneau for discussions, and M. Cappellari for sharing his Multi-Gaussian Expansion fit software publicly. The simulations were performed at the Très Grand Centre de Calcul of the CEA (Commissariat à l’Énergie Atomique et aux énergies alternatives) under GENCI (Grand Équipement National de Calcul Intensif) allocation 2014-GEN2192. We acknowledge financial support from Agence Nationale de la Recherche (contract ANR-12-JS05-0008-01) and the European Commission through European Research Council grants StG-257720 and StG-240039.

Author Contributions A.Z., E.D., E.L.F. and F.B. conceived the work, led the analysis and interpretation, and wrote the paper. R.G., F.V., V.S., A.C., M.O. and C.V. contributed key aspects of the data reduction and analysis. V.P. and F.R. contributed key aspects of the simulations development and analysis. All the authors commented on the manuscript at all stages.

Author Information Reprints and permissions information is available at www.nature.com/reprints. The authors declare no competing financial interests. Readers are welcome to comment on the online version of the paper. Correspondence and requests for materials should be addressed to A.Z. (anita.zanella@cea.fr).

METHODS

Emission line maps. The 16 HST/WFC3 orbits of G141 slitless spectroscopy, taken along three position angles ($\sim 0^\circ$, -30° and $+15^\circ$)¹⁹, were reduced with aXe³¹. Residual defects (such as bad pixels and cosmic ray hits) were removed with L.A.Cosmic³². Two-dimensional spectra were background subtracted with SExtractor³³, and the continuum emissions of the main target and surrounding sources (including higher and lower order dispersion spectra) were removed by fitting their aXe continuum models with free normalization (Fig. 1).

Astrometrically calibrated emission line maps were obtained by cross-correlating the spectral images of [O III] (the brightest line) with the three different position angles. This is preferred over cross-correlating with the continuum image because our target has different broadband and line morphologies. For this step, the spectral images were combined with the IRAF task WDRIZZLE³⁴, weighting each single orientation by its exposure time. The astrometry of the H β and [O II] emission maps was tied to that of [O III]. The resulting redshift agrees accurately with Subaru/MOIRCS longslit spectroscopy³⁵.

The [O III] doublet is resolved at the spectral resolution of our data for relatively compact galaxies. We removed the [O III] λ 4959 Å component by modelling the combined emission line images with GALFIT³⁶ using an effective point-spread function (PSF) consisting of a main lobe for the 5007 Å line and three fainter ones. **Clump continuum emission.** Visual inspection of the multi-band HST imaging did not reveal any evidence of the clump, and the evaluation of the isophotal contours of the galaxy images did not show disturbances at its location. Thus we searched for its presence by modelling the imaging with GALFIT (Extended Data Fig. 3). A single Sérsic³⁷ profile provided a simplified fit, leaving strong positive and negative residuals near the expected position of the clump. Such a pattern is a systematic effect as a result of the presence of clumps at the outskirts of the galaxy major axis, because they are not symmetrically located with respect to the nucleus, resulting in an effective bending of the galaxy isophots. Masking the external regions and fitting the central part of the galaxy with a single Sérsic profile left negligible residuals ($\lesssim 5\%$). As a further check, we fitted the direct images with the Multi-Gaussian Expansion parameterization (MGE) algorithm³⁸, fitting average azimuthal light profiles with ellipsoidal isophots to the central part of the galaxy. The residuals are negligible ($\lesssim 5\%$). Analogous residuals resulted from the use of three spatially offset Sérsic profiles: one centred at the barycentre of the stellar light (as determined by SExtractor from the F140W image) and other two, an order of magnitude fainter, to the top left and bottom right. This is our best fit (baseline) model for the galaxy continuum.

This three-component fit is a technical solution adopted because of the irregular morphology of our target, typical of clumpy high- z disks, and should not mislead one to conclude that the galaxy is an ongoing merger. In this regard, we classified the galaxy as a disk based on the Asymmetry and M_{20} parameters measured on stellar mass maps derived from pixel-to-pixel spectral energy distribution (SED) fitting^{39–41} (Extended Data Fig. 4), a diagnostic calibrated with MIRAGE numerical simulations⁴². Finally, the F105W/F140W ratio (Extended Data Fig. 2) provides no evidence for a bulge.

Limits on the clump continuum were obtained with simulations, injecting PSF components at approximately the same isophotal level as that of the expected clump position, and fitting them together with our baseline model. From these estimates we subtracted the contribution of emission lines ([O III] and H β for F140W; [O II] for F105W), obtaining factors of 2 and 1.3 deeper flux upper limits for F140W and F105W, respectively. Normalizing a series of Starburst99 stellar population synthesis models⁴³ with different stellar ages to the most constraining (F105W) upper limit allowed us to refine the F140W limit, which is relevant for calculating the [O III] and H β emission line EWs (Extended Data Fig. 5).

Clump offset from the galaxy nucleus. The clump is offset from the galaxy centre: the observed distance between the point-like [O III] emission and the barycentre of the galaxy is 1.6 kpc, with formally negligible measurement error. However, there are systematic uncertainties; these are related to the astrometric calibration of the direct imaging and slitless data and to the stability of the wavelength solution. We estimated the systematic uncertainties along the dispersion direction evaluating the distribution of differences between the measured and expected wavelengths of bright emission lines (H α and [O III]) of the full survey data. By comparing the position of galaxies in the direct imaging with that of the continuum emission in the grism data we evaluated the systematics in the cross-dispersion direction. For each orientation of the grism we imposed

$$\chi_{\text{red}}^2 = \frac{1}{N_{\text{dof}}} \sum_{i=1}^N \left(\frac{s_{\text{meas},i} - s_{\text{exp}}}{\sqrt{\sigma_{P,i}^2 + \sigma_{\lambda}^2}} \right)^2 = 1$$

where N_{dof} is the degrees of freedom, $s_{\text{meas},i}$ and s_{exp} are respectively the measured and expected positions of the emission lines (or the continuum) of each galaxy,

and σ_P and σ_{λ} indicate respectively the formal measurement errors on the emission lines (or continuum) positions and the astrometric uncertainties. Average systematic uncertainties are $\sigma_{\lambda} = 0.067''$ along the dispersion direction and $\sigma_{\lambda} = 0.035''$ along the cross-dispersion direction. We computed the uncertainties along the right ascension and declination directions projecting along the orientation of each data set. Because the final, astrometrically calibrated, emission line maps are the weighted average of three different orientations, we estimated the total uncertainties assuming that the errors (ϵ_i) in each orientation were independent:

$$\epsilon = \frac{\sqrt{\sum_{i=1}^3 (t_i \epsilon_i)^2}}{\sum_{i=1}^3 t_i}$$

where t_i represents the exposure times. The clump offset is detected at 7.6σ and its projected distance from the galaxy nucleus (defined as the barycentre of the stellar light) is 1.6 ± 0.3 kpc. If we had chosen the light peak of the direct images as the nucleus, the offset would be comparable in magnitude and significance. We prefer the light barycentre definition because it coincides with the peak of the mass map (Extended Data Fig. 2).

To determine the deprojected distance, the axial ratio of the galaxy and the angle θ between the galaxy major axis and the clump nucleus direction are needed. We estimated them from the range of solutions obtained by modelling the direct images and the mass map with GALFIT and considering the outer isophots of the PSF-deconvolved galaxy. To further account for systematic effects we also considered plausible uncertainties in the PSF derivation, and further estimates based on the MGE software as an alternative to GALFIT. Given an axial ratio $0.21 \leq q \leq 0.35$ (inclination $i \approx 70\text{--}78^\circ$) and $48 \leq \theta \leq 52^\circ$, we computed a maximum plausible range for the deprojected distance of the clump from the nucleus of $3.6 \leq d \leq 6.2$ kpc, beyond the galaxy's effective radius $R_e = 2.8 \pm 0.4$ kpc (Extended Data Table 1). We did not account for the disk's thickness: this uncertain correction could imply a larger deprojected distance by 10–15% (for a typical thickness of a few hundred parsecs).

Dust reddening. Estimating emission line luminosities and SFRs requires corrections for dust extinction (although this is less relevant for emission-line EWs, which are affected only by the differential line versus continuum reddening). We used stellar population modelling of the ultraviolet-to-near-infrared galaxy SED⁴⁴, assuming the reddening law in ref. 45 and constant star formation histories (SFHs) to measure the stellar continuum reddening. We converted this measure into nebular reddening by using $E(B-V)_{\text{nebular}} = E(B-V)_{\text{continuum}}/0.83$ (ref. 46), obtaining $E(B-V)_{\text{nebular}} = 0.30_{-0.07}^{+0.09}$. Independent estimates of the nebular reddening were also obtained on the basis of emission line ratios: H α /H β , assuming case B recombination conditions⁴⁷; [O II]/H α , assuming an intrinsic ratio of 1 (ref. 48), and [O II]/H β , with an intrinsic ratio estimated by following the previous points. For these estimates we used H α fluxes from MOIRCS, [O II] from WFC3, and H β from the weighted average of MOIRCS and WFC3, obtaining $E(B-V)_{\text{H}\alpha/\text{H}\beta} = 0.24 \pm 0.12$, $E(B-V)_{\text{[O II]/H}\alpha} = 0.32 \pm 0.11$, and $E(B-V)_{\text{[O II]/H}\beta} = 0.40 \pm 0.25$. The average of these estimates is nearly identical to that from the stellar continuum. We therefore adopt $E(B-V)_{\text{nebular}} = 0.30$.

For the clump, a reddening estimate can be obtained by using WFC3, from the ratio of the [O II] and H β line fluxes. We derived a fairly noisy measurement consistent with that of the whole galaxy ($E(B-V)_{\text{[O II]/H}\beta, \text{clump}} = 0.24 \pm 0.37$). Although formally this is also consistent with zero attenuation towards the clump, it is unlikely because the galaxy is highly inclined. To improve the estimate of the reddening affecting the clump, we attempted a derivation of the H α flux of the clump in the MOIRCS data, decomposing the two-dimensional spectrum with a PSF-like component for the clump and a single Sérsic profile accounting for the host galaxy disk, finding $H\alpha = (7 \pm 2) \times 10^{-17}$ erg s⁻¹ cm⁻², $\sim 50\%$ of the galaxy's H α emission³⁵. By averaging the reddening estimates from H α /H β , H α /[O II] and [O II]/H β , we obtained $E(B-V)_{\text{nebular,clump}} = 0.55 \pm 0.20$, consistent with the reddening of the host galaxy. We thus assumed that the clump nebular reddening was identical to that of the parent galaxy, which is consistent with the literature⁴⁹. Extended Data Fig. 2 shows the observed F606W/F105W ratio, probing the stellar continuum reddening, which is homogeneous over the galaxy. The optical attenuation (A_V) at the clump position is similar to that at the galaxy nucleus within 0.1–0.2 mag, and is close to the galaxy average. The position of the galaxy nucleus (measured as the light barycentre, light peak or with GALFIT) is stable and does not change with wavelength from F606W to F105W and F140W. The [O III] and F105W continuum should be affected by a similar attenuation and much less than the F606W continuum. Together with the flatness of the reddening map, this demonstrates that the clump emission lines were not an artefact due to modification of the galaxy nucleus position by reddening, because an even stronger effect would have been seen in F606W. Correcting the emission line maps and the imaging for reddening does not significantly alter the nucleus-clump distance.

Adopting the extinction law in ref. 50 (see ref. 51 for example) would produce reddening values $\lesssim 15\%$ higher, consistent within the uncertainties.

Discarding the active galactic nucleus, shock, transient, and low-metallicity region hypotheses. The galaxy has three Chandra photons (one soft and two hard; $\sim 2\sigma$ detection) in 146 ks data, giving $L_{2-10\text{ keV}} \approx 2.9 \times 10^{42} \text{ erg s}^{-1}$ (photon index $\Gamma = 1.8$). This is tenfold the value expected from galaxy star formation⁵². If an active galactic nucleus (AGN) were present, it would produce⁵³ an [O III] luminosity ~ 20 -fold fainter than that of the clump. In Extended Data Fig. 6 both the entire galaxy and the clump are located in the BPT diagram⁵⁴ (we conservatively use $[\text{N II}]_{\text{clump}} \lesssim [\text{N II}]_{\text{galaxy}}$). The emission line ratios are consistent with star-forming galaxies at $z \approx 2$ (ref. 51). The $[\text{O III}]/[\text{N II}] < 2.8$ upper limit is also much lower than typically observed in type 1 AGNs⁵⁵. The high EW further disfavours the hypothesis of an off-nuclear AGN, because AGNs typically have $\text{EW}_{[\text{O III}]} < 500 \text{ \AA}$ (ref. 56). Besides, no AGN signature was found from the galaxy's SED, and no excess possibly arising from nuclear accretion was detected in our deep 24 μm Spitzer, Herschel and VLA data.

The clump's emission-line luminosity is comparable with that of the whole galaxy, so it cannot be due to shock from external outflows impacting the gas. The host SFR would generate ~ 30 -fold weaker galaxy-integrated, shock-excited line luminosities⁵⁷. The brightest shock-powered off-nuclear clouds in local infrared luminous galaxies are >50 -fold weaker⁵⁸. Explicit calculations⁵⁹ for $z = 2$ galaxies, using appropriate wind mass loads^{60,61} and velocities⁶², lead to analogous conclusions. The kinetic energy available in winds cannot account for the clump line luminosities.

There is no evidence for substantial line luminosities variability over a ~ 3 -year timescale. HST/WFC3 G141 spectroscopy was obtained in June and July 2010, and MOIRCS spectroscopy in April 2013 (Extended Data Table 2). Despite their lower resolution (0.6" seeing), MOIRCS spectra show the bright, compact [O III] and H α emissions from the clump, with a consistent flux.

Low-mass ($< 10^9 M_{\odot}$), very metal-poor galaxies ($Z \approx 0.1 Z_{\odot}$) can display extremely high EW emission lines⁶³. Our target is substantially more massive and metal rich: using the [O III]/[O II] ratio we estimated⁶⁴ $Z \approx (0.4 \pm 0.1) Z_{\odot}$ and $Z \approx (0.6 \pm 0.2) Z_{\odot}$, for the clump and the galaxy, respectively (Extended Data Fig. 4 and Extended Data Table 1).

Constraining the age of the clump. We computed the time evolution of the H β EW by using stellar population synthesis models⁴³, adopting $Z = 0.4 Z_{\odot}$, a Salpeter⁶⁵ initial mass function and three different SFHs: an instantaneous burst, constant star formation and a SFH obtained from our hydrodynamic simulations (Fig. 3). All models show high EWs at young ages ($\log(\text{EW}) > \sim 2$, independently of the SFH), which decrease quickly for the instantaneous burst and more smoothly in the other cases. We converted the H β EW into the expected [O III] and [O II] EWs (Fig. 2), assuming the [O III]/H β ratio of $z = 2$ star-forming galaxies⁵¹ and an H α /[O II] luminosity ratio of 1 (ref. 48). Comparison of these values with the EW lower limits yielded an age of < 10 Myr for the clump (Fig. 2).

The directly measured continuum upper limits (rather than the more stringent ones from synthetic spectra; Extended Data Fig. 5), give an age of $\lesssim 15$ Myr. Decreasing the adopted $E(B-V)$ reddening by 0.1 dex would decrease the line EW lower limits by only ~ 0.05 dex but would increase the $L_{\text{H}\beta}/L_{1,500}$ limit by ~ 0.1 dex, therefore hardly affecting the age constraints. Changing the metallicity by 1.6 dex produces only a 0.2 dex age difference. Similarly, the age remains unchanged by adopting, for example, a Kroupa⁶⁶ or a Scalo⁶⁷ initial mass function, and a top-heavy one produces EWs 0.2 dex higher.

SFR estimate. The SFR of the whole galaxy was determined from the total H α luminosity from the MOIRCS spectroscopy, assuming the standard Kennicutt conversion⁶⁸, resulting in $(77 \pm 9) M_{\odot} \text{ yr}^{-1}$, in agreement with that from SED fitting ($\sim 85 M_{\odot} \text{ yr}^{-1}$ with an uncertainty of 0.2 dex; Extended Data Table 1).

The time-dependent conversion of line luminosity to SFR at young ages was computed with Starburst99, adopting the SFH from our numerical simulations (Extended Data Fig. 7). At $t = 10$ Myr this is 20% higher than from the Kennicutt conversion. By averaging the estimates from H β , [O II] and H α we obtained $\text{SFR} = (32 \pm 6) M_{\odot} \text{ yr}^{-1}$ for the clump, where the error includes the uncertainties associated with emission-line luminosities and reddening.

Stellar mass estimate. Assuming the average mass-to-light ratio (M/L) of the host galaxy (Extended Data Fig. 2), the flux upper limit on the continuum emission of the clump implies $M_{\star} \lesssim 3 \times 10^8 M_{\odot}$. Using the M/L ratio from the clump SFH (Extended Data Fig. 7) gives $M_{\star} \lesssim 2.1 \times 10^8 M_{\odot}$. Normalizing the simulations to the observed H β luminosity yields $M_{\star} \approx 3.9 \times 10^8 M_{\odot}$, which is consistent with the previous estimates given the uncertainties (a factor ~ 2 , mainly due to the gas fraction of simulated galaxies and the details of feedback and stellar mass loss modelling at small scales; note that the simulated clumps seem on average to be slightly less massive than our observed one, but their observed physical properties and time behaviour are self-similar).

Gas mass estimate. We inferred an upper limit to the gas mass in the clump from the Jeans mass (M_J) of the galaxy, which is close to the maximum mass of gas that can collapse in a rotation disk^{2,9,69,70}. Assuming a reasonable upper limit for the typical gas velocity dispersion in high- z disk galaxies ($\sigma_v \lesssim 80 \text{ km s}^{-1}$ (refs 21, 22)), we obtained $M_{\text{gas}} \lesssim M_J = 2.5 \times 10^9 M_{\odot}$. Using the $M_{\text{gas}}/\text{H}\beta$ ratio from simulations leads to a gas mass of $M_{\text{gas}} \approx 2.7 \times 10^9 M_{\odot}$. Comparison with older clumps from the literature¹³, using our numerical simulations to relate the physical properties at the 'peak' and later phases, yields

$$M_{\text{gas,clump}} = \frac{\text{SFR}_{\text{clump}}}{\text{SFR}_{\text{lit}}} M_{\star,\text{lit}} \left(\frac{M_{\text{gas,young}}}{M_{\star,\text{old}}} \right)_{\text{sim}} \left(\frac{\text{SFR}_{\text{young}}}{\text{SFR}_{\text{old}}} \right)_{\text{sim}}$$

where SFR_{lit} and $M_{\star,\text{lit}}$ refer to older clumps reported in the literature; $M_{\star,\text{old,sim}}$ and $\text{SFR}_{\text{old,sim}}$ are for old clumps in the simulations, and $M_{\text{gas,young,sim}}$ and $\text{SFR}_{\text{young,sim}}$ are computed at $t = 10$ Myr, as our young clump. This approach leads to $M_{\text{gas}} = 3 \times 10^9 M_{\odot} \pm 0.2$ dex, consistent with the independent estimates discussed above. This agreement supports SFHs with an initial burst as predicted by our simulations.

The Schmidt–Kennicutt relation can be used to provide alternative estimates, on the basis of the clump SFR. The relation for Main Sequence galaxies would imply that $\sim 50\%$ of the total gas in the galaxy is collapsing in an ultra-compact region, which seems hardly believable, confirming that this young clump has a higher SFE. Assuming instead the starburst-like relation, we obtained $M_{\text{gas}} = 2 \times 10^9 \pm 0.36 \text{ dex} M_{\odot}$, consistent with the previous estimates.

Considering an even younger age for the clump, as permitted by the upper limit $t < 10$ Myr, would return higher absolute and specific SFRs (Extended Data Fig. 7; that is, higher $\text{SFR}/L_{\text{H}\beta}$), confirming the starburst behaviour of the clump during the formation phase.

Dynamical time estimate. By measuring the full-width at half-maximum (FWHM) of the H α line detected in the MOIRCS longslit spectroscopic data, we determined a first upper limit on the gas velocity of the clump $v_{\text{FWHM}} \lesssim 450 \text{ km s}^{-1}$ (the MOIRCS instrumental resolution). Given the upper limits on the radius of the clump ($R < 500 \text{ pc}$) and on its dynamical mass ($M_{\text{dyn}} = M_{\text{gas}} + M_{\star} \lesssim 2.8 \times 10^9 M_{\odot}$), we then refined our estimate to $v_{\text{FWHM}} < \sqrt{(M_{\text{dyn}} G/R)} \approx 200 \text{ km s}^{-1}$ (where G is the gravitational constant), consistent with clump velocities typically observed in high-redshift galaxies¹⁷. This leads to a dynamical timescale $t_{\text{dyn}} = 2\pi R/(v_{\text{FWHM}}/2) \approx 29$ Myr, in reasonable agreement with the free-fall time of the clump $t_{\text{ff}} \approx \sqrt{(R^3/M_{\text{dyn}})} \approx 17$ Myr.

Clump formation rate and lifetime. The visibility window of the young phase can be defined as the time during which the EW is above a given threshold, as predicted by stellar population synthesis models. For our clump this ranges between ~ 5 Myr (instantaneous burst) and ~ 10 Myr for SFH from simulations. We used an average visibility window of 7 Myr.

Knowing the visibility window and the observed number of 'formation events' per galaxy, the 'clump formation rate' can be estimated; comparing it with the average number of descendants observable per galaxy (virtually all old) yields the average lifetime of the clumps.

We considered all galaxies in our survey with, first, $M_{\star} > 8.5 \times 10^9 M_{\odot}$ (mass completeness, coinciding with the minimum mass that a galaxy should have to host such a massive clump assuming a gas fraction of $\sim 50\%$); second, $M_{\star} < 2 \times 10^{11} M_{\odot}$ ([O III] emission becomes too weak at higher masses⁷¹); and third, a redshift $1.2 < z < 2.4$ ([O III] emission lying inside the wavelength range of the grism). In this way 57 galaxies were selected. With one 'forming clump' detected, this corresponds to a 'clump formation rate' of 2.5 Gyr^{-1} per galaxy.

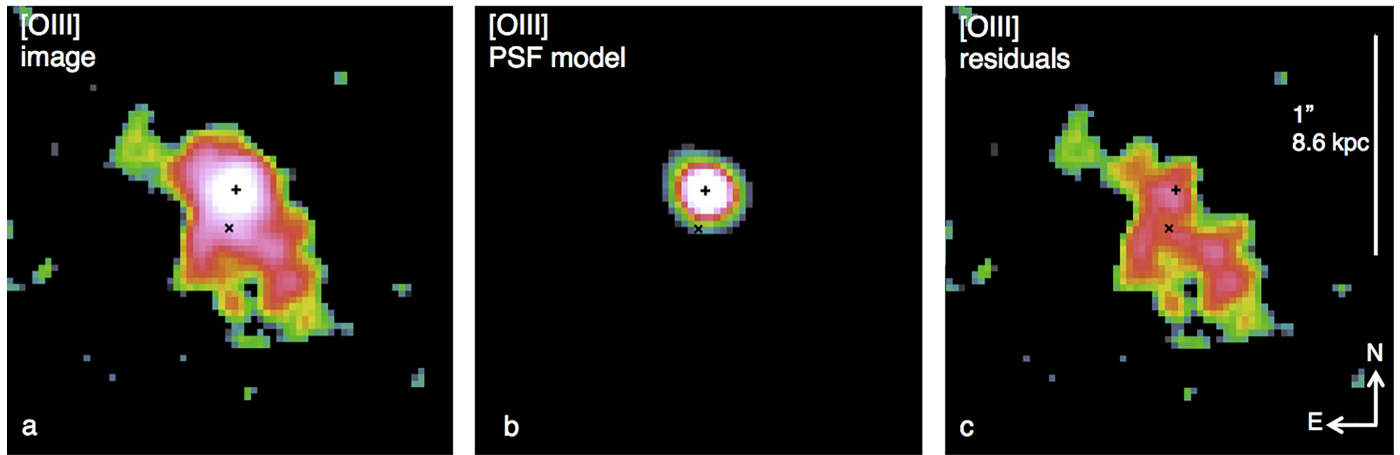
We considered that in our survey we would have detected all formation events of clumps with $M_{\text{gas}} \gtrsim 2.5 \times 10^9 M_{\odot}$. Considering that almost all the initial gas mass of a given clump is consumed at initial stages to form stars, the clump stellar mass at late stages can be approximated to the gas mass at initial collapse, independently of the age of the clump, as supported by our numerical simulations. Typically there are about one or two clumps per galaxy above this mass threshold^{13,17,18}, giving an average lifetime of 500 Myr.

To compute the (large) associated uncertainty, we considered the Poisson error associated with our single object discovery, the Poisson error for older clumps from the literature, and the visibility window uncertainty. The asymmetric 1σ uncertainties that we inferred are $+0.74$ dex and -0.55 dex. The lower envelope of the 1σ range of the lifetime estimate is not far from the upper range of lifetimes suggested by models in which clumps undergo strong feedback (50–100 Myr). However, our estimate is probably a lower limit. The derived lifetime could be affected by a 'discovery bias', because other high-redshift spectroscopic surveys (such as SINS and 3D-HST) have not yet reported the observation of a similar giant young clump. Furthermore, there are indications³⁵ that our target galaxy is living in a gas-enriched environment, which could also have anomalously increased the SFR and thus the 'clump formation rate'. This suggests that the observation of a newly formed giant clump could be an even rarer event than

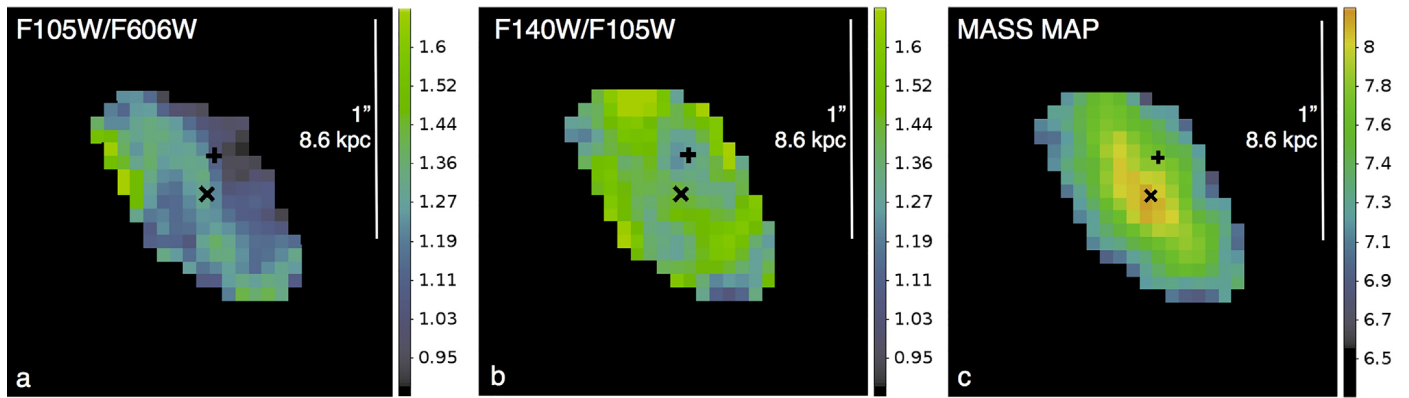
suggested by our data, and that the true average clump lifetime could be longer than estimated here.

Code availability. The RAMSES code used to generate our simulations is available at <http://www.ics.uzh.ch/~teyssier/ramses>.

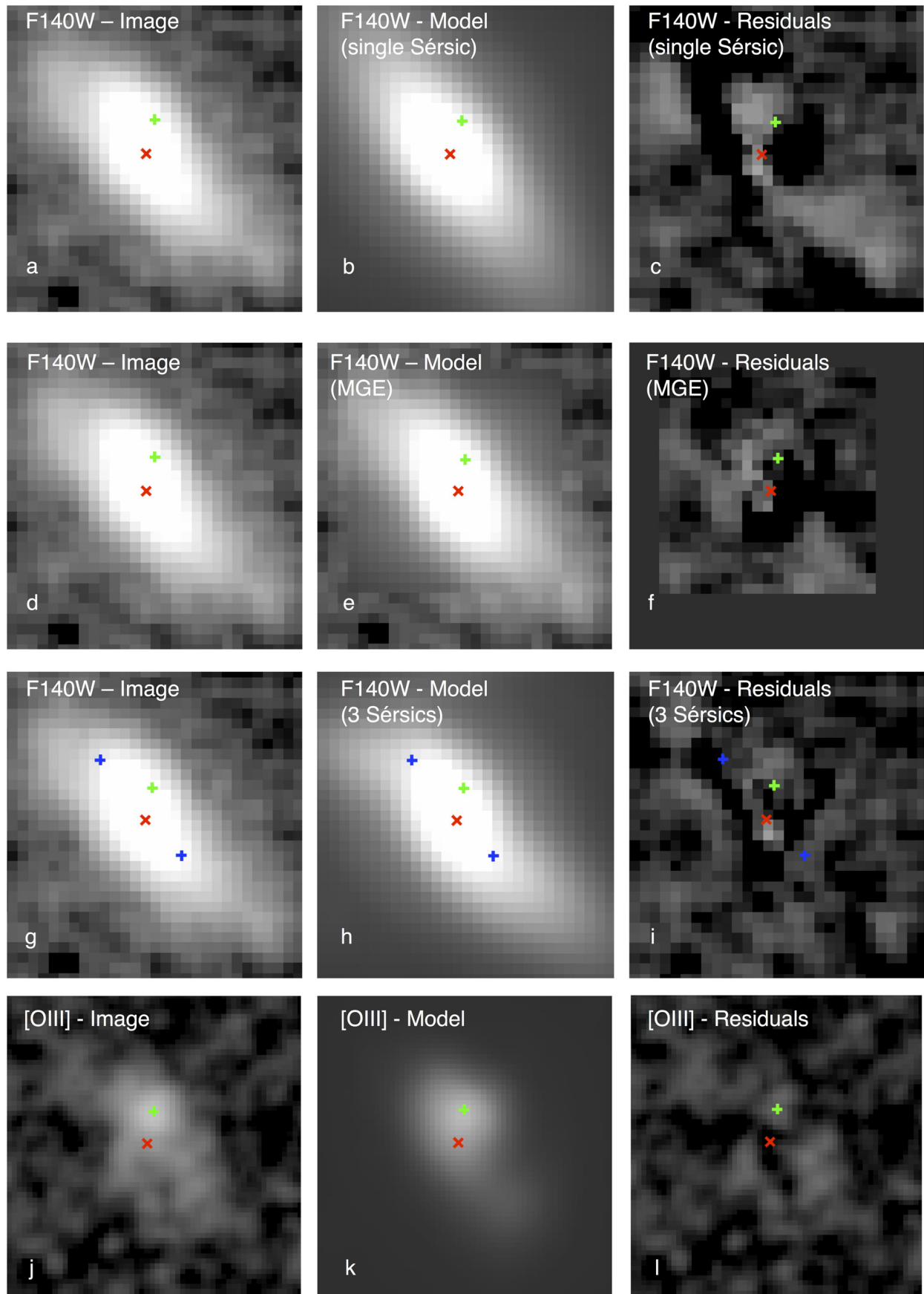
31. Kümmel, M. *et al.* The slitless spectroscopy data extraction software. *Publ. Astron. Soc. Pacif.* **121**, 59–72 (2009).
32. van Dokkum, P. *et al.* Cosmic-ray rejection by Laplacian edge detection. *Publ. Astron. Soc. Pacif.* **113**, 1420–1427 (2001).
33. Bertin, E. & Arnouts, S. SExtractor: software of source extraction. *Astron. Astrophys.* **117** (Suppl.), 393–404 (1996).
34. Fruchter, A. S. & Hook, R. N. Drizzle: a method for the linear reconstruction of undersampled images. *Publ. Astron. Soc. Pacif.* **114**, 144–152 (2002).
35. Valentino, F. *et al.* Metal deficiency in cluster star-forming galaxies at $z=2$. *Astrophys. J.* **801**, 132–150 (2015).
36. Peng, C. Y. *et al.* Detailed decomposition of galaxy images. II. Beyond axisymmetric models. *Astron. J.* **139**, 2097–2129 (2010).
37. Sérsic, J. L. Influence of the atmospheric and instrumental dispersion on the brightness distribution in a galaxy. *Bol. Asoc. Argentina Astron.* **6**, 41–43 (1963).
38. Cappellari, M. Efficient multi-Gaussian expansion of galaxies. *Mon. Not. R. Astron. Soc.* **333**, 400–410 (2002).
39. Conselice, C. J. The relationship between stellar light distributions of galaxies and their formation histories. *Astrophys. J.* **147** (Suppl.), 1–28 (2003).
40. Lotz, J. M. *et al.* A new non-parametric approach to galaxy morphological classification. *Astron. J.* **128**, 163–182 (2004).
41. Cibinel, A. *et al.* A physical approach to the identification of high- z mergers: morphological classification in the stellar mass domain. *Astrophys. J.* (in the press); preprint at <http://arxiv.org/abs/1503.06220>.
42. Perret, V. *et al.* Evolution of the mass, size, and star formation rate in high redshift merging galaxies. *Astron. Astrophys.* **562**, 1–20 (2014).
43. Leitherer, C. *et al.* Starburst99: synthesis models for galaxies with active star formation. *Astrophys. J.* **123** (Suppl.), 3–40 (1999).
44. Strazzullo, V. *et al.* Galaxy evolution in overdense environments at high redshift: passive early-type galaxies in a cluster at $z \sim 2$. *Astrophys. J.* **772**, 118–135 (2013).
45. Calzetti, D. *et al.* The dust content and opacity of actively star-forming galaxies. *Astrophys. J.* **533**, 682–695 (2000).
46. Kashino, D. *et al.* The FMOS-COSMOS survey of star-forming galaxies at $z \sim 1.6$. I. $H\alpha$ based star formation rates and dust extinction. *Astrophys. J.* **777**, 8–14 (2013).
47. Osterbrock, D. E. *et al.* *Astrophysics of Gaseous Nebulae and Active Galactic Nuclei* (University Science Books, 1989).
48. Kewley, L. *et al.* [OII] as a star formation rate indicator. *Astron. J.* **127**, 2002–2030 (2004).
49. Elmegreen, D. M. *et al.* Resolved galaxies in the Hubble Ultra Deep Field: star formation in disks at high redshift. *Astrophys. J.* **658**, 763–777 (2007).
50. Cardelli, J. A., Clayton, G. C. & Mathis, J. S. The relationship between infrared, optical, and ultraviolet extinction. *Astrophys. J.* **345**, 245–256 (1989).
51. Steidel, C. C. *et al.* Strong nebular line ratios in the spectra of $z \sim 2$ –3 star-forming galaxies: first results from KBSS-MOSFIRE. *Astrophys. J.* **795**, 165–205 (2014).
52. Persic, M. *et al.* 2–10 keV luminosity of high-mass binaries as a gauge of ongoing star formation rate. *Astron. Astrophys.* **419**, 849–862 (2004).
53. Panessa, F. *et al.* On the X-ray, optical emission line and black hole mass properties of local Seyfert galaxies. *Astron. Astrophys.* **455**, 173–185 (2006).
54. Baldwin, J. A., Phillips, M. M. & Terlevich, R. Classification parameters for the emission-line spectra of extragalactic objects. *Publ. Astron. Soc. Pacif.* **93**, 5–19 (1981).
55. Stern, J. *et al.* Type 1 AGNs at low z . III. The optical narrow line ratios. *Mon. Not. R. Astron. Soc.* **431**, 836–857 (2013).
56. Caccianiga, A. *et al.* The relationship between [OIII] λ 5007Å equivalent width and obscuration in active galactic nuclei. *Mon. Not. R. Astron. Soc.* **415**, 1928–1934 (2011).
57. Hong, S. *et al.* Constraining stellar feedback: shock-ionized gas in nearby starburst galaxies. *Astrophys. J.* **777**, 63–83 (2013).
58. Soto, K. T. & Martin, C. L. Gas excitation in ULIRGs: maps of diagnostic emission-line ratios in space and velocity. *Astrophys. J. Suppl. Ser.* **203**, 3–13 (2012).
59. Binette, L., Dopita, M. A. & Tuohy, I. R. Radiative shock-wave theory. II. High-velocity shocks and thermal instabilities. *Astrophys. J.* **297**, 476–491 (1985).
60. Genzel, R. *et al.* Evidence for wide-spread active galactic nucleus-driven outflows in the most massive $z \sim 1$ –2 star-forming galaxies. *Astrophys. J.* **796**, 7–31 (2014).
61. Renaud, F. *et al.* A sub-parsec resolution simulation of the Milky Way: global structure of the interstellar medium and properties of molecular clouds. *Mon. Not. R. Astron. Soc.* **436**, 1836–1851 (2013).
62. Förster Schreiber, N. *et al.* The Sins/zC-Sinf survey of $z \sim 2$ galaxy kinematics: evidence for powerful active galactic nucleus-driven nuclear outflows in massive star-forming galaxies. *Astrophys. J.* **787**, 38–50 (2014).
63. Amorín, R. *et al.* Discovering extremely compact and metal-poor, star-forming dwarf galaxies out to $z \sim 0.9$ in the VIMOS Ultra-Deep survey. *Astron. Astrophys.* **568**, 8–16 (2014).
64. Maiolino, R. *et al.* AMAZE. I. The evolution of the mass-metallicity relation at $z > 3$. *Astron. Astrophys.* **488**, 463–479 (2008).
65. Salpeter, E. E. The luminosity function and stellar evolution. *Astrophys. J.* **121**, 161–167 (1955).
66. Kroupa, P. & Boily, C. M. On the mass function of star clusters. *Mon. Not. R. Astron. Soc.* **336**, 1188–1194 (2002).
67. Scalo, J. M. The stellar initial mass function. *Fundam. Cosm. Phys.* **11**, 1–278 (1986).
68. Kennicutt, R. C. The global Schmidt law in star-forming galaxies. *Astrophys. J.* **498**, 541–552 (1998).
69. Bournaud, F. & Elmegreen, B. Unstable disks at high redshift: evidence for smooth accretion in galaxy formation. *Astrophys. J.* **694**, 158–161 (2009).
70. Elmegreen, B. & Burkert, A. Accretion-driven turbulence and the transition to global instability in young galaxy disks. *Astrophys. J.* **712**, 294–302 (2010).
71. Zahid, H. J. *et al.* The universal relation of galactic chemical evolution: the origin of the mass–metallicity relation. *Astrophys. J.* **791**, 130–143 (2014).



Extended Data Figure 1 | GALFIT decomposition of the [O III] emission line map. a, b, [O III] map (a) and model of the point source component (b) for the clump. c, No strong residuals or artefacts are left after removal of the point source component. The positions of the nucleus and of the clump are shown as crosses.

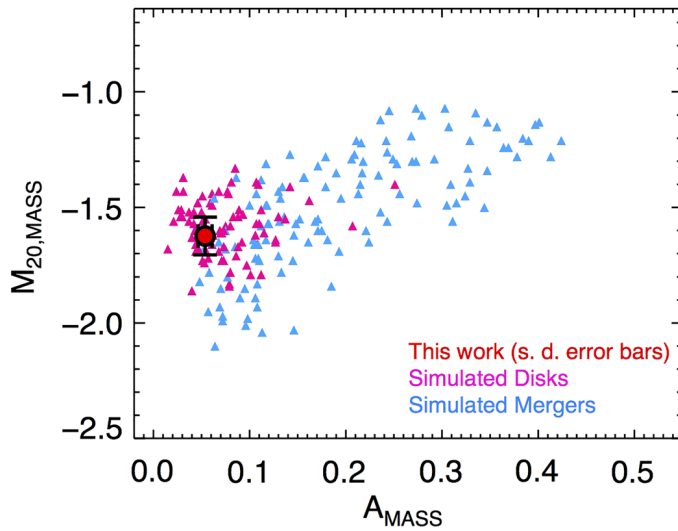


Extended Data Figure 2 | Image ratios and mass map. **a, b,** Ratio of F105W/F606W imaging in spectral flux density (F_ν) scale (**a**), a proxy for the dust reddening of the stellar continuum, and F140W/F105W imaging, sensitive to the M/L ratio (**b**). The positions of the nucleus and the clump are shown as crosses. The maps show only small variations: the observed F_ν ratios for the nucleus and clump positions are respectively 1.34 and 1.16 for F105W/F606W, and respectively 1.39 and 1.25 for F140W/F105W. Galaxy-wide ratios are respectively 1.27 and 1.37 for F105W/F606W and F140W/F105W. **c,** Mass map in units of M_\odot per pixel.

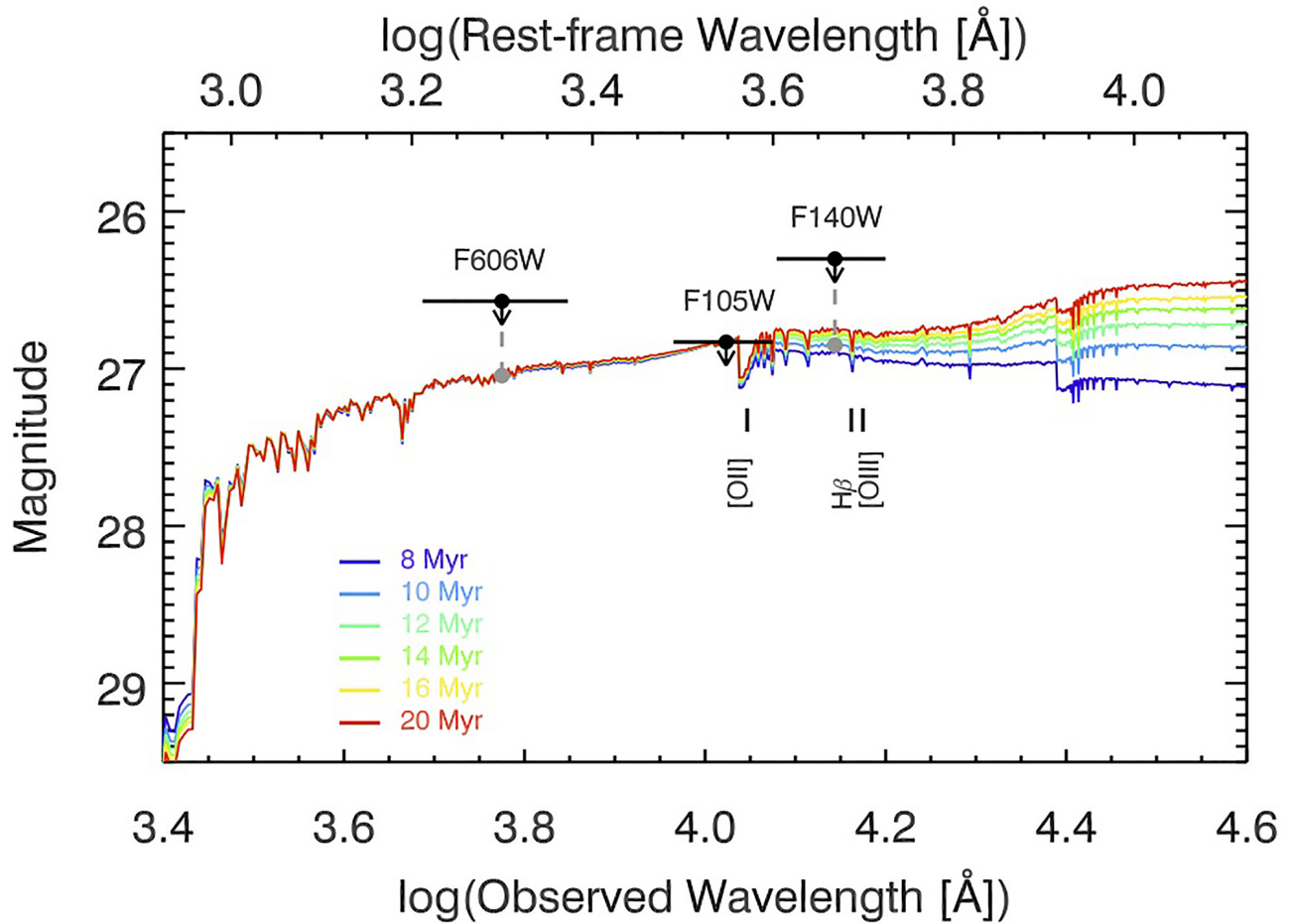


Extended Data Figure 3 | Modelling of the galaxy light profile. F140W direct image and [O III] emission line map (a, d, g, j), GALFIT models (b, e, h, k) and residuals (c, f, i, l). The first row shows the single Sérsic profile solution, the MGE model is in the second row, and our baseline model (the sum

of three Sérsic profiles, in which blue crosses mark the additional components) is in the third row. The red cross indicates the barycentre of the stellar light and the green cross marks the centre of the [O III] off-nuclear component.

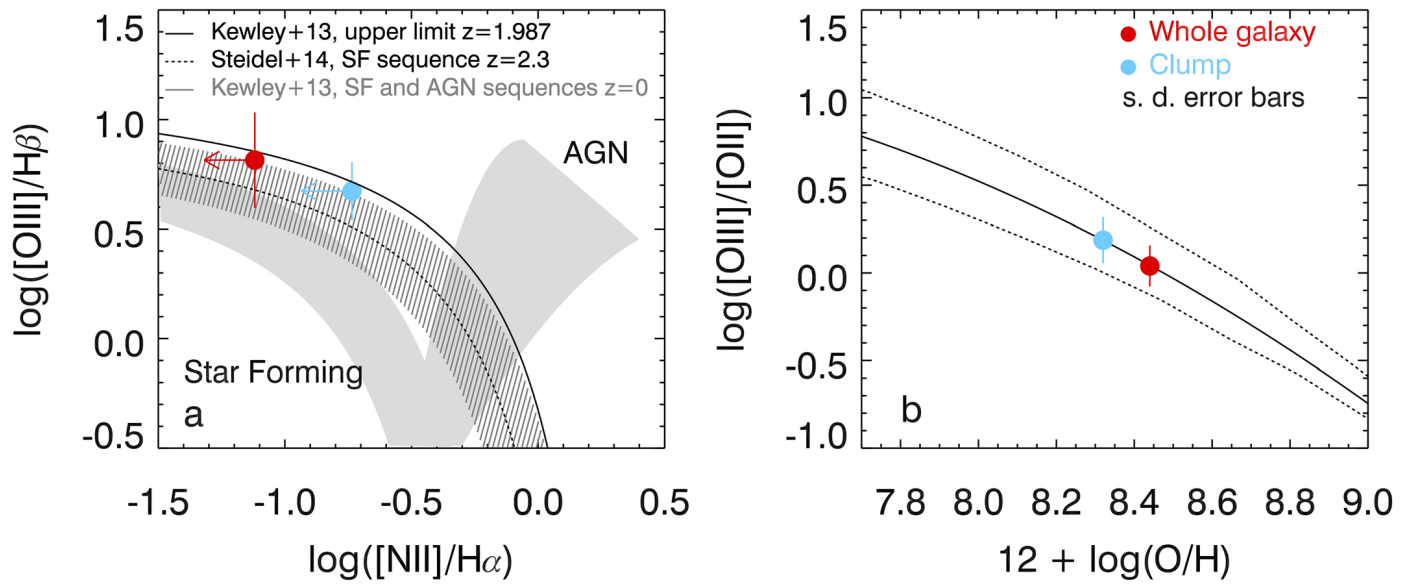


Extended Data Figure 4 | The Asymmetry and M_{20} morphological parameters as determined from the spatial distribution of the galaxy stellar mass. Pink and light blue triangles represent disks and mergers from MIRAGE numerical simulations⁴², respectively. The galaxy presented in this work (red filled circle with error bars indicating s.d.) is located in the typical region occupied by disk galaxies⁴¹; the vast majority of mergers have higher Asymmetry and/or M_{20} parameters. The figure shows the same number of mergers and disks even if mergers are expected to be a minority in optical samples.



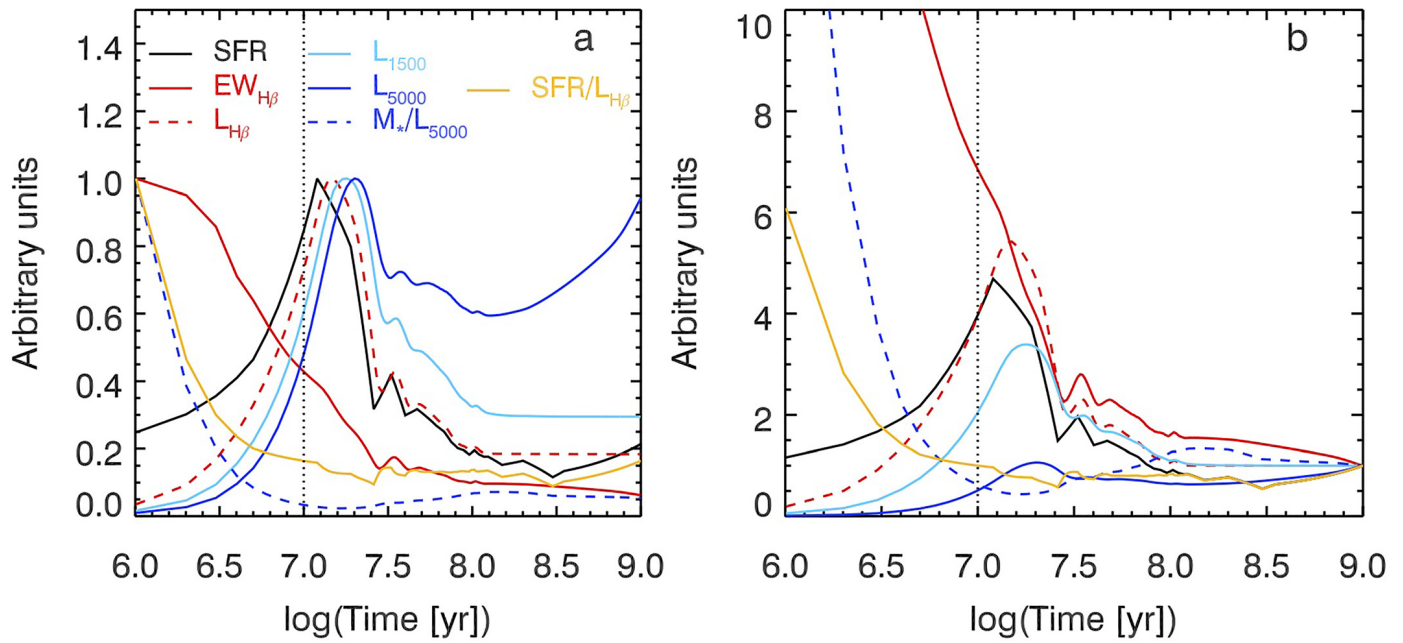
Extended Data Figure 5 | Upper limits to clump continuum flux. The observed flux upper limits estimated from simulations and GALFIT modelling in the three bands are shown as black filled circles. The black horizontal lines indicate the bandpass width of each filter. Coloured curves represent reddened

Starburst99 stellar population synthesis models⁴³ with different ages (from 8 to 20 Myr), normalized to the most stringent upper limit (F105W band). The corresponding upper limits in F140W and F606W, obtained considering a spectrum with an age ~ 10 Myr, are shown as grey filled circles.



Extended Data Figure 6 | Emission line diagnostics. **a**, BPT diagram⁵⁴ showing that the emission line ratios of the whole galaxy and of the clump (red and light-blue points with error bars indicating s.d.) are consistent with being powered by star formation. The $[\text{N II}]/\text{H}\alpha$ upper limit and $\text{H}\alpha$ emission of the whole

galaxy are measured from the Subaru/MOIRCS longslit spectroscopy follow-up, and the $[\text{N II}]/\text{H}\alpha$ upper limit for the clump is computed by assuming the $[\text{N II}]$ of the whole galaxy. **b**, Determination of the metallicities of the whole galaxy and that of the clump from the $[\text{O III}]/[\text{O II}]$ ratio⁶⁴.



Extended Data Figure 7 | Time evolution of physical quantities based on the clump $\text{SFR}(t)$ from our simulations. **a**, The peaks of all the curves normalized to 1 to highlight the time delay occurring between the peak of the SFR and of the luminosities $L_{\text{H}\beta}$, $L_{1,500 \text{ \AA}}$ and $L_{5,000 \text{ \AA}}$. **b**, Peaks normalized to 1 at $t = 1 \text{ Gyr}$ to stress the relative intensity of the observables at the peak and later phases. The

vertical black dotted line indicates the upper limit on the age of the clump ($t = 10 \text{ Myr}$). The units of the plotted quantities are: SFR ($M_{\odot} \text{ yr}^{-1}$), $\text{EW}_{\text{H}\beta}$ (\AA), $L_{\text{H}\beta}$, $L_{1,500 \text{ \AA}}$ and $L_{5,000 \text{ \AA}}$ (erg s^{-1}), $M_{\star}/L_{5,000 \text{ \AA}}$ ($M_{\odot} \text{ erg}^{-1} \text{ s}$) and $\text{SFR}/L_{\text{H}\beta}$ ($M_{\odot} \text{ yr}^{-1} \text{ erg}^{-1} \text{ s}$).

Extended Data Table 1 | Properties of the galaxy and the clump

	Galaxy (ID568)	Clump (Vyc1)
Right ascension [h m s]	14:49:12.578	14:49:12.575
Declination [° ' "]	+8:56:19.42	+8:56:19.62
R_e [kpc]	2.8 ± 0.4*	< 0.5
SFR [M _⊙ /yr]	77 ± 9	32 ± 6
log(M_★/M_⊙)	10.3 ^{+0.2} _{-0.3}	≲ 8.5
log(M_{gas}/M_⊙)	10.7 ± 0.2 [†]	≲ 9.4
Z [Z _⊙]	0.6 ± 0.2	0.4 ± 0.2
F_[OIII]^{obs} [10 ⁻¹⁷ erg s ⁻¹ cm ⁻²]	10.4 ± 0.7	4.3 ± 0.2
F_{Hβ}^{obs} [10 ⁻¹⁷ erg s ⁻¹ cm ⁻²]	1.5 ± 0.8	0.9 ± 0.3
F_[OII]^{obs} [10 ⁻¹⁷ erg s ⁻¹ cm ⁻²]	6.5 ± 1.7	1.9 ± 0.6
F_{F140W}^{obs} [10 ⁻²⁰ erg s ⁻¹ cm ⁻² Å ⁻¹]	67.5 ± 3.4 [‡]	< 1.1
F_{F105W}^{obs} [10 ⁻²⁰ erg s ⁻¹ cm ⁻² Å ⁻¹]	89.2 ± 4.6 [‡]	< 1.8
F_{F606W}^{obs} [10 ⁻²⁰ erg s ⁻¹ cm ⁻² Å ⁻¹]	212.3 ± 10.6 [‡]	< 4.5

*The effective radius of the galaxy is the average of the R_e obtained from a single Sérsic profile fit in the F140W, F105W and F606W imaging.†The gas mass of the galaxy has been determined, given its SFR, as M_{gas} = 9.18 + 0.83 log(SFR) (ref. 29).

‡The observed fluxes of the F140W, F105W and F606W direct images were determined with GALFIT. We associated a standard uncertainty of 5% with the results.

Extended Data Table 2 | HST/WFC3 and Subaru/MOIRCS observations

Instrument	Date	Time (direct imaging) (hr)	Time (spectroscopy) (hr)
<i>HST</i> /WFC3	2010, 6 th June	0.3 (F140W)	2.7
<i>HST</i> /WFC3	2010, 25 th June, 1 st July	0.6 (F140W)	7
<i>HST</i> /WFC3	2010, 9 th July	0.3 (F140W)	2.7
<i>HST</i> /WFC3	2013, 20 th May	3.3 (F105W)	-
<i>HST</i> /WFC3	2013, 20 th May	0.3 (F606W)	-
Subaru/MOIRCS	2013, 7 th - 9 th April	-	7.3



THE ROLE OF QUENCHING TIME IN THE EVOLUTION OF THE MASS–SIZE RELATION OF PASSIVE GALAXIES FROM THE WISP SURVEY*

A. ZANELLA^{1,2,3}, C. SCARLATA¹, E. M. CORSINI^{2,4}, A. G. BEDREGAL⁵, E. DALLA BONTÀ^{2,4}, H. ATEK⁶, A. J. BUNKER^{7,8}, J. COLBERT⁹, Y. S. DAI¹⁰, A. HENRY^{11,16}, M. MALKAN¹², C. MARTIN¹³, M. RAFELSKI^{11,16}, M. J. RUTKOWSKI¹, B. SIANA¹⁴, AND H. TEPLITZ¹⁵

¹ Minnesota Institute for Astrophysics, University of Minnesota, Minneapolis MN 55455, USA; anita.zanella@cea.fr

² Dipartimento di Fisica e Astronomia “G. Galilei,” Università di Padova, vicolo dell’Osservatorio 3, I-35122 Padova, Italy

³ Laboratoire AIM, CEA/DSM-CNRS-Université Paris Diderot, Irfu/Service d’Astrophysique, CEA Saclay, Orme des Merisiers, F-91191 Gif-sur-Yvette Cedex, France

⁴ INAF—Osservatorio Astronomico di Padova, vicolo dell’Osservatorio 5, I-35122, Padova, Italy

⁵ Department of Physics and Astronomy, Tufts University, Medford, MA 02155, USA

⁶ Spitzer Science Center, Caltech, Pasadena, CA 91125, USA

⁷ Department of Physics, University of Oxford, Denys Wilkinson Building, Keble Road, Oxford, OX13RH, UK

⁸ Affiliate Member, Kavli Institute for the Physics and Mathematics of the universe, 5-1-5 Kashiwanoha, Kashiwa, 277-8583, Japan

⁹ Harvard-Smithsonian Center for Astrophysics, 60 Garden Street, Cambridge, MA 02138, USA

¹⁰ Infrared Processing and Analysis Center, 770 South Wilson Avenue, Pasadena, CA 91125, USA

¹¹ Goddard Space Flight Center, Code 665, Greenbelt, MD 20771, USA

¹² Department of Physics & Astronomy, University of California Los Angeles, Los Angeles, CA 90095, USA

¹³ Department of Physics, University of California, Santa Barbara, CA, 93106, USA; cmartin@physics.ucsb.edu

¹⁴ Department of Physics & Astronomy, University of California Riverside, Riverside, CA 92521, USA

¹⁵ Infrared Processing and Analysis Center, Caltech, Pasadena, CA 91125, USA

Received 2015 April 28; accepted 2016 March 31; published 2016 June 14

ABSTRACT

We analyze how passive galaxies at $z \sim 1.5$ populate the mass–size plane as a function of their stellar age, to understand if the observed size growth with time can be explained with the appearance of larger quenched galaxies at lower redshift. We use a sample of 32 passive galaxies extracted from the Wide Field Camera 3 Infrared Spectroscopic Parallel (WISP) survey with spectroscopic redshift $1.3 \lesssim z \lesssim 2.05$, specific star formation rates lower than 0.01 Gyr^{-1} , and stellar masses above $4.5 \times 10^{10} M_{\odot}$. All galaxies have spectrally determined stellar ages from fitting of their rest-frame optical spectra and photometry with stellar population models. When dividing our sample into young (age $\leq 2.1 \text{ Gyr}$) and old (age $> 2.1 \text{ Gyr}$) galaxies we do not find a significant trend in the distributions of the difference between the observed radius and that predicted by the mass–size relation. This result indicates that the relation between the galaxy age and its distance from the mass–size relation, if it exists, is rather shallow, with a slope $\alpha \gtrsim -0.6$. At face value, this finding suggests that multiple dry and/or wet minor mergers, rather than the appearance of newly quenched galaxies, are mainly responsible for the observed time evolution of the mass–size relation in passive galaxies.

Key words: galaxies: evolution – galaxies: fundamental parameters – galaxies: high-redshift – galaxies: structure

1. INTRODUCTION

In recent years many efforts have been devoted to observing early-type galaxies (ETGs) at high redshift to understand how these objects assembled, evolved, and became quenched. The discovery of a widespread population of passively evolving ETGs at redshift $z > 1.5$ showed that the star formation quenching in massive galaxies was already under way by $z \sim 2$ (e.g., Mancini et al. 2010). A large fraction of these high redshift passive galaxies show effective radii between a factor of 2 and 5 smaller than local counterparts of comparable stellar masses (e.g., Daddi et al. 2005). This result has been confirmed by several studies (e.g., Trujillo et al. 2007; Cimatti et al. 2008; Cassata et al. 2010; Carollo et al. 2013; van der Wel et al. 2014), and found to be robust with respect to bias against low surface brightness at high redshifts (e.g., Valentinuzzi et al. 2010). In the local universe, ETGs with similar stellar densities appear to be quite rare (Trujillo et al. 2009; Poggianti et al. 2012), although it has been suggested that they could

have survived as the cores of present-day massive spheroids (Hopkins et al. 2009; van Dokkum et al. 2014).

This discovery has ignited an important debate. The problem is not the existence of these compact ETGs: $z \sim 3$ submillimeter galaxies have comparable masses, sizes and number density, and have been identified as their possible precursors (e.g., Cimatti et al. 2008; Bedregal et al. 2013). The open issue is how these high- z compact galaxies can evolve to their present form, inflating their sizes up to a factor of 4, while at the same time following the tight correlations observed in the local universe (e.g., the fundamental plane).

Various mechanisms have been suggested to explain the growth of ETGs with time, although observations are still inconclusive as to which of them may be favorable. One of the most popular mechanisms invokes the accretion of multiple small satellites (e.g., Naab et al. 2009). These minor mergers leave the mass of the main galaxy relatively unchanged, while completely disrupting the satellites through strong tidal interactions. The accretion of stripped infalling stellar material is expected to increase the size of the merger remnant, without igniting intense star formation, particularly if the satellites do not contain large amounts of gas (e.g., Hopkins et al. 2009;

* Based on observations with the NASA/ESA *Hubble Space Telescope*, obtained at the Space Telescope Science Institute, which is operated by AURA, Inc., under NASA contract NAS 5-26555.

¹⁶ NASA Postdoctoral Program Fellow.

Oser et al. 2012). Some observational studies suggest that this mechanism may account for $\sim 50\%$ of the apparent size evolution, at least at redshift $0 < z < 1$ (López-Sanjuan et al. 2012; Newman et al. 2012). Despite the implications of these observational results, there is a problem explaining the size evolution with multiple minor mergers. Nipoti et al. (2012) found that multiple minor mergers would introduce more scatter than observed in the low-redshift scaling relations that link the galaxy stellar mass, effective radius and velocity dispersion, unless the progenitors were already finely tuned to occupy a very tight region in the mass–radius plane. Such fine tuning is difficult to explain, and leaves open the question of *when* and *how* the mass–size relation is first created. Moreover, Hopkins et al. (2009) highlighted that in the merging scenario a non-negligible fraction of compact galaxies ($\lesssim 10\%$) should survive to $z \sim 0$, while observations by Trujillo et al. (2009) show that only 0.03% of local galaxies have stellar densities comparable to those of high redshift ETGs.

Adiabatic expansion through significant mass loss can also lead to size growth (Fan et al. 2010). A galaxy that loses mass as a result of supernova/AGN-driven winds will adjust its size in response to the shallower central potential (Newman et al. 2012). This mechanism would induce a sort of “puffing-up” of the galaxy arising from the loss of baryonic mass, with an effective size increase. However, the puffing-up only occurs when the system is highly active and young (in terms of its stellar population, Ragone-Figueroa & Granato 2011), and produces a fast expansion (a few dynamical times, $\sim 10^8$ years). Thus one would expect only a minority of objects to be passive and compact, at odds with observations.

The problem has also been explored from a different perspective (the so called “progenitor bias” scenario): instead of explaining the evolution of the mass–size relation with the growth of *individual* galaxies with time, it has been suggested that it is the *population* of ETGs that changes, with larger quenched galaxies appearing later (Valentinuzzi et al. 2010; Saracco et al. 2011; Cassata et al. 2013). This may be linked to the evolution of the average density in the universe due to Hubble expansion, with lower density halos collapsing later in time than denser ones (e.g., Saracco et al. 2011; Carollo et al. 2013). However, the relative importance of the two mechanisms (individual versus population growth) is still highly controversial (Bernardi et al. 2010; Cassata et al. 2011; Poggianti et al. 2013; van der Wel et al. 2014; Belli et al. 2015; Keating et al. 2015). If the redshift evolution of the mass–size relation is due to the appearance of newly quenched large galaxies, then one would expect that, at any given mass and time, the larger galaxies should on average be younger than the smaller ones. Here we test this prediction using a sample of $z \sim 1.5$ passive ETGs observed as part of the Wide Field Camera 3 (WFC3) Infrared Spectroscopic Parallel (WISP) survey (Atek et al. 2010).

Throughout the paper we assume a flat cosmology with $H_0 = 70 \text{ km s}^{-1} \text{ Mpc}^{-1}$, $\Omega_M = 0.3$, and $\Omega_\Lambda = 0.7$. Photometric magnitudes are expressed in the AB system (Oke & Gunn 1983).

2. OBSERVATIONS AND DATA ANALYSIS

The sample presented in this work includes 34 passive galaxies identified in the WISP survey, a pure-parallel *Hubble Space Telescope* (HST) program to obtain near-infrared slitless spectra together with optical and infrared (IR) imaging of

hundreds of independent fields in the sky. The data have been presented in detail in Atek et al. (2010). Briefly, we consider here the first 27 fields observed with both HST WFC3 grisms (G102, and G141; with resolving power $R = 210$ and 130, respectively), as well as with the WFC3-UVIS camera in the optical. The IR spectra cover the wavelength range between $0.85 \leq \lambda \leq 1.6 \mu\text{m}$, with approximately $0.1 \mu\text{m}$ overlap between the two grisms that allows us, together with the IR imaging, to check for proper photometric calibration and sky subtraction. The data were reduced and the spectra extracted with a combination of a custom pipeline described in Atek et al. (2010) and the aXe software (Kümmel et al. 2009). In addition, we implemented a new cleaning algorithm to properly account for contamination from overlapping spectra (see details in Bedregal et al. 2013). The imaging was obtained with the F475X and F600LP (apart from the two deepest fields that were observed with F606W and F814W instead), and with the F110W and F160W filters, respectively (see Bedregal et al. 2013).

Bedregal et al. (2013) studied the properties of a sample of $H < 23$ mag galaxies preselected on the basis of their $J-H$ color. They measured spectroscopic redshifts and stellar population properties of the galaxies by simultaneously fitting the broadband photometric points and spectra. Here we present the size measurements for the subsample of passive galaxies selected to have a specific star formation rate $\text{sSFR} \lesssim 0.01 \text{ Gyr}^{-1}$, redshift $z > 1.3$ and $M_* > 4.5 \times 10^{10} M_\odot$. This is the minimum stellar mass measurable at $z \sim 1.5$ (the average redshift of the sample), for a maximally old stellar population model (SPM). These limits have been chosen to select a sample of massive and passive galaxies and their robustness is discussed in Bedregal et al. (2013). If we were to consider a more conservative sample selection based on the minimum stellar mass measurable at $z \sim 2$ (the highest redshift in our sample) $M_* > 7.9 \times 10^{10} M_\odot$, our results would not change substantially (see Section 4). We verified that the stellar mass function of our galaxy sample is consistent with the one determined by Muzzin et al. (2013), for quiescent galaxies, at the same redshift. All galaxies have accurate luminosity-weighted stellar ages derived fitting the grism spectra with SPMs. Using the same set of simulations performed by Bedregal et al. (2013) we find that for our sample, the stellar ages are recovered with an accuracy of 35%.

3. SIZE ANALYSIS

For the structural analysis of the light distribution of our sample galaxies we use the deeper J_{110} images. The sky background has been previously subtracted as discussed in Atek et al. (2010) and Colbert et al. (2013). We perform the measurements with two different fitting algorithms: the widely used GALFIT code (Peng et al. 2010) and the alternative GASP2D code (Méndez-Abreu et al. 2008). To be consistent with previous works in the field, we fit the galaxy light distribution with a single Sérsic law (Sérsic 1963).

Both codes require as input the instrumental Point-spread Function (PSF). Our data were taken in parallel to observations performed with the Cosmic Origin Spectrograph and Space Telescope Imaging Spectrograph, and no spatial dithering was done in between different exposures. Because of this, the final PSF is undersampled at the pixel size ($0''.13 \text{ pixel}^{-1}$) of the WFC3-IR camera. We provide both GALFIT and GASP2D with a PSF that we obtained as the median of 18 unsaturated

stars across the 27 analyzed fields. We used this median PSF to fit individual stars in each field, and found residuals of at most 20%, irrespective of the field. Before fitting the galaxies, we masked any foreground and background sources, as well as detector artifacts that can contaminate the surface brightness distribution. The main differences between the two codes is in the way the initial values for the parameters are determined. GALFIT does not provide a way to estimate them, while GASP2D internally determines their values by performing a fit on the one-dimensional surface brightness profile obtained using the IRAF task `ellipse` (see Méndez-Abreu et al. 2008 for details). We visually inspected all the residuals to check for the reliability of the fits and we find that for each sample galaxy they are lower than 20%.

The galaxy effective radii (r_e) measured with the two algorithms are consistent within the uncertainties. In the following analysis we use the sizes determined by GASP2D, but our conclusions would not change if we switch to GALFIT instead. For each galaxy we compute the circularized effective radius as $r_e^{\text{circ}} = r_e \sqrt{q}$, where q is the galaxy axial ratio.

We determine the uncertainties associated with the r_e measurements through Monte Carlo simulations. We created 1000 artificial galaxies with Sérsic parameters randomly chosen in the range of values observed for real galaxies (total magnitude $19 \leq m_{\text{tot}} \leq 24$, effective radius $0''.1 \leq r_e \leq 1''.5$, Sérsic index $0.5 \leq n \leq 12$, axial ratio $0.2 \leq q \leq 1$, position angle $0^\circ \leq PA \leq 180^\circ$). All the models were convolved with the PSF image and we added Poisson noise to reproduce the observations. The best-fit Sérsic parameters were then derived using both GALFIT and GASP2D.

For each parameter, we estimated the fractional uncertainty as

$$\epsilon = \frac{p_{\text{out}} - p_{\text{in}}}{p_{\text{out}}}, \quad (1)$$

where p_{out} is the fitted parameter and p_{in} is the input value. We then computed the median and the 16th and 84th percentiles in bins of p_{out} , to estimate the systematics together with upper and lower uncertainties on the parameters. We excluded from the sample two galaxies with output effective radii smaller than 1 kpc since we believe that $r_e < 1$ kpc values are not reliable, and we therefore set 1 kpc as the minimum size we are able to resolve. With Monte Carlo simulations we also checked that galaxies with $r_e < 1$ kpc do not enter the sample with an overestimated size. This limit is higher than similar depth surveys performed with WFC3: it results from the lack of spatial dithering between exposures. With simulations we quantify the impact of this size limit on our results (Section 4). The uncertainty associated with the circularized radius is calculated as $\epsilon_{r_e^{\text{circ}}} = \epsilon_{r_e} \sqrt{q}$, because we find that the axial ratio uncertainty is negligible.

The Sérsic best-fit circularized half-light radius, Sérsic index, stellar mass, stellar age and redshift for each galaxy in the final sample are presented in Table 1. We notice that half of the galaxies in our sample have a Sérsic index $n < 2.5$, typically associated with disk-dominated galaxies, in agreement with, e.g., van der Wel et al. (2011) and Newman et al. (2014, hereafter N14).

Table 1
Circularized Effective Radius, Sérsic Index, Stellar Mass, Age, and Redshift of the Galaxies in the Final Sample

Galaxy	r_e^{circ} (kpc)	n	$\log(M_*/M_\odot)$	Age (Gyr)	z
(1)	(2)	(3)	(4)	(5)	(6)
Par66 ID135	1.33 ± 0.35	2.24	11.24	2.00	1.80
Par67 ID108	1.05 ± 0.33	1.07	10.71	1.02	1.35
Par67 ID140	1.75 ± 0.38	0.72	11.30	2.75	2.05
Par67 ID82	1.36 ± 0.26	2.29	11.08	4.00	1.35
Par73 ID152	2.71 ± 1.19	1.23	10.74	2.75	1.50
Par73 ID47	2.74 ± 0.17	4.03	11.16	0.90	1.45
Par73 ID57	1.67 ± 0.51	1.35	11.22	0.90	1.60
Par74 ID37	2.54 ± 0.82	1.72	11.44	2.50	1.60
Par76 ID26	2.32 ± 1.02	7.38	11.77	4.25	1.40
Par76 ID41	2.29 ± 0.84	0.74	11.26	4.75	1.35
Par76 ID60	2.96 ± 1.15	3.54	11.73	3.50	1.70
Par76 ID62	1.64 ± 0.59	17.53	11.50	3.50	1.70
Par76 ID77	1.23 ± 0.37	0.69	11.31	0.45	2.05
Par79 ID19	3.06 ± 0.70	7.92	11.55	2.20	1.35
Par79 ID86	1.53 ± 0.61	8.76	11.05	1.02	1.90
Par80 ID28	5.04 ± 0.56	4.15	11.43	4.00	1.40
Par80 ID35	1.73 ± 0.54	3.33	11.14	1.61	1.55
Par80 ID50	2.19 ± 0.51	1.10	11.17	3.00	1.40
Par80 ID93	4.13 ± 0.79	2.92	11.04	3.50	1.85
Par84 ID57	1.83 ± 0.57	2.09	11.43	4.00	1.45
Par87 ID118	3.14 ± 0.40	5.14	11.38	2.20	1.70
Par87 ID125	1.34 ± 0.53	7.29	10.66	0.40	1.85
Par87 ID54	1.28 ± 0.35	1.25	11.34	3.00	1.50
Par87 ID87	1.50 ± 0.53	6.05	11.12	2.00	1.65
Par87 ID95	2.73 ± 0.35	0.83	10.71	1.02	1.60
Par96 ID62	1.28 ± 0.35	2.47	10.91	1.02	1.75
Par115 ID83	2.04 ± 0.45	2.66	11.01	1.80	1.65
Par120 ID64	1.74 ± 0.54	3.43	11.23	1.61	1.50
Par120 ID84	4.01 ± 1.60	2.21	11.28	2.20	1.65
Par136 ID55	2.79 ± 1.22	2.11	10.68	0.90	1.65
Par136 ID77	3.55 ± 0.62	0.90	10.84	1.14	1.65
Par147 ID46	2.38 ± 1.04	2.52	11.02	0.64	1.46

Notes. Col. (1): galaxy name defined as in Bedregal et al. (2013). Col. (2): circularized effective radius with associated relative error. Col. (3): Sérsic index. Col. (4): logarithm of the stellar mass. Col. (5): age. Col. (6): redshift.

4. RESULTS AND DISCUSSION

We compare the stellar mass and size of our galaxies with those in the literature in the top panel of Figure 1. Before placing the literature data on the mass–size plane, we homogenized all the masses to Salpeter initial mass function (IMF, Salpeter 1955)¹⁷ and corrected them for the systematics implied by the different ages of the adopted synthetic stellar population models (SPMs). We scaled all masses to the Bruzual & Charlot (2003) SPMs, adopting the Salimbeni et al. (2009) relations $\log(M_{M05}) \simeq \log(M_{CB07})$ and $\log(M_{M05,CB07}) = \log(M_{BC03}) - 0.2$ where BC03, M05, and CB07 indicate Bruzual & Charlot (2003), Maraston (2005), and Bruzual et al. (2007) SPMs, respectively.

We limit the comparison to only those works where the sample selection is based on the galaxy specific star formation rates and that span a similar redshift range to ours. The only exception is the Mancini et al. (2010) sample, where a

¹⁷ The scaling factors between the Chabrier (2003), Kroupa (2001) and Salpeter (1955) IMFs that we adopted are: $\log(M_{\text{Chabrier}}) = \log(M_{\text{Kroupa}}) - 0.04$ (Cimatti et al. 2008) and $\log(M_{\text{Chabrier}}) = \log(M_{\text{Salpeter}}) - 0.25$ (Salimbeni et al. 2009).

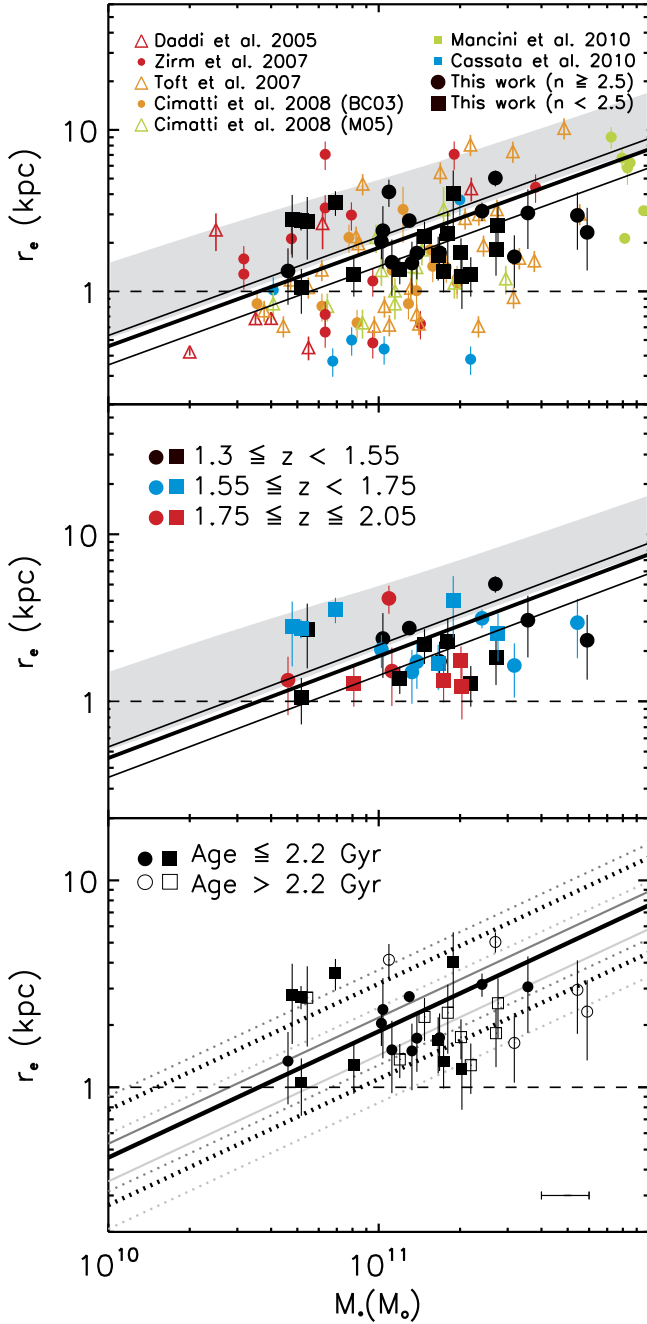


Figure 1. The mass–size relation measured with the WISP data at $z \sim 1.5$. We show circularized effective radius vs. stellar mass for the present sample (black symbols), with a distinction based on the Sérsic index (circles and squares), and compare the results drawn from the literature. Top: circularized effective radius vs. stellar mass. The local mass–size relation and its scatter (from Shen et al. 2003) are shown, for illustrative purposes, as a gray band. The solid thick line shows the best-fit mass–size relation from N14, computed at $z = 1.5$, while the thin lines were computed at the lowest (1.35) and highest (2.05) redshifts of our sample galaxies. All the galaxy radii shown here are circularized, except for those by Mancini et al. (2010). Middle: same as top panel, but showing our sample in three groups of redshift (black, blue, and red symbols). Again we separate galaxies with low and high Sérsic index (circles and squares). Bottom: same as the top panel, but showing our sample in two groups of stellar age (filled and empty symbols). In the bottom right corner we show the median uncertainty in stellar mass for our sample of galaxies (Bedregal et al. 2013). Our effective radii measurement limits are shown (dashed line).

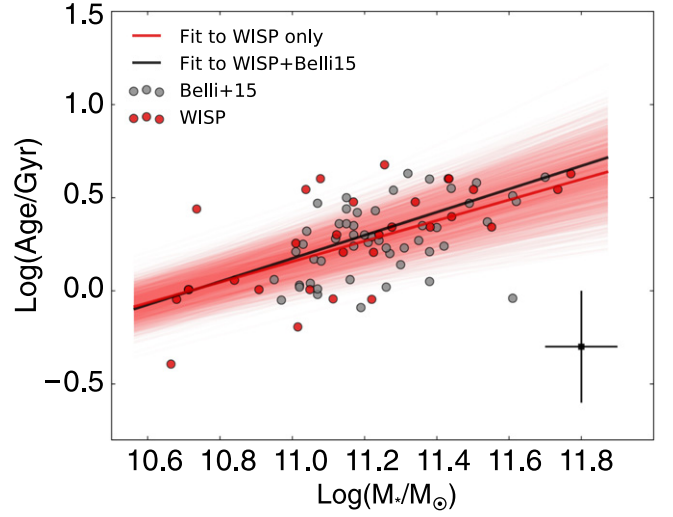


Figure 2. Stellar age and mass of quenched galaxies are strongly correlated. Stellar age as a function of stellar mass for the WISP galaxies (red points) and Belli et al. (2015) sample (gray points). Belli et al. (2015) stellar masses were converted to Salpeter IMF following Salimbeni et al. (2009). The best-fit lines to the WISP sample alone and to the combined WISP and Belli et al. (2015) samples are shown with red and black lines, respectively. The red band shows the uncertainty on the fit to the WISP data alone (the uncertainty on the fit to the combined sample is similar, and not shown for clarity).

morphological selection criterion (based on the Sérsic index) was also applied. Figure 1 shows that our measurements are consistent with the results found at similar redshifts by other works in different fields, once the size lower-limit (dashed horizontal line) is considered. The thick solid line shows the best-fit mass–size relation derived by N14 for field galaxies, computed at the median redshift of the sample. The thin lines were computed at the lowest and highest redshifts of our sample galaxies.

In the bottom panel of Figure 1 we reproduce the mass–size relation for our galaxies, dividing the sample into old (stellar age > 2.1 Gyr) and young objects (age ≤ 2.1 Gyr). The age separation was chosen to divide the galaxies in two similar size samples. Figure 1 shows how the most massive galaxies ($M_* > 2 \times 10^{11} M_\odot$) tend to be older than less massive ones, a trend compatible with other observational results indicating that more massive galaxies form the bulk of their stars earlier (e.g., Thomas et al. 2005; Kaviraj et al. 2013). We quantify this trend in Figure 2, where we show the stellar age versus the stellar mass, for the galaxies in our sample as well as for a sample of similarly selected objects identified by Belli et al. (2015). The correlation between the stellar population age and mass has a Spearman correlation coefficient of 0.66, which has a probability of 10^{-5} of resulting by chance. At any stellar mass, the stellar age (A_M) can be expressed as: $\log(A_M/\text{Gyr}) = (0.55 \pm 0.09)\log M_{10.5} - (0.12 \pm 0.07)$, where $M_{10.5}$ is the stellar mass in units of $10^{10.5} M_\odot$.

To quantify whether a trend between the stellar age and the deviation from the $z \sim 1.5$ mass–size relation exists we compute for each galaxy the parameter $\Delta_{\text{lr}} = \log(R_{\text{obs}}/R_{M,z})$, i.e., the vertical difference between the observed galaxy size (R_{obs}) and the size expected from the galaxy’s redshift and stellar mass ($R_{M,z}$), using the N14 mass–size relation. Values of $\Delta_{\text{lr}} > 0$ (< 0) indicate that galaxies are above (below) the mass–size relation at the galaxy redshift. The distributions of Δ_{lr} for the old and young galaxies with $M_* > 4.5 \times 10^{10} M_\odot$

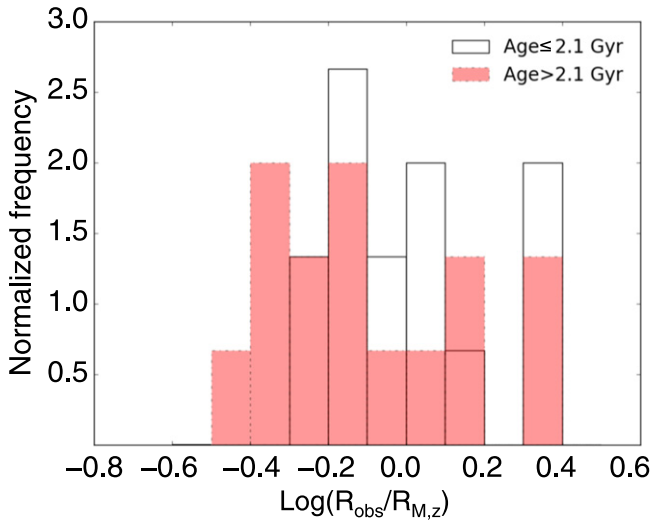


Figure 3. Distribution of Δ_{ir} for the WISP passive galaxies. Although the distributions of young and old galaxies have different median values, they are not statistically different. Pink and white lines represent old and young galaxies, respectively (see text for details).

are shown in Figure 3. The medians of the two distributions are $-0.02^{+0.36}_{-0.16}$ and $-0.13^{+0.31}_{-0.21}$, for the young and old samples, respectively (the upper and lower range show the 84th and 16th percentiles). The result of a two-sample Kolmogorov–Smirnov (KS) test ($D_{\text{KS}} = 0.3$ and $p = 0.3$), however, indicates that we cannot exclude that the two samples are drawn from the same parent distribution and thus the observed age difference is not significant. More conservatively considering only galaxies with $M_* > 7.9 \times 10^{10} M_{\odot}$ we obtain consistent results (the medians of the young and old galaxy distributions of Δ_{ir} are $-0.10^{+0.09}_{-0.16}$ and $-0.18^{+0.17}_{-0.14}$, respectively).

The size measurement limit ($r_e > 1$ kpc), together with the observed dependency between the galaxy stellar age and mass, may introduce a bias, particularly at the smallest masses, where our galaxies tend to populate the mass–size plane above the best-fit relation derived at similar redshifts (N14). To test to what extent we can detect with our data a possible trend of the distance from the best-fit mass–size relation with age, we performed a simulation that accounts for both the size selection bias and the observed mass–age trend. We generated 1000 samples of 32 galaxies with masses and half-light radii distributed according to the field mass–size relation and its scatter, determined by N14 at $z \sim 1.5$. To each galaxy we assign an age (A) that depends on its stellar mass and the distance to the mass–size relation, such that $A = A_M + \alpha \Delta_{\text{ir}}$. We randomize the simulated ages and stellar masses according to the typical uncertainties of our observations. We then apply the WISP survey limits to the simulated galaxy samples (i.e., $M_* > 4.5 \times 10^{10} M_{\odot}$, and $r_e \geq 1$ kpc), and recompute the distributions of Δ_{ir} for the subsamples of old and young galaxies. For each of the 1000 samples we performed the same analysis described above, and compute the KS test between the distributions of Δ_{ir} for the young and old subsamples. For $\alpha = 0$ (i.e., no correlation), we find that only 10% of the simulated samples show detectable differences between the old and young galaxies, due to our size limit and the correlation between the age and stellar mass. We consider decreasing values of α in steps of 0.1, from zero to the α that produces distinguishable distributions. Our simulations show that for any

$\alpha < -0.64$ we would be able to recover the difference between old and young populations at the 95% confidence level in more than 85% of the simulated samples. Repeating the same simulations and applying a mass limit $M_* > 7.9 \times 10^{10} M_{\odot}$, we find $\alpha < -0.7$. Our data, therefore, suggest that the relation between the galaxy age and its distance from the mass–size relation, if it exists, must have $\alpha > -0.64$. Performing these simulations considering the galaxies formation redshift (z_f) instead of age, given the observed redshift and the current cosmology, we conclude that, if a relation $R \sim (1 + z_f)^{\beta}$ exists, then it must be $\beta > -0.67$, otherwise we would have detected the correlation with our current sample.

5. CONCLUSIONS

We studied the mass–size relation of a sample of 32 passive galaxies at $z \sim 1.5$ selected from the WISP survey to have $\text{sSFR} < 0.01 \text{ Gyr}^{-1}$ and $M_* > 4.5 \times 10^{10} M_{\odot}$. All galaxies have accurately determined stellar ages from fitting the galaxy rest-frame optical spectra with SPMs (Bedregal et al. 2013). We investigate whether younger galaxies have preferentially larger sizes than older ones with the same stellar mass. Such an observation would indicate that the mass–size relation evolves due to the appearance of newly quenched large objects in passive samples.

Dividing our sample into young and old galaxies we find no significant difference in the distributions of Δ_{ir} , suggesting that the appearance of newly quenched galaxies may not be the dominant mechanism for the evolution of the mass–size relation. Our simulations also indicate that, if a relation exists between the galaxy age and the distance to the mass–size relation, it has a slope $\alpha > -0.64$, otherwise we would have detected it. It translates into a slope of the galaxies size-formation redshift relation $\beta > -0.67$, given the current cosmology. If we consider in our analysis more conservatively only galaxies with $M_* > 7.9 \times 10^{10} M_{\odot}$ we obtain consistent results.

Our results suggest that the evolution of the mass–size relation of quiescent galaxies is mainly due to the physical growth of individual sources. Recently, Belli et al. (2015) have found that progenitor bias can explain half of the size growth of compact ETGs and that the remaining observed size evolution arises from a genuine growth of individual galaxies. The discrepancy is likely due to the fact that they include in the sample “green valley” sources, with $\text{sSFR} < 0.1 \text{ Gyr}^{-1}$, while we limit the analysis to those galaxies with $\text{sSFR} < 0.01 \text{ Gyr}^{-1}$. In fact, it is exactly these sources with higher sSFR that drive the correlation between the age and the size evolution (see Figure 9 in Belli et al. 2015). Our finding is in contradiction with works implying a slope of $\beta \sim -1$ for the size-formation redshift relation and suggesting that galaxies sizes scale as the density of the universe at the time when they formed (e.g., Saracco et al. 2011; Carollo et al. 2013; Cassata et al. 2013). Our results are instead in agreement with the ones by Trujillo et al. (2011) and Whitaker et al. (2012), which do not see any age segregation depending on the galaxy size. Sonnenfeld et al. (2014) suggest that the observed size growth cannot be explained with models invoking only dry merger, because they would result in a strong flattening of the mass density profile with time. This flattening is not observed in the samples of strong lenses for which the total mass–density profile could be constrained (Sonnenfeld et al. 2014). The size growth could

instead be due to a combination of dry and wet minor mergers: the outer regions of massive ETGs could grow via the accretion of stars and dark matter, while a small amount of nuclear star formation could keep the mass density profile constant with time (e.g., Rutkowski et al. 2014).

We thank the referee for constructive comments that improved the analysis of the results. We thank Francesco Valentino, Emeric Le Floch, and Emanuele Daddi for useful discussions. E.M.C. and E.D.B. are supported by Padua University through grants 60A02-5857/13, 60A02-5833/14, 60A02-4434/15, and CPDA133894.

REFERENCES

- Atek, H., Malkan, M., McCarthy, P., et al. 2010, *ApJ*, **723**, 104
- Bedregal, A. G., Scarlata, C., Henry, A. L., et al. 2013, *ApJ*, **778**, 126
- Belli, S., Newman, A. B., & Ellis, R. S. 2015, *ApJ*, **799**, 206
- Bernardi, M., Shankar, F., Hyde, J. B., et al. 2010, *MNRAS*, **404**, 2087
- Bruzual, G. 2007, arXiv:astro-ph/0703052
- Bruzual, G., & Charlot, S. 2003, *MNRAS*, **344**, 1000
- Carollo, C. M., Bschorr, T. J., Renzini, A., et al. 2013, *ApJ*, **773**, 112
- Cassata, P., Giavalisco, M., Guo, Y., et al. 2010, *ApJL*, **714**, L79
- Cassata, P., Giavalisco, M., Guo, Y., et al. 2011, *ApJ*, **743**, 96
- Cassata, P., Giavalisco, M., Williams, C. C., et al. 2013, *ApJ*, **775**, 106
- Chabrier, G. 2003, *PASP*, **115**, 763
- Cimatti, A., Cassata, P., Pozzetti, L., et al. 2008, *A&A*, **482**, 21
- Colbert, J. W., Teplitz, H., Atek, H., et al. 2013, *ApJ*, **779**, 34
- Daddi, E., Renzini, A., Pirzkal, N., et al. 2005, *ApJ*, **626**, 680
- Fan, L., Lapi, A., Bressan, A., et al. 2010, *ApJ*, **718**, 1460
- Hopkins, P. F., Bundy, K., Murray, N., et al. 2009, *MNRAS*, **398**, 898
- Kaviraj, S., Cohen, S., Ellis, R. S., et al. 2013, *MNRAS*, **428**, 925
- Keating, S. K., Abraham, R. G., Schiavon, R., et al. 2015, *ApJ*, **798**, 26
- Kroupa, P. 2001, *MNRAS*, **322**, 231
- Kümmel, M., Walsh, J. R., Pirzkal, N., Kuntschner, H., & Pasquali, A. 2009, *PASP*, **121**, 59
- López-Sanjuan, C., Le Fèvre, O., Ilbert, O., et al. 2012, *A&A*, **548**, A7
- Mancini, C., Daddi, E., Renzini, A., et al. 2010, *MNRAS*, **401**, 933
- Maraston, C. 2005, *MNRAS*, **362**, 799
- Méndez-Abreu, J., Aguerri, J. A. L., Corsini, E. M., & Simonneau, E. 2008, *A&A*, **478**, 353
- Muzzin, A., Marchesini, D., Stefanon, M., et al. 2013, *ApJ*, **777**, 18
- Naab, T., Johansson, P. H., & Ostriker, J. P. 2009, *ApJL*, **699**, L178
- Newman, A. B., Ellis, R. S., Andreon, S., et al. 2014, *ApJ*, **788**, 51
- Newman, A. B., Ellis, R. S., Bundy, K., & Treu, T. 2012, *ApJ*, **746**, 162
- Nipoti, C., Treu, T., Leauthaud, A., et al. 2012, *MNRAS*, **422**, 1714
- Oke, J. B., & Gunn, J. E. 1983, *ApJ*, **266**, 713
- Oser, L., Naab, T., Ostriker, J. P., & Johansson, P. H. 2012, *ApJ*, **744**, 63
- Peng, Y.-j., Lilly, S. J., Kovač, K., et al. 2010, *ApJ*, **721**, 193
- Poggianti, B. M., Calvi, R., Bindoni, D., et al. 2012, arXiv:1212.3207
- Poggianti, B. M., Moretti, A., Calvi, R., et al. 2013, *ApJ*, **777**, 125
- Ragone-Figueroa, C., & Granato, G. L. 2011, *MNRAS*, **414**, 3690
- Rutkowski, M. J., Jeong, H., Cohen, S. H., et al. 2014, *ApJ*, **794**, 101
- Salimbeni, S., Fontana, A., Giallongo, E., et al. 2009, in AIP Conf. Ser. 1111, ed. G. Giobbi et al. (Melville, NY: AIP), 207
- Salpeter, E. E. 1955, *ApJ*, **121**, 161
- Saracco, P., Longhetti, M., & Gargiulo, A. 2011, *MNRAS*, **412**, 2707
- Sérsic, J. L. 1963, *BAAA*, **6**, 41
- Shen, S., Mo, H. J., White, S. D. M., et al. 2003, *MNRAS*, **343**, 978
- Sonnenfeld, A., Nipoti, C., & Treu, T. 2014, *ApJ*, **786**, 89
- Thomas, D., Maraston, C., Bender, R., & Mendes de Oliveira, C. 2005, *ApJ*, **621**, 673
- Trujillo, I., Cenarro, A. J., de Lorenzo-Cáceres, A., et al. 2009, *ApJL*, **692**, L118
- Trujillo, I., Conselice, C. J., Bundy, K., et al. 2007, *MNRAS*, **382**, 109
- Trujillo, I., Ferreras, I., & de La Rosa, I. G. 2011, *MNRAS*, **415**, 3903
- Valentinuzzi, T., Poggianti, B. M., Saglia, R. P., et al. 2010, *ApJL*, **721**, L19
- van der Wel, A., Franx, M., van Dokkum, P. G., et al. 2014, *ApJ*, **788**, 28
- van der Wel, A., Rix, H.-W., Wuyts, S., et al. 2011, *ApJ*, **730**, 38
- van Dokkum, P. G., Bezanson, R., van der Wel, A., et al. 2014, *ApJ*, **791**, 45
- Whitaker, K. E., Kriek, M., van Dokkum, P. G., et al. 2012, *ApJ*, **745**, 179

List of Abbreviations

AGN: Active Galactic Nuclei
CEA: Commissariat à l'Énergie Atomique et aux énergies alternatives
CFR: Clumps Formation Rate
co-I: co-Investigator
ETG: Early-Type Galaxy
EW: Equivalent width
FWHM: Full Width at Half Maximum
HST: Hubble Space Telescope
IMF: Initial Mass Function
IR: Infrared
ISM: Interstellar Medium
MS: Main-Sequence
M/L: Mass-to-Light ratio
PI: Principal Investigator
PSF: Point-Spread Function
SED: spectral Energy Distribution
SFE: Star Formation Efficiency
SFH: Star Formation History
SFR: Star Formation Rate
SLED: Spectral Line Energy Distribution
SN: Supernova
sSFR: Specific Star Formation Rate
S/N: Signal-to-Noise ratio
UV: Ultraviolet
VLT: Very Large Telescope
WFC3: Wide Field Camera 3
WISP: WFC3 Infrared Spectroscopic Parallel
2D: Two-Dimensional

Bibliography

- Abraham, R. G., van den Bergh, S., Glazebrook, K., et al. 1996, *ApJS*, 107, 1
- Agertz, O., Teyssier, R., & Moore, B. 2009, *MNRAS*, 397, L64
- Amorín, R., Grazian, A., Castellano, M., et al. 2014, *ApJL*, 788, L4
- Atek, H., Malkan, M., McCarthy, P., et al. 2010, *ApJ*, 723, 104
- Baldwin, J. A., Phillips, M. M., & Terlevich, R. 1981, *PASP*, 93, 5
- Barro, G., Faber, S. M., Pérez-González, P. G., et al. 2014, *ApJ*, 791, 52
- Baugh, C. M., Lacey, C. G., Frenk, C. S., et al. 2005, *MNRAS*, 356, 1191
- Beckwith, S. V., Stiavelli, M., Koekemoer, A. M., et al. 2006, *AJ*, 132, 1729
- Bedregal, A. G., Scarlata, C., Henry, A. L., et al. 2013, *ApJ*, 778, 126
- Belli, S., Newman, A. B., & Ellis, R. S. 2015, *ApJ*, 799, 206
- Bernardi, M., Shankar, F., Hyde, J. B., et al. 2010, *MNRAS*, 404, 2087
- Bertin, E., & Arnouts, S. 1996, *A&AS*, 117, 393
- Binette, L., Dopita, M. A., & Tuohy, I. R. 1985, *ApJ*, 297, 476
- Birnboim, Y., & Dekel, A. 2003, *MNRAS*, 345, 349
- Bournaud, F. 2016, *Bulge Growth Through Disc Instabilities in High-Redshift Galaxies*, ed. E. Laurikainen, R. Peletier, & D. Gadotti, Vol. 418 (Switzerland: Springer), 355
- Bournaud, F., Daddi, E., Elmegreen, B. G., et al. 2008, *A&A*, 486, 741
- Bournaud, F., Daddi, E., Weiß, A., et al. 2015, *A&A*, 575, A56
- Bournaud, F., Dekel, A., Teyssier, R., et al. 2011, *ApJL*, 741, L33
- Bournaud, F., Elmegreen, B. G., & Elmegreen, D. M. 2007, *ApJ*, 670, 237
- Bournaud, F., Elmegreen, B. G., & Martig, M. 2009, *ApJL*, 707, L1
- Bournaud, F., Perret, V., Renaud, F., et al. 2014, *ApJ*, 780, 57
- Brewer, B. J., Dutton, A. A., Treu, T., et al. 2012, *MNRAS*, 422, 3574
- Brusa, M., Comastri, A., Daddi, E., et al. 2005, *A&A*, 432, 69
- Bruzual, A. G. 2007, in *IAU Symposium, Stellar Populations as Building Blocks of Galaxies*, ed. A. Vazdekis, & R. Peletier, Vol. 241 (Cambridge, MA: Cambridge University Press), 125
- Bruzual, G., & Charlot, S. 2003, *MNRAS*, 344, 1000

- Buitrago, F., Trujillo, I., Conselice, C. J., & Häußler, B. 2013, *MNRAS*, 428, 1460
- Caccianiga, A., Marchã, M. J., Thean, A., & Dennett-Thorpe, J. 2001, *MNRAS*, 328, 867
- Calzetti, D., Armus, L., Bohlin, R. C., et al. 2000, *ApJ*, 533, 682
- Campisi, M. A., Vignali, C., Brusa, M., et al. 2009, *A&A*, 501, 485
- Caon, N., Capaccioli, M., & D’Onofrio, M. 1993, *MNRAS*, 265, 1013
- Cappellari, M. 2002, *MNRAS*, 333, 400
- Cappellari, M., McDermid, R. M., Alatalo, K., et al. 2012, *Nature*, 484, 485
- Cardelli, J. A., Clayton, G. C., & Mathis, J. S. 1989, *ApJ*, 345, 245
- Carollo, C. M., Bschorr, T. J., Renzini, A., et al. 2013, *ApJ*, 773, 112
- Cassata, P., Giavalisco, M., Guo, Y., et al. 2010, *ApJL*, 714, L79
- Cassata, P., Giavalisco, M., Guo, Y., et al. 2011, *ApJ*, 743, 96
- Cassata, P., Giavalisco, M., Williams, C. C., et al. 2013, *ApJ*, 775, 106
- Ceverino, D., Dekel, A., & Bournaud, F. 2010, *MNRAS*, 404, 2151
- Ceverino, D., Dekel, A., Mandelker, N., et al. 2012, *MNRAS*, 420, 3490
- Ceverino, D., Klypin, A., Klimek, E. S., et al. 2014, *MNRAS*, 442, 1545
- Chabrier, G. 2003, *PASP*, 115, 763
- Cibinel, A., Le Floch, E., Perret, V., et al. 2015, *ApJ*, 805, 181
- Cid Fernandes, R., & González Delgado, R. M. 2010, *MNRAS*, 403, 780
- Cid Fernandes, R., Stasińska, G., Mateus, A., & Vale Asari, N. 2011, *MNRAS*, 413, 1687
- Cimatti, A., Cassata, P., Pozzetti, L., et al. 2008, *A&A*, 482, 21
- Cimatti, A., Daddi, E., & Renzini, A. 2006, *A&A*, 453, L29
- Colbert, J. W., Teplitz, H., Atek, H., et al. 2013, *ApJ*, 779, 34
- Conroy, C., & van Dokkum, P. G. 2012, *ApJ*, 760, 71
- Conselice, C. J. 2003, *ApJS*, 147, 1
- . 2014, *ARA&A*, 52, 291
- Conselice, C. J., Blackburne, J. A., & Papovich, C. 2005, *ApJ*, 620, 564
- Cowie, L. L., Songaila, A., Hu, E. M., & Cohen, J. G. 1996, *AJ*, 112, 839
- Daddi, E., Bournaud, F., Walter, F., et al. 2010, *ApJ*, 713, 686
- Daddi, E., Dannerbauer, H., Liu, D., et al. 2015, *A&A*, 577, A46
- Daddi, E., Renzini, A., Pirzkal, N., et al. 2005, *ApJ*, 626, 680
- Davis, M., Guhathakurta, P., Konidaris, N. P., et al. 2007, *ApJL*, 660, L1
- De Lucia, G., Springel, V., White, S. D., Croton, D., & Kauffmann, G. 2006, *MNRAS*, 366, 499
- Dekel, A., & Burkert, A. 2014, *MNRAS*, 438, 1870
- Dekel, A., Sari, R., & Ceverino, D. 2009, *ApJ*, 703, 785
- Dressler, A., Faber, S. M., Burstein, D., et al. 1987, *ApJL*, 313, L37
- Eggen, O. J., Lynden-Bell, D., & Sandage, A. R. 1962, *ApJ*, 136, 748

- Elmegreen, B. G., Bournaud, F., & Elmegreen, D. M. 2008, *ApJ*, 688, 67
- Elmegreen, B. G., & Burkert, A. 2010, *ApJ*, 712, 294
- Elmegreen, B. G., & Elmegreen, D. M. 2005, *ApJ*, 627, 632
- Elmegreen, B. G., Elmegreen, D. M., Fernandez, M. X., & Lemonias, J. J. 2009, *ApJ*, 692, 12
- Elmegreen, B. G., Elmegreen, D. M., Knapen, J. H., et al. 2007, *ApJL*, 670, L97
- Elmegreen, B. G., Elmegreen, D. M., Sánchez Almeida, J., et al. 2013, *ApJ*, 774, 86
- Elmegreen, D. M., Elmegreen, B. G., & Hirst, A. C. 2004, *ApJL*, 604, L21
- Epinat, B., Tasca, L., Amram, P., et al. 2012, *A&A*, 539, A92
- Fan, L., Lapi, A., Bressan, A., et al. 2010, *ApJ*, 718, 1460
- Ferland, G. J., Porter, R. L., van Hoof, P. A., et al. 2013, *Revista Mexicana de Astronomia y Astrofisica*, 49, 137
- Forbes, J. C., Krumholz, M. R., Burkert, A., & Dekel, A. 2014, *MNRAS*, 438, 1552
- Förster Schreiber, N. M., Genzel, R., Bouché, N., et al. 2009, *ApJ*, 706, 1364
- Förster Schreiber, N. M., Genzel, R., Newman, S. F., et al. 2014, *ApJ*, 787, 38
- Förster Schreiber, N. M., Shapley, A. E., Genzel, R., et al. 2011, *ApJ*, 739, 45
- Fruchter, A. S., & Hook, R. N. 2002, *PASP*, 114, 144
- Gabor, J. M., & Bournaud, F. 2013, *MNRAS*, 434, 606
- Genel, S., Naab, T., Genzel, R., et al. 2012, *ApJ*, 745, 11
- Genzel, R., Burkert, A., Bouché, N., et al. 2008, *ApJ*, 687, 59
- Genzel, R., Förster Schreiber, N. M., Lang, P., et al. 2014, *ApJ*, 785, 75
- Genzel, R., Newman, S., Jones, T., et al. 2011, *ApJ*, 733, 101
- Genzel, R., Tacconi, L. J., Eisenhauer, F., et al. 2006, *Nature*, 442, 786
- Genzel, R., Tacconi, L. J., Gracia-Carpio, J., et al. 2010, *MNRAS*, 407, 2091
- Giavalisco, M., Ferguson, H. C., Koekemoer, A. M., et al. 2004, *ApJL*, 600, L93
- Gobat, R., Daddi, E., Onodera, M., et al. 2011, *A&A*, 526, A133
- Gobat, R., Strazzullo, V., Daddi, E., et al. 2013, *ApJ*, 776, 9
- Grogin, N. A., Kocevski, D. D., Faber, S. M., et al. 2011, *ApJS*, 197, 35
- Guo, Y., Ferguson, H. C., Bell, E. F., et al. 2015, *ApJ*, 800, 39
- Guo, Y., Giavalisco, M., Ferguson, H. C., Cassata, P., & Koekemoer, A. M. 2012, *ApJ*, 757, 120
- Hong, S., Calzetti, D., Gallagher III, J. S., et al. 2013, *ApJ*, 777, 63
- Hopkins, P. F., Bundy, K., Murray, N., et al. 2009, *MNRAS*, 398, 898
- Hopkins, P. F., Kereš, D., Murray, N., Quataert, E., & Hernquist, L. 2012, *MNRAS*, 427, 968
- Hopkins, P. F., Narayanan, D., & Murray, N. 2013, *MNRAS*, 432, 2647
- Hubble, E. P. 1936, *Realm of the Nebulae* (New Haven, CT: Yale University Press)

- Jones, T. A., Swinbank, A. M., Ellis, R. S., Richard, J., & Stark, D. P. 2010, *MNRAS*, 404, 1247
- Kashino, D., Silverman, J. D., Rodighiero, G., et al. 2013, *ApJL*, 777, L8
- Kaviraj, S., Cohen, S., Ellis, R. S., et al. 2013, *MNRAS*, 428, 925
- Keating, S. K., Abraham, R. G., Schiavon, R., et al. 2015, *ApJ*, 798, 26
- Kennicutt Jr., R. C. 1998, *ApJ*, 498, 541
- Kereš, D., Katz, N., Weinberg, D. H., & Davé, R. 2005, *MNRAS*, 363, 2
- Kewley, L. J., Geller, M. J., & Jansen, R. A. 2004, *AJ*, 127, 2002
- Klypin, A. A., Trujillo-Gomez, S., & Primack, J. 2011, *ApJ*, 740, 102
- Koekemoer, A. M., Faber, S. M., Ferguson, H. C., et al. 2011, *ApJS*, 197, 36
- Kormendy, J., & Bender, R. 2012, *ApJS*, 198, 2
- Kriek, M., van Dokkum, P. G., Labbé, I., et al. 2009, *ApJ*, 700, 221
- Kroupa, P. 2001, *MNRAS*, 322, 231
- Krumholz, M. R., Dekel, A., & McKee, C. F. 2012, *ApJ*, 745, 69
- Kümmel, M., Walsh, J. R., Pirzkal, N., Kuntschner, H., & Pasquali, A. 2009, *PASP*, 121, 59
- Lada, C. J., Lombardi, M., & Alves, J. F. 2010, *ApJ*, 724, 687
- Larson, R. B. 1975, *MNRAS*, 173, 671
- Leitherer, C., Schaerer, D., Goldader, J. D., et al. 1999, *ApJS*, 123, 3
- López-Sanjuan, C., Le Fèvre, O., Ilbert, O., et al. 2012, *A&A*, 548, A7
- Lotz, J. M., Primack, J., & Madau, P. 2004, *AJ*, 128, 163
- Madau, P., & Dickinson, M. 2014, *ARA&A*, 52, 415
- Magnelli, B., Lutz, D., Saintonge, A., et al. 2014, *A&A*, 561, A86
- Maiolino, R., Nagao, T., Grazian, A., et al. 2008, *A&A*, 488, 463
- Mancini, C., Daddi, E., Renzini, A., et al. 2010, *MNRAS*, 401, 933
- Mandelker, N., Dekel, A., Ceverino, D., et al. 2014, *MNRAS*, 443, 3675
- Mandelker, N., Dekel, A., Ceverino, D., et al. 2015, arXiv:1512.08791, *MNRAS*, submitted
- Mannucci, F., Basile, F., Poggianti, B. M., et al. 2001, *MNRAS*, 326, 745
- Maraston, C. 2005, *MNRAS*, 362, 799
- Martig, M., Bournaud, F., Teyssier, R., & Dekel, A. 2009, *ApJ*, 707, 250
- McCarthy, P. J. 2004, *ARA&A*, 42, 477
- Méndez-Abreu, J., Aguerri, J. A., Corsini, E. M., & Simonneau, E. 2008, *A&A*, 478, 353
- Mortlock, A., Conselice, C. J., Hartley, W. G., et al. 2013, *MNRAS*, 433, 1185
- Muzzin, A., Marchesini, D., Stefanon, M., et al. 2013, *ApJ*, 777, 18
- Naab, T., Johansson, P. H., & Ostriker, J. P. 2009, *ApJL*, 699, L178
- Newman, A. B., Ellis, R. S., Andreon, S., et al. 2014, *ApJ*, 788, 51
- Newman, A. B., Ellis, R. S., Bundy, K., & Treu, T. 2012a, *ApJ*, 746, 162
- Newman, S. F., Shapiro Griffin, K., Genzel, R., et al. 2012b, *ApJ*, 752, 111

- Nipoti, C., Treu, T., Leauthaud, A., et al. 2012, *MNRAS*, 422, 1714
- Noguchi, M. 1999, *ApJ*, 514, 77
- Oklopčić, A., Hopkins, P. F., Feldmann, R., et al. 2016, arXiv:1603.03778, *MNRAS*, submitted
- Onodera, M., Renzini, A., Carollo, M., et al. 2012, *ApJ*, 755, 26
- Oser, L., Naab, T., Ostriker, J. P., & Johansson, P. H. 2012, *ApJ*, 744, 63
- Osterbrock, D. E. 1989, *Astrophysics of gaseous nebulae and active galactic nuclei* (Mill Valley, CA: University Science Books)
- Panessa, F., Bassani, L., Cappi, M., et al. 2006, *A&A*, 455, 173
- Peebles, P. J. 1982, *ApJL*, 263, L1
- Peng, Y.-j., Lilly, S. J., Kovač, K., et al. 2010, *ApJ*, 721, 193
- Perret, V., Renaud, F., Epinat, B., et al. 2014, *A&A*, 562, A1
- Persic, M., Cappi, M., Rephaeli, Y., et al. 2004, *A&A*, 427, 35
- Poggianti, B. M., Calvi, R., Bindoni, D., et al. 2013a, *ApJ*, 762, 77
- Poggianti, B. M., Moretti, A., Calvi, R., et al. 2013b, *ApJ*, 777, 125
- Ragone-Figueroa, C., & Granato, G. L. 2011, *MNRAS*, 414, 3690
- Ravindranath, S., Ferguson, H. C., Conselice, C., et al. 2004, *ApJL*, 604, L9
- Renaud, F., Bournaud, F., Emsellem, E., et al. 2013, *MNRAS*, 436, 1836
- Renzini, A. 2006, *ARA&A*, 44, 141
- Rodighiero, G., Daddi, E., Baronchelli, I., et al. 2011, *ApJL*, 739, L40
- Salimbeni, S., Fontana, A., Giallongo, E., et al. 2009, in *American Institute of Physics Conference Series*, ed. G. Giobbi, A. Tornambe, G. Raimondo, et al., Vol. 1111 (Melville, NY: AIP), 207
- Salpeter, E. E. 1955, *ApJ*, 121, 161
- Sandage, A. 1961, *The Hubble atlas of galaxies* (Washington, DC: Carnegie Institution)
- Saracco, P., Longhetti, M., & Gargiulo, A. 2011, *MNRAS*, 412, 2707
- Sargent, M. T., Daddi, E., Béthermin, M., et al. 2014, *ApJ*, 793, 19
- Scalo, J. M., & Struck-Marcell, C. 1986, *ApJ*, 301, 77
- Scoville, N., Abraham, R. G., Aussel, H., et al. 2007, *ApJS*, 172, 38
- Sérsic, J. L. 1968, *Atlas de galaxias australes* (Cordoba, Argentina: Observatorio Astronomico)
- Shapiro, K. L., Genzel, R., & Förster Schreiber, N. M. 2010, *MNRAS*, 403, L36
- Shen, S., Mo, H. J., White, S. D., et al. 2003, *MNRAS*, 343, 978
- Sonnenfeld, A., Nipoti, C., & Treu, T. 2014, *ApJ*, 786, 89
- Soto, K. T., & Martin, C. L. 2012, *ApJS*, 203, 3
- Stadel, J., Potter, D., Moore, B., et al. 2009, *MNRAS*, 398, L21
- Steidel, C. C., Rudie, G. C., Strom, A. L., et al. 2014, *ApJ*, 795, 165
- Stern, J., & Laor, A. 2013, *MNRAS*, 431, 836
- Strazzullo, V., Gobat, R., Daddi, E., et al. 2013, *ApJ*, 772, 118

- Swinbank, A. M., Smail, I., Chapman, S. C., et al. 2010, *MNRAS*, 405, 234
- Tacchella, S., Lang, P., Carollo, C. M., et al. 2015, *ApJ*, 802, 101
- Tacconi, L. J., Genzel, R., Neri, R., et al. 2010, *Nature*, 463, 781
- Tamburello, V., Mayer, L., Shen, S., & Wadsley, J. 2015, *MNRAS*, 453, 2490
- Thomas, D., Maraston, C., Bender, R., & Mendes de Oliveira, C. 2005, *ApJ*, 621, 673
- Toomre, A. 1964, *ApJ*, 139, 1217
- . 1977, in *Evolution of Galaxies and Stellar Populations*, ed. B. M. Tinsley, & R. B. Larson D. Campbell (New Haven, CT: Yale University Observatory), 401
- Trenti, M., Bertin, G., & van Albada, T. S. 2005, *A&A*, 433, 57
- Trujillo, I., Cenarro, A. J., de Lorenzo-Cáceres, A., et al. 2009, *ApJL*, 692, L118
- Trujillo, I., Conselice, C. J., Bundy, K., et al. 2007, *MNRAS*, 382, 109
- Trujillo, I., Ferreras, I., & de La Rosa, I. G. 2011, *MNRAS*, 415, 3903
- Valentino, F., Daddi, E., Finoguenov, A., et al. 2016, arXiv:1605.03194, *ApJ*, submitted
- Valentino, F., Daddi, E., Strazzullo, V., et al. 2015, *ApJ*, 801, 132
- Valentinuzzi, T., Poggianti, B. M., Saglia, R. P., et al. 2010a, *ApJL*, 721, L19
- . 2010b, *ApJL*, 721, L19
- van Albada, T. S. 1982, *MNRAS*, 201, 939
- van den Bergh, S., Abraham, R. G., Ellis, R. S., et al. 1996, *AJ*, 112, 359
- van der Wel, A., Franx, M., van Dokkum, P. G., et al. 2014, *ApJ*, 788, 28
- van der Wel, A., Rix, H.-W., Wuyts, S., et al. 2011, *ApJ*, 730, 38
- van Dokkum, P. G. 2001, *PASP*, 113, 1420
- van Dokkum, P. G., Bezanson, R., van der Wel, A., et al. 2014, *ApJ*, 791, 45
- Vika, M., Bamford, S. P., Häußler, B., et al. 2013, *MNRAS*, 435, 623
- Wang, T., Elbaz, D., Daddi, E., et al. 2016, arXiv:1604.07404, *ApJ*, accepted
- Whitaker, K. E., Kriek, M., van Dokkum, P. G., et al. 2012, *ApJ*, 745, 179
- White, S. D., & Frenk, C. S. 1991, *ApJ*, 379, 52
- White, S. D., & Rees, M. J. 1978, *MNRAS*, 183, 341
- Williams, C. C., Giavalisco, M., Cassata, P., et al. 2014, *ApJ*, 780, 1
- Williams, R. E., Baum, S., Bergeron, L. E., et al. 2000, *AJ*, 120, 2735
- Worthey, G., Faber, S. M., & Gonzalez, J. J. 1992, *ApJ*, 398, 69
- Wuyts, S., Förster Schreiber, N. M., Genzel, R., et al. 2012, *ApJ*, 753, 114
- Wuyts, S., Förster Schreiber, N. M., Nelson, E. J., et al. 2013, *ApJ*, 779, 135
- Yoshikawa, T., Akiyama, M., Kajisawa, M., et al. 2010, *ApJ*, 718, 112
- Zahid, H. J., Kashino, D., Silverman, J. D., et al. 2014, *ApJ*, 792, 75
- Zanella, A., Daddi, E., Le Floch, E., et al. 2015, *Nature*, 521, 54
- Zanella, A., Scarlata, C., Corsini, E. M., et al. 2016, *ApJ*, 824, 68
- Zolotov, A., Dekel, A., Mandelker, N., et al. 2015, *MNRAS*, 450, 2327